Coherent Dynamics of Low Dimensional Quantum Fluids of Light and Matter

Ivan Amelio

Ph.D. thesis submitted to the University of Trento

Coherent Dynamics of Low Dimensional Quantum Fluids of Light and Matter

Ivan Amelio

A dissertation submitted to the
Department of Physics
University of Trento

In fulfilment of the requirements for the Degree of
Philosophiæ Doctor in Physics

Under the Supervision of
Dr. Iacopo Carusotto

Dottorato di Ricerca XXXIII ciclo
4 December 2020

Supervisor:

Iacopo Carusotto

Members of the committee:

Prof. Franco Dalfovo

Prof. Boubacar Kanté

Dr. Marzena Szymanska

Contents

Introduction **3**

Part I: Resonantly driven polariton fluids **8**

1 Gross–Pitaevskii description of exciton-polariton fluids **9**
- 1.1 Strong coupling in semiconductor microcavities . . . 9
  - 1.1.1 Dielectric mirrors . . . 9
  - 1.1.2 Wannier excitons in GaAs . . . 10
  - 1.1.3 Exciton-polaritons . . . 11
- 1.2 Polariton fluids . . . 13
- 1.3 Collective physics of resonantly driven polaritons . . . 15
  - 1.3.1 Bistability . . . 15
  - 1.3.2 Bogoliubov excitations . . . 16
  - 1.3.3 Landau criterium . . . 18
- 1.4 Galilean boosts and polariton fluids* . . . 19
- 1.5 Driven-dissipative aspects of polariton superfluids . . . 21
- 1.6 Hydrodynamics from a finite pump spot* . . . 23
  - 1.6.1 Outward 1D polariton flow from a localized pump spot . . . 24
  - 1.6.2 Superfluidity and instabilities in two-dimensional flows . . . 29
  - 1.6.3 Solitonic and shock-wave-like patterns . . . 32
- 1.7 Conclusions . . . 34

2 Excitations and superfluidity of resonantly driven polariton fluids in the presence of a dark excitonic reservoir **35**
- 2.1 The polariton-polariton interaction constant . . . 35
  - 2.1.1 Theory of exciton-exciton interactions . . . 36
  - 2.1.2 Measuring the coupling constant . . . 36
- 2.2 Measuring the collective excitations of a polariton fluid . . . 37
  - 2.2.1 The experiment . . . 38
- 2.3 Excitations in the presence of a dark reservoir* . . . 45
  - 2.3.1 Singly polarized model . . . 45
  - 2.3.2 Spinorial model . . . 50
  - 2.3.3 Modelling the photoluminescence . . . 52
- 2.4 Superfluidity in the presence of an incoherent reservoir* . . . 54
- 2.5 Conclusions . . . 60

Part II: Coherence of extended lasing systems **62**

3 Theory of the coherence of extended 1D laser systems **63**
- 3.1 Coherent laser emission . . . 63
  - 3.1.1 The LASER principle . . . 63
  - 3.1.2 Semiclassical theory and Schawlow-Townes linewidth . . . 67

3.2 Kardar-Parisi-Zhang physics in 1D nonequilibrium fluids 70
3.2.1 Spatio-temporal phase dynamics 70
3.2.2 KPZ universality 73
3.3 Linewidth of extended 1D laser systems* 78
3.4 Conclusions 82

4 Theory of the coherence of the Harper-Hofstadter topological laser 85
4.1 Topological lasers 85
4.1.1 Topological photonics 85
4.1.2 Topological lasers: Experimental implementations 87
4.1.3 The Harper-Hofstadter laser 88
4.2 Bogoliubov theory: elementary excitations and coherence* 90
4.2.1 Semi-analytical considerations on the steady-state 91
4.2.2 Bogoliubov modes 92
4.2.3 Chiral edge dynamics 94
4.2.4 Linewidth and Petermann factor 98
4.3 Nonlinear phase physics* 100
4.4 Lasing and coherence in disordered arrays* 105
4.4.1 Lasing in non-topological 1D arrays with disorder 106
4.4.2 Topological robustness to disorder 107
4.5 Discussion* 109
4.6 Conclusions 110

Conclusions and Outlooks 113

Acknowledgements 115

Appendix A: Petermann factor of two coupled resonantors 117

References 118

Introduction

Quoting the precious lesson by Anderson [1972], the study of emergent phenomena provides a bridge between very different scales and is conceptually as fundamental as the search for the microscopic laws of nature. Condensed matter physics is pretty much about the emergence of order, symmetry breaking and low energy properties. One intriguing class of systems is represented by quantum fluids, for which the thermal De Broglie wavelength is larger or comparable to the mean inter-particle distance and the quantum statistics of the particles becomes relevant. Spectacular phenomena like superfluidity and superconductivity are in fact characterized by the onset of some kind of order on macroscopic scales.

A peculiar class of quantum fluids is provided by light in nonlinear media and examples of symmetry breaking include lasing and polariton condensation. Since the first realizations in the 1960s, the laser represents a fundamental mechanism in both theoretical physics and in everyday life applications. Polariton fluids, on the other hand, have been developed in the last two decades as a very convenient paradigm for enhancing the effective interactions of the photons via strong radiation-matter coupling. The dynamics and the coherence properties of quantum fluids of light and matter have been modeled in a few simple regimes, but many central questions remain open concerning vortical or turbulent flows, the role of dissipation, superfluidity in spatially inhomogeneous configurations, coupled laser oscillators and nonlinear physics in topological systems.

In this Thesis we apply several theoretical techniques developed in the fields of Quantum and Nonlinear Optics, Statistical Mechanics and Condensed Matter to the study of a few relevant examples of fluids of light. While the original results presented here are of analytical or computational origin, the experimental aspects of the available platforms are thoroughly discussed all over the manuscript.

One main approach underlying most of the Thesis is to describe a quantum fluid via a classical field; this is possible when the fluid possesses a high degree of coherence, as a result of the transition to a lasing state or because the fluid is coherently created by an external drive. These two scenarios of a resonant drive or of an incoherent one display different features and motivate the division of the Thesis in Part I (Chapters 1,2) and Part II (Chapters 3,4). In both cases, focusing on the coherent component of the dynamics of the quantum fluid allows to obtain an effective description of many interesting phenomena without the formidable effort of dealing with the full quantum problem. The starting point of such a semiclassical analysis will typically be a generalized nonlinear Schroedinger equation: the Gross-Pitaevskii equation for weakly interacting quantum gases and its driven-dissipative extensions and the Complex Ginzburg Landau equation for the dynamics of laser systems will be two important declinations of this concept.

Another element which plays a major role is dimensionality. Basically all the devices that we will review are implementations of one or two dimensional models. Correspondingly, polariton hydrodynamics will be investigated in one and two dimensions; even more importantly, the low dimensionality of the lattice determines the lack of long-range order of the field emitted from a 1D laser array or from the edge of a 2D topological device, resulting in a broadening of the linewidth.

In contrast to these unifying methodological elements, whose two main flavors have been grouped in Part I and II, the range of experimental platforms discussed is quite wide. For this reason, the division in Chapters has been chosen based on the physical system, while the separation between known and original results has been performed via the use of the Sections, the material contained in a Section marked by an asterisk being mostly due to ourselves[1]. Having stated the general scope and features of the Thesis, let's briefly introduce the contents of the individual parts.

Chapter 1 deals with hydrodynamics and superfluidity of resonantly injected polariton fluids (Carusotto and Ciuti [2013]). In semiconductor microcavities, a mode of the electromagnetic field can be strongly coupled to the excitonic transitions of the embedded quantum well, resulting in quasi-particle excitations called exciton-polaritons (Yu and Cardona [2010]). These have bosonic nature, light mass and short-range interactions. Depending on the pumping scheme, polariton condensation can be achieved (Kasprzak et al. [2006]), which brings many analogies with the physics of lasers and atomic Bose-Einstein condensates; alternatively, polaritons can be injected quasi-resonantly, giving rise to a rich phenomenology which can be described in terms of the generalized Gross-Pitaevskii equation introduced by Carusotto and Ciuti [2004] and which includes bistable behaviors and flow without scattering.

After reviewing these well known results, we report some interesting features of the generalized Gross-Pitaevskii equation. First, we provide, via a formal argument based on Galilean boosts, a rederivation of the Doppler shift and of the link between critical velocity and speed of sound. In particular, under an infinite excitation spot, the flow of a polariton fluid against a static defect and the displacement of a moving defect in a fluid at rest are related by a mathematical boost and in some sense are the same situation pictured in two different reference frames (Amelio et al. [2020b]).

The other important finidings spring from a careful reconsideration of the results by Pigeon et al. [2011], which suggested that, in analogy to weakly interacting atomic gases, a polariton fluid ejected from a finite spot against a static defect would alternate a superfluid, turbulent and solitonic behaviour for increasing injection velocity. Instead, we show that the dynamics of the ejected flow is an extremly nonlinear one and it is not possible to directly control the flow velocity via the pump wavevector (Amelio and Carusotto [2020a]). Correspondingly, the flow against a defect always features a solitonic pattern, which can be shallower or deeper, but never displays clean superfluidity and never breaks down in vortical or turbulent dynamics. These numerical observations call for quantitative tests of the generalized Gross-Pitaevskii description and for a better understanding of the conditions in which the experiment by Amo et al. [2011] was performed, where a scenario compatible with the atomic gas predictions was claimed.

Chapter 2 is devoted to the study of the physics of resonantly injected polariton fluids in the presence of a dark excitonic reservoir. Since such reservoir introduces an important bias when trying to estimate the polariton-polariton interaction constant from the observed blueshift (Sun et al. [2017], Estrecho et al. [2019]), we start reviewing the theory of exciton-exciton interactions (Ciuti et al. [1998]). The experimental efforts directed at measuring the dispersion of the collective excitations of the polariton fluids are then summarized, and the experiment by Stepanov et al. [2019], which is the leading thread of the Chapter, is discussed in details.

In this experiment, the excitation laser is linearly polarized and the detection occurs in the opposite polarization. The energy and angle resolved photoluminescence from the fluid is collected as close as possible to the acoustic regime. Looking at the measured dispersion of the excitations on top of the fluid, as presumably induced by thermal phonons, a much reduced slope is observed with respect to the standard theory of a fully coherent polariton fluid, where the speed of sound is determined by the blueshift.

This fact, together with other recent findings (Sarkar et al. [2010], Walker et al. [2017]), suggests the existence of dark excitonic states which are populated by polariton-polariton scatterings, contribute to the blueshift of the fluid and have a slower dynamics than the polaritons, so that they impact on the dynamics only at frequencies lower than the linewidth. As a consequence, our theoretical analysis highlights that the speed of sound is mostly determined by the fraction of the Hartree energy due to polariton-polariton scattering, while exciton-polariton interactions mainly produce a blueshift of the fluid.

While these concepts are first illustrated for a circularly polarized fluid, a careful quantitative analysis has been performed to include the interplay of the two linear polarizations and to model the excitation of the photoluminescence by thermal phonons. Keeping into account all these features allows for an estimate of the reservoir parameters and for the polariton-polariton interaction constant.

---

[1] For example, notice that Sec. 2.2, while it refers to (Stepanov et al. [2019]) and reports original experimental results, does not bear an asterisk because it mainly springs from the work in the lab of Petr Stepanov and Maxime Richard; our theoretical contribution to that paper is illustrated in Sec. 2.3

In the final Section, the influence of the resevoir on the superfluid phenomenology of the polaritons is highlighted (Amelio et al. [2020b]). In particular, the breaking of the formal Galilean invariance argument discussed in Chapter 1 entails that the critical velocity is not in general given by the speed of sound. The two are equivalent for a defect moving in a fluid at rest, while in the steady state situation of a fluid flowing past a static defect the critical velocity is determined by the total blueshift.

Chapter 3 addresses the spatial and temporal coherence of 1D non-equilibrium quasi-condensates, or equivalently of tight binding models of 1D laser arrays.

In the first Section the basic concepts underlying laser operation are illustrated. We show how the celebrated Schawlow-Townes linewidth (Schawlow and Townes [1958]) can be derived in a simple semi-classical analysis: due to the phase invariance of the laser equations, spontaneous emission events (or other sources of white noise) lead to a diffusion of the phase of the laser field and an exponential decay of the coherence in time (Henry [1982]). A brief overview of different laser devices is also provided.

While the Schawlow-Townes treatment is adequate for an effectively point-like laser field, the statistical mechanics literature focuses on the spatio-temporal correlation functions of infinitely extended non-equilibrium fluids described by the Complex Ginzburg Landau equation (Gladilin et al. [2014], He et al. [2015], Ji et al. [2015], Squizzato et al. [2018]), of which polariton condensates are an example. In 1D in particular, any linearization approach is bound to fail due to the absence of long-range order; conversely, a nonlinear Kuramoto-Sivashinskii equation for the dynamics of the phase can be derived by eliminating the fast density fluctuations. Then, the renormalization group approach predicts that the infrared physics falls into the Kardar-Parisi-Zhang (KPZ) universality class (Kardar et al. [1986]), which was originally proposed to describe the stochastic growth process of a classical interface.

Our contribution (Amelio and Carusotto [2019]) consists in elucidating the connection between the Schawlow-Townes linewidth and KPZ physics, or in other words how spatial fluctuations affect the temporal coherence properties. More precisely, the Schawlow-Townes linewidth can be viewed as a finite-size effect that will dominate at very long times, while KPZ universality is visible at intemediate times and for large enough systems. Moreover, while when the system size is small enough the linewidth is the one described by the Bogoliubov-Schawlow-Townes theory, a marked broadening occurs for large enough systems, where corrections due to the nonlinear phase dynamics are expected. More specifically, the coherence time is expected to scale as the length of the system in the linear regime and as its square root in the nonlinear one.

Chapter 4 presents the first theoretical study of the coherence properties of a topological laser. First, we review the impetuous development of the topological photonics field and how lasing in the edge modes of a topological lattice for photons has been achieved by several groups in the last four years (Bahari et al. [2017], Harari et al. [2018], Zeng et al. [2020]).

A theoretical model of a topological laser is provided by the 2D Harper-Hofstadter laser (Longhi et al. [2018]). The core of this Chapter reports the semiclassical solution of this model in the case of a class-A device and for small intensity fluctuations (Amelio and Carusotto [2019]). To this end, the Bogoliubov modes are computed and explained via a dimensional reduction argument (Loirette-Pelous [2020]). Moreover, the structure of the correlation functions reflects the fact that fluctuations travel in a chiral way around the edge of the system.

The linewidth is computed via the Bogoliubov method. We generalize the notion of the transverse Petermann factor and show that it is close to 1, clarifying the nature of topological lasing as opposed to gain guiding. For large enough arrays, in analogy with the analysis of the previous Chapter, the field on the edge brings the signatures of KPZ universality and of the linewidth broadening due to the nonlinear phase dynamics.

Then, we demonstrate the robustness of the coherence properties to the presence of static onsite disorder: more precisely, the disorder threshold for the topological array is roughly set by the band-gap and is orders of magnitude higher than for a topologically trivial array. The robustness of the KPZ universality in the correlation functions is instead mostly determined by the density of states of the edge mode. Remarkably, the coherence time is enhanced by an intermediate amount of disorder, since the Bogliubov modes of the Goldstone dome acquire a shorter lifetime and the nonlinear phase dynamics is hampered.

These results have been derived within a very simple model. We expect that including nonlinearities and the carrier dynamics within the tight binding framework should not introduce major qualitative modifications as long as no instabilities arise; the time and length scales entering the correlation functions will instead change, per example yielding a Henry factor for the linewidth (Henry [1982]). Finally, the tight binding approximation has no predictive power in determining whether the emission is single or multi-moded in the very relevant case of semiconductor laser arrays; however, if single moded emission is verified experimentally, our guess is that the qualitative structure of the correlation functions described here should apply also to that situation.

Other PhD research NOT in this Thesis

Before entering in the core of the Thesis, I would like to briefly list here also some other research efforts which couldn't find their place in this manuscript or have not brought to any publishable results (yet), but still deserve some mention for the amount of time they took during these three years.

Just before the start and during the first year of my PhD I collaborated with Davide Galli and Luciano Reatto on the study of vortices in Helium via Quantum Monte Carlo techniques: I learned a lot in this first taste of quantum fluids and we also obtained some interesting results on the role of rotons in quantum turbulence (Amelio et al. [2018]).

At the end of the first year, I started a collaboration, funded by the Unitn–College de France exchange program, with Giacomo Mazza and Antoine Georges on the interplay of strong light-matter coupling and phase transitions in correlated electronic materials. We investigated several aspects of the problem, including the dynamics of superradiant excitonic states, some strategies to cut off degrees of freedom in the ultrastrong coupling regime, and an Exact Diagonalization study of the Hubbard and Heisenberg models in a cavity. In spite of the tremendous amount of time spent in this project (2 months as visitor at College de France and at least one year of effective work), we couldn' t get to any solid results yet, also because of the many subtleties hidden in this field. Still, I am pretty convinced that this experience has been a very good investment in view of my future research directions.

Finally, I took some steps in the direction of continuing the work by Elia Macaluso and study bosonic Pfaffian states with Tree Tensor Networks under the supervision of Matteo Rizzi, but the pandemic plus hacker attacks to our supercomputer plus the writing of this Thesis killed these attempts quite soon... However, I am happy to have had a taste of these fascinating topics!

Part I: Resonantly driven polariton fluids

Chapter 1

Gross–Pitaevskii description of exciton-polariton fluids

The central topic of this Chapter is the discussion of the properties and predictions stemming from the generalized Gross-Pitaevskii equation that it is used to describe resonantly-driven exciton-polariton fluids.

We set off in Section 1.1 by introducing strongly coupled exciton-polaritons in 2D semiconductor microcavities. As explained in Sec. 1.2, under a proper pump scheme these quasi-particles can be excited to form coherent fluids, described by generalized Gross-Pitaevskii equations. The basic properties of a resonantly driven fluid are then reviewed in Sec. 1.3, as a prelude to the original results of the Chapter: a formal theory of Galilean transformations between different pump configurations is presented in Sec. 1.4; then, Sec. 1.5 deals with how drive and dissipation (and the corresponding imaginary poles of the dispersion) affect superfluidity; finally, in Sec. 1.6 the study of polariton flows off finite pump spots closes the Chapter by reporting some unexpected behavior, which ultimately calls for new experimental assessment of the validity limits of the generalized Gross-Pitaevskii approach.

1.1 Strong coupling in semiconductor microcavities

Along the next pages we will see that particles that arise from the strong coupling of matter and radiation degrees of freedom have very intriguing properties. In this and in the next Chapter we will mostly concerned with one outstanding platform where the strong coupling regime can be realized, that is 2D semiconductor microcavities.

The basic idea, sketched in Fig. 1.1.a, is to have a central layer, usually called a quantum well (QW), in which the interband exciton will be confined; this is sandwiched in between two Distributed Bragg Reflectors (DBRs), consisting of different layers with alternating refractive index. The DBRs act as dielectric mirrors and create a cavity for the optical radiation. With a proper design of the structure, the interband transition occurring in the QW can be set into resonance with one transverse electromagnetic (EM) cavity mode to give rise to a large Rabi splitting exceeding the small radiative losses, a regime called of strong coupling. The quasiparticle excitation stemming out of this interaction is called the exciton-polariton; polaritons can be excited and controlled via optical means, p.e. by shining a laser on the microcavity, and the interaction between polaritons gives rise to very rich nonlinear physics, which will be the main topic of the next Sections.

1.1.1 Dielectric mirrors

Let's now review more in details the basic ingredients of a 2D microcavity (Savona et al. [1999], Kavokin et al. [2007], Liscidini and Andreani [2015]). First, we hint at how alternating dielectric layers can serve as a mirror. The starting point is Maxwell equations in matter with no free sources, which can be rearranged so that electromagnetic waves should satisfy the hermitian eigenproblem

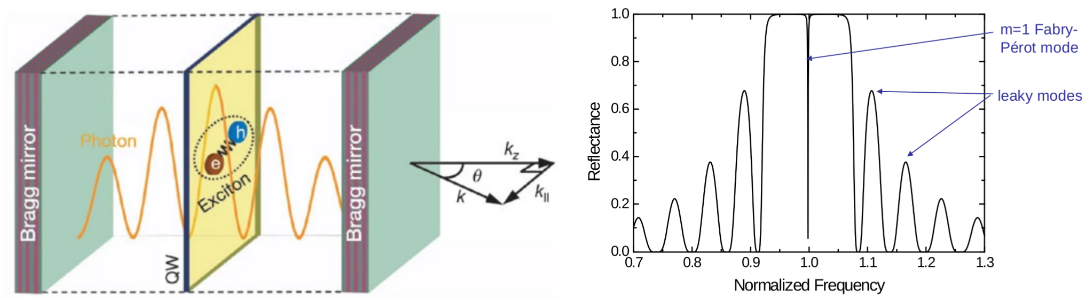

Figure 1.1: *Semiconductor microcavity.* (left) Sketch of a typical microcavity for achieving strong coupling between the EM field confined by two dielectric mirrors and excitons confined in a QW. (right) Frequency dependent reflectance for a simple Fabry-Perot cavity model; the sharp Fabry-Perot resonance is here centered in the middle of the DBR stop band. Plots respectively taken from (Kasprzak et al. [2006]) and (Liscidini and Andreani [2015])

$$\nabla \times \left[\frac{1}{\varepsilon(\mathbf{r})} \nabla \times \mathbf{H} \right] = \frac{\omega^2}{c^2} \mathbf{H}, \tag{1.1}$$

where $\varepsilon(\mathbf{r})$ is the local dielectric constant and we assumed unit magnetic permeability so that $\mathbf{H}$ is the magnetic field, subject to the constraint $\nabla \cdot \mathbf{H} = 0$. In a 2D dielectric mirror the dielectric constant depends only on the normal coordinate $\varepsilon(\mathbf{r}) = \varepsilon(z)$ and due translational invariance along the plane the EM modes will be in the form $\mathbf{H}(\mathbf{r}) = \mathbf{H}(z) e^{i\mathbf{k}_{\parallel} \cdot \mathbf{r}_{\parallel}}$; it is convenient to consider a periodic Bragg structure $\varepsilon(z) = \varepsilon(z + a)$, so that the Bloch theorem allows to label the eigenvectors by a wavevector q_z in the first Brillouin zone and a photonic band number, together with the polarization index. In particular, the periodic $\varepsilon(z)$ couples Fourier waves $e^{ik_z z}$ differing by a multiple of $2\pi/a$; with respect to the light cone in vacuum or in a homogeneous medium, it is clear that one Fourier wave will be mostly coupled to a wave with opposite group velocity in the z direction; if two layers of different ε are alternated, the constructive interference of these reflections from successive interfaces provides the way to maximize the photonic band gap around a given frequency ω, goal that is achieved by designing the structure in the so called $\lambda/4$ configuration: this consists in choosing the thickness of each one of the two layers as $c/(\omega n_l)$, $l = 1, 2$. A wave incident on the structure with frequency falling in the photonic bandgap doesn't find any available state for propagation and it is reflected; the reflectivity is closer to one if more and more layers are stacked. (One can also reason in terms of evanescent waves, related to non-normalizable eigenstates with complex wavevectors, which allows to compute the penetration length of the reflected wave.)

Now, two Bragg mirrors of reflectivity $|r(\omega)| \simeq 1$ in a given spectral window form a Fabry-Perot cavity, as sketched in Fig. 1.1.b. The input-output treatment of this structure yields a transmission coefficient in the form

$$t_{cav}(\omega) = \frac{1 - r(\omega)}{1 - r^2(\omega) e^{2ik_z(\omega)L_z}} \tag{1.2}$$

where L_z is the effective length of the cavity (closely related to the thickness of the central structure) and $k_z(\omega)$ is determined by the refractive index of the inner layers and by the frequency and incidence angle of the wave. Equivalently, this expression can be derived by summing the harmonic series arising from the multiple reflections inside the two mirrors: any time the constructive interference condition is matched, a sharp transmission window of Lorentzian shape appears. The full width at half maximum (FWHM) of the resonance at frequency ω_m is denoted γ_m and the quality factor of the mode $Q = \omega_m/\gamma_m$ counts the number of optical cycles the trapped radiation performs before leaking out.

1.1.2 Wannier excitons in GaAs

Then, we discuss the interband exciton arising in semiconductor materials with a direct band gap. In the particularly relevant case of gallium arsenide GaAs (Blakemore [1982], Schlesinger [2001]), the crystal structure, depicted in Fig. 1.2.a, is of the zinc-blende type, that is a bipartite version of the diamond lattice, with Ga (As) belonging to the III (V) group of the periodic table. This structure can also be thought as two interpenetrating fcc solids, with the nearest neighbours of

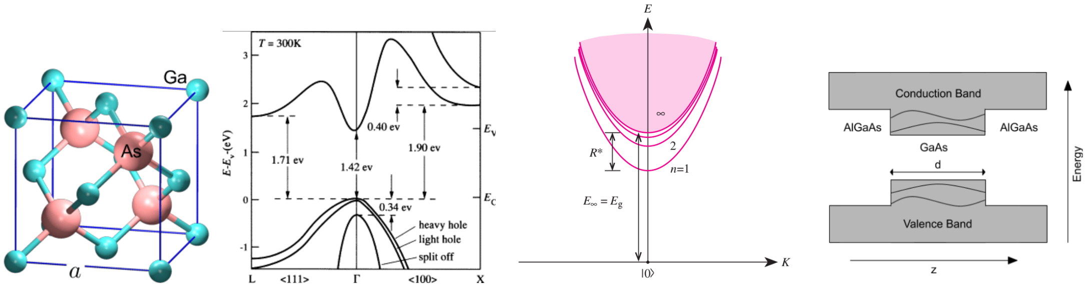

Figure 1.2: *GaAs electronic states.* (a) Unit cell of the zinc-blende crystal structure of GaAs. (b) Single electron bands of GaAs computed via a pseudo-potential method. (c) Sketch of excitonic hydrogen-like levels $n = 1, 2, 3$ emerging as narrows peaks below the single particle continuum in the excitation spectrum of a direct gap semiconductor. (d) Typical QW for GaAs, with external layers containing aluminium to give type-I band alignment, i.e. lower (higher) edge of the valence (conduction) band. Plots respectively taken from (Du et al. [2013]), (Schlesinger [2001]), (Yu and Cardona [2010]) and (Wikipedia – Quantum well).

each atom forming a regular tetrahedron. The band structure, or more precisely the single particle energies versus momentum along two crystal axes, is plotted in Fig. 1.2.b for the bulk material at the temperature $T = 300$K. The band gap reaches its minimum of 1.42 eV at the Γ point and the bandgap decreases with increasing temperatures, since the lattice expands. The conduction band features an effective mass of $0.067 m_e$ at the Γ point, with m_e the mass of the free electron, and has s-wave orbital symmetry. The valence band instead is p-symmetric and splits in a heavy hole and a light hole branches, with effective masses of $0.50 m_e$ and $0.076 m_e$ respectively and total anglular momentum $j_h = 3/2, j_h^z = \pm 3/2$ and $j_h = 3/2, j_h^z = \pm 1/2$. (There is also another sub-branch $j^h = 1/2$ which lies deeper in energy by a spin-orbit splitting of 0.34 eV.)

In order to obtain the spectrum of the semiconductor at low temperatures, as probed p.e. by optical spectroscopy, the single particle approach is not enough. Nonetheless, the many electron problem can be simplified by considering an hole in the valence band and an electron in the conduction one, interacting by an effective potential that keeps into account Coulomb screening by the other electrons. In semiconductors, this gives rise to hydrogen-like bound states with a Bohr radius extending typically over many unit cells: such states are called Wannier-Mott excitons (Yu and Cardona [2010]) and their spectrum is sketched in Fig. 1.2.c.

Such an excitation can be then spatially confined in a layer sandwiched between two layers with some different alloy composition. To this end, the band gap of the central layer has to be smaller, so that it provides an effective well potential for the exciton. It is convenient to adopt the envelope approximation and consider the electron-hole pair frozen in the $1s$ bound state and in the lowest subband along z, while translational symmetry along the plane allows for a parabolic dispersion of the center of mass degree of freedom.

For example, in GaAs structures the exciton binding energy is of the order of a few meV, the precise value depending on the temperature and thickness of the structure, and the Bohr radius is ~ 10nm. In order to obtain a quantum well, the GaAs layer is sandwiched between two $\mathrm{Al}_x\mathrm{Ga}_{1-x}\mathrm{As}$ regions, as illustrated in Fig. 1.2.d. While the heavy hole and light hole are degenerate at $\mathbf{k} = 0$ in the bulk, this degeneracy is lifted when the hole is confined in the QW, with the heavy hole being energetically favourable by typically a few meV. In the following we restrict to heavy holes excitons with $J_z = \pm 1 \equiv \sigma$, to satisfy the selection rule for optical excitation.

1.1.3 Exciton-polaritons

Having hinted at the microscopic aspects of the semiconductor 2D microcavities, it is now possible to write down a simplified Hamiltonian to grasp the basic features of light matter interaction in the strong coupling regime. Non-interacting excitons in the envelope approximation and in the the first QW subband are described by

$$H_X = \sum_{\mathbf{k}_\parallel \sigma} \omega_X(\mathbf{k}_\parallel) \hat{b}^\dagger_{\mathbf{k}_\parallel \sigma} \hat{b}_{\mathbf{k}_\parallel \sigma}, \tag{1.3}$$

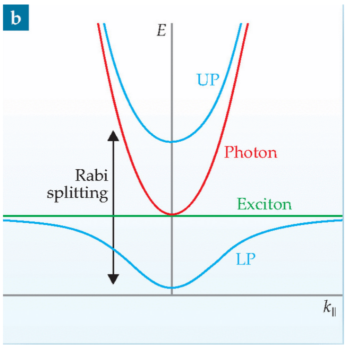

Figure 1.3: *Polariton dispersion.* Sketch of how the coupling of exciton and photon modes yields an upper and lower polarion branch. The Rabi coupling determines the width of the avoided crossing splitting. Plot taken from (Snoke and Littlewood [2010]).

where the excitons can be considered as a bosonic excitation as long as their density is low enough not to resolve the two fermionic constituents (Hopfield [1958], Keldysh and Kozlov [1968]). Since the exciton mass is quite heavy for our purposes, it is possible to consider a dispersionless line $\omega_X(\mathbf{k}_\parallel) = \omega_X$.

On the other hand, the parameters are tuned so that a specific photonic branch $\hat{a}_{\mathbf{k}_\parallel \sigma}$ is nearly resonant with the exciton line; focusing only on these modes, the cavity Hamiltonian reads

$$H_C = \sum_{\mathbf{k}_\parallel \sigma} \omega_C(\mathbf{k}_\parallel) \hat{a}^\dagger_{\mathbf{k}_\parallel \sigma} \hat{a}_{\mathbf{k}_\parallel \sigma}. \tag{1.4}$$

If one injects photons with small incidence angle, the condition $k_\parallel L_z \ll 1$ allows to approximate the polarization unit vectors as perpendicular to the z axis and take the dispersion independent of the polarization σ, neglecting the so-called TE/TM splitting (Shelykh et al. [2009]). For a perfect and infinite planar cavity the dispersion looks like a rounded light-cone

$$\omega_C(\mathbf{k}_\parallel) = \sqrt{\omega_0^2 + \frac{c^2}{n^2}\mathbf{k}_\parallel{}^2} \simeq \omega_0 + \frac{\hbar}{2m_0}\mathbf{k}_\parallel^2, \tag{1.5}$$

where for the M-th transverse mode one has the $\mathbf{k}_\parallel = 0$ frquency $\omega_0 = \frac{\pi c}{n L_z} M$ and the photon effective mass $m_0 = \frac{\hbar \omega_0}{c^2/n^2}$.

The excitation of an exciton corresponds to an optically active transition with dipole moment d. Since the exciton is confined in a region of a few nanometers, it is possible to resort to the dipole approximation very much used in quantum optics and neglect the spatial dependence of the electric field over the scale of the dipole moment. Keeping only nearly resonant terms, the so-called rotating wave approximated (RWA) coupling term reads

$$H_{LM} = \hbar \Omega_R \sum_{\mathbf{k}_\parallel \sigma} \hat{a}^\dagger_{\mathbf{k}_\parallel \sigma} \hat{b}_{\mathbf{k}_\parallel \sigma} + h.c. \ , \tag{1.6}$$

where the Rabi frequency is given by $\Omega_R = dE_0/\hbar$ with $E_0 = \sqrt{\frac{\hbar \omega_0}{\epsilon V}}$ with V the effective volume of the cavity. From this expression it is evident that for achieving strong light matter coupling it is necessary to confine the electromagnetic field within the cavity and confining the exciton at one anti-node of the EM field.

The Hamiltonian $H_X + H_C + H_{LM}$ can be easily diagonalized by the rotation $\hat{p}^{LP}_{\mathbf{k}_\parallel \sigma} = \cos\theta \hat{b}_{\mathbf{k}_\parallel \sigma} + \sin\theta \hat{a}_{\mathbf{k}_\parallel \sigma}$, $\hat{p}^{UP}_{\mathbf{k}_\parallel \sigma} = \cos\theta \hat{a}_{\mathbf{k}_\parallel \sigma} - \sin\theta \hat{b}_{\mathbf{k}_\parallel \sigma}$. The new bosonic operators create and annhilate excitations called exciton-polaritons (Hopfield [1958]). The dispersion of the coupled system consists of two branches $\omega_{LP}(\mathbf{k}_\parallel)$, $\omega_{UP}(\mathbf{k}_\parallel)$ arising from the avoided crossing of the light-cone with the exciton line, as depicted in Fig. 1.3. The excitonic versus photonic character of a polariton of given wavector is given by the Hopfield coefficients characterizing the above rotation. In experiments the microcavity can contain N_{QW} quantum wells located at different anti-nodes of the field. Repeating the diagonalization of the light-matter Hamiltonian in this case, one sees that the photon field couples only with the symmetric combination of the exciton operators, with the other $N_{QW} - 1$ fields remaining dark. The Rabi coupling to this bright exciton is enhanced by a factor $\sqrt{N_{QW}}$, so that having multiple QWs is a practical strategy to have a stronger coupling. For instance, the microcavities used in (Bajoni et al. [2007], Stepanov et al. [2019]) consist in a $\lambda/2$ AlAs region stacked in between two DBRs made of 16 and 20 $\lambda/4$ pairs of $Al_{0.2}Ga_{0.8}As$/AlAs layers; in total

12 GaAs QWs are embedded in the central AlAs and the innermost DBR AlAs layers, at the anti-nodes of the cavity field.

This very simple treatment can now be enriched if one reintroduce by hand two essential ingredients: losses and interactions. Losses arise both from the leaking of photons out of the cavity and from the decay of the exciton due to scattering with electrons, phonons and impurities. A formal treatment of the coupling of the cavity to the external EM environment and of the electronic decay and dephasing channels requires the use of a master equation with Linblad terms accounting for losses and dephasing (Gardiner and Zoller [2004], Walls and Milburn [2007]). Nonetheless, for many puposes it is sufficient to deal with a Hamiltonian containing complex eigenfrequencies $\omega \to \omega - i\frac{\gamma}{2}$.

Having introduced losses, we can now define the strong coupling regime via the condition $\Omega_R \gg \gamma$. Physically, this means that energy is exchanged over many cycles between the photon and exciton fields before being lost in the EM or electronic environment. Within this regime, in a spectroscopic experiment we are able to resolve the avoided crossing splitting between the photon dispersion and the exciton line.

The picture presented so far holds as far as the system is probed linearly, i.e. the density of excited polaritons is low enough. However, the electronic constituents of the overall neutral polaritons start to see each other for close-by quasiparticles: at high polaritons densities, achieved for strong pumping, polariton-polariton interactions need to be taken into account. A detailed discussion of these issues is postponed to the next Chapter, where the polarization dependence of the interactions and the subtle problem of determining the coupling constant will play a central role. For our purposes, here it is sufficient to add to the Hamiltonian the quartic local Hartree term $\sum_{\sigma\sigma'} g_{\sigma\sigma'} \int d^2\mathbf{x}\ \hat{b}^\dagger_{\mathbf{x}\sigma}\hat{b}_{\mathbf{x}\sigma}\hat{b}^\dagger_{\mathbf{x}\sigma'}\hat{b}_{\mathbf{x}\sigma'}$.

With the further approximation that we focus on the lower polariton branch and on just one polarization, all the complex physics of the undriven polariton field is summarized in the bosonic Hamiltonian

$$H_{LP} = \int \frac{d^2\mathbf{k}}{(2\pi)^2} \left[\omega_{LP}(\mathbf{k}) - \frac{i}{2}\gamma(\mathbf{k})\right] \hat{p}^\dagger_{\mathbf{k}}\hat{p}_{\mathbf{k}} + g \int d^2\mathbf{x}\ \hat{p}^\dagger_{\mathbf{x}}\hat{p}_{\mathbf{x}}\hat{p}^\dagger_{\mathbf{x}}\hat{p}_{\mathbf{x}}\ ; \tag{1.7}$$

this equation describes the polariton excitations considered in the rest of this Chapter. Notice that one of the limits of exploiting photons in many Quantum Technologies, including Quantum Computation, is the fact that in the vacuum two photons interact very weakly via the QED one-loop vertex containing four electronic propagators; this vertex is then negligible at optical frequencies, which are well below the Compton scale. However, dressing the photon with matter degrees of freedom endows it with the possibility of exerting a strong interaction on another polariton. The quest for strong photon-photon nonlinearities, with the ultimate goal of reaching a perfect photon blockade (Imamoḡlu et al. [1997]), has motivated a tremendous amount of work in the solid state, atomic and superconducting qubits communities over the last two decades.

In the following Section we will discuss different strategies to excite polaritons. Clearly, many of the approximations illustrated above are well motivated only retrospectively, because one drives the microcavity in regimes in which we have good theoretical control.

1.2 Polariton fluids

In this Section we will sketch three different schemes to macroscopically populate a state in the lower polariton band: via incoherent pumping, by resonant driving and through optical parametric conversion (Carusotto and Ciuti [2013]). The basic mechanism underlying the first two of these is bosonic stimulated scattering and in all the three cases the bosonic nature of the polaritonic excitations allows to write down a generalized Gross-Pitaevskii equation (GPE) (Pitaevskii and Stringari [2016]), which is the starting point for studying collective effects in polariton fluids.

Let' s start with incoherent pumping. This relies on exciting in uncontrolled way many high energy excitonic and electronic states of the microcavity, which will then relax into the bottom of the LP band (Porras et al. [2002]). In practice, excitation is usually performed by shining a laser with frequency above the conduction band edge or via electrical injection of carriers. A first stage of the relaxation process via scattering with optical and acoustic phonons leads to an accumulation of incoherent polaritons around the inflection point of the LP band. At this point polaritons can further relax into the bottom of the LP band. If driven by scattering with phonons, this process is usually very slow because of the small phase space of the final polariton states. However, for high enough polariton densities, polariton-polariton scattering is fast enough to create a finite

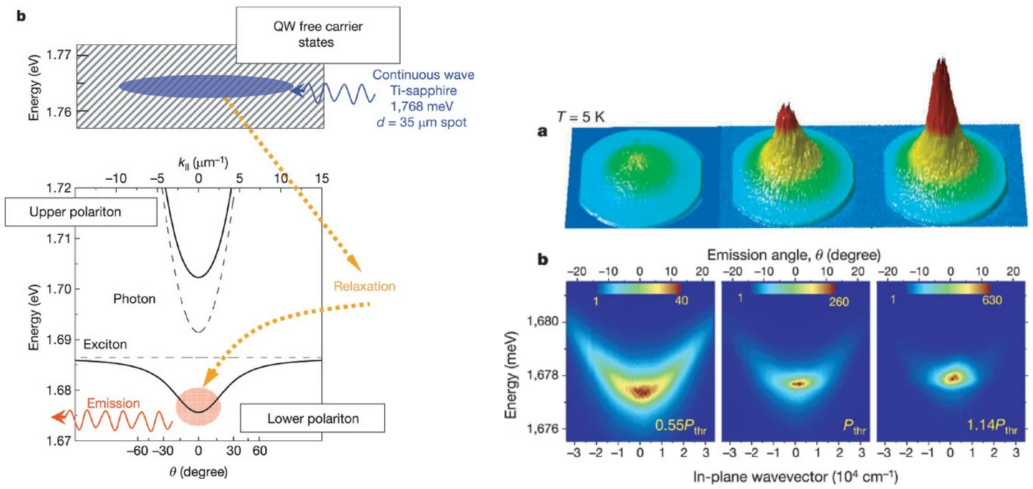

Figure 1.4: *Polariton condensation.* (left panel) The incoherent optical pumping scheme is sketched: a high frequency laser excites electronic states in the conduction band, which relax in polariton states at large wavevector. Further relaxation into the bottom of the LP band is only effective for high polariton densities, based on stimulated polariton-polariton scattering. This is further demonstrated in the right panel, where the far-field emission of the microcavity is plotted below threshold, at threshold and above threshold, showing macroscopic occupation of the $\mathbf{k}_{\parallel} = 0$ LP state. Plots are taken from (Kasprzak et al. [2006]).

population around the $k = 0$ polariton states. This spontaneous seed can then trigger stimulated polariton-polariton scattering into itself. For strong enough pumping these processes result in the formation of a non-equilibrium Bose-Einsten condensate, corresponding to a coherent macroscopic polariton population in the bottom of the LP band. The phase of the condensate is spontaneously selected based on the random phase of the initial seed. This physics was first experimentally demonstraed by Kasprzak et al. [2006] and it is summarized in Fig. 1.4.

With respect to atomic BECs which need to be cooled down below the μK range, polariton condensation has the advantage of taking place at much higher temperatures. This is due to the very light mass of the lower polariton as inherited from the confined photon, which typically is of the order of $m_{LP} \sim 10^{-4} m_e$: indeed, the critical temperature for having a quantum degenerate system is reached when the thermal De Broglie length $\hbar \frac{2\pi}{m k_B T}$ approaches the average distance between the particles. This allows to have Bose condensation [1] at temperatures of a few Kelvin (19K in the aforementioned experiment), or even at room temperature if one uses materials with a large enough exciton binding energy (Ardizzone et al. [2019], Su et al. [2020]). In this perspective, polariton condensates harness the best features of their matter and radiation constituents: they are interacting as material particles, but on the other hand they are very light and allow for all-optical control and imaging.

The emergence of coherence in a fully quantum model and the excitations of the non-equilibrium fluid were first studied by Szymańska et al. [2006]. A simpler mean-field model that captures many features of this polariton laser has been proposed by Wouters and Carusotto [2007] and it is based on the single-particle wavefunction $\psi(\mathbf{x})$ describing the macroscopically occupied state and on the the incoherent density of polaritons $n_R(\mathbf{x})$ populating the inflection point states. The corresponding generalized GPE plus the rate equation for the reservoir density read

$$i\hbar\partial_t\psi = \left[\hbar\omega_0^{LP} - \frac{\hbar^2}{2m_{LP}}\nabla^2 + g|\psi|^2 - i\frac{\hbar\gamma}{2} + i\frac{\hbar R}{2}\left(1 - 2i\frac{g_R}{\hbar R}\right) n_R\right]\psi, \tag{1.8}$$

$$\partial_t n_R = P - \left(\gamma_R + R|\psi|^2\right) n_R, \tag{1.9}$$

where R is the stimulated scattering rate, g_R takes into account the variation of the QW refractive index due to the presence of incoherent excitons, P measures the injection rate of incoherent polaritons and it is closely related to the pump strength, γ_R describes the rate of polariton recombination out of the condensed state. Notice that the parabolic approximation with effective mass m_{LP} for the LP dispersion holds because only states at its bottom are considered.

---

[1] in 2D condensation is well defined only for finite pump spots.

Two very important features typical of lasing and Bose-Einstein condensation are captured by equations (1.8,1.9): the existence of a threashold under which the steady-state condensate wavefucntion is zero and the symmetry under global phase shift $\psi(\mathbf{x},t) \to e^{i\phi}\psi(\mathbf{x},t)$. Above threashold, in order to have a steady-state lasing state it is then necessary to spontaneously break this $U(1)$ invariance; nevertheless, this microscopic symmetry survives through the Goldstone mode in the spectrum. These issues will be considered in full details later on in the subsection 3.2.1; in particular we refer to Fig. 3.2 and surroundings for the discussion of the collective excitations.

These two important features are missing if the microcavity is instead driven resonantly. In this case a laser is tuned at a frequency ω_p close to the bottom of the LP band and with an incidence angle corresponding to the in-plane wavevector $\mathbf{k}_p$. The use of a single-particle wavefunction in this case is justified because the polaritons are created by the laser in the same state and with a phase inherited by the one of the laser. The appropriate generealized GPE here is (Carusotto and Ciuti [2004])

$$i\hbar\partial_t\psi(\mathbf{r},t) = \left(\hbar\omega_0^{LP} - \frac{\hbar^2}{2m}\nabla^2 + g|\psi|^2 - i\frac{\hbar\gamma}{2}\right)\psi + F(\mathbf{r})e^{i\omega_p t}, \tag{1.10}$$

where the driving term $F(\mathbf{r})$ includes the spatial dependence of the laser field, its amplitude and the coupling with the microcavity states. As it is apparent, due to this pump term the global phase shift $\psi(\mathbf{x},t) \to e^{i\phi}\psi(\mathbf{x},t)$ is not a symmetry of Eq. (1.10), leading to completely different features of the excitation spectrum and superfluid properties. Resonantly injected fluids will be the main topic of the rest of this Chapter and of the following one, so we posticipate the discussion of their basic features to the next Section.

Even though we will not focus on it in this Thesis, for completeness we briefly mention a third commonly used experimental setup, usually referred to as optical parametric oscillation (OPO). One can resonantly drive the microcavity with parameters $(\omega_p, \mathbf{k}_p)$ corresponding to the inflection point of the LP band: in this region it is possible to satisfy the condition of phase-matching for four-wave mixing processes (Boyd [2019]), for which two pump photons $(\omega_p, \mathbf{k}_p)$ are converted in a signal $(\omega_s, \mathbf{k}_s)$ and an idler $(\omega_i, \mathbf{k}_i)$ photons while conserving energy and momentum, $2\omega_p = \omega_s + \omega_i$, $2\mathbf{k}_p = \mathbf{k}_s + \mathbf{k}_i$. This polariton-polariton scattering process can be stimulated by an external probe laser at the signal frequency and momentum or by the spontaneous accumulation of signal and idler polaritons which in turn triggers the nonlinear process and leads to a polariton condensate via breaking of the $U(1)$ symmetry (Baumberg et al. [2000]). Mathematically, this physics can be described by a resonantly driven generalized GPE with complete LP dispersion $\omega_{LP}(-i\hbar\nabla)$ and where the formation of the signal and idler beams are signaled by instabilities of the single-mode steady-state wavefunction (Carusotto and Ciuti [2005]).

1.3 Collective physics of resonantly driven polaritons

In this Section we will be concerned with the theoretical study of resonantly driven GPE Eq. (1.10) in the case of a plane wave pump field $F(\mathbf{r},t) = F_0 e^{i\mathbf{k}_p\cdot\mathbf{r} - i\omega_p t}$. Since we will rely a lot on these results in the course of the thesis, we will discuss in great details the bistability of the steady-state solutions, the spectrum of the collective excitations and the superfluid behaviour in the presence of defects.

1.3.1 Bistability

As a first step, for any shape of the laser spot, one can adopt the transformation $\psi(\mathbf{r},t) \to e^{-i\omega_p t}\psi(\mathbf{r},t)$ and move to a rotating frame where the steady-state field is time independent. In this frame, the GPE reads

$$i\hbar\partial_t\psi(\mathbf{r},t) = \left(\Delta - \frac{\hbar^2}{2m}\nabla^2 + g|\psi|^2 - i\frac{\hbar\gamma}{2}\right)\psi + F(\mathbf{r}), \tag{1.11}$$

where we introduced the detuning $\Delta = \hbar\omega_0^{LP} - \hbar\omega_p$. Since, as we will show below, a Galilean symmetry argument allows to reduce the general case $\mathbf{k}_p \neq 0$ to the treatment of $\mathbf{k}_p = 0$ (Amelio et al. [2020b]), we will start considering a uniform pump $F(\mathbf{r}) = F_0$. The staedy-state solutions then are also uniform with amplitude ψ_0 which satisfy

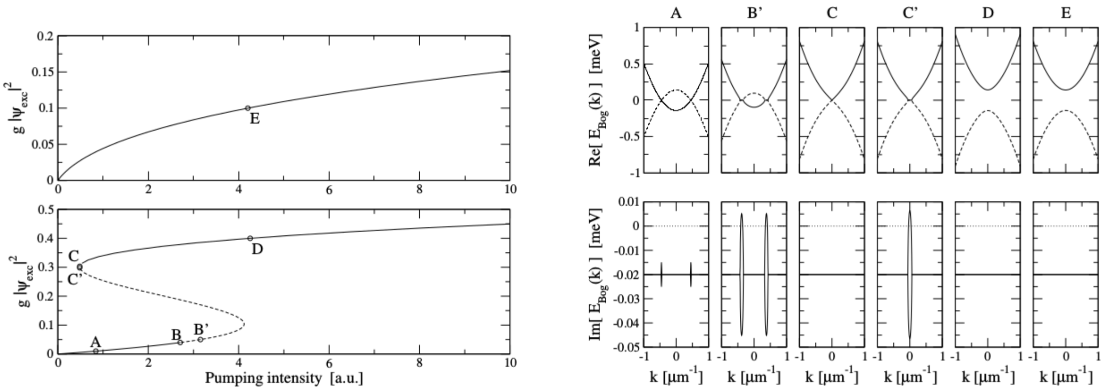

Figure 1.5: *Bistability and Bogoliubov spectra.* Left panel: typical μ versus I_F diagram in the optical limiter (upper) and bistability (lower) regimes. Right: Bogoliubov spectra, showing Reω (upper) and Imω (lower) as function of k_x at the various working points highlighted on the diagrams on the left. Plot taken from (Carusotto and Ciuti [2013]).

$$0 = \left(\Delta + g|\psi_0|^2 - i\frac{\hbar\gamma}{2} \right) \psi_0 + F_0. \tag{1.12}$$

Squaring this equation one can study the blueshift or Hartree interaction energy of the polariton field $\mu = g|\psi_0|^2$ in terms of the effective pump intensity $I_F = g|F_0|^2$:

$$\left[(\Delta + \mu)^2 + \left(\frac{\hbar\gamma}{2} \right)^2 \right] \mu = I_F. \tag{1.13}$$

This is a third order equation for μ and it is easily shown that $I_F(\mu)$ is monotonic for $\mu \geq 0$ as long as $\Delta > -\frac{\sqrt{3}}{2}\gamma$, so that in this optical limiter regime for any value of F_0 there is only one stable ψ_0. When $\Delta < -\frac{\sqrt{3}}{2}\gamma$ instead, for $I_F \in [I_F^1, I_F^2]$ there are three values of μ satisfying Eq. (1.13), but it will turn out that at most two of them are dynamically stable. This result, depicted in Fig. 1.5.a, indicates that, if the driving laser is blue-detuned at least by $\frac{\sqrt{3}}{2}\gamma$, there is a range of values of the pump intensity for which the polariton field configuration is bistable (Boyd [2019]). In practice one has to deal with a hysteresis cycle: ramping on the pump the polariton state follows the lower bistability branch; when I_F passes I_F^2 the laser gets resonant with the blue-detuned polariton state so that μ jumps up; when ramping down instead, the pump power μ follows the upper bistability branch before jumping down.

Bistable behaviors have indeed been found in a number of experiments (Baas et al. [2004], Sarkar et al. [2010], Paraïso et al. [2010], Rodriguez et al. [2017], Stepanov et al. [2019]), although it turns out to be very difficult to obtain quantitative agreement with theory, likely because of the sensitivity of this phenomenon to external noise sources. We also mention that, while bistability holds rigorously in this mean-field treatment, strictly speaking the full quantum theory forbids bistability, because of the finite tunneling rate between the two candidate bistable states (Vogel and Risken [1988], Vicentini et al. [2018]). In practice, the auto-correlation time diverges with the number of photons and the size of the spot, so that within an observation window of finite duration the phenomenology gets hysteretical (Rodriguez et al. [2017]).

1.3.2 Bogoliubov excitations

We now move to consider the dynamics of small excitations on top of the uniform steady-state. This is done by inserting $\psi(\mathbf{r}, t) = \psi_0 + \delta\psi(\mathbf{r}, t)$ in Eq. (1.11) and keeping terms of the first order in $\delta\psi$:

$$i\hbar\partial_t \delta\psi(\mathbf{r}, t) = \left(\Delta - \frac{\hbar^2}{2m}\nabla^2 + 2g|\psi_0|^2 - i\frac{\hbar\gamma}{2} \right) \delta\psi + g\psi_0^2 \delta\psi^*. \tag{1.14}$$

Because of the last term, arising from the nonlinearity, this linear problem is not diagonalized just by exploing translational invariance and expanding in Fourier waves $e^{i\mathbf{k}\cdot\mathbf{r} - i\omega(\mathbf{k})t}$. Instead, since each plane wave is coupled to its complex conjugate, one has to consider the general ansatz $\delta\psi(\mathbf{r},t) = ue^{i\mathbf{k}\cdot\mathbf{r}-i\omega(\mathbf{k})t} + v^{*}e^{-i\mathbf{k}\cdot\mathbf{r}+i\omega^{*}(\mathbf{k})t}$ (Pitaevskii and Stringari [2016], Carusotto and Ciuti [2004]) and diagonalize the 2×2 Fourier-Bogoliubov blocks

$$\hbar\omega\begin{pmatrix}u\\v\end{pmatrix} = \left[-i\frac{\hbar\gamma}{2} + \begin{pmatrix}\Delta+\frac{\hbar^2}{2m}\mathbf{k}^2+2\mu & \mu\\ -\mu & -\Delta-\frac{\hbar^2}{2m}\mathbf{k}^2-2\mu\end{pmatrix}\right]\begin{pmatrix}u\\v\end{pmatrix} \equiv \mathscr{L}(\mathbf{k})\begin{pmatrix}u\\v\end{pmatrix}. \tag{1.15}$$

The excitations have dispersion

$$\hbar\omega_{\pm}(\mathbf{k}) = -i\frac{\hbar\gamma}{2} \pm \sqrt{\left(\Delta+\frac{\hbar^2}{2m}\mathbf{k}^2+2\mu\right)^2-\mu^2} \tag{1.16}$$

and are depicted in Fig. 1.5.b for different values of μ and both in the optical limiter and bistable regimes. In the former case and for $\Delta>0$, the Bogoliubov excitations are always dynamically stable, i.e. $\mathrm{Im}\omega_{\pm}<0$ and the particle (hole) branch, defined by the condition $|u|>|v|$ ($|u|<|v|$) has positive (negative) real part. When this is the case the dispersion does not cross the $\omega=0$ line and it is said to be gapped; also the hole fraction of particle-like excitations will be small and vice versa. In particular, in the linear regime of small pump intensities $\mu \ll \gamma$, the nonlinearity doesn't play any role, the particle branch starts at Δ and the Bogoliubov modes closely follow the polariton modes of the undriven cavity,

The situation is much richer in the second regime, for which $\Delta < -\frac{\sqrt{3}}{2}\gamma$. For small pump intensities (point A of Fig. 1.5.b), we recover the bare LP band, which is the linear regime explained above. At very high pump intensity (point D), for which $\Delta+\mu>0$, the polariton band is blue-shifted because of interactions and the dispersion is gapped. When the special condition $\Delta+\mu=0$ is met (point C), the dispersion is acoustic:

$$\omega_{\pm}(\mathbf{k}) = \pm c_s|\mathbf{k}| - i\frac{\gamma}{2} \tag{1.17}$$

with the speed of sound defined by

$$mc^2 = \mu. \tag{1.18}$$

We will return on this regime later. For slightly lower intensities, the particle and hole branches stick together and an imaginary part develops (point C') around $\mathbf{k}=0$, which finally becomes an instability when at the turning point $I_F = I_F^1$. Other instabilities at finite wavevector develops at the end of the lower bistability branch via the same sticking mechanism (points B, B'). The central bistability branch is characterized by the unphysical property $\frac{d\mu}{dI_F}<0$ and it is always unstable.

The symmetric structure of the spectrum is explained by noticing that the Bogoliubov matrix $\mathscr{L}(\mathbf{k})$ is characterized by particle-hole and parity symmetries, that combine in

$$\mathscr{P}\mathscr{L}(\mathbf{k}) = -\mathscr{L}(\mathbf{k})\mathscr{P} \tag{1.19}$$

where

$$\mathscr{P} = \mathscr{K}\begin{pmatrix}0 & 1\\ 1 & 0\end{pmatrix} \tag{1.20}$$

and $\mathscr{K}$ stands for complex conjugation. For a generic eigenvector $|\omega_{\mathbf{k}}\rangle = (u\ v)^T$ of $\mathscr{L}(\mathbf{k})$ of eigenvalue ω, this symmetry implies that

$$\mathscr{L}(\mathbf{k})\,\mathscr{P}|\omega_{\mathbf{k}}\rangle = -\omega^{*}\mathscr{P}|\omega_{\mathbf{k}}\rangle\,, \tag{1.21}$$

i.e. that $\mathscr{P}|\omega_{\mathbf{k}}\rangle = (v^{*}\ u^{*})^T$ is itself an eigenvector of $\mathscr{L}(\mathbf{k})$ of eigenvalue $-\omega^{*}$. This imposes the presence of pairs of eigenvectors with the same imaginary part and opposite real parts, corresponding to complex dispersions of the form $\omega^{\pm}(\mathbf{k}) = \pm\epsilon(k) - i\gamma(k)/2$, or to two purely imaginary and in principle unrelated eigenvalues $\omega^{\pm}(\mathbf{k}) = -i\gamma_{\pm}(k)/2$.

Because of this connection and of the form of the ansatz for $\delta\psi$, the positive and negative excitations cannot be excited independently: when an external probe is present both branches are in general visible in the spectrum. This can be easily understood from the linear kernel obtained by inverting the Bogoliubov matrix and we will see some examples of this procedure later.

1.3.3 Landau criterium

It is now time to introduce a notion of superfluidity. In equilibrium quantum fluids there exists a particularly precise definition, stating that a superfluid yields no resistence to a transverse probe, or in the linear response language the transverse current-current correlation function is zero. This definition may apply to polariton condensates, but it has been shown rigorously by Juggins et al. [2018] that such correlation function is certainly nonzero in coherently driven fluids. The fundamental difference with standard BECs is that the polaritons are injected with the phase of the laser, so that there is no $U(1)$ spontaneous symmetry breaking; on the contrary, the phase is fixed and this rigidity prevents the formation, under the pump spot, of any current which is not directly imprinted by the drive, such as the currents involved in vortices. It is nevertheless possible to measure how much a resonantly injected polariton flow gets distorted in passing around an obstacle, and how strong is the drag force exerted on it. As shown below, a regime can be clearly identified when this distortion and drag force are strongly suppressed. This is phenomenolgical sense in which the polariton community uses the word superfluidity for resonantly driven fluids.

The study of the collective excitations provides a good starting point for discussing the superfluid properties of equilibrium quantum fluids. According to the Landau criterion (Landau et al. [1981], Pitaevskii and Stringari [2016]), a standard superfluid is able to flow without friction at speed $\mathbf{v}$ around a static defect until it is energetically favourable to create excitations in it, i.e. if $\omega(\mathbf{k}) + \mathbf{k} \cdot \mathbf{v} \geq 0$, where $\omega(k)$ is the excitation dispersion of the fluid at rest. This provides the well-known expression for the critical velocity,

$$v_c = \min_{\mathbf{k}} \frac{\omega(\mathbf{k})}{k}. \tag{1.22}$$

For a weakly interacting fluid of bosons with acoustic dispersion $\omega(\mathbf{k}) = c_s|\mathbf{k}|$ at low momenta, the Landau criterium yields $v_c = c_s$, where the equilibrium analogue of Eq. 1.18 typically holds for c_s.

Alternatively, a weak defect is able to move through a superfluid without friction if the dispersion $\omega(\mathbf{k})$ of elementary excitations in the latter has no intersection with a straight line $\omega = -\mathbf{v} \cdot \mathbf{k}$. For particles with a parabolic dispersion and local interactions, equivalence of the two points of view is ensured by the Galilean invariance.

This formulation applies well to superfluids of material particles with a long lifetime of the collective excitations, i.e. where the imaginary part $\mathrm{Im}[\omega(\mathbf{k})]$ of the dispersion relation is much smaller than the real part $\mathrm{Re}[\omega(\mathbf{k})]$ and can be neglected at long wavelength. However, subtleties arise in the case of driven-dissipative fluids, e.g. the polariton ones, where the real and imaginary parts of the dispersion $\omega(\mathbf{k})$ may have comparable magnitudes. The importance of this effect for incoherently pumped polariton condensates was first discussed by Wouters and Carusotto [2010], who suggested a generalized form of the Landau criterion for driven-dissipative systems in terms of real frequencies and complex momenta. In particular, for a polariton superfluid flowing against an obstacle it was shown that a pattern forms when the velocity of the fluid is larger than the critical velocity, thus showing clear superfluid-like features even in the presence of drive and dissipation. In the case of coherent pumping, for which a phenomenological way of assessing superfluidity is by computing the drag force, a pioneering discussion of the effect of drive and losses was reported in (Berceanu et al. [2012]).

In spite of these issues, the naive application of the Landau criterium provides very good indications about the behaviour of polariton flows injected by a coherent spatially infinite pump. This was first discussed in (Carusotto and Ciuti [2004]), using the version of Landau criterium for a moving fluid against a shallow static defect. Their results, depicted in Fig. 1.6, show how the intersection of the dispersion with the $\omega = 0$ plane allows to predict the distribution in Fourier space of the scattered wave. Also, the regime of panels (e,f) is what one would call superfluid and it translates to a very small perturbattion of the real space profile of the flow (not shown here). On the experimental side, this physics has been beautifully demonstrated by Amo et al. [2009] by making use of a defect centered under a large pump spot.

To derive the dispersion curves shown on the left side of Fig. 1.6, let' s study via simple algebra how the $\mathbf{k}_p \neq 0$ case of the GPE (1.10) gets mapped to the $\mathbf{k}_p = 0$ one. The ultimate origin of this connection will be clarified in the next Section via a Galilean transformation. The GPE (1.10) with $F(\mathbf{r}, t) = F_0 e^{i\mathbf{k}_p \cdot \mathbf{r} - i\omega_p t}$ can be treated by making the transformation $\psi(\mathbf{r}, t) \to \psi(\mathbf{r}, t) e^{i\mathbf{k}_p \cdot \mathbf{r} - i\omega_p t}$ to yield

$$i\hbar\partial_t \psi(\mathbf{r}, t) = \left(\Delta + \frac{\hbar^2}{2m}(\hat{\mathbf{k}} + \mathbf{k}_p)^2 + g|\psi|^2 - i\frac{\hbar\gamma}{2} \right) \psi + F_0, \tag{1.23}$$

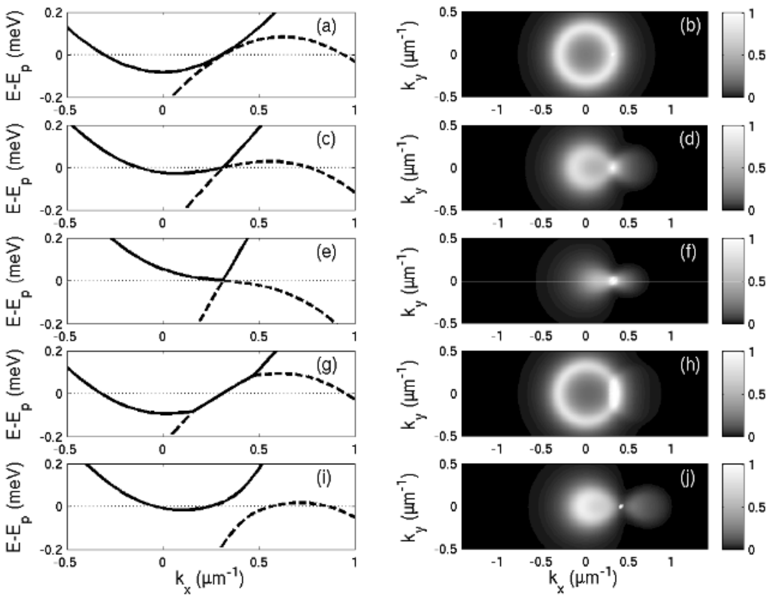

Figure 1.6: *Scattering from a static defect.* On the left sides, the dispersion relation along the $k_y = 0$ cut is plotted for different values of the pump intensity and of $k_{p,x}$. On the right side the far-field emission of the scattered part of the polariton wave is reported, as computed via Eq. (1.36). In particular, the first row (a,b) shows the linear with the usual Rayleigh ring. In the third row (e,f) the superfluid regime is depicted. Plot taken from Carusotto and Ciuti [2004].

where $\hat{\mathbf{k}} \equiv -i\nabla$. The search for a "uniform" steady-state leads to the condition

$$0 = \left(\Delta + \frac{\hbar^2}{2m}\mathbf{k}_p^2 + g|\psi_0|^2 - i\frac{\hbar\gamma}{2} \right) \psi_0 + F_0, \tag{1.24}$$

which is the same of Eq. (1.12) provided that one considers a new and more proper definition of detuning $\Delta_p \equiv \Delta + \frac{\hbar^2}{2m}\mathbf{k}_p^2 = \omega_{LP}(\mathbf{k}_p) - \omega_p$, which quite naturally is the detuning not with respect to the bottom of the LP band, but rather relatively to $\omega_{LP}(\mathbf{k}_p)$. The discussion of the bistability diagram is then inherited from the previous paragraphs.

Moving to the Bogoliubov spectra, one can plug the ansatz $\psi(\mathbf{r}, t) = \psi_0 + ue^{i\mathbf{k}\cdot\mathbf{r} - i\omega(\mathbf{k})t} + v^* e^{-i\mathbf{k}\cdot\mathbf{r} + i\omega^*(\mathbf{k})t}$ into Eq. (1.23) and obtain the linearized eigenproblem

$$\hbar\omega \begin{pmatrix} u \\ v \end{pmatrix} = \left[-i\frac{\hbar\gamma}{2} + \frac{\hbar^2}{2m}\mathbf{k}_p \cdot \mathbf{k} + \begin{pmatrix} \Delta_p + \frac{\hbar^2}{2m}\mathbf{k}^2 + 2\mu & \mu \\ -\mu & -\Delta_p - \frac{\hbar^2}{2m}\mathbf{k}^2 - 2\mu \end{pmatrix} \right] \begin{pmatrix} u \\ v \end{pmatrix} \equiv \mathscr{L}(\mathbf{k}) \begin{pmatrix} u \\ v \end{pmatrix}. \tag{1.25}$$

The dispersion is now

$$\hbar\omega_\pm(\mathbf{k}) = -i\frac{\hbar\gamma}{2} + \frac{\hbar}{2m}\mathbf{k}_p \cdot \mathbf{k} \pm \sqrt{\left(\Delta_p + \frac{\hbar^2}{2m}\mathbf{k}^2 + 2\mu \right)^2 - \mu^2}, \tag{1.26}$$

with the Doppler term $\frac{\hbar}{2m}\mathbf{k}_p \cdot \mathbf{k}$ which tilts the dispersion. Apart from this shear mapping and with the sagacity of using Δ_p instead of Δ, all the needed knowledge has already been explained in Fig. 1.5 and in the relative discussion. This Doppler shift is in perfect analogy with standard quantum fluids and it allows to use interchangeably the two formulations of the Landau criterium, for a moving defect in a fluid at rest or for a fluid flowing against a static defect.

1.4 Galilean boosts and polariton fluids*

(this Section closely follows Section II of Amelio et al. [2020b])

In the first half of this Section we will illustrate a mathematical mapping that relates the GPE dynamics of polariton fluids driven with different pump wavevectors. As a corollary, if the relative velocities and the polariton densities are the same, the two cases of polaritons injected against a static defect and of a defect moving in a fluid at rest turn out to be the same situation depicted in two different systems of coordinate. Because of its formal analogy, we call this transformation a Galilean boost, even though it does not correspond to a physical change of reference frame.

The starting point is the GPE Eq. (1.10) for the field $\psi_{lab}(\mathbf{x},t)$ expressed in the coordinates of laboratory frame

$$i\partial_t\psi_{lab}(\mathbf{x},t) = \left(\omega_0 - \frac{\hbar}{2m}\nabla^2 + \mathrm{g}|\psi_{lab}|^2 + V_{ext}(\mathbf{x}) - i\frac{\gamma}{2}\right)\psi_{lab} + F_{lab}(\mathbf{x},t), \tag{1.27}$$

where $\mathrm{g} = g/\hbar$ and $\hbar V_{ext}(\mathbf{x})$ is the static potential acting on the polaritons, including static defects.

Now we develop the aforementioned formal Galilean boost and with some abuse of notation employ the terminology commonly adopted for physical Galilean transformations. For instance, when within this analogy we refer to the "frame of reference moving at velocity $\mathbf{v}_G$ with respect to the lab", we have in mind the change of coordinates $\mathbf{y} = \mathbf{x} - \mathbf{v}_G t$ (the lab is just one chosen frame), while the time variable remains the same in the two coordinate systems. The chosen convention for the sign of $\mathbf{v}_G$ is such that a fluid moving at velocity $\mathbf{v}_G$ in the laboratory frame is seen as at rest in the boosted one. The Galilean transformation is given by the unitary operator

$$\hat{U}_{lab\rightarrow G} = e^{i\frac{\hat{\mathbf{p}}\mathbf{v}_G t - \hat{\mathbf{x}} m \mathbf{v}_G}{\hbar}} = e^{i\frac{\hat{\mathbf{p}}\mathbf{v}_G t}{\hbar}} e^{-i\frac{\hat{\mathbf{x}} m \mathbf{v}_G}{\hbar}} e^{+i\frac{m v_G^2 t}{2\hbar}}, \tag{1.28}$$

so that applied on the wavefunction reads

$$\psi_G(\mathbf{y}) = [\hat{U}_{lab\rightarrow G}\psi_{lab}](\mathbf{y}) = e^{-i\frac{m\mathbf{y}\mathbf{v}_G}{\hbar}} e^{-i\frac{m v_G^2 t}{2\hbar}} \psi_{lab}(\mathbf{y} + \mathbf{v}_G t)\,. \tag{1.29}$$

Galilean invariance of the conservative part of the GPE evolution (1.27) is then guaranteed by the parabolic form of the kinetic energy according to elementary quantum mechanics (Cohen-Tannoudji et al. [1991]), so that in our terminology the (undriven) polariton field is Galilean invariant; instead, the covariance of the driving term is to be discussed in a moment. For usual polariton systems resulting from the strong coupling of a cavity photon mode to an excitonic transition this parabolic approximation is accurate for the typical flow speeds considered in the experiments (Carusotto and Ciuti [2013]).

The pump and loss terms can be treated by taking a step back and considering the Hamiltonian that generates the GPE (1.27); in particular the pump term in this Hamiltonian reads $\hat{H}^{drive}_{lab} = \int d\mathbf{x} F_{lab}(\mathbf{x},t)\hat{\Psi}^\dagger(\mathbf{x}) + \text{h.}c.$, which transforms as

$$\hat{H}^{drive}_{G} = \hat{U}_{lab\rightarrow G}\hat{H}^{drive}_{lab}\hat{U}^\dagger_{lab\rightarrow G} = \int d\mathbf{y} F_{lab}(\mathbf{y} + \mathbf{v}_G t, t) e^{-i\frac{m\mathbf{y}\mathbf{v}_G}{\hbar}} e^{-i\frac{m\mathbf{v}_G^2 t}{2\hbar}} \hat{\Psi}^\dagger(\mathbf{y}) + \text{h.c.}. \tag{1.30}$$

The dynamics in the boosted frame is then described by the same GPE

$$i\partial_t\psi_G(\mathbf{y},t) = \left(\omega_0 - \frac{\hbar}{2m}\nabla^2 + \mathrm{g}|\psi_G|^2 + V_{ext}(\mathbf{y} + \mathbf{v}_G t) - i\frac{\gamma}{2}\right)\psi_G + F_G(\mathbf{y},t), \tag{1.31}$$

provided the pump term is covariantly transformed according to

$$F_G(\mathbf{y},t) = F_{lab}(\mathbf{y} + \mathbf{v}_G t, t) e^{-i\frac{m\mathbf{y}\mathbf{v}_G}{\hbar}} e^{-i\frac{m\mathbf{v}_G^2 t}{2\hbar}}. \tag{1.32}$$

Note that this transformation involves a shift of the wavevector proportional to the velocity as well as an overall frequency shift $m v_G^2 t/(2\hbar)$. The loss term remains unchanged thanks to the spatio-temporally local form that we have assumed from the outset.

Eqs. (1.27) and (1.31) describe the same dynamics, the observables in the two frames being linked by the usual Galilean prescriptions: $|\psi_{lab}(\mathbf{x},t)|^2 = |\psi_G(\mathbf{y},t)|^2$ for the density and $\mathbf{v}^{flow}_{lab}(\mathbf{x},t) = \mathbf{v}^{flow}_G(\mathbf{y},t) + \mathbf{v}_G$ for the flow velocity, defined in terms of the wavefunction as usual as $\mathbf{v}^{flow} = \hbar\,\mathrm{Im}[\psi^*\nabla\psi]/(2m\,|\psi|^2)$. Note that the overall phase factor in Eq. (1.32) is needed to ensure that the density (and thus the bistability properties, the acoustic shape of the dispersion etc.) is independent of the Galilean frame.

For a plane-wave coherent drive with frequency ω_p and wavevector $\mathbf{k}_p$ the detuning $\Delta_p = \hbar\omega_0 + \hbar^2\mathbf{k}_p^2/2m - \hbar\omega_p$ pops out again quite naturally in the frame comoving with the fluid at the flow velocity imprinted by the pump $\mathbf{v}_p = \hbar\mathbf{k}_p/m$. Our approach then gives a formal insight on the algebraic trick used in the previous Section to treat the case $\mathbf{k}_p \neq 0$. Notice that for finite pump spots the Galilean arguments still hold: per example, they relate a stationary spot centered at wavevector $\mathbf{k}_p$ is related to a spot with spatial envelope moving at velocity $-\hbar\mathbf{k}_p/m$ and carrier centered, in a given instant, at zero wavevector. The second situation is not so relevant for our discussion, so we always consider pump spots that can be considered spatially "uniform" (where the quote marks mean apart from the plane wave factor).

Before proceeding, it is important to stress that the Galilean transformation discussed here is useful to mathematically relate the dynamics of fluids injected with different speed, but it does *not* correspond to a physical change of reference frame, for instance an experimentalist running parallel to the cavity mirrors. Indeed, for a medium with a refractive index different from unity, light propagation in a *physically* boosted Lorentz frame at velocity $\mathbf{v}_L$ is affected by the celebrated Fresnel drag effect (Jackson [1975], Landau et al. [1984], Jones [1972], Artoni et al. [2001], Carusotto et al. [2003]), which changes the dispersion relation to the same order in v_L/c as the Doppler shift:

$$\omega'(\mathbf{k}') = \omega(\mathbf{k}') + \left(\frac{1}{n_{cav}^2} - 1\right) \mathbf{v}_L \cdot \mathbf{k}' + ... \tag{1.33}$$

where the apex refers to quantities measured in the Lorentz frame and n_{cav} is the refractive index inside the cavity.

In conclusion, despite the covariance of the pump term, the Galilean invariance of the (undriven) polariton field allows to state that the critical (relative) speed depends on the density but not on the reference frame, as a corollary of what shown in the previous section; importantly, this does *not* assume to work at the acoustic point. More precisely, in the approximation of an infinite uniform excitation spot, the pattern created by scattering against a defect (hence the superfluidity threshold) depends only on density and on the relative velocity between the defect and the fluid: the flow against a static defect and the defect moving through the fluid at rest correspond to the same dynamics viewed in two different Galilean frames.

1.5 Driven-dissipative aspects of polariton superfluids

(this Section closely follows Section III of Amelio et al. [2020b])

Now we turn to a formal study of the density pattern created when a polariton fluid is coherently excited into motion against a static obstacle by a monochromatic pump of frequency ω_p and in-plane wavevector $\mathbf{k}_p$, with a special focus on the effects due to drive and dissipation. The Galilean argument just discussed entails that these results extend straightforwardly to the case of a defect moving in a fluid at rest.

In order to determine the density modulation pattern of the fluid flowing around a weak defect at rest, we adopt the method explained in Carusotto and Ciuti [2004] and linearize the GPE (1.10) on top of the homogeneous solution at the pump's wavevector $\mathbf{k}_p$ and frequency ω_p, via the ansatz

$$\psi(\mathbf{x}, t) = e^{i(\mathbf{k}_p\cdot\mathbf{x} - \omega_p t)} \left[\psi_0 + \int d\mathbf{k}\ \ \delta\psi_\mathbf{k} e^{i\mathbf{k}\cdot\mathbf{x}}\right] , \tag{1.34}$$

with $\delta\psi$ of the same order of the weak defect potential $\delta V_{\rm def}$. Importantly, since the defect produces a static perturbation on the fluid, the wavefunction (1.34) keeps a monochromatic form at the pump frequency ω_p.

Inserting this ansatz into the GPE (1.27) and keeping the terms of the first order in $\delta V_{\rm def}$, one finds that the different Fourier components $\delta\psi_\mathbf{k}$ are decoupled and each of them satisfies

$$\left(\omega_0 + \frac{\hbar(\mathbf{k}_p + \mathbf{k})^2}{2m} + 2g|\psi_0|^2 - \omega_p - i\frac{\gamma}{2}\right) \delta\psi_\mathbf{k} + \psi_0^2\, \delta\psi^*_{-\mathbf{k}} = -\delta V_{\rm def}(\mathbf{k})\psi_0\,. \tag{1.35}$$

Then, by combining this equation with the complex conjugate one and solving the matrix inversion problem, we obtain for an arbitrary (real) potential

$$\delta\psi_\mathbf{k} = \chi_V(\mathbf{k})\psi_0\delta V_{\rm def}(\mathbf{k}) \tag{1.36}$$

where the response function to an external potential is defined as

$$\chi_V(\mathbf{k}) = [\mathscr{L}(\mathbf{k})]^{-1}_{11} - [\mathscr{L}(\mathbf{k})]^{-1}_{12} \tag{1.37}$$

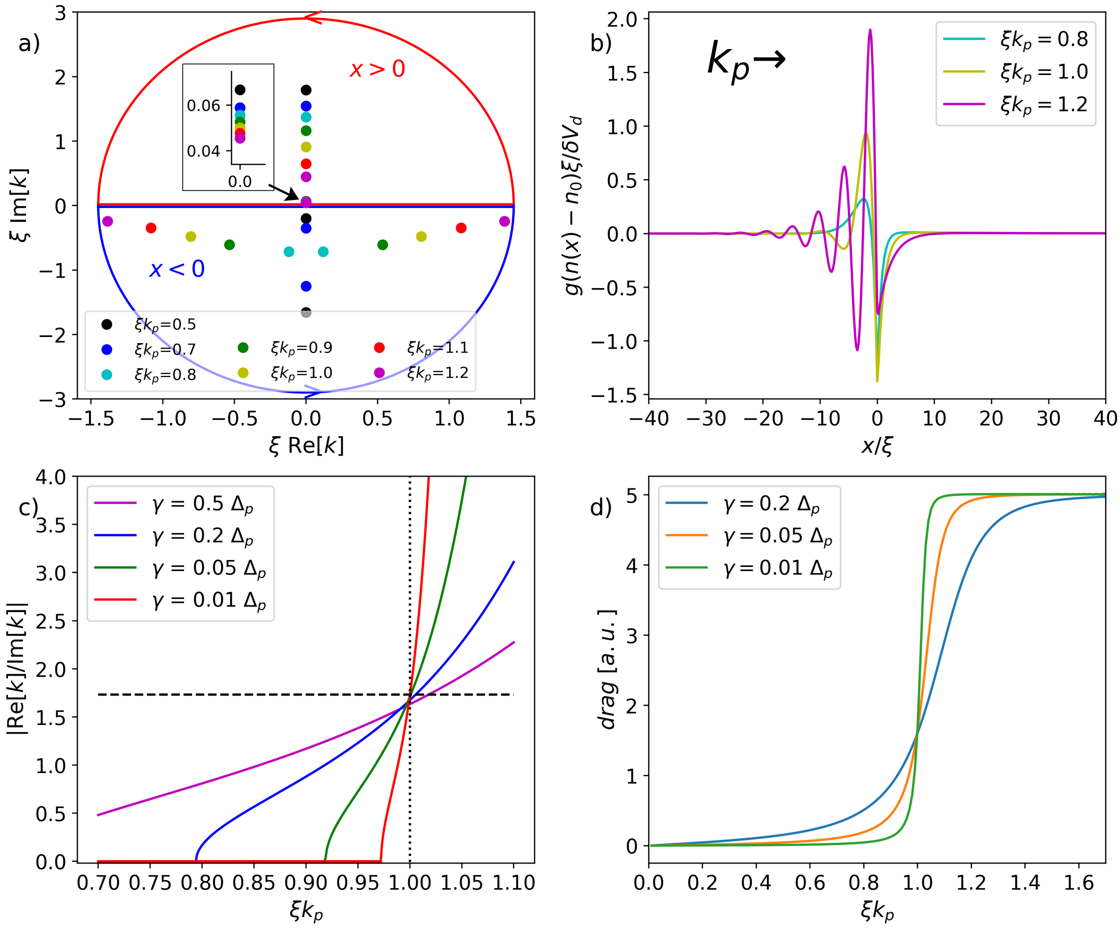

Figure 1.7: (a) Evolution of the four complex poles of the one-dimensional response function $\chi_V(k \in \mathbb{C})$ for different values of the flow speed $k_p > 0$. The residue theorem is to be applied to the upper (lower) half–plane for $x > 0$ ($x < 0$). (b) Spatial profile of the density modulation induced by the defect (located at $x = 0$) for different values of k_p. More precisely, the renormalized density perturbation $\frac{g[n(x)-n_0]}{\delta V_{def}}$ is reported. (c) Ratio $|\mathrm{Re}[k]/\mathrm{Im}[k]|$ between the real and imaginary part of the poles as a function of k_p and for different dissipation rates; the horizontal dashed line indicates $\sqrt{3}$. (d) Drag force as a function of the flow speed for different loss rates γ. Across (a–d) the pump frequency is kept at the sonic resonance point $\Delta_p = gn_0$, unless differently specified the damping is set to $\gamma/gn_0 = 0.2$, and no incoherent reservoir is present.

and the 2×2 Bogoliubov matrix reads

$$\mathscr{L}(\mathbf{k}) = \begin{pmatrix} \eta(\mathbf{k_p}+\mathbf{k}) + gn_0 - i\gamma/2 & g{\psi_0}^2 \\ -g{\psi_0^*}^2 & -\eta(\mathbf{k_p}-\mathbf{k}) - gn_0 - i\gamma/2 \end{pmatrix} . \tag{1.38}$$

Here, $\mathbf{k} = \mathbf{k}_p + \mathbf{k}$ is the (real-valued) total momentum and the detuning function

$$\eta(\mathbf{k}) = \omega_0 + \hbar k^2/2m + gn_0 - \omega_p \,. \tag{1.39}$$

The perturbed wavefunction in real space is finally obtained from (1.36) by means of the Fourier transform (1.34). The Bogoliubov dispersion relation $\omega(\mathbf{k})$ corresponds to the eigenvalues of the matrix (1.38), i.e. the zeros of $\det[\omega - \mathscr{L}(\mathbf{k})]$ on the manifold $\mathbf{k} \in \mathbb{R}^D, \omega \in \mathbb{C}$.

While these complex frequency modes allow to study dynamical excitations, it was hinted at in Wouters and Carusotto [2010] that the response of the steady state to static external perturbations is most conveniently characterized in terms of modes with a real frequency and a complex momentum. In classical electromagnetism (Tait [1972]), such waves naturally appear when dealing with monochromatic light incident on an absorbing medium. In our context, this point of view is implicitly assumed upon using the residue theorem to evaluate the Fourier integral (1.34): since the defect is at rest, it generates a static perturbation in the fluid at $\omega = 0$, whose peak wavevectors $\mathbf{k}$ are determined by the zeros of $\det \mathscr{L}(\mathbf{k})$, i.e. the poles of $\chi_V(\mathbf{k})$ as a function of $\mathbf{k} \in \mathbb{C}^D$.

In the simplest case of a one-dimensional geometry and a delta-like potential at rest giving a momentum-independent $\delta V_{\rm def}(k) = \delta V_{\rm def}$, the position of the poles in the complex k plane are shown in Fig. 1.7(a) for different values of the pump wavevector $k_p > 0$ (that is, of the speed $\hbar k_p/m$ of the fluid) and a resonant laser frequency $\omega_p = \hbar k_p^2/(2m) + gn_0 + \omega_0$ such that the Bogoliubov dispersion is gapless and has a sonic behaviour with a well-defined speed of sound c_s.

With the residue theorem technique, evaluation of the Fourier integral (1.34) for $x > 0$ ($x < 0$) only picks the poles in the upper (lower) complex half-plane. For the $x > 0$ region, a single pole is present and this has a vanishing real part. It corresponds then to the exponentially decaying perturbation that is visible in Fig.1.7(b) in the $x > 0$ downstream region. The faster the flow, the closer the pole to the real axis, so the slower the exponential decay.

The behaviour is richer in the $x < 0$ upstream region: for small speeds k_p, the two poles have again a vanishing real part and the perturbation displays a monotonic decay. Around $\hbar k_p/mc_s \simeq 0.75$ the poles merge in the complex k plane at a finite $\mathrm{Im}[k]$ and then separate again along a direction parallel to the real axis. For sufficiently large speeds, their real part exceeds the imaginary one so that the perturbation in the fluid starts displaying a clear oscillatory character upstream of the defect.

As the association between the real part of the wavevector and the transferred momentum suggests, this change in behaviour is expected to result into a sharp change in the value of the drag force exerted by the moving fluid onto the defect, defined as (Astrakharchik and Pitaevskii [2004], Wouters and Carusotto [2010], Berceanu et al. [2012])

$$F_d = -\int dx\, \nabla V_{\rm def}(x)\, |\psi(x)|^2. \tag{1.40}$$

A plot of F_d as a function of the fluid speed is shown in Fig.1.7(d) for the sonic case and qualitatively agrees with this prediction.

In particular, the position of the threshold position is consistent with the naive Landau criterion based on comparing the flow speed with the speed of sound. The velocity-independent value of the friction force at high speeds is typical of one-dimensional superfluids and was first anticipated by Astrakharchik and Pitaevskii [2004] for conservative atomic systems. Finally, the smaller the loss rate γ, the sharper the transition from a frictionless superfluid behaviour at slow speeds to a finite friction force at fast speeds.

While this picture is qualitatively accurate, establishing a precise relation between the location of the threshold and the behaviour of the poles in the k-complex plane requires a bit more careful analysis. As one can see in the lower half-plane of panel (a), the k vectors aquire a real part in fact at a smaller value $k_p \approx 0.75$ than the threshold that is visible in the force plot around $k_p \approx 1$. To explain this feature, one can see in panel (c) that the different curves of $\mathrm{Re}[k]/\mathrm{Im}[k]$ for different values of the loss rate cross at a single value close to $\sqrt{3}$ [2] for a value of the pump wavevector $\hbar k_p \simeq mc_s \simeq 1$ that approximately corresponds to the threshold for the drag force shown in panel (d). This suggests that the threshold is not determined by the point where the k vectors aquire a real part, but rather by the point when the real part exceeds (by a factor $\sqrt{3}$) the imaginary part.

1.6 Hydrodynamics from a finite pump spot*

(this Section closely follows Amelio and Carusotto [2020a])

In this Section we discuss, within the Gross–Pitaevskii framework, superfluidity, soliton-like patterns, and instabilities in a non-equilibrium polariton fluid injected by a spatially localized and continuous-wave coherent pump and flowing against a defect located outside the pump spot. In the case of resonant and continuous-wave (as opposed to pulsed) excitation, the use of finite laser spots is necessary to avoid the fixing of the polariton field phase that occurs in the pumped region and thus open to the possibility of observing nontrivial phenomena including vortical or turbulent states (Amo et al. [2011]) and even analogue Hawking radiation close to the trans-sonic horizon of the flow (Gerace and Carusotto [2012], Nguyen et al. [2015]).

---

[2] Indeed, at $\hbar k_p \simeq mc_s \simeq 1$ the pole condition in terms of $z = k/k_p$ simply reads $z^4 + iaz + a^2$, whose solution satisfy $|\mathrm{Re}[z]/\mathrm{Im}[z]| \to \sqrt{3}$ as $a \equiv \frac{\hbar\gamma}{mc_s^2} \to 0$.

Most studies on polariton hydrodynamics have been so far guided by the analogies to equilibrium superfluids such as liquid Helium and Bose-Einstein condensates of ultracold atoms (Carusotto and Ciuti [2013]): along these lines, Bose–Einstein condensation (Kasprzak et al. [2006]), superfluidity (Amo et al. [2009]) and turbulence (Amo et al. [2011], Sanvitto et al. [2011], Nardin et al. [2011]) have been experimentally explored in polariton fluids in the last decade. In the resonant case, the starting point is once again the GPE (1.11) where, in order to escape the phase locking induced by the external laser and the consequent impossibility of generating vortices[3], it is necessary to consider a driving field with a spatially finite support. Outside the pump spot, one has $F(\mathbf{r}) = 0$ and it is convenient to also consider a hydrodynamic velocity – density formalism,

$$\partial_t n + \nabla \cdot (n\mathbf{v}) = -\gamma n \tag{1.41}$$

$$m\partial_t \mathbf{v} + \nabla\left(\Delta + \frac{m}{2}\mathbf{v}^2 + gn - \frac{\hbar^2}{2m\sqrt{n}}\nabla^2\sqrt{n}\right) = 0 \tag{1.42}$$

where $n(\mathbf{r},t) = |\psi(\mathbf{r},t)|^2$ and $\mathbf{v}(\mathbf{r},t) = \frac{\hbar}{m}\nabla \arg[\psi(\mathbf{r},t)]$ are the local density and velocity of the fluid. Without loss of generality, in this Section we always take $g = \hbar^2/m = 1\,\mathrm{meV}\,\mu\mathrm{m}^2$. These equations correspond to density and energy conservation respectively, and, exception made for the decay term γ, they are *locally* identical to the ones used for conservative atomic BECs (Pitaevskii and Stringari [2016]). Of course, the calculation of an actual flow profile using Eqs. (1.41,1.42) requires that these local equations in the undriven region are supplemented with proper boundary conditions to match the flow in the driven region. These boundary conditions are responsible for the unexpected behaviours that are illustrated below.

Because of this connection to the equilibrium equations, most of the previous work on soliton formation, vortex nucleation and turbulence when the polariton flow exits the pump spot and impacts against a static defect has been permeated by the equilibrium approach and has tended to highlight the similarities with the physics of ultracold gases rather than the differences (Carusotto and Ciuti [2013]). In particular, for equilibrium quantum fluids flowing against a static obstacle it is known (Winiecki et al. [2000], Neely et al. [2010], Kamchatnov and Pitaevskii [2008]) that, for increasing flow velocity, three regimes are scanned, going from a superfluid to a turbulent regime and again to soliton nucleation.

A similar behavior was observed for polaritons in the experiment by Amo et al. [2011]. However, that observation was backed by a flawed numerical study (Pigeon et al. [2011]) which confirmed the equilibrium scenario of the three phases, so that a critical quantitative analysis of the experimental data was never performed. In our work we reopen this issue and by solving carefully the GPE we question this theoretical equilibrium prediction.

More specifically, we show that according to the resonantly driven GPE the superfluid-turbulent-soliton picture is replaced by a crossover from a shallow to a deep soliton-like perturbation. In particular, a clean superfluid flow around the defect is never reached in our simulations. This is explained in terms of the properties of one-dimensional flows, in particular their weak dependence on the pump parameters: acceleration of polaritons by the quantum-pressure-driven density gradient outside the pump spot is shown to quickly induce a transition from sub- to super-sonic flow in the close vicinity of the pump spot. This feature restricts our possibility to explore the superfluid hydrodynamics in the undriven region outside the pump. Such complex and highly nonlinear behaviours call for quantitative experimental tests of the underlying Gross–Pitaevskii equation.

The role of disorder in inducing non-stationary behaviours with moving phase singularities is also highlighted and the possibility of forming shock-wave-like patterns around a circular laser spot is finally investigated.

1.6.1 Outward 1D polariton flow from a localized pump spot

In this paragraph we discuss a first application of the GPE formalism to one-dimensional geometries under a coherent drive with a finite pump spot. In almost all works so far on superfluidity and vortex nucleation in polariton fluids (Amo et al. [2011], Pigeon et al. [2011]), the fluid was quasi–resonantly driven using a finite but large pump spot, and it was often implicitly assumed that the flow velocity of the polariton fluid is controlled by the wave vector of the pump $\mathbf{v} = \hbar\mathbf{k}_p/m$.

---

[3] When the polaritons condense spontaneously instead, vortices have been generated by a probe pulse in the OPO scheme (Sanvitto et al. [2010]) or under pulsed non-resonant pumping (Lagoudakis et al. [2011]), and their dynamics has been imaged in real time.

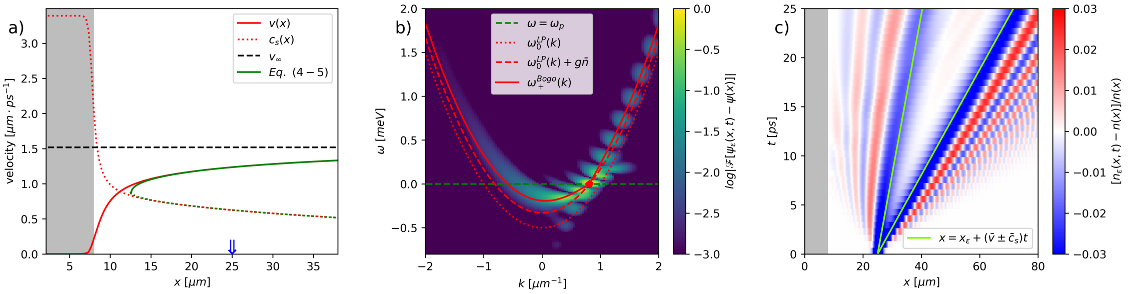

Figure 1.8: Panel (a) Numerical GPE calculations of the one- dimensional polariton flow profile under a spatially localized pump spot (grey–shaded area). Solid and dotted red lines respectively indicate the local speed of sound $c_s(x)$, which is a measure of density, and the local flow velocity $v(x)$. Green lines show the prediction of the local density approximation (1.45,1.46). The dashed black line indicates the asymptotic velocity v_∞ given by Eq. (1.50). Panel (b): frequency-momentum spectrum obtained from the Fourier transform of the wavefunction evolution in response to a weak δ–like perturbation localized at $t = 0$ and $x_\epsilon = 25\mu$m (blue arrow in panel a). The red curves represent the bare polariton dispersion (dotted), a rigidly blueshifted polariton dispersion (dashed) and the acoustic Bogoliubov dispersion (solid line), computed using the local values of the speed of sound $\bar{c}_s = c_s(x_\epsilon)$ and flow velocity $\bar{v} = v(x_\epsilon)$. Panel (c): space–time evolution of the density modulation $n_\epsilon(x,t) - n(x)$ induced by a small gaussian perturbation of width $1\,\mu$m around $x_\epsilon = 25\mu$m at $t = 0$. The solid green line indicates the light–cone emerging from the perturbation's location, also computed using the local values of the speed of sound $\bar{c}_s = c_s(x_\epsilon)$ and flow velocity $\bar{v} = v(x_\epsilon)$. Parameters: $\Delta = -0.5\,$meV, $\hbar\gamma = 0.02$ meV and $g = \hbar^2/m = 1\,$meV μm^2. The drive is defined in Eq. (1.43) with $\sqrt{g}F_0 = 10$meV$^{\frac{1}{2}}$, $x_{pe} = 8.0\mu$m, $\sigma_{pe} = 0.25\mu$m and $k_p = 0$. Numerical calculations were performed by means of the 4th order Runge–Kutta method in a simulation box of size $L_x = 1280\mu$m with a grid of 2^{12} points and periodic boundary conditions.

In the following we show that the physics of polariton fluids driven by spatially localized pumps can be significantly more complicate than that: in spite of the simplicity of the configuration, intriguing features are found for the polariton fluid that propagates away from the pump spot, namely a quick transition to a super-sonic flow and an unexpectedly weak dependence of the flow profile on the pump intensity and wavevector. Polariton wire devices (Wertz et al. [2010]) appear as ideal candidates where to experimentally investigate this physics in a quantitative way.

We consider 1D systems and pump configurations $F(x)$ of the kind

$$F(x) = F_0 e^{ik_p x}\left[1 - \exp\left\{-\frac{(|x| - x_{pe})^2}{2\sigma_{pe}^2}\right\}\right]\,\Theta(x_{pe} - |x|), \tag{1.43}$$

where $\Theta(X)$ is the Heaviside step function, equal to 0 (1) for $X > 0$ ($X < 0$). The parameters x_{pe} and σ_{pe} respectively determine the position and the sharpness of the pump edge, so that $F(x)$ is a plane wave with wavevector k_p in the central region, and smoothly decays to zero outside of $[-x_{pe}, x_{pe}]$. To avoid artifacts, the numerical integration box is chosen to have a much larger extension $-L/2 < x \leq L/2$ with periodic boundary conditions.

Local density approximation and local speed of sound

The qualitative physics of one-dimensional polariton flows under such a spatially finite coherent pump is represented in Fig.1.8(a), which displays the stationary solution of the GPE evolution Eq. (1.11). The solid lines indicate the spatial profile of the flow velocity $v(x)$ defined above and the dotted lines indicate the *local speed of sound*

$$c_s(x) = \sqrt{\frac{g|\psi(x)|^2}{m}} \tag{1.44}$$

which serves as a convenient proxy for the polariton density $|\psi(x)|^2$.

Within the pumped region indicated by the gray shading, the polariton fluid is well described by the usual theory by Carusotto and Ciuti [2004]. In the undriven region, the density and flow profile show a rapid crossover through a trans-sonic point towards a ballistic flow at large distances.

Because of polariton losses, the density then slowly decreases to zero, while the flow speed tends to an asymptotic value v_∞.

In analogy with the Thomas–Fermi approximation of atomic BECs (Pitaevskii and Stringari [2016]), for sufficiently smooth flow profiles the last "quantum pressure" term in eq. (1.42) can be neglected, which gives explicit equations for the steady-state flow profile in one-dimensional configurations within a local density approximation (LDA)

$$\frac{d(gn)}{dx} = -mv\frac{dv}{dx}, \tag{1.45}$$

$$\frac{dv}{dx} = -\frac{\gamma}{1-\frac{mv^2}{gn}} \tag{1.46}$$

From the second equation, we immediatly see that the Thomas–Fermi approximation breaks down in the neighborhood of the trans-sonic point where $mv^2 = gn$ and the derivative of the velocity diverges. On the other hand, when these equations hold, the current profile satisfies the modified continuity equation

$$j(x) \equiv nv = j(x_0)\, e^{-\gamma \int_{x_0}^{x} \frac{dx'}{v(x')}} \tag{1.47}$$

which includes the effect of the polariton decay.

The last equation suggests that away from the pump spot the steady–state wavefunction can be approximated by a decaying plane wave

$$\psi(x) \sim e^{-\frac{\gamma\, x}{2v_\infty}}\, e^{i\frac{mv_\infty}{\hbar}x}, \tag{1.48}$$

with the real part of the Laplacian in Eq. (1.11) requiring

$$\Delta + \frac{m}{2}v_\infty^2 - \frac{\hbar^2}{8m}\frac{\gamma^2}{v_\infty^2} = 0\ ; \tag{1.49}$$

the presence of Δ in this equation (and the very existence of a steady-state in the frame rotating with frequency ω_p) has the physical meaning that the pump fixes the time dependence of the field also in the undriven region. While the last term plays an important role for $\Delta \gtrsim 0$, it is fully negligible when the laser frequency is well above the bottom of the polariton band $(-\Delta \gg \hbar\gamma)$ and the asymptotic speed

$$\Delta + \frac{m}{2}v_\infty^2 \simeq 0. \tag{1.50}$$

is correspondingly large. This shows that the asymptotic flow velocity v_∞ is fixed (in modulus) by the (assumed negative) laser detuning according to energy conservation; in contrast, the pump wavevector does not play any role in determining v_∞.

The quantitative accuracy of the LDA past the trans-sonic point is confirmed in Fig.1.8(a). Comparing the LDA predictions (1.45-1.46) to the numerical solution of the GPE, one sees that the agreement is excellent far in the downstream region and, as expected, a significant discrepancy only occurs in the vicinity of the trans-sonic point where the LDA equation (1.46) has an unphysical divergence.

The physical meaning of the speed of sound c_s in our context is highlighted in the plots shown in panels (b-c). As reviewed in Sec. 1.3, the Bogoliubov dispersion in the driven region is generally not an acoustic one (Carusotto and Ciuti [2004, 2013]), unless the pump power, wavevector and detuning are precisely tuned to fulfill the resonant condition

$$\Delta + \frac{\hbar^2}{2m}k_p^2 + gn = 0 \tag{1.51}$$

The situation is different far in the undriven region where, for sufficiently small losses γ, the wavefunction $\psi(x)$ is locally well approximated by a plane–wave $\sqrt{\bar{n}}\exp[i\bar{k}x]$ with slowly varying density $\bar{n}$ and wavevector $\bar{k}$ that automatically satisfy the resonance condition (1.51). Within the LDA, this is straightforwardly derived by inserting the plane wave ansatz into the GPE (1.11) and taking the small γ limit. Here the bar stands for averaging over a region broader than the healing length $\sqrt{\hbar^2/(mgn)}$, but smaller than the typical decay length $\hbar\bar{k}/(m\gamma)$. In this case, in fact, one recovers an acoustic dispersion similar to the one of equilibrium fluids. This statement is verified in panels (b) and (c) respectively in the frequency-momentum plane and in the physical space-time.

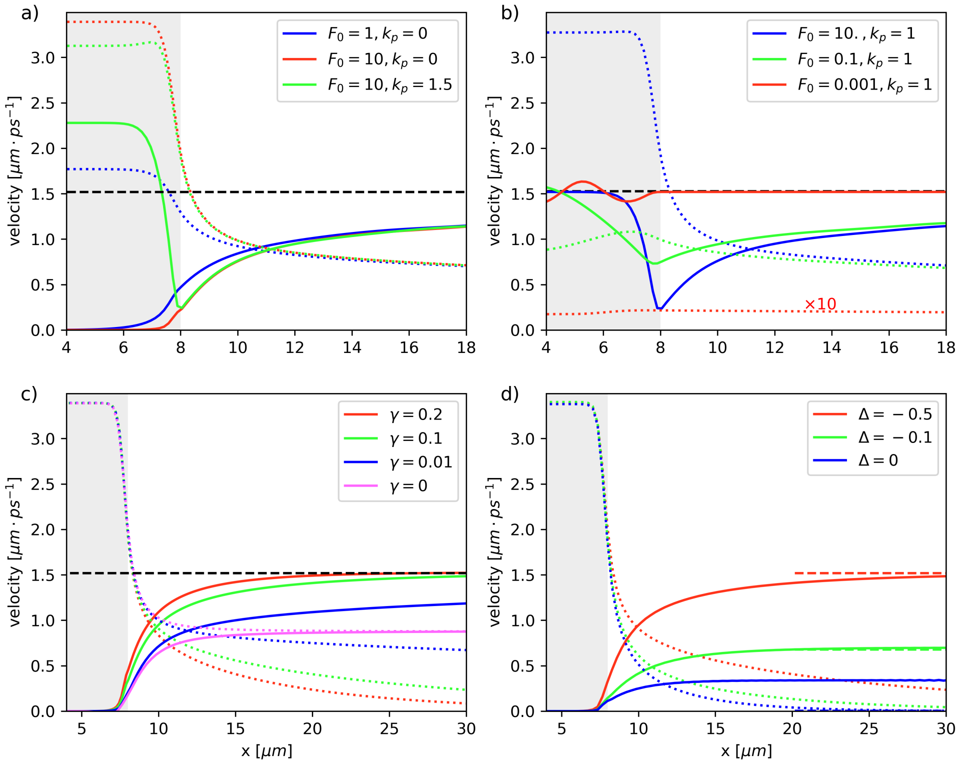

Figure 1.9: Steady-state solutions of Eq. (1.11), for a pump with support in the grey–shaded region. Continuous lines indicate the flow velocity, while the dotted ones indicate the local speed of sound as defined in (1.44). Within each panel, the curves in different colors refer to the different sets of pump parameters as indicated in the inset. The horizontal black dashed lines indicates the asymptotic flow velocity $v_\infty = \sqrt{2\,|\Delta|/m}$. A detailed explanation of the specific physics underlying each panel is given in the text. The grey shaded region indicates the extension of the pump spot, whose profile is given by (1.43) with $x_{pe} = 8.0\mu$m and $\sigma_{pe} = 0.25\mu$m. If not otherwise specified, $\Delta = -0.5\,$meV, $\hbar\gamma = 0.02$ meV, $k_p = 0$. Units in the legends are meV$\,\mu$m^{-1} for the pump amplitude F_0 and μm^{-1} for the pump wavevector k_p. In (d), the decay rate is set to $\hbar\gamma = 0.1$ meV.

Panel (b) shows the spatio-temporal Fourier transform of the wavefunction (i.e. the spectral distribution of the emission) after this has been suddenly perturbed at $t = 0$ at the position $x_\epsilon = 25$ μm far in the downstream region. Specifically, the plot displays the (logarithm of the modulus of the) Fourier transform of the perturbation $\psi_\epsilon(x,t) - \psi(x)$ in the momentum–frequency plane. To reduce the spectral broadening due to the spatial inhomogeneity, the emission from a region around the excitation point has been selected by using a spatial filter of Gaussian shape with standard deviation 10μm. Except for the fringes visible at positive wavevector (due to interference with the perturbation that is reflected off the high-density region) and the obvious broadening γ, the distribution follows the expected equilibrium-like Bogoliubov dispersion shown as a solid line. The distinction from the bare polariton dispersion (dotted line) and from a rigidly shifted parabolic dispersion (dashed line) are apparent, which puts the concept of speed of sound on solid grounds.

Further evidence in this direction is shown in panel (c) where we show the temporal evolution of the density modulation $n_\epsilon(x,t)/n(x) - 1$ in response to a localized perturbation at $t = 0$ and $x = 25$ μm. To focus on the low-wavevector modes and improve the visibility, a spatially smooth perturbation of Gaussian shape with standard deviation 1 μm has been used. As expected, the perturbation peaks along the light–cone corresponding to the values of the speed of sound and the speed of flow extracted at the excitation position, $\bar{v} = v(x_\epsilon)$ and $\bar{n} = n(x_\epsilon)$. Higher-wavevector Bogoliubov modes propagate at a faster group velocity, so to have well visible fringes outside of the light-cone and only a small signal inside the light-cone. Of course the physical meaning of the sound velocity breaks down in the vicinity of the pump edge, where the flow parameters feature large variations on the scale of the healing length and the local density picture is no longer valid.

Before proceeding, it is important to remind a different configuration where the usual concept of speed of sound was recovered in spite of the driven-dissipative condition, namely the time-dependent experiments by Nardin et al. [2011]. Here, a pulsed excitation is used to inject a polariton cloud with a given wavevector, that is then left free to evolve according to the undriven GPE. As the experiments have demonstrated, in this case the speed of sound defined in (1.44) is a useful concept to characterize the Bogoliubov dispersion on top of the (decaying) polariton fluid in a sort of temporal LDA.

Weak dependence of the flow profile on the pump parameters

In spite of the complex physics determining it, a most remarkable feature of the polariton flow outside a localized pump spot is its weak dependence on the specific parameters chosen for the pump. A first illustration of this physics is given in Fig.1.9.a which shows how the flow profile right outside the pumped region features small variations across a wide range of very different excitation powers and pump wavevectors. This can be clearly seen by looking at the position x^* of the trans-sonic point such that $c_s(x^*) = v(x^*)$, which does not display major variation for all choices of parameters. Further to this point, the velocity displays a monotonic growth towards the asymptotic value v_∞: within the local density approximation, this follows by energy conservation the decrease of the polariton density and, thus, of the interaction energy,

$$\frac{m}{2} v(x)^2 = -\Delta - gn(x). \tag{1.52}$$

On the other hand, the extension of the sub-sonic $c_s(x) > v(x)$ flow region remains quite limited even with a very strong drive and very long lived polaritons and, most importantly, the complex shape of the flow profile in this region is determined by the matching of the asymptotic long-distance flow at wavevector $k_\infty = mv_\infty/\hbar$ with the one in the pumped region, whose wavevector k_p and intensity are fixed by the pump via the usual nonlinear equations for spatially homogeneous configurations (Carusotto and Ciuti [2004]). For instance, depending on the relative value of k_p and k_∞, the velocity profile shows a monotonic (red and blue lines) profile for $k_p < k_\infty$ or a non-monotonic one (green line) one for $k_p > k_\infty$: to understand this last behaviour, one needs to remind that at intermediate distances the local flow speed is smaller than the asymptotic speed and grows towards it according to (1.52), while in the pumped region it has to match the (larger) pump wavevector k_p. These two conditions impose the existence of a minimum of the flow velocity in the vicinity of the pump edge. A further mathematical interpretation of this variety of behaviours is found in the denominator of the expression (1.46): imagining to integrate the steady–state with initial condition at large x, solutions that are initially close will strongly deviate from each other as the trans-sonic point x^* is approached and the denominator tends to 0.

The specific effect of interactions is illustrated in Fig.1.9.b, where we fix the pump wavevector to a value close to the asymptotic velocity for the chosen pump frequency and we vary the pump power from the linear regime of very weak pumping towards high intensities well above the bistability loop. In the linear regime (red lines), the density is so low so that v sticks to v_∞ as soon as the flow exit the driven spot. The oscillations in the velocity and density profile in the pumped region are due to partial reflection of polaritons at the edge of the pumped region. As it was also experimentally observed by Nguyen et al. [2015], these oscillations disappear in the strongly nonlinear regime where superfluidity sets in (green and blue lines). In this regime, the speed right outside the pump spot is strongly reduced by the higher density according to (1.52) and recovers the asymptotic value only at large distances.

To better understand the peculiar hydrodynamic features in the sub-sonic region, in Fig.1.9.c we report results for varying decay rate while the pump wavevector and the (relatively strong) intensity are kept constant. No appreciable change is found in the pumped region where the system is far on the upper bistability branch and the density is fixed by the interplay of pump intensity and density-dependent detuning (Carusotto and Ciuti [2004, 2013]). Even though the size of the subsonic region up to the trans-sonic point at x^* indeed increases with decreasing γ, the dependence is a very slow one and sub-sonic flows of macroscopic size are hardly obtained.

This observation is corroborated by comparison with the magenta curves for the conservative $\gamma = 0$ limit (in the undriven region). In this case absorbing boundary conditions were implemented at large distances by means of a smooth imaginary potential. These dissipationless curves suggest that the flow outside the pump spot tends to self–regulate itself to the maximal velocity that can be supported without creating scattering, so to asymptotically have $v \to c_s$. Even though the trans-sonic point x^* is now at infinity, the flow is only barely sub-sonic in most of the space. Since the non-dissipative condition allows for spatially uniform flows at large distances, the long-distance limit of the speed is now $c_s \sim v \sim v_\infty/\sqrt{3}$, with v_∞ computed from Eq. (1.50). Note in particular how the quick decay of the density right outside the pump spot is not an effect of losses (that are not present here), but originates from hydrodynamics effects dominated by the quantum pressure term.

This crucial result is confirmed by the comparison with the curves for non-zero losses shown in the same panel: the transition from the pumped region in the vicinity of the trans-sonic point depends only weakly on γ and is qualitatively similar to the $\gamma = 0$ conservative case. This indicates the crucial role of the quantum pressure term that was neglected in Eq. (1.46) and that is responsible for the fast, almost γ-independent drop of the density right outside the pump spot. In contrast, the long-distance behaviour beyond the trans-sonic point is dominated by the decay rate γ and is well captured by the local density picture of Eqs. (1.45-1.46).

Finally, in Fig. 1.9.d we show the result of simulations varying the detuning Δ and keeping fixed the decay rate, the pump wavevector and the inner polariton density (by adjusting the laser strength). For negative enough values of the detuning, the asymptotic velocity is well captured by v_∞ (dashed red and green lines). For $\Delta = 0$, it is instead determined by the decay rate and is equal to $\sqrt{\gamma/(2m)}$. Even though both the density and the speed of sound c_s increase with more negative detunings, the behaviour of the fluid in the outer region is dominated by the even faster growing asymptotic speed, so the size of the sub-sonic region actually decreases with the pump intensity.

The calculations discussed here illustrate the dependence of the outward flow on the different pump parameters. From this, one can extract physical insight on the behaviour of the system and anticipate the most favourable regimes to observe a given effect. In particular, if one wants to study superfluidity using a defect located outside the pump spot, it looks beneficial to have x^* as large as possible so to maximize the size of the sub-sonic region. To this purpose, the most favourable regime (for a given γ) appears to be at small negative Δ.

1.6.2 Superfluidity and instabilities in two-dimensional flows

The features pointed out in the previous paragraphs in the simplest one-dimensional geometry have profound consequences on the hydrodynamics of two-dimensional driven–dissipative fluids generated by a laterally very wide pump (in the y direction) which induces an effectively one–directional flow directed along the x direction. Translational invariance along y is broken by a static obstacle inserted in the flow.

While the usual behavior discussed in theoretical literature (Carusotto and Ciuti [2004, 2013]) and reviewed in Sec. 1.3 is numerically observed for obstacles located in the pumped region, the small extension of the sub-sonic region and the quick quantum-pressure-driven density drop discussed above entail that defects located outside the pump always produce a solitonic pattern. As a result, superfluidity or vortex nucleation are hardly found, even for very small dissipation, being replaced by a smooth deep–to–shallow perturbation crossover as the pump power is increased. A time-dependent behaviour is recovered when a realistic amount of static disorder is included in the model: the ensuing spatial motion of the phase singularities that appear in the low-density region around the solitonic troughs is responsible for a localized loss of coherence. Remarkably, this non-stationary behaviour turns out to be facilitated by the presence of a incoherent reservoir.

Here we consider a pump profile that is a function of x only and does not depend on the lateral coordinate y, $F_0 = F_0(x)$. The defect is located completely outside of the driven region. The main feature that one can observe in Fig.1.10 is that a (possibly shallow) V-shaped, soliton-like density modulation always appears past the defect and extends to the edge of the cloud in the downstream direction. Such a breaking of superfluidity occurs even for weak dissipation, high powers, small defect size, and small distance of this latter from the pumped region. For the case shown in panel (a), the density depletion along the slice marked by the dashed magenta line [shown in panel (b)] is as high as 25% even though the defect is fully in the region of locally sub-sonic $c_s > v$ flow delimited, in the absence of defect, by the green dash-dotted line. Furthermore, in contrast to the conservative case of atomic superfluids (Winiecki et al. [2000], Neely et al. [2010]), no turbulent

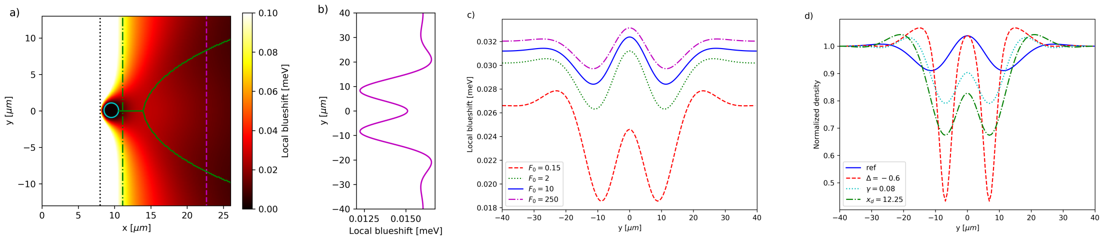

Figure 1.10: Panel (a): Steady-state density profile [in units of the corresponding blue-shift $gn(\mathbf{r})$] of a two-dimensional flow under a coherent pump profile of the form (1.43). The vertical black dotted line indicates the edge of the pump spot at $x = x_{pe}$, while the green dash-dotted line indicates the trans-sonic point $x = x^*$ in the absence of the defect. Note that the density is heavily saturated in the pumped region, where the blueshift attains values as high as 0.7 meV. A cut of the density along the vertical dashed magenta line at $x = 23\,\mu$m is shown in panel (b). Parameters: $\Delta = -0.1$ meV, $F_0 = 0.5$ meVμm^{-1}, $\hbar\gamma = 0.04$ meV, $k_p = 1.0\mu$m^{-1}, $x_{pe} = 8.0\mu$m and $\sigma = 0.25\mu$m. The defect is of effectively infinite strength $V_d = 20$ meV, has radius $r_d = 1\,\mu$m and is centered outside the pump spot at $x_d = 9.25\,\mu$m. Panel (c): cuts of the density along the same vertical magenta line at $x = 23\,\mu$m for different pump powers. Panel (d) the same cuts when various parameters are varied with respect to the curve in (c) for $F_0 = 10$ meVμm^{-1}. Given the small polariton decay rate $\hbar\gamma_=$0.02 meV used in (c,d), these simulations had to be performed in a large box of sides $L_x = 640\mu$m, $L_y = 80\mu$m with a grid of $2^{11} \times 2^8$ points.

state with a time-dependent vortex nucleation has been found. Note that this last prediction is not in contrast with the experiment by Nardin et al. [2011], which was performed in a completely different regime where the coherent pump had a pulsed character and the polariton phase was afterwards free to evolve.

Whereas panels (a,b) show the breaking of superfluidity in an experiment with realistic parameters of state-of-the-art samples, panels (c,d) aim at demonstrating that, as soon as dissipation is present, no clean superfluidity is possible for a defect located outside the pump spot. As a first step, in panel (c) we plot sections of the steady-state density for an extremely small decay rate and a series of different values of the pump strength. The cuts are taken far downstream from the defect (along the same line as in the top panel). In agreement with our discussion in Sec.1.6.1, the density does not appear to change much even under a very large (possibly unrealistic) increase of the pump power. Note that the very small value of the decay rate used in this panel requires to perform the simulation in a large box to avoid numerical artifacts [4].

We now try to convince the reader that the configuration plotted as a solid blue line in the middle panel is optimal to achieve superfluid-like features given the constraints imposed by the presence of dissipation at a given decay rate. To this purpose, in panel (d) we present cuts of the density profile at a given x normalized to their large y value for different choices of parameters that differ from the reference one by the variation of a single parameter. Specifically, the blue solid line is the reference, the red dashed line is for a larger detuning ($\Delta = -0.6$ meV instead of $\Delta = -0.1$ meV) for which the flow gets more quickly supersonic, the cyan dotted line is for a larger dissipation ($\hbar\gamma = 0.08$ meV instead of $\hbar\gamma = 0.02$ meV) which again reduces the size of the subsonic region, and the green dashed–dotted line is for a defect located farther away from the pump (at $x_d = 12.25\mu$m instead of $x_d = 9.25\mu$m), that is closer to the trans-sonic point. As discussed in Sec. 1.6.1, the dependence on k_p is a very weak one and thus not worth being illustrated here.

Building on these numerical results, we can trace back the imperfection of the superfluid behaviour to the relatively quick decay of the polariton density outside the pump spot studied in Sec.1.6.1. In order to assess whether a defect is able to generate a density perturbation in a spatially inhomogeneous flow, it is in fact not enough to apply the Landau criterion for superfluidity at the defect's location only (which would in any case be questionable in our case, given the strong density gradient in the subsonic region), but one has to look for all points where the flow

---

[4] The vortical, non–stationary phases reported in (Pigeon et al. [2011]) are likely due to interference of the back–scattered flow by the pumped region through the periodic boundary conditions. Simulations with small decay are in fact very sensitive to scattering effects and we have encountered similar problems when smaller boxes were used. Notice that the box used here is 16×4 times larger than the one used in (Pigeon et al. [2011]) and with the same numerical grid spacing.

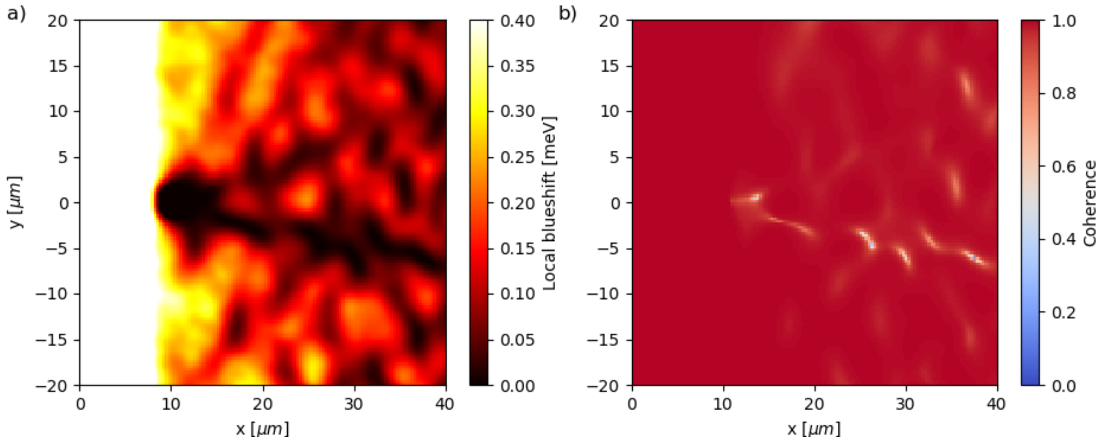

Figure 1.11: (a) Time averaged polariton density and (b) first–order coherence function in the presence of static disorder. This has the Gaussian distribution described in (1.54) with correlation length $\sigma_W = 0.5\mu$m, and amplitude $W_0 = 0.06$ meV. Pump parameters: $\Delta = -0.4$ meV, $k_p = 0$ and $F_0 = 0.25$ meV μm^{-1}. The strong defect is of radius $r_d = 2\mu$m and is located at $x_d = 10.5\mu$m.

is supersonic: even though locally in the subsonic region there are no on-shell phonon modes that can be excited by the defect, the perturbation can in fact "tunnel" across the forbidden subsonic region before getting "on-shell" again in the supersonic region. This mechanism of tunnel-assisted radiation is well known in electromagnetism, e.g. in the theory of the Cherenkov emission from particles moving through vacuum holes drilled in material media (Jelley [1958]).

For our case of polariton superfluids, this mechanism is illustrated by the green line in Fig.1.10(a) which shows, for each value of x, the position along y of the density minima. Since the defect is located upstream of the trans-sonic point, the perturbation is initially evanescent and does not propagate in the lateral direction. Only later, well in the downstream supersonic region, it transforms into the usual, laterally expanding V-shaped structure.

The calculations above have shown how the presence of dissipation makes a superfluid flow more fragile: no matter the pump parameters and the spatial position of the defect outside the pump spot, this latter is generally able to induce a significant perturbation in the flow. However, it turned out hard if not just impossible to observe vortex nucleation and the polaritons flow remains generally stationary in time at all points.

Since experiments (Amo et al. [2011]) have instead observed a loss of coherence, it is important to assess the importance of other effects on the dynamical stability of the polariton flow. In what follows we will characterize non-stationarity in terms of a first–order coherence function

$$g^{(1)}(\mathbf{r}) = \frac{|\langle\psi(\mathbf{r})\rangle_t|}{\sqrt{\langle n(\mathbf{r})\rangle_t}}, \tag{1.53}$$

which uses the phase of the pump as a reference. As usual, perfect coherence corresponds to having $g^{(2)} = 1$.

Fig.1.11 shows the spatial profiles of the time-averaged density (measured in terms of the local blue-shift $g\langle n(\mathbf{r})\rangle_t$) and of the $g^{(1)}$ coherence function in the presence of a static disorder modeled as a Gaussian-distributed random real potential $W(\mathbf{r})$ with $\langle\langle W(\mathbf{r})\rangle\rangle = 0$ and

$$\langle\langle W(\mathbf{r})W(\mathbf{r}')\rangle\rangle = W_0^2 e^{-\frac{(\mathbf{r}-\mathbf{r}')}{4\sigma_W^2}}, \tag{1.54}$$

where $\langle\langle ...\rangle\rangle$ stands for average over disorder, σ_W is the correlation length of the field and W_0 its amplitude, chosen of magnitude comparable to the decay rate.

As expected, the density profile (slighty saturated in the left part of the figure) is perturbed by the presence of disorder. But even more importantly, the fluid often fails to converge to a stationary state and keeps displaying irregular oscillations in time. Further insight in this behaviour is obtained by looking at the time evolution of the phase shown in the Movie M1 included as supplemental material of (Amelio and Carusotto [2020a]): here, one can see how the disorder

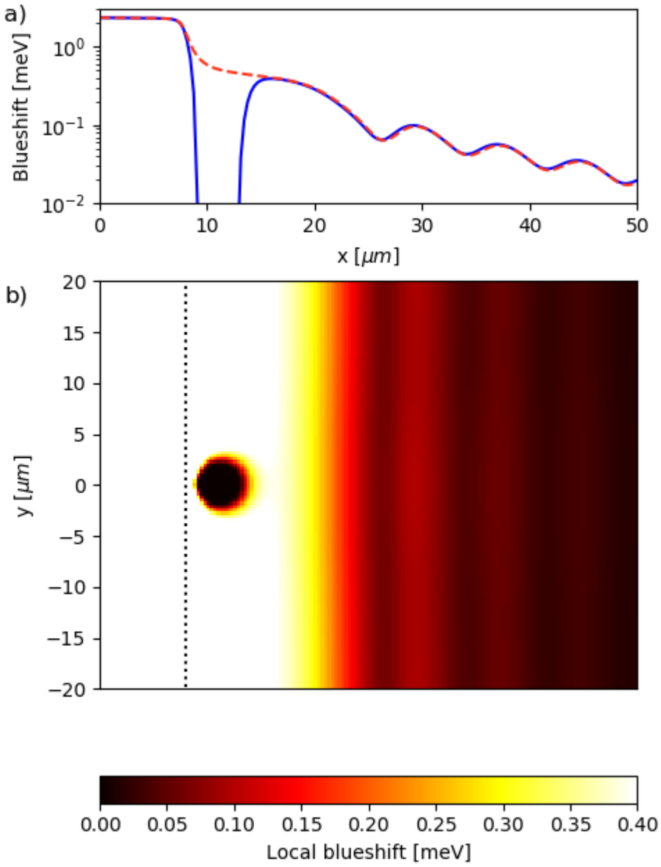

Figure 1.12: Main (b) panel: density profile under a long-tailed coherent pump as described in Eq.(1.55) with $x_{pe} = 8\mu$m (indicated by the vertical black dotted line) and $\zeta = 0.25\mu$m. The defect is centered at $x_d = 11\mu$m and has a radius $r_d = 2\mu$m. Parameters $F_0 = 3.0$ meVμm^{-1}, $\hbar\gamma = 0.05$ meV, $\Delta = -0.4$ meV and $k_p = 0$. Upper (a) panel: cuts of the local blueshift along the $y = 0$ (solid blue) and $y = 20\mu$m (red dashed) lines.

perturbs the phase fronts and makes them perform small oscillations. This time dependence has the strongest impact in the neighborhood of the vortex-like phase singularities induced by the disorder, in particular in the low density region around the solitonic troughs. Since the phase displays a singular 2π variation around the phase singularity, any minor modification of the wavefunction in this vicinity will result in a dramatic suppression of the $g^{(1)}$ phase coherence.

As a general trend, we have found that a stronger disorder is required to break the stationary state for stronger decay rates. For instance, for a doubled decay rate $\hbar\gamma = 0.04$ meV close to experimental parameters, no instability is generated for static disorder of amplitude up to around $W_0 = 0.1$ meV. Also, having a short correlation length σ_W enhances the instabilities. While a stronger pump intensity typically leads to a reinforced stability, no instability can ever occur for weak pumps in the linear regime where the wavefunction smoothly tends to its steady-state. Of course, the vanishing speed of sound in the linear regime prevents a superfluid behaviour, so that any defect produces a sizable density modulation.

Finally, we mention that the effect of disorder in generating vortical behaviour has been experimentally investigated by Grosso et al. [2011], who observed the evolution of the injected fluid but did not consider the issue of reaching a steady state.

1.6.3 Solitonic and shock-wave-like patterns

In this last subsection, we complete our discussion by considering additional configurations whose interesting features may be of importance to understand experimental observations.

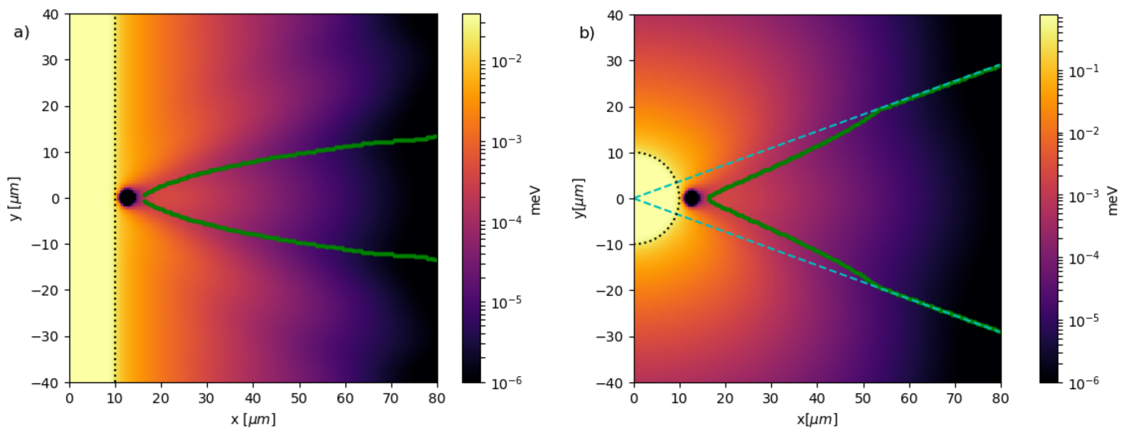

Figure 1.13: Polariton density profile under the linear pump spot of Eq.(1.43) [upper panel (a)] and under the circular pump spot of Eq.(1.56) [lower panel (b)]. Black dots indicate the edge of the pumped region, while the green points indicate for each x the position of the density minima. Parameters: $\Delta = -0.2$ meV, $\hbar\gamma = 0.08$ meV, $F_0 = 0.5$ meV μm^{-1}, $k_p = 0$, $r_{pe} = 10\,\mu$m, $\sigma_{pe} = 0.25\,\mu$m and $x_d = 12.5\,\mu$m.

Long-tailed pump spot

We will start from the case of a pump profile whose intensity is mostly concentrated in a small region of space, but also presents a long tail extending outside the main spot. Unless specific efforts are made to restrict the light intensity to a finite spot, in any experiment diffraction is in fact likely to be responsible for a weak light intensity to be present in the whole space.

This physics is illustrated in Fig.1.12. We focus on a model configuration where the pump spot is uniform along y, but displays along x a sharp jump around x_{pe} and a slowly decaying tail for $x \to \infty$,

$$F(x) = \frac{F_0}{\pi}\left[\frac{\pi}{2} + \text{atan}\left(\frac{x_{pe} - x}{\zeta}\right)\right]. \tag{1.55}$$

In contrast to pump configurations with a finite spatial support, the fact that the pump wavevector is now locking the velocity at all points facilitates the observation of a robust superfluidity. This robustness is illustrated in the figure by the absence of a density modulation around the defect, even though this latter is located well outside the high-intensity part of the pump spot delimited by the vertical black dotted line.

As another interesting feature, we notice clear vertical fringes in the right part of the figure. Such fringes were clearly visible in the experiment (Stepanov et al. [2019]) as reported in Fig. 2.6 of the next Chapter, but do not appear when the pump has a finite support or has a fast decaying, e.g. Gaussian, tail. Rather than shock waves, a natural interpretation for these fringes involves the interference between the tail of the coherent pump with the polaritons that are simultaneously ejected from the high-density region according to the outward flow mechanism discussed in Sec.1.6.1. An evidence for this mechanism is provided by the approximate $\sqrt{-\Delta}$ dependence of the fringe wavevector on the detuning Δ for vanishing pump wavevector $k_p = 0$ (not shown). Note that a related but different mechanism for controlling superfluid and turbulent behaviours was investigated by Pigeon and Bramati [2017] using a support field on the downstream side.

Circular spot geometry

We conclude our discussion with some remarks on the experimentally relevant case of a finite circular laser spot,

$$F(\mathbf{r}) = F_0 e^{ik_p x}\left[1 - \exp\left\{-\frac{(r - r_{pe})^2}{2\sigma_{pe}^2}\right\}\right] \tag{1.56}$$

for $r < r_{pe}$ and 0 for $r > r_{pe}$. In this geometry, illustrated in Fig.1.13, reaching the superfluid regime for a defect located outside the pump spot is even more difficult than in the linear geometry of Fig. 1.10. This is a direct consequence of the geometrical spreading of an outgoing circular wave, which results in a reinforced decay of the density along the radial direction.

Another interesting consequence of the radial flow is the different shape of the solitonic dark lines. These are illustrated in the top and bottom panels of Fig.1.13 for the two cases of a linear or a circular pump [Eqs.(1.43) and (1.56)], in the absence of disorder. The black dots indicate the geometrical boundary of the pump spot, while the green points mark for each x the position of the density minimum. While the solitonic troughs start from the defect with a similar aperture in the two cases, their shape becomes markedly different further downstream. For a linear pump spot (upper panel), the rapid growth of the flow speed over the speed of sound leads to solitonic lines that asymptotically approach the x direction. For a circular pump spot (lower panel), the solitonic lines eventually approach the radial direction of the flow (cyan dashed lines) and have the quite rectilinear shape observed in the experiments (Amo et al. [2011]).

1.7 Conclusions

To summarize, we have reviewed the microscopic aspects of exciton-polaritons in semiconductor microcavities in Sec. 1.1, the generation of polariton fluids under incoherent, resonant and parametric pumping in Sec. 1.2 and the basic properties of uniform resonantly injected fluids in the Gross–Pitaevskii framework in Sec. 1.3. In the original part of the Chapter, we have discussed some general properties of the generalized, driven-dissipative GPE.

First, we have shown in Section 1.4 how a formal Galilean transformation relates the two situations of a fluid flowing against a static defect and of a defect moving in a fluid at rest. As a result, the dispersions of the Bogoliubov excitations are related by a simple Doppler shift and the density modulation pattern are identical in the two cases, as it normally happens in Galilean invariant fluids of material particles in free space.

Then, in Sec. 1.5 the effect of driving and dissipation has been considered in 1D, where our analysis of the complex momentum poles complements the usual loose formulation of the Landau criterium.

In Section 1.6 we have reported some unexpected predctions of polariton hydrodynamics when the polaritons are injected by a spatially localized coherent pump. In contrast to the case of a spatially homogeneous pump considered in (Carusotto and Ciuti [2004]), the combination of the driven-dissipative condition and of the quantum pressure term beyond the local density approximation are responsible for a quick drop of the polariton density right outside the pump spot; an experiment currently running in Alberto Bramati's lab aims at exploring this feature. Importantly, this effect strongly reduces the spatial extension of the subsonic flow region and suppresses its superfluidity features. In particular, a sizable soliton-like density modulation appears downstream of a static defect located outside the pump spot even when this is located still in the subsonic region. Finally, the impact of a static disorder on the dynamical stability of the flow and on the development of turbulent behaviors is highlighted. Qualitative comparisons with available experimental data are drawn.

Our results highlight the importance of a new generation of experiments aimed at going beyond the pioneering experimental studies of polariton superfluidity (Amo et al. [2009, 2011], Sanvitto et al. [2011], Nardin et al. [2011]) and exploring polariton hydrodynamic effects in a quantitative way. In particular, new experiments are needed to firmly assess the mechanisms at play in realistic microcavity devices and possibly isolate phenomena that are not yet included in present non-equilibrium Gross-Pitaevskii equation models, due e.g. to the exciton reservoir and its spatial dynamics (Caputo et al. [2017]), interaction with the static disorder, and polariton scattering on phonons (Savenko et al. [2013]). This analysis will be of paramount importance in view of using polariton fluids as a platform for quantum simulation of the physics of quantum fluctuation effects such as analog Hawking radiation from a trans-sonic horizon (Gerace and Carusotto [2012], Nguyen et al. [2015]).

Chapter 2

Excitations and superfluidity of resonantly driven polariton fluids in the presence of a dark excitonic reservoir

In this Chapter we move to consider the physics of resonantly driven polariton fluids in the presence of a dark excitonic reservoir. Indeed, the fully coherent model illustrated in the previous Chapter does not account for all the experimental observations, in particular with respect to spin-dependent bistability (Sarkar et al. [2010]), soliton formation following pulsed excitation (Walker et al. [2017]) and measurments of the polariton-polariton coupling from the blueshift (Sun et al. [2017]).

Our work takes inspiration from the measurement of the collective excitation reported in the experiment by Stepanov et al. [2019], which lies at the heart of the Chapter. The speed of sound extracted from the data turned out to be significantly lower than the theoretical prediction based on the fully coherent theory; this suggested us to take into consideration the presence of a reservoir, which relaxes on a slow timescale and contributes to the blueshift but not to the speed of sound: the refined theory is in very good agreement with the measured dispersion relations. However, this work also opened a few conceptual questions concerning the superfluid behavior of the polariton plus reservoir model and in particular the relation with the experiments by Amo et al. [2009], where the critical velocity was consistent with the fully coherent theory. These issues are discussed and resolved below.

In Section 2.1 we review the theory of the spin dependent polariton-polariton interaction constant and the attempts to measure it. In Sec. 2.2 we explain the aforementioned experiment in great detail. Coming now to our contributions, in Sec. 2.3 the model including the dark excitonic reservoir is introduced and the collective excitations are derived. Finally, in Sec. 2.4 superfluidity in the presence of a defect is investigated, showing that in general the critical velocity is not determined by the speed of sound.

2.1 The polariton-polariton interaction constant

In the previous Chapter we analyzed the nonlinear physics of polariton fluids by restricting to a single polarization, which allowed us to focus on the spin-diagonal component of the polariton-polariton coupling constant. Also, both in the derivation of the steady-state and of the Bogoliubov spectra the interaction constant entered only via the combination $\mu = gn$ or $I_F = F_0^2/g$. In an experiment one has easy access to the blueshift μ while is much harder to count the polaritons and have a direct estimate of $|\psi|^2$. Also, one can measure the power of the laser outside of the cavity, but F_0 includes also a radiative coupling factor between light external to the cavity and the polariton field, which is non-trivial to estimate. Similarly, studying the dispersion of the excitations of the microcavity gives access to μ (with some important caveats which will be one main topic of the follwing Sections), but not to g or n separately. Because of this experimental difficulty, the community has not reached a strong consensus on the magnitude of g yet. Moreover, in the following Section we will need to consider a linearly polarized excitation scheme: in this spin basis the interaction is no longer diagonal and some considerations about the spin dependence of the coupling constant are needed.

Therefore, the goal of this Section is first to review the microscopic theory of the polarization dependent interaction constant and then to briefly discuss recent experimental efforts towards its measurement.

2.1.1 Theory of exciton-exciton interactions

A clean theoretical treatment of the spin dependence of exciton-exciton interactions was first provided by Ciuti et al. [1998]. Here they consider excitons made of a hole from the heavy-hole valence band and a conduction band electron. Neglecting higher order many-body effects leading to an electron-hole exchange interaction, the electron and the hole are effectively distinguishable particles: as a result, the orbital and spin parts of the exciton wavefunction are factorized; plus, the spin wavefunction is just the tensor product of the electron and hole spins, so that a basis for the exciton spin consists of the 4 states $|J_z = \pm 1\rangle = |s_z^e = \mp 1/2, j_z^h = \pm 3/2\rangle$ and $|J_z = \pm 2\rangle = |s_z^e = \pm 1/2, j_z^h = \pm 3/2\rangle$. Importantly, only the first two states allow for dipole transitions, while the other two are optically inactive.

With very good approximation, the orbital part of the exciton wavefunction is just the $1s$ hydrogen-like bound state in the 2D QW times a center of mass plane wave. Indeed, the excitons that are in strong coupling with photons in typical experiments with polaritons have very small kinetic energy with respect to their binding energy, so that the exciton-exciton scattering processes are not energetic enough to excite the relative electron-hole coordinate component of the wavefunction and can be considered elastic collisions.

Denoting $\langle \mathbf{r}_e, \mathbf{r}_h, s_e^z, j_h^z | \mathbf{k}, 1s, J_z\rangle$ the wavefunction of a single-exciton, when the scattering of two excitons $|\mathbf{k}, 1s, J_z\rangle$ and $|\mathbf{k}', 1s, J_z'\rangle$ is studied the initial and final states need to be anti-symmetrized according to the fermionic statistics of their electron and hole component, yielding the Slater determinants $\langle \mathbf{r}_{e1}, \mathbf{r}_{h1}, \mathbf{r}_{e2}, \mathbf{r}_{h2}, s_{e1}^z, j_z^{h1}, s_{e2}^z, j_z^{h2} | \mathbf{k}, \mathbf{k}', J_z, J_z'\rangle$ in the first quantization formalism. The interaction is provided by the Coulomb attraction or repulsion between the charged fermions and the matrix element between an inital and final 2 exciton state consists of 4 terms, corresponding to the "classical" electrostatic direct interaction term, to the electron exchange and hole exchange terms and to the exciton exchange term. It is clearly seen the electron exchange and hole exchange terms are dominating and have a further spin dependence, which is tabulated in (Ciuti et al. [1998]). In particular, circularly polarized excitons $J_z = J_z' = \pm 1$ can scatter only into circularly polarized excitons $J_z = J_z' = \pm 1$; on the other hand, excitons excited in an elliptical polarization of the $J_z = \pm 1$ states can scatter into the dark states with $J_z = \pm 2$. This physics gives rise to spin relaxation phenomena, as first experimentally probed by Amand et al. [1997], and to a density dependent contribution to the exciton homogeneous linewidth.

For small exciton densities, the exciton can be bosonized and the matrix element between two excitons is extrapolated to have in the excitonic Hamiltonian the quartic local Hartree term $\sum_{\sigma\sigma'} g_{\sigma\sigma'}^{XX} \int d^2\mathbf{x}\, \hat{b}^\dagger_{\mathbf{x}\sigma} \hat{b}_{\mathbf{x}\sigma} \hat{b}^\dagger_{\mathbf{x}\sigma'} \hat{b}_{\mathbf{x}\sigma'}$ with a theoretical estimate of

$$g_T^{XX} \equiv g_{+1,+1}^{XX} = g_{-1,-1}^{XX} \sim 6 E_b a_B^2 \tag{2.1}$$

for the diagonal interaction coupling (Tassone and Yamamoto [1999]). The polariton-polariton coupling is then obtained multipling by the fourth power of the excitonic Hopfield coefficient and dividing by the number of quantum wells: $g_{\sigma\sigma'} = g_{\sigma\sigma'}^{XX} |X|^4 / N_{QW}$. According to Ciuti et al. [1998], $g_S^{XX} \equiv g_{+1,-1}^{XX} = 0$. However, while all experiments confirm that $g_T^{XX} \gg |g_S^{XX}|$, a more advanced analysis suggests a contribution arising from the bi-exciton state which can yield a weakly attractive $g_S^{XX} < 0$ (Wouters [2007], Shelykh et al. [2009], Takemura et al. [2014]).

2.1.2 Measuring the coupling constant

For realistic values $a_B = 10$ nm and $E_b = 10$ meV the estimate of Eq. (2.1) yields $g_T^{XX} \sim 6 \mu\mathrm{eV}\ \mu\mathrm{m}^2$. As reviewed in (Estrecho et al. [2019]), in the literature one can find experimental measurements of g spanning 4 orders of magnitudes (in Fig. 5 of that work the different experimental g's are properly plotted as a function of the Hopfield coefficient and rescaled by N_{QW}; below, if not explicitly written, we report the not rescaled measured g's).

When polaritons are incoherently created (as explained in Sec. 1.2) the reservoir of intermediate carrier and exciton states contributes a large part of the blueshift; for this reason, in (Sun et al.

[2017]) the excitation laser is shined on a ring with a radius of a few tens μm, so that the fast polaritons reach the center of the ring and get spatially separated from the much heavier excitons, which decay before travelling a few μm. The polariton density is calibrated both by directly counting the transmitted photons and by comparison with the critical density for Bose-Einstein condensation. In spite of these precautions, the value of the extracted from the blueshift was $g \simeq 1700\mu\text{eV}\ \mu\text{m}^2$, dramatically larger than the theoretical estimate.

On the other hand, if polaritons are resonantly injected one doesn't have to deal with intermediate electronic states, but counting the number of polaritons in the microcavity is more involved, since they are mixed with photons of the laser and a spectral separation is not possible. To avoid this inconvenience, in (Walker et al. [2017]) they use a waveguide geometry so that the number of polaritons is given by the intensity transmitted by the waveguide, with the input laser field being spatially separated. The interaction energy is then measured from the width of the soliton created by a phase defect of the input laser. If the experiment is performed in continuous wave, a value of $g \sim 30\mu\text{eV}\ \mu\text{m}^2$ is found; however, repeating the experiment with short pulse yielded $g \sim 0.3\mu\text{eV}\ \mu\text{m}^2$.

A tentative explanation of these results was attempted in the same works by introducing a reservoir of dark excitonic states which is replenished by polaritons; the reservoir has a slow dynamics and it has no time to get populated during a short laser pulse. A similar model was first considered in connection to polarization dependent bistable behaviour (Sarkar et al. [2010], Wouters et al. [2013]), where it was explicitly checked that the reservoir is unpolarized in spite of the degree of polarization of the emission, since spin relaxation typically occurs on the scale of a few picoseconds. These states presumably arise from disorder-induce localization of the excitons, with some estimates having been provided by Krizhanovskii et al. [2001]; it is however important to stress the very strong sample dependence of the reservoir characteristics.

Following these advances, the strategy of (Sun et al. [2017]) was refined by using pulsed excitation: the experimental estimate of g is then consistent with microscopic theory (Estrecho et al. [2019]), provided a correction from the saturation of the exciton oscillator strength at high densities is also included. We recall also the method by Delteil et al. [2019], who measured the polariton $g^{(2)}(\tau)$ correlation function and extracted a lower bound for g consistent with theory from a 5% anti-bunching induced by polariton-polariton repulsion; this measurement intrinsically avoids problems with any excitonic reservoir. As detailed in the next Sections, an explicit correction of the contribution of the excitonic reservoir is instead provided by us in (Stepanov et al. [2019]), to yield $gN_{QW} = 8 \pm 2\mu\text{eV}\ \mu\text{m}^2$.

2.2 Measuring the collective excitations of a polariton fluid

In the previous Chapter we discussed superfluidity starting from the elementary excitations of the superfluid. Interestingly, in the early days of quantum fluids things went the other way round. For liquid ^{4}He superfluid behaviour was first discovered by Kapitza and London made the connection with Bose-Einstein condensation . Landau then developed his hydrodynamical model and conjectured the linear dispersion of the excitations, while a fully microscopic theory in the limit of weak interactions and small thermal and quantum depletion of the condensate was provided by Bogoliubov.

For polariton fluids, a first study of the Bogoliubov dispersion relation in the high density regime $\mu > \hbar\gamma$ was conducted by Utsunomiya et al. [2008] on an incoherently pumped condensate. A marked deviation from the non-interacting parabolic dispersion obtained by blue-shifting the bare LP band was demonstrated, as shown on the left of Fig. 2.1. Notice that the condensate is created with circular polarization and the detection is co-polarized; the cross-polarized spectrum instead appears as a small rigid blue-shift of the free parabola. One important feature missing in these data is the signal from the hole branch, also called ghost branch, possibly overcome by the large signal due to the condensate and noise due to the excitonic reservoir. These difficulties were partially overcome using pulsed excitation by Pieczarka et al. [2015], who managed to find a clear signal from the ghost branch.

Other interesting investigations have been carried out by Ballarini et al. [2020], where an asymmetric dispersion is measured on top of the outward flow from a non-resonant pump spot and the transition to the acoustic regime is clearly demonstrated; by Pieczarka et al. [2020], who found the possible signatures of quantum depletion in the ghost branch of a polariton condensate. The more important open issue though is the lack of a measurement of the diffusive part of the

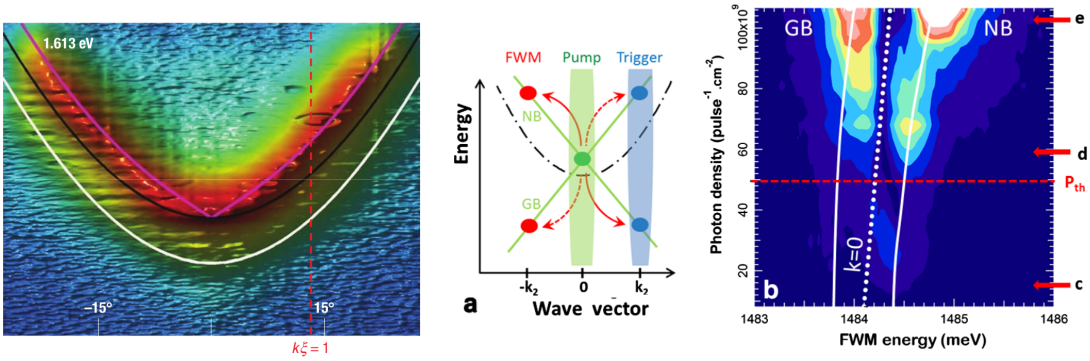

Figure 2.1: *Measuring the Bogoliubov spectrum.* (left) Spectrally and angularly resolved photoluminescence from a polariton condensate (Utsunomiya et al. [2008]). The white solid line denotes the bare LP dispersion; this is replotted in black after being blue-shifted by ~ 1 meV to fall at the center of the spectral peak at $k = 0$. The Bogoliubov prediction is the magenta line instead. (center and right) Plots from (Kohnle et al. [2011]): the four-wave mixing technique is sketched, highlighting the coupling in the Bogoliubov problem between the normal branch at $\pm\mathbf{k}_2$ and the ghost at $\mp\mathbf{k}_2$; this coupling is significant only in the high density regime, so that a pulse at $\mathbf{k}_2$ excites a signal at $\mathbf{k}_2$ only above a certain pumping threashold P_{th}. This is recoved in the experimental data, showing the spectrally resolved and angularly selected at $-\mathbf{k}_2$ emission for different excitation intensities.

dispersion relation, defined as the region where the real branches stick together and a Goldstone dome appears in the imaginary part; probably this is due to the fact that with typical parameters this occurs in a quite small window of wavevectors.

While the above mentioned works provide a good characterization of the excitations of incoherently driven polariton condensates by looking to the energy of emitted photons, in the case of resonanly injected fluids this is much more challenging because of the driving laser itself who overcome the signal of the Bogoliubov signal around the relevant spectral range; moreover, due to elastic Rayleigh scattering with imperfections of the microcavity, the laser light appear in the far-field detector as a very bright line spanning all $\mathbf{k}$'s.

A way to circumvent these problems was implemented by Kohnle et al. [2011], by resonantly injecting $\mathbf{k} = 0$ polaritons via pulsed excitation centered at the bottom of the LP band. A short trigger pulse of finite $\mathbf{k}_2$ is then shined on the sample: as depicted in the central panel of Fig. 2.1, since in the Bogoliubov nonlinear problem the $ue^{i\mathbf{k}_2\cdot\mathbf{r}-i\omega(\mathbf{k}_2)t} + v^* e^{-i\mathbf{k}_2\cdot\mathbf{r}+i\omega^*(\mathbf{k}_2)t}$ waves are mixed, the $\mathbf{k}_2$ seed stimulates emission of both the normal and ghost branches at $-\mathbf{k}_2$, which can be resolved in the far field emission. As shown on the right of Fig. 2.1, the authors were then able to prove deviations from the free LP dispersion in the high density regime, even though the final results were not very clear because of the temporally inhomogeneous broadening due to the use of pulsed excitation. (Actually, the proposal of using four-wave mixing to study the Bogoliubov spectra was first advanced by Wouters and Carusotto [2009] for the specific goal of probing the ghost branch of a polariton condensate.) The ghost branch was also found by Zajac and Langbein [2015], who injected polaritons with negligible detuning $|\Delta| < \hbar\gamma$, thus probing only the optical limiter regime physics.

2.2.1 The experiment

(this subsection follows closely the exposition by Stepanov et al. [2019])

A detailed quantitative study of the Bogoliubov dispersion of a resonantly driven polariton fluid is then the main goal of (Stepanov et al. [2019]); the experiment, which now we illustrate, was designed by Maxime Richard and carried out by Petr Stepanov and Jean-Guy Rousset. The theoretical analysis, mostly developed by us, is posponed to the next Section.

The GaAs/AlAs microcavity used in this experiment is identical to that used in Bajoni et al. [2007] and consists of 12 QWs and features a quality factor $Q = 3000$. The heavy-hole and light-hole excitonic transitions energy are at $E_{hh} = 1612.05\,\text{meV}$ and $E_{lh} = 1644\,\text{meV}$ at $T = 30\,\text{K}$, and

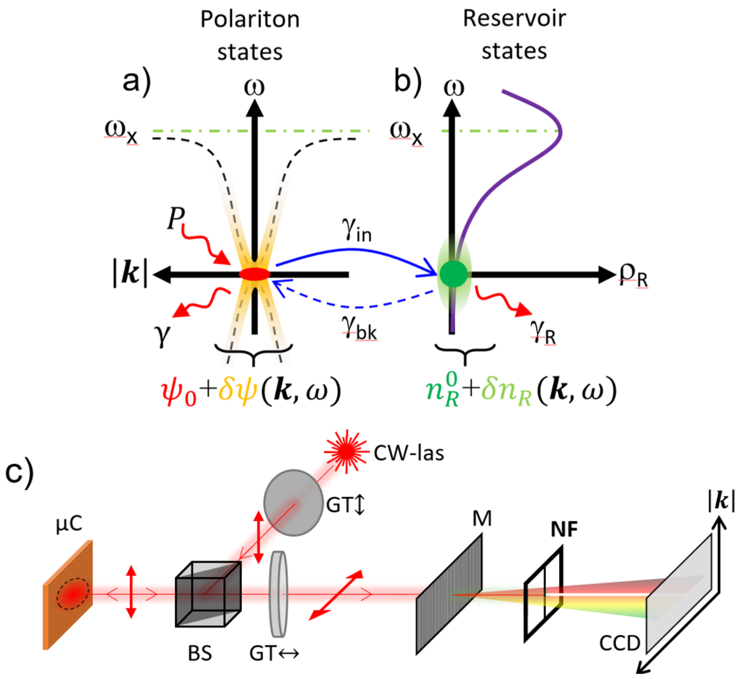

Figure 2.2: *Fluid components and the detection scheme* - a) A polariton field (red spot) of wavefunction ψ_0, and of radiative loss rate γ_c is resonantly excited by the laser of power P. The excitations $\delta\psi(\mathbf{k},\omega)$ on top of the injected wave are shown in yellow in the $(\mathbf{k},\omega$ plane, with a typical dispersion relation (DR) $\omega(|\mathbf{k}|)$ shown by the black dashed line. The bare quantum well excitonic transition energy $\hbar\omega_X$ is shown as a green dashed line. An illustration of the typical quantum well excitonic density of state $\rho_R(\omega)$ is shown as a purple line in b). Owing to their effective mass differences, ρ_R's peak value exceeds the polaritonic density-of-state by 5 orders of magnitude. The low energy tail of $\rho_R(\omega)$ originates from disorder in the quantum well, and can accommodate a reservoir (green spot) of long-lived excitons (loss rate γ_R, fluctuations δn_R represented in light green). Interconversion of polaritons into reservoir excitons and back by optical absorption or scattering, occur at rates γ_{in} and γ_{bk} respectively. c) sketch of the experimental set-up used to measure the DR. The excitation laser light is linearly polarized by a Glan-Thompson polarizer (GT) and passed through a beam splitter (BS) to excite resonantly the polariton fluid. The cross-polarized reflected signal is selected by another GT and passed through a monochromator (M).The polariton emission at the laser frequency is further rejected by a metallic filter playing the role of notch filter (NF) and the remaining EPL is detected on a CCD camera. Some optical elements are omitted, that provide resolution on the EPL emission angle θ, and thus on its in-plane wavevector $|\mathbf{k}| = (\omega/c)\sin(\theta)$ ($\hbar\omega$ is the photon energy, and c the speed of light in vacuum).

the corresponding Rabi splittings resulting from the strong coupling regime with the cavity mode of energy E_{c0} are $\hbar\Omega_{hh} = 15\,\text{meV}$ and $\hbar\Omega_{lh} = 12.5\,\text{meV}$ respectively. The microcavity is intentionally wedged in order to tune E_{c0} with respect to E_{hh}. The background index of the microcavity is $n_{bg} = 3.65$. The microcavity is placed in the vacuum chamber of a temperature-tunable Helium flux cryostat.

The polariton fluid is driven resonantly with a single longitudinal mode CW Ti-Sapphire laser of 5 MHz linewidth, and linearly polarized with a high purity. The laser beam is shaped with pinholes into a spatially Fourier-limited Gaussian mode of $50\,\mu\text{m}$ diameter as measured on the surface of the microcavity, and a corresponding $\delta\theta = \pm 2°$ angular spread (i.e. $\delta k_{\parallel} = \pm 0.28\,\mu\text{m}^{-1}$) in momentum space.

A sizable population of excitations is spontaneously created on top of the resonantly driven polariton fluid by the interaction of polaritons with the thermal bath of acoustic phonons naturally present within the solid-state microcavity (see the paragraph 2.3.3 below). The temperature is set at $T = 30K$, that it is found as a good trade-off between a sufficient thermal phonon population and a narrow polariton linewidth. The polaritons involved in these excitations can then relax radiatively, so that their energy and momentum with respect to the injected wave constitute a direct measurement of the DR of the excitations. This emission, that we will refer to as excitations

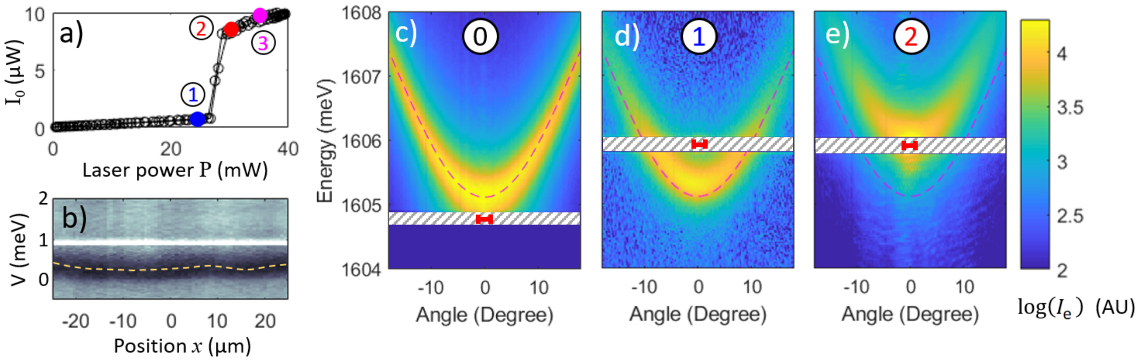

Figure 2.3: *Characterization of WPA* - a) Measured cross-polarized polaritonic emission intensity I_0 vs laser power P; the bistability area is very small, due to the fast duty cycle of the laser. b) Color-scaled microreflectivity measured across a region of 50μm in linear size. The black area is the polariton absorption dip. The white streak is due to residual laser light. The orange dashed line show the extracted potential $V(x, y)$ across the working point. Angle and energy resolved cross-polarized EPL measurements $I_e(\theta_p, \hbar\omega)$ in the free-particle regime (c), in the lower branch of $I_0(P)$ (d), in the upper branch (e). The intensity is color coded on a logarithmic scale. The hatched rectangles show the spectral range rejected by the notch filter. The laser energy and angular spread is shown as a red segment. WPA is characterized by $\delta = +1.2\,5\text{meV}$.

photoluminescence (EPL), is collected by the detection scheme illustrated in Fig.2.2.c.

The EPL I_e is isolated from the much brighter signal I_0 of the $(\mathbf{k}_p, \omega_p)$ polaritons and from the Rayleigh scattered laser light using a two-stage filtering scheme. The first stage builds on the fact that the injected linearly polarized polaritons can scatter into the cross polarized stated because of a weak residual birefringence: detecting the EPL in the cross-polarized direction gets rid of most of the elastically scattered laser light. For the second stage, a narrow band notch filter was designed (labelled 'NF' in Fig.2.2.c), made up of a featureless metallic stripe and placed in the output focal plane of the monochromator. The resulting rejection is such that the EPL signal can be well identified even as close as 0.1 meV from the injection frequency. Fig.2.3.c-e show measured angle-resolved EPL patterns $I_e(\theta, \omega)$ obtained with this method.

In order to measure sharply-defined dispersion relations, we chose two regions of the microcavity of $\sim 50\mu$m diameter characterized by a weak disorder amplitude of the potential experienced by polaritons $V(x, y)$. They are labelled further on as 'working points' (WPs) A and B and are characterized by a photon-exciton detuning $\delta = E_{c0} - E_{hh} = +1.25\,\text{meV}$ and $\delta = -1.82\,\text{meV}$ respectively. The microreflectivity measurement shown in Fig.2.3.b provides a cross-section of V across WPA showing that its spatial fluctuations are smooth and small as compared to the linewidth, defined as the full width at half maximum and measured to be $\hbar\gamma_c = 0.4\text{meV}$ The reference free-particle DR at WPA is extracted from the EPL measurement shown in Fig.2.3.c. It is obtained under weak excitation at normal incidence, with the laser energy $\hbar\omega_l$ red-detuned from the $\mathbf{k} = 0$ lower polariton resonance by $\Delta = \hbar\omega_l - \hbar\omega(0) = -0.5\,\text{meV}$. The corresponding extracted free-particle DR is labeled '0' in Fig.2.4.a.

Having the reference, the laser frequency was shifted to $\Delta = -0.79\,\text{meV}$ on the blue side of the polariton resonance, in order to access the regime for which the polariton density dependence $n(P)$ on the driving laser power P exhibits a bistable behaviour. In the context of the GPE theory reviewed in Section 1.3, the regime of collective excitations corresponds to the upper bistability branch: at the lower laser power edge of this branch (just before switch down) sits the gapless sonic regime, in which the excitations are expected to be phonon-like with a well-defined speed of sound. Higher up along this branch, a gap opens up for increasing P and the DR adopts a more curved shape. In order to characterize this bistability curve, the unfiltered $(\mathbf{k}_p, \omega_p)$ emission I_0 is collected in the cross-polarized direction vs the laser power P. Note that in this measurement the excitations have a negligible contribution. The measured $I_0(P)$ curve is shown in Fig.2.3.a: the lower and upper branch are separated by a sharp jump: it is likely that since the laser is chopped with a 5% duty-cycle to prevent unwanted heating effects the bistable region appears closed.

Moreover, under a finite pump spot there is a current flowing outward (the phase not being completely fixed by the pump) and the polariton density is not homogeneous: as a consequence, at the center of the spot the blueshift needs to be larger than $|\Delta|$ (even at the end of the upper branch) to compensate for the outward flow, so that strictly speaking the acoustic regime will never be realized. Note that in spite of these limitations, the sonic regime appears to be quite close in the measurements.

Based on this preliminary calibration measurement, the DR of the collective excitations was extracted at several laser powers P along the upper branch $I_0(P)$. Due to the stringent requirements of the driving laser beam shape both in Fourier and real space, a balance was reached by working with a large laser spot of Gaussian intensity profile of $50\,\mu$m diameter. As a result, for states in the upper branch of $I_0(P)$, the polariton density is organized into two large spatial structures: The high polariton density is contained in a large diameter disk-shaped area at the center of the laser spot, separated from a low density outer region by a sharp switching front, see Fig. 2.6 below. The nonlinearity thus acts as an effective 'top-hat' spatial filter for the Gaussian pump mode, that homogenize the high-density region of main interest.

In order to collect EPL only from the high density area, the signal from the outer region was rejected using an iris of diameter D_i matching that of the switching front of typically $\sim 35\,\mu$m diameter. While this spatial selection introduces a spurious angular spread $\leq 1.5°$ to the EPL, it does not prevent resolving the collective features in the dispersion relation, that are visible within a $\sim 5°$ window as can be seen in Fig.2.4. This finite angular resolution was taken into account also in the numerical simulations.

Two raw results of angle- and energy-resolved EPL are shown in Fig.2.3.d and Fig.2.3.e that correspond to two states on the curve $I_0(P)$ labeled '1' and '2' respectively in Fig.2.3.a: '1' is a state on the lower branch of $I_0(P)$, while '2' is on the upper branch and as close as possible to the switch-down point.

Fig. 2.4.a show the resulting DRs for WPA, for the free polariton dispersion (dark green line, labelled '0'), and three states at increasing blue-shifts (blue, red and magenta lines, labelled '1', '2' and '3' respectively). The collective excitations DR of '2' and '3' $\hbar\omega_e(\theta) = \hbar\omega - \hbar\omega_l$, properly shifted by the laser frequency, are shown in greater detail in Fig.2.4.b and Fig.2.4.d respectively, and the 95% confidence interval for the determination of $\hbar\omega_e$ shown in Fig.2.4.c and Fig.2.4.e. The same analysis is shown for WPB, defined by excitation incidence angle of $-1°$ and by the detuning $\Delta = -0.47\,$meV, in Fig.2.4.f-j. The free polariton DRs from both WPA and WPB are very well-fitted with the near-parabolic theoretical free polariton DR (light green line) as obtained from the coupled oscillators model.

Let's start with WPA, for which the laser drive is at normal incidence. Curve '1' shows the DR of a polariton fluid for which the blueshift with respect to DR '0' amounts to $\hbar\omega_{BS} = 0.18\,$meV, and which is still on the lower branch of $I_0(P)$. Its shape is identical to '0', indicating that in spite of the Hartree shift, the excitations have mostly single particle features. Curves '2' and '3' are obtained in the upper branch of $I_0(P)$ and feature a clearly modified shape with respect to '0', which is an unambiguous signature that the nature of the excitations has changed from free-particle to collective as a result of strong interaction energy ('2' and '3' are blueshifted by $\hbar\omega_{BS} = 0.85\,$meV and $\hbar\omega_{BS} = 0.90\,$meV respectively, with respect to '0'). In Fig.2.4.b and 2.4.g, the low-energy low-angle part of both DR are compared with the theoretical shape expected in two limiting situations: (i) the DR consists of a rigidly blue-shifted free-particle dispersion (as we will discuss in the next Section, this situation arise for instance if all the blueshift is due to the interaction with excitons in the dark reservoir, whose density overcomes the density of polaritons); (ii) the system consists only of polaritons (without any reservoir fraction) so that the standard theory described in the previous Chapter applies and the DR has the form given by Eq. (1.16).

In mathematical form, the rigidly blue-shifted DR in case (i) reads

$$\omega_{RB}(\mathbf{k}) = \omega_{BS} + \omega_0(\mathbf{k}) - i\,\frac{\gamma_c}{2}, \tag{2.2}$$

where γ_c is the polariton radiative loss rate, $\hbar\omega_0(\mathbf{k})$ is known from the DR measurement at point '0', and ω_{BS} is the measured blue-shift. $\hbar\omega_{RB}(\theta)$ is plotted as a black dashed line in Fig.2.4.b and g. The comparison between this model and the measured dispersion '2' and '3' show a clear mismatch, in which the measured dispersion is steeper. The theoretical shape of the dispersion in case (ii) is given by Eq. (1.16) that here we rewrite as

$$\omega_\pm(\mathbf{k}) = \omega_p \pm \sqrt{(\omega_0(\mathbf{k}) + 2gn - \omega_p)^2 - (gn)^2} - i\,\frac{\gamma_c}{2}, \tag{2.3}$$

where we use the notation $\hbar g = g$ (so that gn denotes a frequency, gn an energy) and similarly for

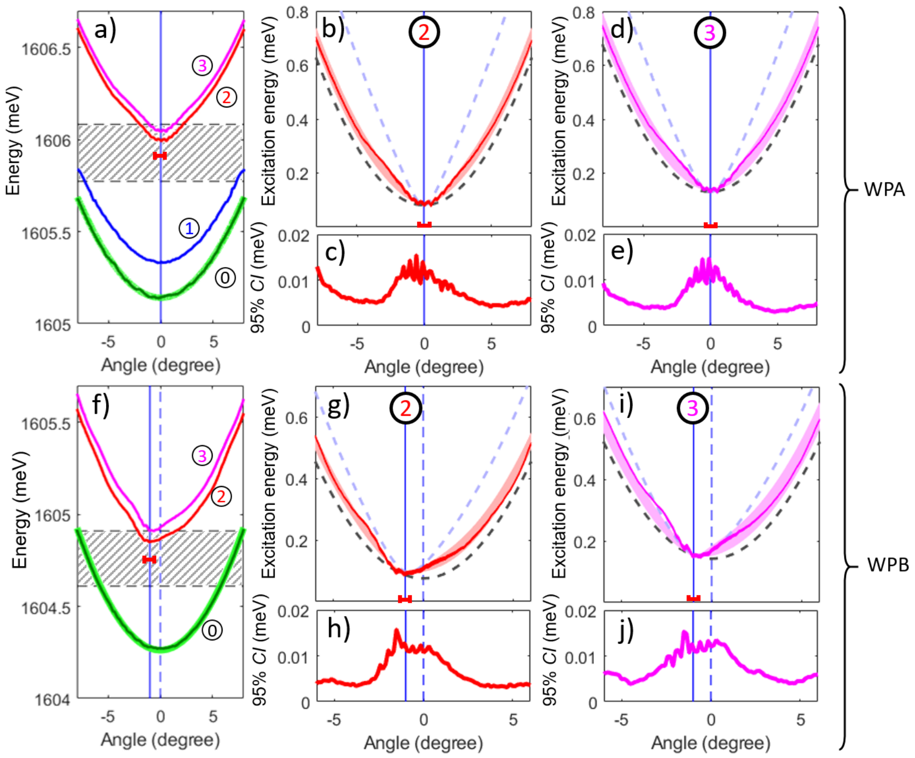

Figure 2.4: *Dispersion relations of the elementary excitations* - Measured DR $\hbar\omega(\theta)$ as obtained from the numerical analysis (see below) of the EPL (solid lines) for WPA (a) and WPB (f). Four states of the fluids are shown according to their position along $I_0(P)$ (plotted in Fig.2.3.a for WPA): '0' is the free-particle DR (green line), '1' is a lower branch state of $I_0(P)$ (blue), '2' and '3' are two upper branch states (red and magenta). The free polariton DR calculated via the Rabi model is the thick light green line underneath the measured one. (b,d) and (g,i) are zoomed plots of DR '2' (narrow red line) and '3' (narrow magenta line) of WPA and WPB respectively, shifted according to $\hbar\omega_e = \hbar\omega - \hbar\omega_l$ to highlight the energy of the excitations themselves. The 95% confidence interval amplitude (CI) of the measured DRs is shown for each DRs in panels c,h and e,j for WPA and WPB respectively, with the same color codes. The theoretical DRs in the rigid blueshift limit Eq. (2.2) (dashed black line) and in the standard theory Eq. (2.3) (blue dashed line) are shown in (b), (d), (g) and (i). The full vectorial theory developed in Section 2.3 is also shown as a thick red and magenta lines visible underneath the measured DR; the line thickness represents the 95% confidence interval of the fitting procedure with the data. In each panel, the laser energy and angular spread is shown as a red segment and the vertical blue line shows the angle of excitation. The hatched rectangle in (a,f) is the spectral range rejected by the notch filter.

the other coupling that will appear below, with the hope that possible confusion between the two symbols will not produce any misunderstanding of the physics.

Like in the previous case, the interaction energy gn, is inferred unambiguously from the experimentally measured blueshift $gn = \hbar\omega_{BS}$, which fixes also the position on the theoretical curve $I_0(P)$. These calculated DRs are shown in Fig.2.4.b and g as dashed light blue lines. This time, both for '2' and '3', the measured dispersions are now clearly not steep enough to match the theory.

The same analysis can be performed also for the other working point WPB at nonzero laser incidence angle $\theta_p = -1°$. In WPB, owing to the microcavity tuning, the interactions are smaller by a factor ~ 2 and a smaller laser detuning of $-\Delta = 0.47$ meV is chosen accordingly. The local disorder is obviously different, but of similar average amplitude and characteristic length, as in WPA. The measured DRs for WPB are shown in Fig.2.4.f-j with the same labelling conventions as for WPA. For dispersions '2' and '3', situated on the upper branch of $I_0(P)$, with '2' as close as possible to the switch down point, an asymmetric shape of the DR is obtained, as expected for the collective excitations when the fluid is injected at a nonzero velocity. Like in WPA, the comparison with the two theoretical limiting cases are shown in Fig.2.4.d,i and demonstrates that the measured DRs do not agree with either of them.

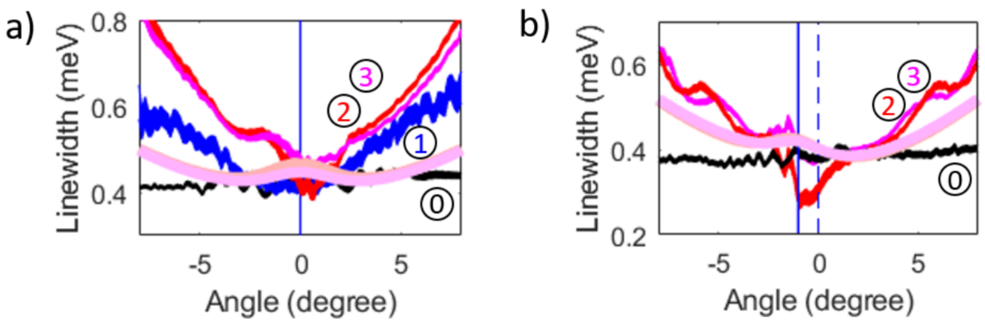

Figure 2.5: *Momentum dependence of the linewidth* - Measured excitations linewidth $\hbar\gamma(\theta)$ versus angle, as obtained from the numerical analysis of the EPL (narrow solid lines) for WPA (a) and WPB (b). The full vectorial theory is shown as the thick solid lines. For the experimental data, the line thickness show the 95%-confidence interval. The same labelling convention is used as in Fig.2.4. The solid vertical line show the laser excitation incidence angle, while the dashed one shows the zero incidence reference ($\theta_{\mathrm{p}} = 0°$)

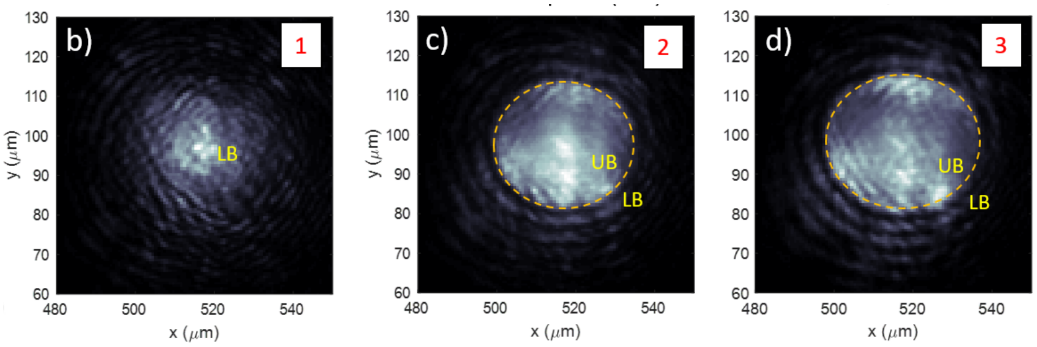

Figure 2.6: *Spatial density of the polariton fluid* The cross-polarized emission from the polariton fluid is shown in real space for the states '1' (b), '2' (c) and '3' (d) defined in the text. 'LB' ('UB') stands for the lower (upper) branch of $I_0(P)$. The dashed orange line shows the circular switching front separating the 'LB' and the 'UB' areas.

The analysis of the raw measurement $I_{\mathrm{e}}(\theta,\omega)$ also gives access to the excitations spectral linewidth $\hbar\gamma$. The results are shown in Figure 2.5 for both WPA (a) and WPB (b) together with the results of the full theory calculation. In the low excitation regime, (solid black line labelled '0' in WPA), the measured linewidth is essentially angle-independent. This is expected as over such a small angular range, the excitonic and photonic fraction hardly change vs θ: i.e. the kinetic energy increase as compared to the Rabi splitting is small (1 meV increase between 0° and 10°). For the measurement of $\hbar\gamma(\theta)$ in states '2' and '3', both the finite spatial extension of the high density area illustrated in Fig. 2.6 and the use of a circular aperture filter have a significant influence: in both cases, the excitations of the condensate have a finite transit time either throughout the circular aperture of the detection or within the switched up area, depending on which one has the smallest diameter D. The switched-down state '1' features an intermediate inhomogeneity and then an intermediate k-dependence of the linewidht. The transit time is fixed by the excitation group velocity via $\tau(k) = D/v_g(\theta)$, which is a decreasing function of θ, regardless of the detailed nature of the excitation. A complementary view is that the frequency of the excitations is well defined but its momentum is blurred by the finite spatial spot; also in this case the effect on $I_{\mathrm{e}}(\theta,\omega)$ is more important for steeper dispersions. In any case, the increase of $\hbar\gamma$ versus θ reflects the presence of the switching front, and can thus be considered as a characteristic feature of a locally switched-up polariton fluid driven by a Gaussian laser spot.

The large discrepancy of the measured DR with respect to the standard theory of Eq. (2.3) is well characterized by looking at the slope at small wavevectors: if the data were taken at the acoustic point, on could say that the speed of sound of the experimental curve is significantly lower then the theoretical expectation $c_s = \sqrt{\frac{gn}{m}} = \sqrt{\frac{\hbar\omega_{BS}}{m}}$: the reduction, according to the analysis of

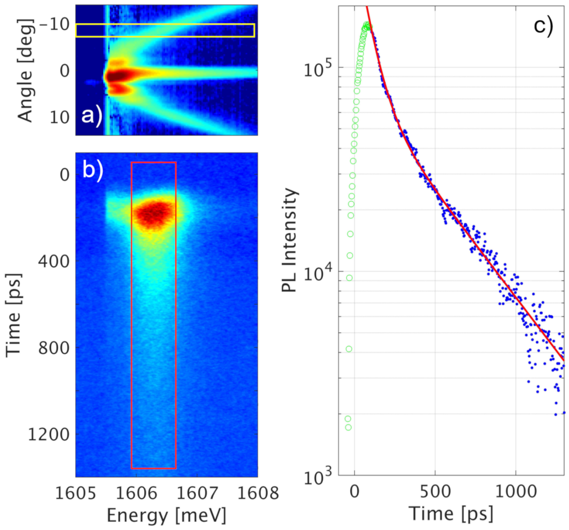

Figure 2.7: *Time-resolved photoluminescence* - a) Angle and energy resolved excitation photoluminescence obtained under weak picosecond-pulse excitation. The yellow rectangle show a cross-section at 7° which is sent onto the streak camera. The resulting time-resolved trace is shown in b) in a time energy color plot, and the relevant cross-section $I(t)$, integrated in energy over the polariton emission linewidth (red rectangle) is shown in c) along with a fit (red line) consisting of a sum of two exponential decays with characteristic times $\tau_1 = 58\,\mathrm{ps}$ (instrument-limited) and $\tau_2 = 400\,\mathrm{ps}$ (attributed to the excitonic reservoir).

the next Section and as shown in Fig. 2.12, is of the order of 50%. These findings instead suggest that only a fraction of the blue-shift is due to the polariton fluid $gn < \omega_{BS}$, with the rest of the blueshift to be attributed to interactions of the polariton with a background which does not partecipate in the coherent dynamics. Such background suggests the introduction of a reservoir of dark excitons, whose dynamics is quite slow on the timescales set by the polariton-polariton interactions so that it can be considered as a static background only contributing by an Hartree shift.

In addition to these indirect signatures visible in the DR, a direct characterization of the reservoir properties was presented in the paper in the form of a time-resolved photoluminescence decay measurement. The excitation strategy is similar to that used to measure the free particle dispersion relation: quasi-resonant laser excitation, red detuned central frequency with respect to the polariton ground state, weak peak intensity in order to minimize nonlinear dynamics and small angular spread. The laser consists in picosecond pulses of 0.5 meV linewidth (FWHM). It was checked that the laser high-energy tail has a negligible overlap with the upper polariton branch. Figure 2.7.a shows the thus obtained time-integrated excitation photoluminescence (EPL) pattern $I_{\mathrm{e}}(\theta, \omega)$. The emission at the angle of 7°, where the contribution from the laser light is negligible (yellow rectangle in the figure), was sent into the streak-camera. The corresponding raw time-resolved trace is shown in Fig. 2.7.b and analyzed in Fig. 2.7.c. By fitting it with a sum of two exponential decays, two characteristic timescales $\tau_{\mathrm{res}} = 58\,\mathrm{ps}$ and $\tau_2 = 400\,\mathrm{ps}$ are found. The first one corresponds to the instrumental time-resolution, which is fixed by the (sharp) spectral resolution of the detection. It thus reflects a dynamics τ_1 much faster than τ_{res}, that can be unambiguously attributed to the polariton state decay. The lifetime τ_2, also read as $\hbar\gamma_R = 1.6\,\mu\mathrm{eV}$, is too slow to be photon or polariton related, and corresponds to the typical timescale of long-lived excitons. The photoluminescence itself from the dark states is explained in the paper by assuming that dark excitons can scatter back into polaritons with a rate γ_{bk}. Alternatively, the photoluminescence may also be attributed to the fact that in the presence of disorder angular momentum is not a completely well defined quantum number, so that these exciton states are not perfectly dark.

Another strategy that we proposed here but there was not the technical time to be implemented in the lab, is to look at the time and energy resolved photoluminescence. As it will be clear after writing down the model in the next Section, the blue-shift should then consist of a fast polaritonic decay plus a slow excitonic decay; the fraction of the blueshift which survives the first decay is then a direct measurement of the background blueshift fraction, contributing to the DR just via a rigid shift but not entering the speed of sound.

2.3 Excitations in the presence of a dark reservoir*

(this Section mostly builds on material contained in Section IV from [Amelio et al., 2020b] and the Supplementary Information of Stepanov et al. [2019])

In this Section we state explicitly the model anticipated in the previous Sections, where the coherent polariton field is coupled to a reservoir of dark excitons, and derive how the latter affects the collective excitations of the fluid. For illustrative purpose, we start by discussing the dispersion relation in the "vanilla" case of polaritons in a given circular polarization; aiming at a thorough modelization of the experiment by Stepanov et al. [2019], we then consider both polarizations and study in details the photoluminescence signal as excited by thermal phonons in the microcavity.

2.3.1 Singly polarized model

The recent experimental findings by Sarkar et al. [2010], Walker et al. [2017], Stepanov et al. [2019] reviewed above suggest that an incoherent reservoir of dark-excitons is excited even under a coherent pump via non-radiative absorption processes. Even though a full direct characterization of these states is the subject of ongoing research, it is legitimate to assume that the reservoir mostly consists of excitonic states that are energetically close to bottom of the lower polariton band where the coherent polariton fluid is located. Since these states are detuned from the center of the exciton line by the Rabi splitting, they must be trapped around the minima of the disorder potential in the quantum well. As such, they are spatially localized and attached to the microcavity frame of reference. The situation would of course be different in the case of an incoherent pumping, where an important role is played by spatially extended electronic and excitonic states, which can move in response to the motion of the polariton fluid, e.g. by drag effects (Berman et al. [2010], Chestnov et al. [2019]). Yet different is the physics of atomic or Helium superfluids at finite temperature, where a sizable normal component fraction is present in addition to the superfluid: while an isolated fluid would fulfill Galilean invariance, the incoherent normal component of a fluid contained in a tube is able to move but still feels the friction of the walls, which then define a privileged reference frame (Pitaevskii and Stringari [2016]).

For the system of coherently pumped polaritons under consideration here, the effect of the incoherent reservoir can be theoretically modeled by including the reservoir density $n_R(\mathbf{x})$ to the equations of motion,

$$
\begin{aligned}
i\partial_t\psi &= \left(\omega_0 - \frac{\hbar\nabla^2}{2m} + g|\psi|^2 + +g_R n_R - i\frac{\gamma}{2}\right)\psi + F(\mathbf{x},t) && (2.4)\\
\partial_t n_R &= -\gamma_R n_R + \gamma_{inc}|\psi|^2\,. && (2.5)
\end{aligned}
$$

Here, the decay of coherent polaritons into incoherent excitations occurs at a rate γ_{inc}. These latter give a local contribution $\hbar g_R n_R = g_R n_R$ to the polariton blue-shift, do not move in space and decay at a rate γ_R. The total decay of polaritons γ includes the γ_{inc} contribution; notice that since the reservoir density is the sum of the occupation of many scarcely populated states the stimulated scattering processes into the reservoir are negligible.

At stationarity under a monochromatic pump at ω_p, one has $\psi(\mathbf{x},t) = \psi_0\exp(-i\omega_p t)$ and, from (2.5), one gets a time-independent $n_R(\mathbf{x}) = \frac{\gamma_{inc}}{\gamma_R}|\psi_0(\mathbf{x})|^2$. Reinjecting this expression into (2.4), one simply obtains a renormalized nonlinear coupling strength

$$
g_{\text{eff}} = g + \frac{\gamma_{inc}}{\gamma_R} g_R\,. \tag{2.6}
$$

Except for the reinforced interactions and the consequently reinforced blue shift $\mu_T = g_{\text{eff}} n_0 = g n_0 + g_R n_R$, the reservoir has thus no effect on the stationary state. The usual optical bistability and optical limiting behaviours are found depending on whether the laser frequency ω_p is blue- or red-detuned as compared to the polariton mode at $\mathbf{k}_p$.

Even more importantly for our purposes, superfluidity features the usual behaviours with a speed of sound defined by the total blue-shift as $mc_{s,T}^2 = \mu_T = g n_0 + g_R n_R$. Since this reasoning requires stationarity of both the polariton $\psi(\mathbf{x})$ and the reservoir $n_R(\mathbf{x})$ densities, this result only holds for static defects that do not induce time-dependent modulations to the fluid density, that is defects at rest in a (possibly moving) fluid. And, of course, these statements are only relevant if the fluid is indeed able to reach a dynamically stable steady state: as it was pointed out in (Amelio and Carusotto [2020a]) and reviewed in Fig. 2.17 of the next Section, the presence of a slow reservoir can in fact give rise to dynamical instabilities that prevent from reaching the stationary state. In the experiment by Walker et al. [2017] they could suspect the presence of the reservoir because they have a good calibration of the number of polaritons in the waveguide and the theoretical estimate for g; on the other hand the hallmark of the (slow) reservoir is only obtained when comparing with pulsed excitation, so going beyond stationarity.

For these reasons, the physics gets more interesting if one looks at the dynamics of the excitations on top of the fluid, as first noticed in (Stepanov et al. [2019]). In the homogeneous case under a plane-wave coherent pump of wavevector $\mathbf{k}_p$ and frequency ω_p, the steady-state solution has the form $\psi_0(\mathbf{r},t) = \psi_0 \exp[i(\mathbf{k_p}\cdot\mathbf{r} - \omega_p t)]$ and the Bogoliubov theory involves a 3×3 matrix

$$\mathscr{L}(\mathbf{k}) = \begin{pmatrix} \eta(\mathbf{k}_p+\mathbf{k}) + gn_0 - i\frac{\gamma}{2} & g{\psi_0}^2 & g_R\psi_0 \\ -g{\psi_0}^{*2} & -\eta(\mathbf{k}_p-\mathbf{k}) - gn_0 - i\frac{\gamma}{2} & -g_R\psi_0 \\ i\gamma_{inc}\psi_0 & i\gamma_{inc}{\psi_0}^* & -i\gamma_R \end{pmatrix}, \tag{2.7}$$

where $\mathbf{k}$ is again the relative wavevector of the excitation on top of the moving fluid and the effective detuning function is now $\eta(\mathbf{k}) = \omega_0 + \hbar k^2/2m + gn_0 + g_R n_R - \omega_p$. The first and second columns/rows of $\mathscr{L}(\mathbf{k})$ correspond to the polariton modulation $\delta\psi_{\mathbf{k}}$ and $\delta\psi^*_{-\mathbf{k}}$, while the third column/row corresponds to the modulation of the reservoir density δn_R.

The corresponding eigenvalue problem can be formulated in a physically trasparent way by defining a frequency–dependent effective coupling

$$g_{\rm eff}(\omega) = g + \frac{\gamma_{inc}}{-i\omega + \gamma_R} g_R, \tag{2.8}$$

which allows to eliminate the reservoir and reduce to the usual 2×2 eigenproblem

$$\left(\omega - \frac{\hbar\mathbf{k}_p}{m}\cdot\mathbf{k} + i\frac{\gamma}{2}\right)^2 = \eta(\tilde{k})\left[\eta(\tilde{k}) + 2g_{\rm eff}(\omega)n_0\right] \tag{2.9}$$

with $\tilde{k} = \sqrt{k_p^2 + k^2}$ and where g has been replaced by $g_{\rm eff}(\omega)$ [1]. While this expression is formally nearly identical to the usual one (1.38), the ω-dependence of the right–hand side has crucial consequences onto the dispersion of collective excitations. Of course, the usual Bogoliubov dispersion is recovered in the limit where high-ω perturbations are considered, so that $g_{\rm eff}$ recovers g. On the other hand, the static value (2.6) for $g_{\rm eff}$ is recovered for stationary perturbations at $\omega = 0$.

Polaritons at rest $\mathbf{k}_p = 0$

Let us start from the $\mathbf{k}_p = 0$ case. In this case, the Bogoliubov matrix (2.7) is characterized by particle-hole and parity symmetries, that combine in

$$\mathscr{P}\mathscr{L}(\mathbf{k}) = -\mathscr{L}(\mathbf{k})\mathscr{P} \tag{2.10}$$

where

$$\mathscr{P} = \mathscr{K}\begin{pmatrix} 0 & 1 & 0 \\ 1 & 0 & 0 \\ 0 & 0 & 1 \end{pmatrix} \tag{2.11}$$

and $\mathscr{K}$ stands for complex conjugation. For a generic eigenvector $|\omega_{\mathbf{k}}\rangle$ of $\mathscr{L}(\mathbf{k})$ of eigenvalue ω, this symmetry implies that

$$\mathscr{L}(\mathbf{k})\,\mathscr{P}|\omega_{\mathbf{k}}\rangle = -\omega^*\mathscr{P}|\omega_{\mathbf{k}}\rangle\,, \tag{2.12}$$

i.e. that $\mathscr{P}|\omega_{\mathbf{k}}\rangle$ is itself an eigenvector of $\mathscr{L}(\mathbf{k})$ of eigenvalue $-\omega^*$. This imposes the presence of pairs of eigenvectors with the same imaginary part and opposite real parts. Since the size of the matrix is three, this guarantees that at least one eigenvalue is purely imaginary. This mode can be interpreted as a reservoir branch $\omega^R(\mathbf{k}) = -i\gamma^R(k)$, while the remaining two eigenvalues,

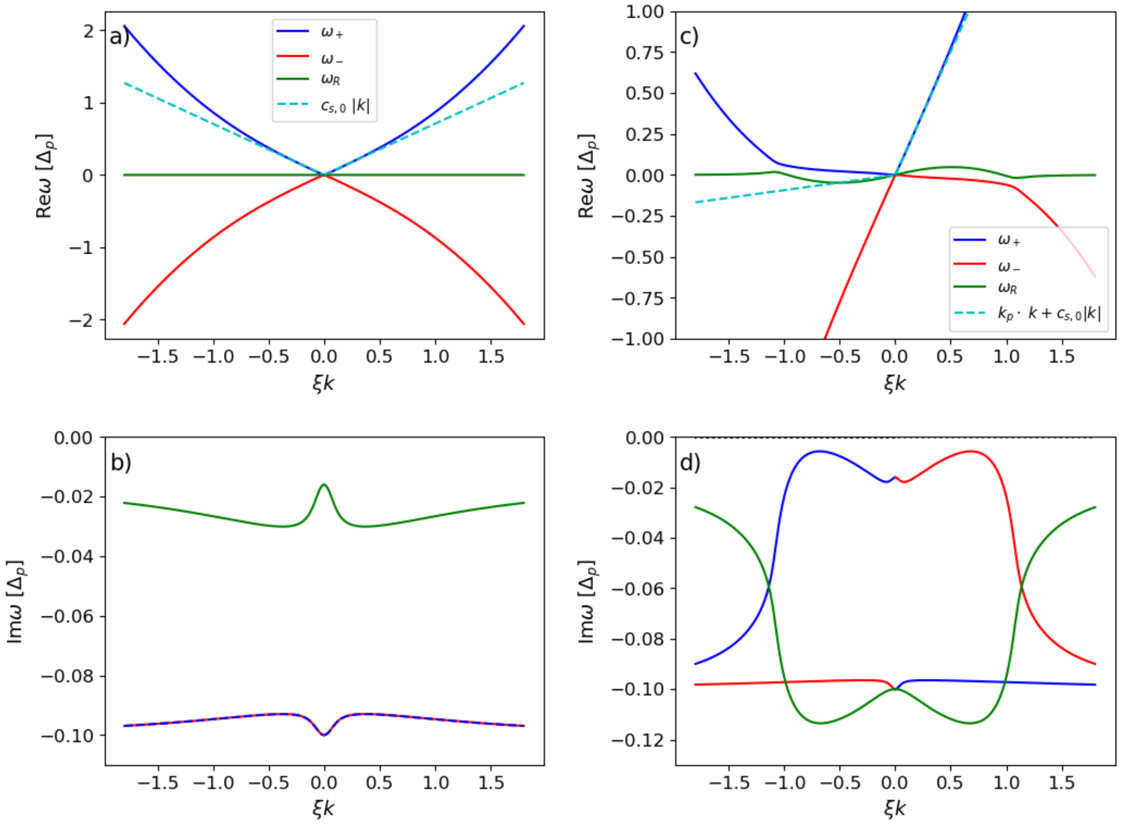

Figure 2.8: Dispersion of collective excitations in a polariton fluid at rest $k_p = 0$ [left column, panels (a,b)] and in motion at $v_p = 0.8c_{s,T}$ along the x direction [right column, panels (c,d)] in the presence of an incoherent reservoir. Upper (a,c) panels show the real part of the dispersion, the lower (b,d) panels show the imaginary part. The total blue-shift μ_T is the same in all panels and pumping is tuned at the resonance point such that $\Delta_p = \mu_T$. Other parameters: $\hbar\gamma/\mu_T = 0.2$, $g_R = 2g$ and $\gamma_R = 2\gamma_{inc} = 0.08\,\gamma$ which means $c_{s,0} = c_{s,T}/\sqrt{2}$ and $c_s \simeq 0.9c_{s,0}$. Note that for a slightly larger $\gamma_{inc} \simeq 0.05\gamma$ or for $v_p \simeq 0.9c_{s,T}$, the flow configuration in the right panels would become dynamically unstable. The different curves are colored according to their nature at large wavevector k. The dashed cyan lines in the upper panels indicate the low-k sonic dispersions (2.14) and (2.21).

corresponding to particle- and hole-like branches have general complex dispersions of the form $\omega^{\pm}(\mathbf{k}) = \pm\epsilon(k) - i\gamma(k)/2$.

Let us focus on the most relevant resonant case $\omega_p - \omega_0 = \mu_T = gn_0 + g_R n_R$ where the dispersion is expected to be gapless and sonic. In this regime, it is possible to obtain some analytical insight on the eigenvalue problem, which can be recast as

$$\left(\omega + i\frac{\gamma}{2}\right)^2 = \frac{\hbar k^2}{2m}\left[\frac{\hbar k^2}{2m} + 2g_{\text{eff}}(\omega)n_0\right]. \tag{2.13}$$

At small k, this yields

$$\omega^{\pm}(\mathbf{k}) = \pm c_s k - i\gamma/2 \tag{2.14}$$

with

$$mc_s^2 = \mu_T + \frac{\gamma}{2\gamma_R - \gamma} g_R n_R \tag{2.15}$$

In the fast reservoir limit $\gamma_R \gg \gamma$, the contribution of the reservoir is negligible and one recovers the usual speed of sound

$$mc_{s,T}^2 = \mu_T \tag{2.16}$$

---

[1] Of course, the replacement must not be applied to the g appearing in the definition of the detuning function η, which involves the stationary background.

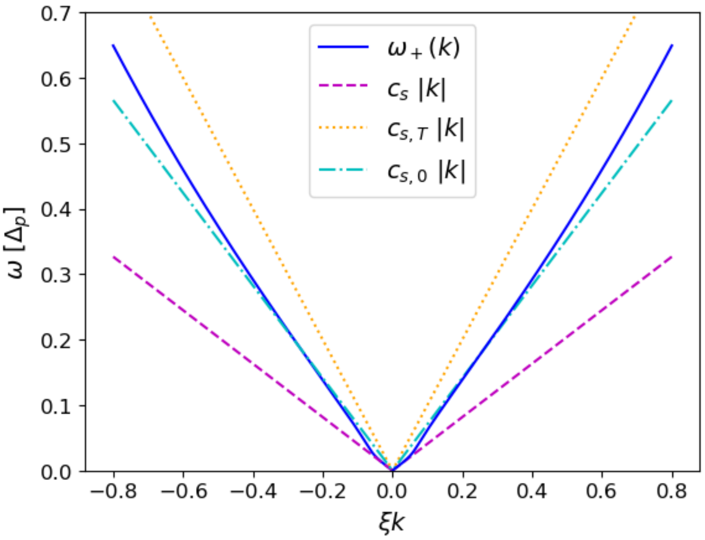

Figure 2.9: *Frequency dependent speed of sound.* Dispersion of the collective excitations of a polariton fluid at the acoustic point and in the presence of reservoir with parameters tuned so to make clear the distinction between the three definitions of the speed of sound: c_s is the slope of the dispersion at $k = 0$, $c_{s,T}$ takes into account the total blueshift and it is correct in the adiabatic limit, $c_{s,0}$ is only due to the self-interaction of the coherent polariton fluid and grasps the correct slope at frequencies $\gamma_R \ll |\omega| \ll gn_0$. The reservoir parameters are $\gamma_R \ll |\omega + i\gamma/2| \ll \mu_T$. For the parameters in this figure, $\mu_R = g|\psi_0|^2 = \mu_T/2$, $c_{s,0} = c_{s,T}/\sqrt{2} \approx 0.71c_{s,T}$ and $c_s \approx 0.41c_{s,T}$.

in terms of the total blue-shift μ_T.

In the opposite limit $\gamma_R \ll \gamma$, corresponding to the typical experimental conditions where the reservoir reacts on a much slower timescale (Sarkar et al. [2010], Walker et al. [2017], Stepanov et al. [2019]), the speed of sound has the smaller value

$$mc_{s,0}^2 = \mu_T - g_R n_R = gn_0 \ . \tag{2.17}$$

This means that, out of the total blue-shift μ_T, only the component ($gn_0 = g|\psi_0|^2$) due to the polaritons contributes to the speed of sound, while the one ($g_R n_R$) due to the incoherent reservoir only provides a global blue shift of the pumped mode. As described in the previous Section, this feature was exactly what motivated us to consider this model in the first place, and is illustrated in the left panels of Fig. 2.8, showing the real and imaginary parts of the dispersion in panels (a) and (b), respectively. As expected, the cyan dashed lines in panel (a) indicate the sonic dispersion $\omega_s = \pm c_{s,0}k$ with the speed of sound $c_{s,0}$ predicted by (2.17) are in excellent agreement with the exact dispersion at low k's. At higher k's, the dispersion recovers the parabolic single-particle shape. As one can see in panel (b), the imaginary part of the reservoir mode (on the order of γ_R) remains always much smaller than the one of the sonic modes (on the order of $\gamma/2$).

While this picture is fully accurate when γ is very much larger than γ_R, a subtle distinction must be done when γ is larger but still somehow comparable to γ_R. In this regime, corrections in γ_R/γ are important and one must distinguish the low-k speed of sound set by (2.15) to the one at higher-k's such that $|-i\omega(k) + \gamma/2| \gg \gamma_R$, for which one instead recovers (2.17). Also in this case, of course, the sonic behaviour is only visible up to the interaction energy gn_0, beyond which the dispersion recovers a single-particle behaviour [2]. The physical explanation is that at very small frequencies the reservoir can still (weakly) respond, while at higher ω's it behaves as a completely static background for the coherent field fluctuations. In order to clearly see the kink in the dispersion coming from distinction between c_s and $c_{s,0}$, in Fig. 2.9 we tune γ_R closer to γ. These different characteristic velocities are also summarized in Table 2.1, which is reported in the next Section.

In the intermediate case where γ_R and γ have comparable values and the blue-shift due to the reservoir is a significant fraction of μ_T, the squared speed of sound c_s^2 predicted by (2.15)

---

[2] This transition is determined by (the inverse of) the usual healing length, $\sqrt{\hbar^2/(gn_0m)}$ computed including the polariton density only and the bare coupling g.

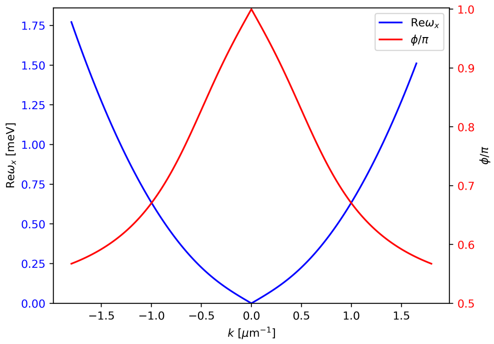

Figure 2.10: *Relative phase between the polariton density and reservoir excitations* - Blue, left axis: real part of the particle branch $\omega^+(\mathbf{k})$. The phase difference $\phi = \arg \delta n_{\mathrm{R}}/\delta|\psi|^2$ for the same excitations is shown in red, (right axis). For the calculation we have chosen $\Delta = 0.8$ meV, $\hbar^2/m = 1.0$ meVμm^2, $g_{\mathrm{R}} = 2.0g$, $\hbar\gamma_{\mathrm{R}} = 0.0016$ meV, $\hbar\gamma = 0.4$ meV, and $\gamma_{\mathrm{in}} = 2\gamma_{\mathrm{R}}$.

may become negative. This results in a flat $\mathrm{Re}[\omega_\pm(\mathbf{k})] = 0$ at small k and a linear shape of the $\mathrm{Im}[\omega_\pm(k)]$ starting from $-\gamma/2$. For larger k, the slope of the dispersion approaches the real-valued speed of sound $c_{s,0}$. A sonic regime with a real-valued c_s is nonetheless recovered for a higher value of the total blueshift $\mu_T > |\Delta|$.

It is finally interesting to analyze how the reservoir influences the nature of the eigenmodes of the Bogolubov excitations. Taking the variation of Eq.(2.5) above we get the relation between the variation of the polariton density and the one of the reservoir density,

$$\frac{\delta n_{\mathrm{R}}}{\delta|\psi|^2} = \frac{\gamma_{\mathrm{in}}}{\gamma_{\mathrm{R}} - i\omega_a(\mathbf{k})}, \tag{2.18}$$

that holds for any eigenmode a. Fig. 2.10 shows the argument of this quantity for the case of the particle branch and at the point with gapless excitation spectrum. We notice that at small wavevector $|\mathrm{Re}[\omega^+(k)]| \ll |\mathrm{Im}[\omega^+(k)]| \simeq \gamma$ the density fluctuations of the condensate and of the reservoir are in phase opposition. This is in agreement with the fact that the excitation branch $\omega^+(\mathbf{k})$ is a Goldstone mode, so at small k the system tries to keep constant density by making δn_{R} and $\delta|\psi|^2$ oscillate with a relative phase π to compensate each other. At large momentum $|\mathrm{Re}[\omega^+(k)]| \gg |\mathrm{Im}[\omega^+(k)]|$ instead, δn_{R} follows $\delta|\psi|^2$ in quadrature of phase, with the condensate density fluctuations driving the reservoir density ones. Given the complex nature of $\omega_a(\mathbf{k})$, the transition between the two regimes occurs when the real part of the Bogoliubov energy $\mathrm{Re}[\omega_a(\mathbf{k})]$ is of the order of the loss rate γ.

Moving polaritons at finite $\mathbf{k}_p$

We conclude this section by extending the analysis to the case of a finite in-plane momentum $\mathbf{k_p} \neq 0$, which breaks parity. Therefore, the action of the $\mathscr{P}$ symmetry only entails

$$\mathscr{P}\mathscr{L}(\mathbf{k}) = -\mathscr{L}(-\mathbf{k})\mathscr{P} \tag{2.19}$$

and relates eigenvectors at opposite $\mathbf{k}$,

$$\mathscr{L}(-\mathbf{k})\, \mathscr{P}|\omega_{\mathbf{k}}\rangle = -\omega^* \mathscr{P}|\omega_{\mathbf{k}}\rangle\,, \tag{2.20}$$

that is $\mathscr{P}|\omega_{\mathbf{k}}\rangle$ is an eigenvector of $\mathscr{L}(-\mathbf{k})$ of eigenvalue $-\omega^*$. This no longer implies the presence of a purely imaginary reservoir mode and the three branches are now strongly mixed as one can see in the right panels of Fig. 2.8. Note that the branches are colored here according to their nature at large wavevectors, while their mixing at small and intermediate k complicates their classification. For instance, in the supersonic flow case considered here, the sonic mode with a wavevector $\mathbf{k}$ directed in the upstream direction (that is, $k_x < 0$) is strongly mixed with the reservoir. In panel (c), the Doppler-shifted sonic dispersions

$$\omega = \pm c_{s,0}k + \mathbf{v}_p \cdot \mathbf{k} - i\gamma/2 \tag{2.21}$$

with the speed of sound (2.17) and the flow speed $\mathbf{v}_p = \hbar \mathbf{k}_p/m$ (directed along the x axis) are plotted as a dashed cyan line. Note that this form of the Doppler shift is only accurate for small values of the momentum k, in contrast to the case with no reservoir where it holds for any k.

While the dispersions shown in Fig. 2.8 are all dynamically stable, it is worth stressing that the presence of the reservoir can make a uniform flow at finite k_p dynamically unstable, as signaled by a positive imaginary part of the dispersion. With respect to panels (c-d) of Fig. 2.8, a slight increase of γ_{inc} and thus of the reservoir fraction, or of the flow velocity k_p will make the flow unstable by pushing the peaks in $\mathrm{Im}[\omega]$ above zero. Similar modulational instabilities in the presence of a reservoir have been discussed in (Wouters and Carusotto [2007], Bobrovska et al. [2014, 2017], Baboux et al. [2018].)

2.3.2 Spinorial model

The second step in order to obtain a correct modelization of our experiment is to consider the coupled dynamics of the polaritons in the two linear polarizations. The cavity used in the experiment has some intrinsic birifringence. In the linear polarization basis $|s\rangle, |f\rangle$, associated to the axis of the cavity, the Hamiltonian for the lower polariton (LP) branch reads

$$H_{\mathrm{bir}} = \int d^2r\, \hat{\psi}_s^\dagger \left(\omega_{\mathrm{LP}}(\hat{\mathbf{k}}) - \frac{\alpha}{2}\right) \hat{\psi}_s + \hat{\psi}_f^\dagger \left(\omega_{\mathrm{LP}}(\hat{\mathbf{k}}) + \frac{\alpha}{2}\right) \hat{\psi}_f, \tag{2.22}$$

where the LP band is taken in the parabolic approximation $\omega_{\mathrm{LP}}(\hat{\mathbf{k}}) = \omega_0^{LP} - \frac{\hbar}{2m}\nabla^2$, with m the effective polariton mass and the field operators $\hat{\psi}_s(\mathbf{r})$, $\hat{\psi}_f(\mathbf{r})$ destroy a boson with polarization s, f respectively at spatial position $\mathbf{r}$.

As it can be determined by reflectivity measurements using a weak polarized beam, the birefringence splitting is $\alpha \sim 0.1 \pm 0.05$ meV; in the core part of the experiment, the excitation laser is pumped with a linear polarization x rotated by an angle $\Theta \simeq -19°$ with respect to the s axis, i.e. we have

$$\begin{pmatrix} \hat{\psi}_s \\ \hat{\psi}_f \end{pmatrix} = \begin{pmatrix} \cos\Theta & \sin\Theta \\ -\sin\Theta & \cos\Theta \end{pmatrix} \begin{pmatrix} \hat{\psi}_x \\ \hat{\psi}_y \end{pmatrix}, \tag{2.23}$$

so that the kinetic part of the Hamiltonian in the $|x\rangle, |y\rangle$ linear polarization basis reads

$$H_{\mathrm{kin}} = \int d^2r \begin{pmatrix} \hat{\psi}_x^\dagger & \hat{\psi}_y^\dagger \end{pmatrix} \left[\omega_{\mathrm{LP}}(\hat{\mathbf{k}})\mathbb{I} + \frac{\alpha}{2}\begin{pmatrix} -\cos 2\Theta & -\sin 2\Theta \\ -\sin 2\Theta & \cos 2\Theta \end{pmatrix}\right] \begin{pmatrix} \hat{\psi}_x \\ \hat{\psi}_y \end{pmatrix}. \tag{2.24}$$

Using spin conservation, the polariton–polariton interaction is naturally written in the circular polarization basis $|\sigma_\pm\rangle = (|x\rangle \pm i|y\rangle)/\sqrt{2}$ as

$$\begin{aligned} H_{\mathrm{int}} &= \frac{1}{2}\int d^2r \left[\, g_{\mathrm{T}}(\hat{\psi}_+^\dagger \hat{\psi}_+^\dagger \hat{\psi}_+ \hat{\psi}_+ + \hat{\psi}_-^\dagger \hat{\psi}_-^\dagger \hat{\psi}_- \hat{\psi}_-) + 2g_{\mathrm{S}} \hat{\psi}_+^\dagger \hat{\psi}_-^\dagger \hat{\psi}_+ \hat{\psi}_- \right] = \\ &= \frac{1}{2}\int d^2r \left[\, \frac{g_{\mathrm{T}} + g_{\mathrm{S}}}{2} \hat{\psi}_x^\dagger \hat{\psi}_x^\dagger \hat{\psi}_x \hat{\psi}_x + \frac{g_{\mathrm{T}} - g_{\mathrm{S}}}{2} \hat{\psi}_x^\dagger \hat{\psi}_x^\dagger \hat{\psi}_y \hat{\psi}_y + g_{\mathrm{T}} \hat{\psi}_x^\dagger \hat{\psi}_y^\dagger \hat{\psi}_x \hat{\psi}_y + x \leftrightarrow y \right] \end{aligned} \tag{2.25}$$

where $\hat{\psi}_\pm(\mathbf{r})$ denote the field operators for $\sigma_\pm$ circular polarizations respectively. In the simulations we take the values $g_{\mathrm{S}}/g_{\mathrm{T}} \sim -0.1$, $g_{\mathrm{T}} > 0$, in agreement with what discussed at the beginning of this Chapter.

The full vectorial Hamiltonian for the polariton field then reads

$$H_0 = H_{\mathrm{kin}} + H_{\mathrm{int}} + \int d^2r \left[F(\mathbf{r},t)\hat{\psi}_x^\dagger(\mathbf{r}) + F^*(\mathbf{r},t)\hat{\psi}_x(\mathbf{r})\right] \tag{2.26}$$

where $F(\mathbf{r},t) = F_0 e^{i\mathbf{k}_{\mathrm{p}}\cdot\mathbf{r} - i\omega_{\mathrm{p}}t}$ is the laser pump. Notice that in the experiment only the x-polarization component of the polariton field is pumped.

Considering also the coupling to a dark excitonic reservoir (assumed as a mixture of both polarizations), the generalized Gross-Pitaevskii equations read

$$\begin{aligned} i\partial_t\psi_x = &\left[\omega_{\mathrm{LP}}(\hat{\mathbf{k}}) - \frac{\alpha}{2}\cos(2\Theta) + \frac{g_{\mathrm{T}} + g_{\mathrm{S}}}{2}|\psi_x|^2 + g_{\mathrm{T}}|\psi_y|^2 + g_{\mathrm{R}}n_{\mathrm{R}} - i\frac{\gamma_{\mathrm{c}} + \gamma_{\mathrm{in}}}{2}\right]\psi_x - \\ &- \frac{\alpha}{2}\sin(2\Theta)\,\psi_y - \frac{g_{\mathrm{T}} - g_{\mathrm{S}}}{2}\psi_x^*\psi_y^2 + F \end{aligned} \tag{2.27}$$

$$i\partial_t\psi_y = \left[\omega_{\mathrm{LP}}(\hat{\mathbf{k}}) + \frac{\alpha}{2}\cos(2\Theta) + \frac{g_{\mathrm{T}}+g_{\mathrm{S}}}{2}|\psi_y|^2 + g_{\mathrm{T}}|\psi_x|^2 + g_{\mathrm{R}}n_{\mathrm{R}} - i\frac{\gamma_{\mathrm{c}}+\gamma_{\mathrm{in}}}{2}\right]\psi_y - \\ - \frac{\alpha}{2}\sin(2\Theta)\,\psi_x - \frac{g_{\mathrm{T}}-g_{\mathrm{S}}}{2}\psi_y^*\psi_x^2 \tag{2.28}$$

$$\partial_t n_{\mathrm{R}} = -\gamma_{\mathrm{R}}n_{\mathrm{R}} + \gamma_{\mathrm{in}}(|\psi_x|^2 + |\psi_y|^2). \tag{2.29}$$

Notice that the co-linear-polarization coupling g_T is larger than the cross-linear-polarization coupling $\frac{g_{\mathrm{T}}+g_{\mathrm{S}}}{2}$; this fact enhances the competition between the ψ_x and ψ_y fluids.

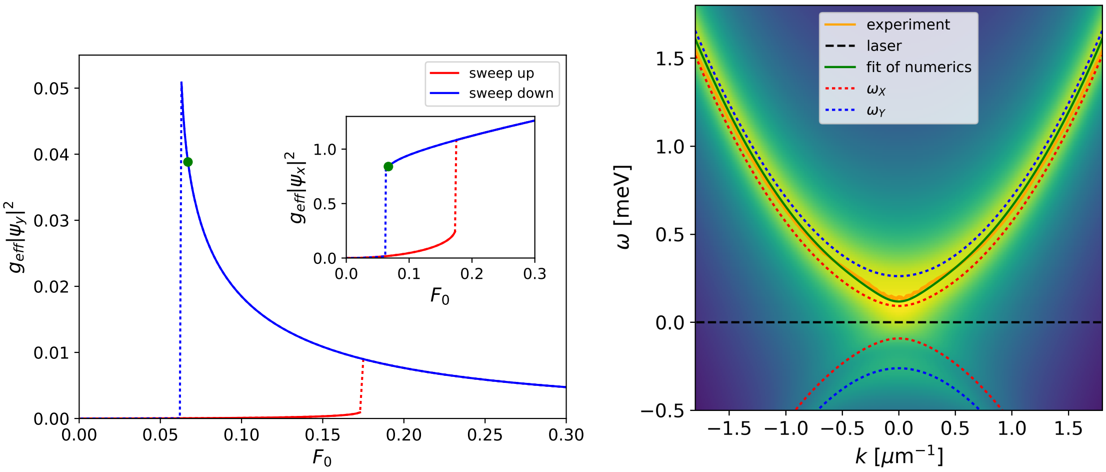

Figure 2.11: *Collective physics of spinorial fluid* (left) Bistable behaviour $|\psi_y|^2$ for a homogeneous system. In blue the upper branch, in red the lower one; the green spot corresponds to the working point where the dispersion of the left panel is computed. We remark the decreasing behaviour above threshold of the cross–polarized component. Inset: the same for the co–polarized field, which closely resembles the result of the scalar theory when $\alpha \sin\Theta$ is small. The densities are multiplied by g_{eff} so that in the inset the jump occurs for a blueshift close to Δ. (right) Numerically computed dispersion according to Eq. (2.40). Notice that the signal lies in between the two poles ω_x, ω_y, and this partially explains the fact that, even though the experimental dispersion is quite gapped, it looks linearly shaped.

For negative enough detuning Δ, the steady state solution $\{\psi_x^s, \psi_y^s, n_{\mathrm{R}}^s\}$ of Eqs. (2.27-2.29) displays a bistable behaviour for ψ_x^s as a function of the pump intensity $|F_0|^2$, similar to the well-known solution in the single-polarization case; looking at the cross-polarized density ψ_y^s instead, for such small angle Θ the upper branch of the hysteresis is decreasing, due to the competing interactions with ψ_x^s. This phenomenology is depicted on the left side of Fig. 2.11.

On top of the steady state, one can compute the Bogoliubov excitations in the usual way, by diagonalizing the linearized problem

$$i\partial_t\delta\vec{\psi}(\mathbf{r},t) = \hat{\mathscr{L}}(\hat{\mathbf{k}})\delta\vec{\psi}(\mathbf{r},t) \tag{2.30}$$

where $\delta\vec{\psi} = (\delta\psi_x, \delta\psi_x^*, \delta\psi_y, \delta\psi_y^*, \delta n_{\mathrm{R}})$ is the fluctuation vector. The Bogoliubov spectrum then consists of five eigenbranches $\mathrm{Re}\omega(k)$ related by particle-hole symmetry. The right panel of figure 2.11 reports (on top of the emission intensity that will be explained below) the five eigenbranches, calculated with the parameters of WPA and a pump intensity $|F_0|^2$ larger by 3% than the intensity for having the acoustic dispersion. Red (blue) dots correspond to a predominantly x (y) polarized character, respectively; the reservoir-like branch has zero real frequency.

One important feature visible in the fact that the y particle branch lies at higher energies than the x one. This can be elucidated by turning off the birefringence; for $\alpha = 0$ the steady state features $\psi_y^s = 0$, while ψ_x^s is given by the obtained according to the procedure above, with renormalized nonlinear coupling strength $g_{\mathrm{eff}} = \frac{g_{\mathrm{T}}+g_{\mathrm{S}}}{2} + \frac{g_{\mathrm{R}}\gamma_{\mathrm{in}}}{\gamma_{\mathrm{R}}}$. Also, the Bogoliubov equations for the excitations for the condensate with y polarization are decoupled from those of the condensate with x polarization and the reservoir:

$$i\partial_t\delta\psi_x = \left[-\Delta - \frac{\hbar}{2m}\nabla^2 + 2\bar{g}|\psi_x^s|^2 + g_{\mathrm{R}}n_{\mathrm{R}}^s - i\frac{\bar{\gamma}}{2}\right]\delta\psi_x + \bar{g}{\psi_x^s}^2\delta\psi_x^* + g_{\mathrm{R}}\psi_x^s\delta n_{\mathrm{R}} \tag{2.31}$$

$$\partial_t \delta n_{\mathrm{R}} = -\gamma_{\mathrm{R}} \delta n_{\mathrm{R}} + \gamma_{\mathrm{in}} (\psi_x^s \delta\psi_x^* + \psi_x^{s\,*} \delta\psi_x), \tag{2.32}$$

and

$$i\partial_t \delta\psi_y = \left[-\Delta - \frac{\hbar}{2m}\nabla^2 + g_{\mathrm{T}} |\psi_x^s|^2 + g_{\mathrm{R}} n_{\mathrm{R}}^s - i\frac{\bar{\gamma}}{2} \right] \delta\psi_y - g_{\mathrm{d}} \psi_x^{s\,2} \delta\psi_y^*, \tag{2.33}$$

where $\Delta = \omega_{\mathrm{p}} - \omega_{LP}^0$, $\bar{g} = (g_{\mathrm{T}} + g_{\mathrm{S}})/2$, $g_{\mathrm{d}} = (g_{\mathrm{T}} - g_{\mathrm{S}})/2$ $\bar{\gamma} = (\gamma_{\mathrm{c}} + \gamma_{\mathrm{in}})$. The corresponding 5×5 Bogoliubov matrix $\mathscr{L}(\hat{\mathbf{k}})$ separates into two block matrices, namely a $3{\times}3$ part for the x-polarized condensate and reservoir, and a 2×2 part for the y-polarized condensate. In the former, in the case $\Delta = \hbar\omega_{\mathrm{BS}}$, where now $\hbar\omega_{\mathrm{BS}} = \bar{g}|\psi_x|^2 + g_{\mathrm{R}} n_{\mathrm{R}}$, the excitation spectrum has the linear gapless dispersion discussed above, with speed of sound

$$c_x^2 = \frac{\hbar\omega_{\mathrm{BS}}}{m} - \frac{\bar{\gamma}}{(\bar{\gamma} - 2\gamma_{\mathrm{R}})} \frac{g_{\mathrm{R}} n_{\mathrm{R}}}{m}, \tag{2.34}$$

holding for $c_x^2 > 0$. In the slow reservoir limit most relevant here $\gamma_{\mathrm{R}} \ll \bar{\gamma} = (\gamma_{\mathrm{c}} + \gamma_{\mathrm{in}})$, we obtain $c_x^2 = \hbar\omega_{\mathrm{BS}}/m - g_{\mathrm{R}} n_{\mathrm{R}}/m = \bar{g}|\psi_x^s|^2/m$.

In the y-polarization sector the Bogolubov matrix reads

$$\mathscr{L}(\mathbf{k})\big|_y = \begin{pmatrix} \eta_y(\mathbf{k}) - i\frac{\bar{\gamma}}{2} & g_{\mathrm{d}} \psi_x^{s\,2} \\ -g_{\mathrm{d}} \psi_x^{s\,*2} & -\eta_y(-\mathbf{k}) - i\frac{\bar{\gamma}}{2} \end{pmatrix}, \tag{2.35}$$

where $\eta_y(\mathbf{k}) = -\Delta/\hbar + \hbar k^2/2m + g_{\mathrm{T}}|\psi_x^s|^2 + g_{\mathrm{R}} n_{\mathrm{R}}$. The condition for having gapless Bogoliubov excitations in the above equation is $-\Delta + g_{\mathrm{T}}|\psi_x^s|^2 + g_{\mathrm{R}} n_{\mathrm{R}}^s = g_{\mathrm{d}}|\psi_x^s|^2$. Interestingly, this coincides with the condition $\Delta = \hbar\omega_{\mathrm{BS}}$ required for having a gapless x branch (this is true only for $\alpha = 0$). At low momenta the dispersion relation of the y branch reads $\omega_y^{\pm}(\mathbf{k}) = \pm c_y k - i\bar{\gamma}/2$, with

$$c_y^2 = \frac{g_{\mathrm{d}}(\mu_y - g_{\mathrm{R}} n_{\mathrm{R}})}{m} = \frac{g_{\mathrm{T}} - g_{\mathrm{S}}}{2} \frac{|\psi_x^s|^2}{m} \tag{2.36}$$

where $\mu_y = g_{\mathrm{T}}|\psi_x^s|^2 + g_{\mathrm{R}} n_{\mathrm{R}}$. Notice that our choice of parameters $g_{\mathrm{T}} > 0$, $g_{\mathrm{S}}/g_{\mathrm{T}} = -0.1$ implies that the y branch of the phonon dispersion lies at higher energy than the x branch for all $k \neq 0$, which implies that $c_y > c_x$ and the y particle branch lies above the x branch. For continuity, when a small α is turned on, the y branch becomes gapped.

2.3.3 Modelling the photoluminescence

Having discussed the poles of the Bogoliubov matrix, we will now see how to numerically predict the photoluminescence, which is the main observable of our experiment.

As demonstrated in Fig. S3 of (Stepanov et al. [2019]), the energy resolved emitted intensity is perfectly consistent with a Boltzmann distribution at $T = 30$ K. This observation suggests that the excitation mechanism giving rise to the EPL consists of thermal acoustic phonons scattering polaritons from the injection state to Bogoliubov quasi-particle states.

We describe the coupling of polaritons to acoustic phonons by via the Frolich Hamiltonian (Piermarocchi et al. [1996])

$$H_{\mathrm{pol-phon}} = \sum_{\mathbf{q},q_z} G_{\mathbf{q},q_z} (b_{\mathbf{q},q_z} - b^{\dagger}_{-\mathbf{q},-q_z}) \rho_{\mathbf{q}} \tag{2.37}$$

where $G_{\mathbf{q},q_z}$ is the acoustic phonon-polariton coupling strength taking into account the anisotropy due to the presence of the quantum well confinement in the z direction (Piermarocchi et al. [1996], **?**), $b_{\mathbf{q},q_z}$ is the phononic field operator and $\rho_{\mathbf{q}}$ is the density fluctuation of the polariton condensate with cavity in-plane momentum $\mathbf{q}$. The origin of this coupling stems from the fact that, in a Bohr-Oppenheimer view of the electronic wavefunction, the exciton line depends on the unit length of the lattice cell of the material: the phonon field describes the displacement field of the ions of the lattice, so that the volume variation of a unit cell it's given by the divergence of the field (this in particular entails $G_{\mathbf{q},q_z} \to 0$ for $\mathbf{q}, q_z \to 0$).

The above Hamiltonian yields a stochastic phonon field in the Gross-Pitaevskii equation acting on both polarization components $\sigma = x, y$ of the polariton condensate according to $(\sum_{\mathbf{q}}[\mathcal{T}(\mathbf{q},t) + \mathcal{T}^*(-\mathbf{q},t)]e^{i\mathbf{q}\cdot\mathbf{r}})\psi_\sigma(\mathbf{r})$, where

$$\langle\langle \mathcal{T}^*(\mathbf{q},t)\mathcal{T}(\mathbf{q}',t')\rangle\rangle_{ph} = \sum_{q_z} |G_{\mathbf{q},q_z}|^2 \delta_{\mathbf{q},\mathbf{q}'} n(\omega_{\mathbf{q},q_z}) \delta(t-t') = \int \frac{d\omega}{2\pi} e^{-i\omega(t-t')} S(\mathbf{q},\omega), \tag{2.38}$$

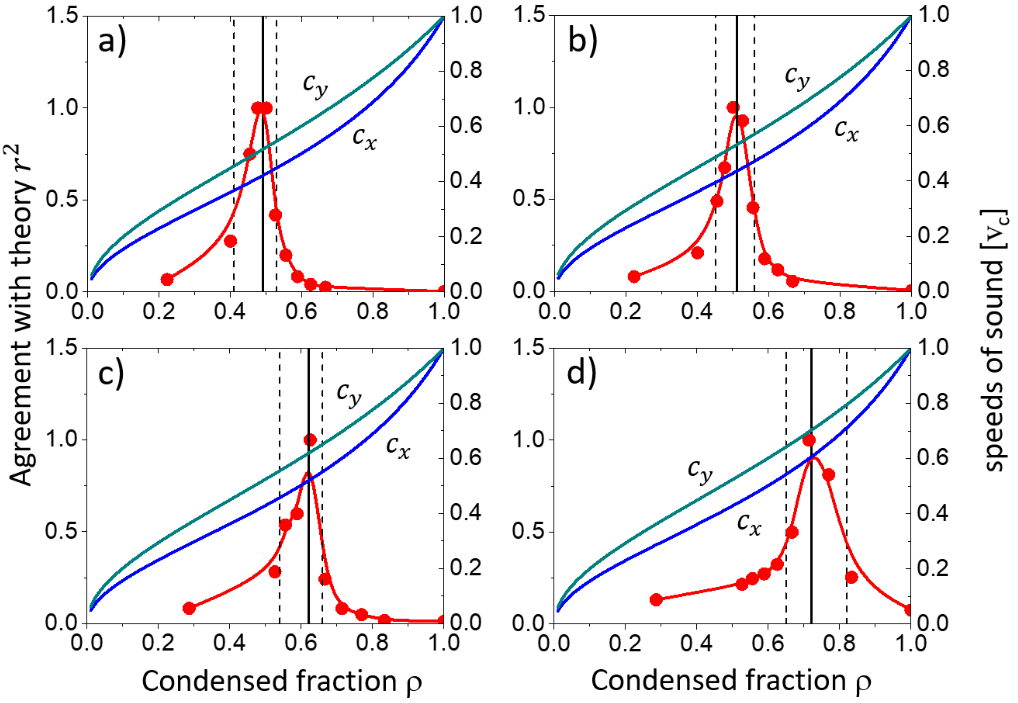

Figure 2.12: *Coherent versus reservoir fractions by quantitative comparison between experiment and theory* - Agreement between the measured dispersion relation and the full vectorial theory, quantified as $r^2(\rho)$ =min$(R^2)/R^2(\rho)$ (red symbols), versus the condensate fraction $\rho = n_c/(n_\mathrm{R}+n_c)$ for WPA.2 (a),WPA.3 (b), WPB.2 (c) and WPB.3 (d). The red solid line is a guide for the eye. The right axis show the calculated speed of sounds of the two cross polarized excitations c_x/v_c (blue line) and c_y/v_c (blue green line) versus ρ, in the limit where $n_y = 0$ (see text).

with $\langle\langle\cdot\cdot\cdot\rangle\rangle_{ph}$ being the average over the noise realizations, $n(\omega_{\mathbf{q},q_z}) = 1/(e^{\hbar\omega_{\mathbf{q},q_z}/k_\mathrm{B}T}-1)$, T the temperature and $\omega_{\mathbf{q},q_z}$ the acoustic phonon dispersion. The sum over q_z appears because the exciton is confined in the QW so that k_z is not a good quantum number and it couples to phonons of any q_z; in particular, the q_z dependence of the coupling matrix is determined by the overlap between the exciton and phonon field and becomes vanishing for $q_z \gg 2\pi/L_{QW}$. The use of a constant power spectral density $S(\mathbf{q},\omega)$ is motivated in a high temperature approximation.

Then, within the linear response theory we treat the field $\mathcal{T}(\mathbf{q},\omega)$ to order one in perturbation theory and calculate the linear response of the polariton field to this stochastic phononic field. The field amplitude is obtained as $\delta\vec{\psi} = (\delta\psi_x(\mathbf{k}), \delta\psi_x^*(-\mathbf{k}), \delta\psi_y(\mathbf{k}), \delta\psi_y^*(-\mathbf{k}), \delta n_\mathrm{R}(\mathbf{k}))$

$$\delta\vec{\psi} = [\omega - \hat{\mathscr{L}}(\mathbf{k})]^{-1}\delta\vec{F}, \tag{2.39}$$

where the stochastic drive is denoted $\delta\vec{F} = (\delta F_x(\mathbf{k},\omega), -\delta F_x^*(-\mathbf{k},-\omega), \delta F_y(\mathbf{k},\omega), -\delta F_y^*(-\mathbf{k},-\omega), 0)$. After averaging over the random realizations of the phonon field and with the definition $\chi_{ij}(\mathbf{k},\omega) = \left[\frac{1}{\omega - \hat{\mathscr{L}}(\mathbf{k})}\right]_{ij}$, the field intensity reads

$$\langle\langle|\delta\psi_y(\mathbf{k},\omega)|^2\rangle\rangle_{ph} = |\chi_{31}\psi_x^s - \chi_{32}\psi_x^{s*} + \chi_{33}\psi_y^s - \chi_{34}\psi_y^{s*}|^2 \; S_\mathrm{ph}(\mathbf{k},\omega) \tag{2.40}$$

where the phonon density of states S_ph is taken in this work as constant. Finally, in order to model the effect of the finite pump spot and of the filter, we multiply the polariton field by a spatial filter function f corresponding to a circular hole of diameter $35\mu m$, $\psi_y^{out}(\mathbf{r},t) = f(\mathbf{r})\psi_y(\mathbf{r},t)$; in the end, the measured Fourier space intensity is $I(\mathbf{k},\omega) = \int d\mathbf{k}'|f(\mathbf{k}-\mathbf{k}')|^2\langle\langle|\delta\psi_y(\mathbf{k}',\omega)|^2\rangle\rangle_{ph}$. $I(\mathbf{k},\omega)$ is our actual experimental observable. We thus apply to it the same numerical analysis as for the experimental one: we fit it with a single Lorentzian lineshape, in order to obtain a single theoretical dispersion relation (two if we accounts for positive and negative energy branches), to be compared with the experimental one.

The result of this procedure is shown as a black line in Figure 2.11.b. It is apparent that the peak of the emitted signal (green solid line) falls in between the poles of the x-like and y-like quasi-particles (blue and red dotted lines). This accidentally results in a V-like shape of the observed dispersion, even though we are not so close to the acoustic point. Another interesting features is that the ghost emission is very weak here because of a destructive interference of the contributions coming from the x and y poles.

The most important observation though is that with this model we are able to closely fit the experimental data. Once the reservoir decay rate and exciton-polariton coupling are fixed according to $\gamma_R = 1.6\mu\text{eV}$ and $g_R = 2g_T$, the relevant fitting parameter is γ_{in} (notice that the numerical results depend only mostly depend on the product $g_R\gamma_{in}$ while are only weakly sensitive on g_R, γ_{in} individually).

The comparison between the theoretical dispersion relations and the measured ones is plotted quantitatively in Figure 2.12 using $r^2(\rho) = \min(R^2)/R^2(\rho)$, where the normalized deviation is $R^2(\rho) = \sum_i[\omega_{\text{exp}}(k_i) - \omega_{\text{th}}(\rho, k_i)]^2 / \sum_i \omega_{\text{exp}}(k_i)^2$. Here, the results are organized as a function of the coherent fraction

$$\rho = \frac{n_c}{n_\text{R} + n_c} = \frac{\gamma_\text{R}}{\gamma_\text{in} + \gamma_\text{R}}, \tag{2.41}$$

where $n_c = n_x + n_y = |\psi_x^s|^2 + |\psi_y^s|^2$ is the coherent density and γ_in is the actual fit free parameter. The closer r^2 is to 1, the better the agreement. The full width at half maximum of $r^2(\rho)$ provides an estimate of its 1σ-confidence interval. The line connecting the red dots in Fig. 2.12 is a guide for the eye. The thus determined confidence intervals has been used in Fig. 2.4 above, where the theoretical dispersion plots is obtained by plotting the two dispersion relations calculated at the two confidence interval boundaries, and by coloring the area that they delimit.

This analysis also gives an estimate of the two speeds of sound that characterize the two cross-polarized Bogoliubov branches at the sonic point of the hysteresis. In the simplifying assumption that $n_y = 0$, i.e $\rho = n_x/(n_x + n_\text{R})$, they have the analytical expression given in eq.(2.34) and eq.(2.36). The results are shown in Figure 2.12 (right axis), where the speeds of sound c_x and c_y normalized to the critical velocity $v_\text{c} = \sqrt{\hbar\omega_\text{BS}/m}$ are plotted alongside $r^2(\rho)$.

Knowing approximatively ρ hence the fraction of blue-shift to be attributed to coherent polariton-polariton interactions, which in our sample is of the order of 30%, and carefully calibrating a count of the number of polaritons in the microcavity, it is possible to have a reliable estimate of the polariton-polariton coupling constant. In our experiment we reported the theoretically reasonable value of $gN_{QW} = 8 \pm 2\mu\text{eV}\ \mu\text{m}^2$ (as already mentioned, a plot summarizing several measurements of gN_{QW} from different groups has been provided by Estrecho et al. [2019]).

In conclusion, in this Section we have predicted how the presence of an incoherent excitonic reservoir affects the collective excitations of a resonantly injected polariton fluid. In particular, while it provides a contribution to the Hartree energy as it can be observed in the blueshift, the excitonic degrees of freedom are too slow to partecipate in the finite frequency dynamics and thus the speed of sound is determined only by the polariton-polariton interaction energy. Once also the interplay of the two linear polarization and the response function corresponding to the photoluminescence are properly kept into account, the experimental curves by Stepanov et al. [2019] can be reproduced assuming a polariton-reservoir Hartree energy of the same order of the one due to polariton-polariton interactions; the characteristics of the reservoir are expected to depend very strongly on the particular sample. The next natural question is to what extent the reduction of the speed of sound affects superfluid properties.

2.4 Superfluidity in the presence of an incoherent reservoir*

(this Section mostly builds on material contained in Section V from [Amelio et al., 2020b])

In Sec.1.4 we have seen that in the absence of reservoir, the generalized Gross-Pitaevskii equation (1.27) has specific invariance properties under Galilean boosts, which entail that the superfluidity properties must be then the same in the two cases of a defect moving through a polariton fluid at rest and of a moving polariton fluid hitting a static defect: these two configurations represent in fact the same process seen in two different Galilean frames. Correspondingly, since the (not invariant but) covariant coherent pump does not explicitely enter the linearized Bogoliubov calculation, the complex-valued dispersion $\omega(\mathbf{k})$ simply gets Doppler-shifted $\omega(\mathbf{k}) \to \omega(\mathbf{k}) + \mathbf{k}\cdot\mathbf{v}$ when going to a reference frame moving at speed $\mathbf{v}$.

The situation is completely different in the presence of an incoherent reservoir, as described by the generalized dynamics of Eqs.(2.4-2.5). This latter, in fact, defines a privileged frame of

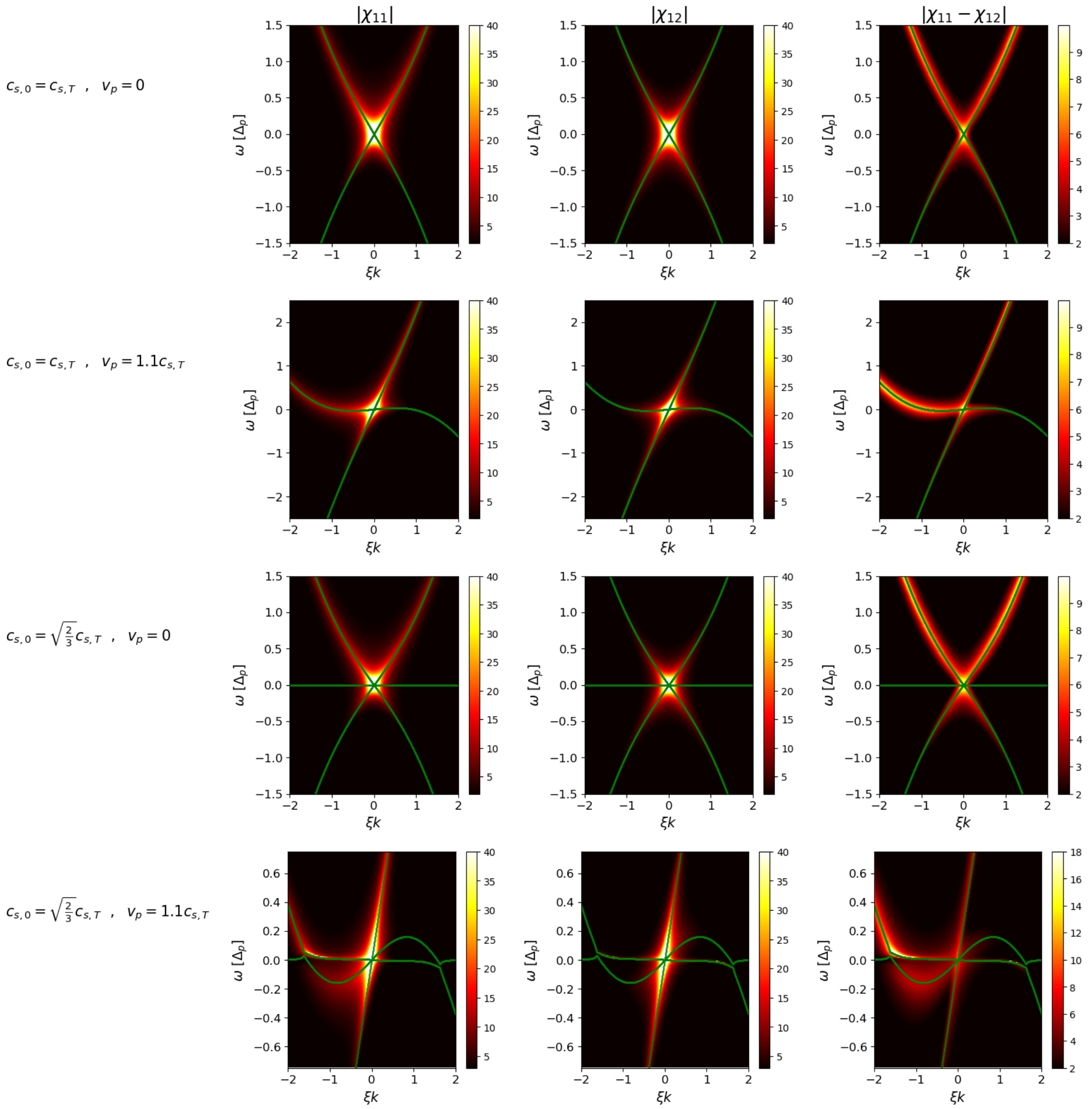

Figure 2.13: From left to right: color plots of $|\chi_{11}|, |\chi_{12}|, |\chi_{11}-\chi_{12}|$ as functions of (k,ω), where the dynamic response function is defined as $\chi(\mathbf{k},\omega)=\frac{1}{\omega-\mathscr{L}(\mathbf{k})}$. Physically, $\chi_{11}(\mathbf{k},\omega)$ is the response to a probe at $(\mathbf{k}_p+\mathbf{k},\omega_p+\omega)$ measured at the probe momentum and frequency, while χ_{12} describes the response in a four-wave mixing setup; finally, $\chi_{11}-\chi_{12}$ was considered above in Sec. 2.3.3 and represents the susceptibility to scattering with phonons (or to any real field that couples to the polariton density). From top to bottom: without reservoir and $k_p=0$, without reservoir and $v_p=1.1c_{s,T}$, with reservoir and $k_p=0$, with reservoir and $v_p=1.1c_{s,T}$. The reservoir parameters are $\gamma_R=2\gamma_{inc}=0.08\,\gamma$. In particular, looking at the last column, it is clear that having both $\mathbf{k}_p\neq 0$ and a reservoir allows for having different luminescence (as generated by phononic white noise) on the left and right particle branches, while the colorplot is only Doppler shifted (shear mapping) if the reservoir is absent.

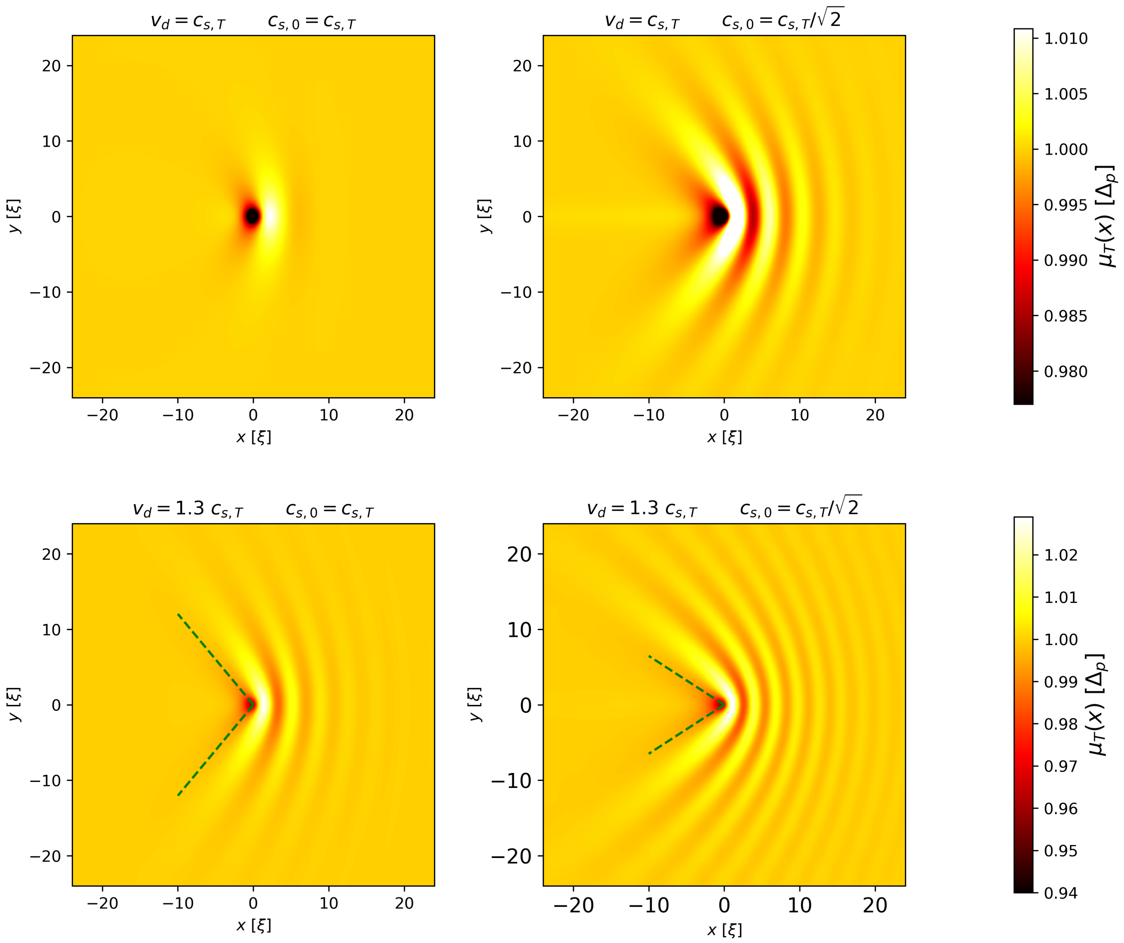

Figure 2.14: Density modulation induced by a moving defect in the absence (left) and in the presence (right) of an incoherent reservoir. The total blue-shift μ_T is the same in all panels. The polariton fluid is at rest $k_p = 0$ and the pump frequency is tuned at the resonant point $\Delta_p = \mu_T$. In the upper panels, the defect speed is chosen in the vicinity of the critical speed for superfluidity in the absence of incoherent reservoir, $v_d = c_{s,T}$. In the lower panels, the defect speed is larger $v_d = 1.3\,c_{s,T}$. The dashed green lines in the lower panels indicate the Mach cone of angle 2α expected from the chosen values of the flow v_d and sound (2.17) speeds, $\sin\alpha = c_{s,0}/v_d$. Reservoir parameters are close to the ones estimated in (Stepanov et al. [2019]), $g_R = 2g$, $\gamma_R = 2\gamma_{inc} = 0.08\,\gamma$. For thse values, the contributions of the polaritons and the incoherent reservoir to the blueshift are equal, $g_R n_R = g n_0 = \mu_T/2$.

reference linked to the underlying semiconductor cavity structure. Such a feature is visible by comparing the Bogoliubov spectra shown in the left and right panels of Fig.2.8: even though the total blue-shift is the same in the two cases, the dispersions are markedly different in both the real and the imaginary parts. That not only the poles of the quasi-particles but also their nature is affected by the breaking of the Galilean invariance is apparent also in Fig. 2.13, where we plot three different response functions in the four cases with and without the incoherent reservoir and for a fluid at rest or in motion. When a polariton fluid is considered in the absence of reservoir, Galilean invariance ensures that the physical susceptibility of a fluid at rest (first row) gets Doppler shifted when setting the fluid into motion (second row). Notice that the Doppler shift corresponds to a $k-$dependent translation or *shear mapping* and not to a rigid rotation, so that one of the branches appears broader, but the point is that the “pixels” are moved but do not change their color (p.e. the peaks at $\pm k$ reach the same maximum). In the plots in the last row, which refer to the case with a resevoir, the left and right particle branches have different shapes and luminosity, which is only possible because Galilean invariance is broken. In particular, in the very last plot, which mimicks an experiment where Bogoliubov excitations are generated by a phononic white noise, the particle branch is very bright in proximity of the intersection with $\omega = 0$. As mentioned

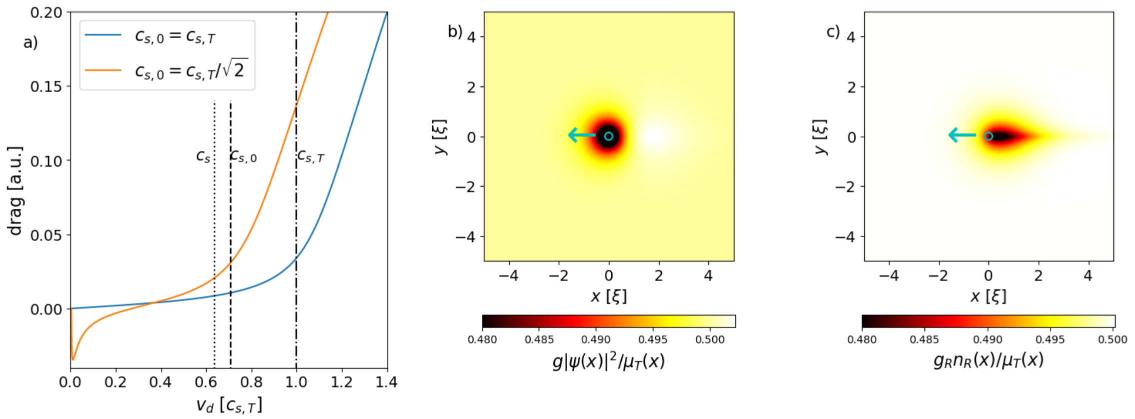

Figure 2.15: Critical speed for superfluidity in the presence of a reservoir, for a small and shallow defect moving in a polariton fluid pumped at the sonic point $\Delta_p = \mu_T$ and at rest $k_p = 0$. (a) Drag force as a function of the defect velocity v_d in the absence (blue) and in the presence (orange) of the incoherent reservoir. The force is here renormalized by the effective coupling $g_{\text{eff}} F_d$, so to have a fair comparison of the two cases with and without reservoir. The vertical lines confirm that in the former case the critical speed is at $c_{s,T}$, while in the latter case it is at $c_{s,0}$. An explanation for the negative drag at small v_d is provided in panels (b,c) where $v_d = 0.02 c_{s,T}$ is taken. Panel (b) shows the polariton-induced component to the blueshift $g|\psi(x)|^2$. Panel (c) shows the incoherent reservoir contribution $g_R n_R(x)$. The defect consists of a gaussian perturbation indicated in the plot by the cyan circle of radius three times its width. The depletion of the (slow) reservoir density that it leaves behind it is partly filled by the (faster) polariton. Same parameters as in the previous figures, namely $\hbar\gamma = 0.2\mu_T$, $g_R = 2g$, $\gamma_R = 2\gamma_{inc} = 0.08\,\gamma$, so that $c_{s,0} = c_{s,T}/\sqrt{2}$.

in the previous Section, in the presence of a reservoir the imaginary part of the dispersion can even become positive, signaling a modulational instability, analogously to the case of incoherently driven fluids (Wouters and Carusotto [2007], Bobrovska et al. [2014, 2017], Baboux et al. [2018]).

In Fig.2.14, we illustrate this breaking of Galilean invariance by looking at the effect of the incoherent reservoir on the density modulation pattern generated by a defect in motion through a fluid at rest. As we expected and explicitly verified by numerical integration of the Gross-Pitaevskii equation (2.4-2.5), a defect moving with constant velocity $\mathbf{v}_d$ in a fluid at rest with respect to the semiconductor substrate generates a pattern which is stationary in the frame of reference of the defect.

Therefore, within linear response to a shallow defect, it is possible to solve for the field perturbation in this frame by using the technique illustrated in Eq. (1.35). Since the reservoir equation in the defect frame[3] reads

$$\partial_t n_R = -\mathbf{v}_d \cdot \nabla n_R - \gamma_R n_R + \gamma_{inc}|\psi|^2 \ , \tag{2.42}$$

the $\omega = 0$ condition discussed in Sec.2.3 allows for elimination of the reservoir via a momentum-dependent effective coupling

$$g_{\text{eff}}(\mathbf{k}) = g + \frac{\gamma_{inc}}{-i\mathbf{v}_d \cdot \mathbf{k} + \gamma_R} g_R \ . \tag{2.43}$$

Notice that this procedure of imposing $\omega = 0$ in the defect frame can be equivalently implemented in the lab frame by solving for $\omega = \mathbf{v}_d \cdot \mathbf{k}$; this is proven by expressing the defect potential as $\delta V_{def}(\mathbf{x} - \mathbf{v}_d t) = \int d\mathbf{k} d\omega \ \delta(\omega - \mathbf{v}_d \cdot \mathbf{k}) \ \delta V_{def}(\mathbf{k}) e^{i\mathbf{k}\cdot\mathbf{x} - i\omega t}$, and similarly for the Ansatz of the field and reservoir.

For a fully coherent polariton fluid in the absence of a reservoir, the Galilean invariance holds and the physics only depends on the relative velocity of the fluid and the defect. As a result, the left panels of Fig. 2.14 equivalently represent the two cases of a fluid flowing against a static defect or of a moving defect in a fluid at rest.

---

[3] Remember that first-order equations for scalar quantities require total time derivatives (also called convective derivatives) in order to be Galileo invariant, like the one for density in the incompressible Euler continuity equation.

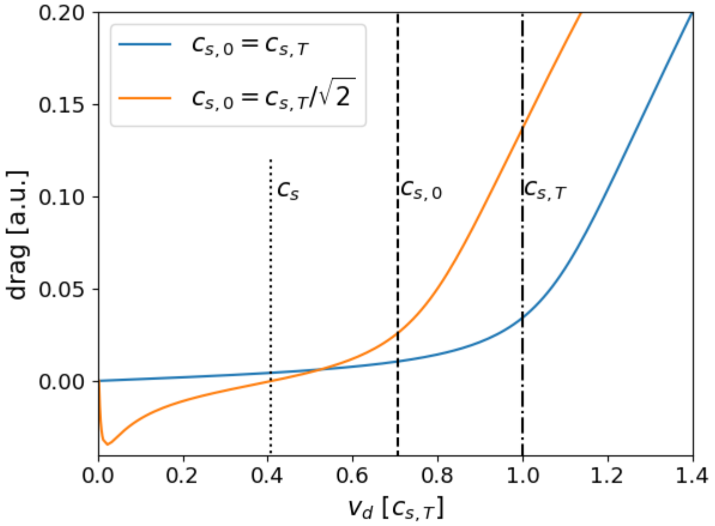

Figure 2.16: *Critical velocity versus speed of sound.* The speed $c_{s,0}$ turns out to be the critical speed when superfluidity is considered for a moving defect, e.g. by computing the drag force (solid orange line). For comparison, the blue line shows the drag force for a purely coherent fluid without reservoir at the same μ_T. The parameters of the fluid are the same as in Fig. 2.9

Summary of the characteristic velocities		
$c_{s,T}$	$mc^2_{s,T} = \mu_T$ (total blueshift)	Critical speed for a stationary flow against a static defect at $\omega = 0$
$c_{s,0}$	$mc^2_{s,0} = gn_0$ (coherent component only)	Propagation speed of dynamical excitations at $\gamma_R \ll \lvert\omega + i\gamma/2\rvert \ll \mu_T$. Critical speed for a moving defect
c_s	$mc^2_s = \mu_T + \frac{\gamma}{2\gamma_R - \gamma} g_R n_R$ (slope of dispersion at $k = 0$)	Propagation speed of very low frequency dynamical excitations up to $\lvert\omega + i\gamma/2\rvert \approx \gamma_R$

Table 2.1: Summary of the three characteristic velocities introduced in the text. From left to right, the three columns indicate the notation, the mathematical definition, the physical meaning.

On the basis of the discussion in the previous sections, it is natural to expect that the situation be completely different in the presence of an incoherent reservoir, which sets a privileged reference frame linked to the semiconductor matrix. To start with, a pattern identical to the fully coherent case is found for a static defect via the renormalized coupling (2.6), as long as the total blueshift is the same and no dynamical instabilities develop (Amelio and Carusotto [2020a]). Instead, when it is the defect to move in a polariton fluid at rest in the presence of a reservoir. the density modulation pattern is shown in the right panels of Fig. 2.14. These panels are plotted in the experimentally relevant $\gamma_R \ll \gamma$ regime for the same values of the speed $\mathbf{v}_d$ and the total interaction energy μ_T used in the left panels. It is apparent that the critical speed is strongly reduced, as expected from the Bogoliubov dispersion discussed in Sec.2.3. Moreover, the shape of the density modulation profile shows a clear Mach cone of angle 2α with $\sin\alpha \simeq c_{s,0}/v_d$.

A more quantitative insight on the critical speed can be obtained looking at the plot of the friction force as a function of the defect speed for a polariton fluid at rest shown in Fig.2.15. The force is evaluated using (1.40) under the assumption that the defect only interacts with the coherent polaritons. Both in the absence (blue line) and in the presence (orange) of the reservoir, the friction force displays a clear threshold behaviour, losses being as usual Berceanu et al. [2012] responsible for a smoothening of the threshold. In contrast to the 1D case of Fig.1.7, in the high-speed limit the force tends to the asymptotically linear dependence on v_d predicted by Astrakharchik and Pitaevskii [2004] in 2D.

As expected, the position of the threshold occurs at a markedly lower speed in the presence of the reservoir, at a value consistent with the effective speed of sound $c_{s,0}$. The fact that the critical

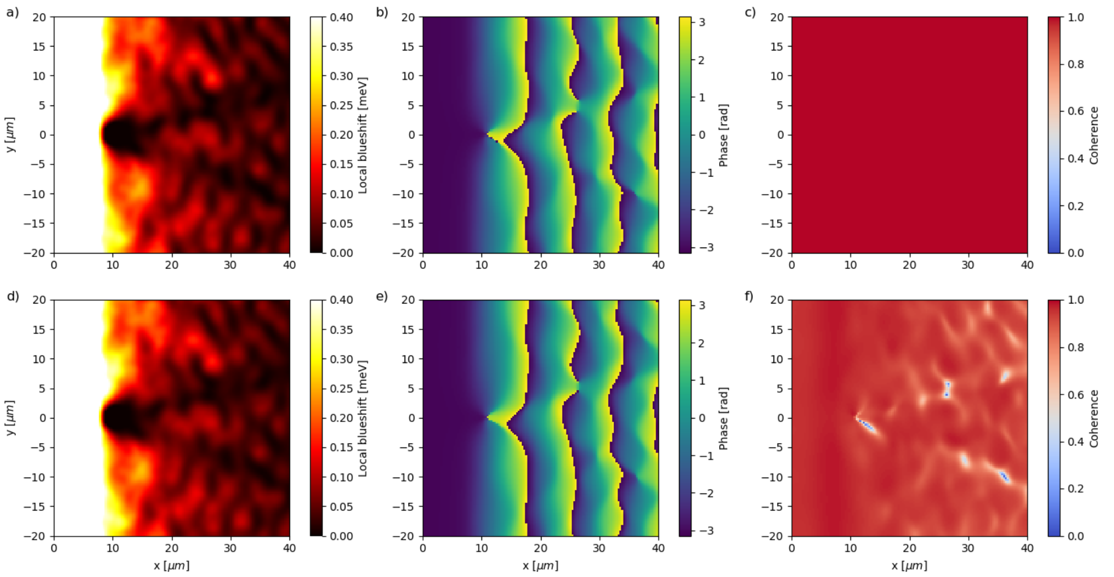

Figure 2.17: Panels (a-c): time-averaged polariton density (a), local phase at the final time (b), and coherence function $g^{(1)}(\mathbf{r})$ for a polariton fluid evolving according to (1.11) in the presence of disorder. Panels (d-f): same quantities for the same parameters in the presence of a incoherent reservoir as in Eqs.(2.4-2.5). Parameters: $\hbar\gamma = 0.04$ meV, $\Delta = -0.4$ meV, $k_p = 0$, $F_0^{eff} = 0.25$ meV μm^{-1}, $W_0 = 0.06$ meV, $\sigma_W = 0.5\mu$m. In panels (d-f), the reservoir has $\hbar\gamma_R = 0.01$ meV, $\hbar\gamma_{inc} = 0.02$ meV and $g_R = 2g$.

speed is set by the effective high-k speed of sound $c_{s,0}$ rather than by the low-k value c_s is physically understood by noting that the density modulation is peaked in $\mathbf{k}$-space at the intersection of the Bogoliubov dispersion with the $\omega = \mathbf{k} \cdot \mathbf{v}_d$ condition for the moving defect. A further confirmation of this statement can be found in Fig. 2.16.a, where we show the same plot for a faster reservoir for which the distinction between $c_{s,0}$ and c_s is more evident.

The origin of the peculiar negative value $F_d < 0$ found in the presence of the reservoir is illustrated in the panels (b,c) of Fig.2.15. A very slow defect excites quasi–resonantly the reservoir branch of the dispersion, leaving in its wake a reservoir depletion, which is partially refilled by the faster polaritons. This results in an excess of polaritons behind the defect and, thus, to a negative drag. Of course, the fact that the force tends to accelerate (rather than brake) the defect does not violate energy conservation, since we are dealing with a driven-dissipative system. It is also interesting to mention the recent calculations of the drag force of a polariton condensate in the presence of a reservoir and in the gapped regime (He and Liang [2020]).

Coming back to the case of a defect at rest in a moving fluid, here the density modulation pattern is stationary in the frame of the semiconductor cavity structure, so the $\omega = 0$ value of the effective interaction constant $g_{\text{eff}}(\omega)$ is to be used. As we have discussed in the previous sections, this value recovers the interaction constant g_{eff} defined in (2.6) that enters the expression for the total blue shift μ_T, so that the critical speed for superfluidity is set by $c_{s,T}$ such that $mc_{s,T}^2 = \mu_T$. It is quite remarkable how this simple result holds independently of the relative magnitude of the polariton and reservoir contributions to this latter and of the details of the complex Bogoliubov dispersion in a moving fluid discussed in Sec.2.3. This last subtle feature is the reason why the pioneering experiments in (Amo et al. [2009]) were in quantitative agreement with a theory that did not include the reservoir. For what concerns the dynamical experiments in (Nardin et al. [2011]), instead, the quantitative agreement with the reservoir-less theory was guaranteed by the fact that the experiments were performed using a short pulse of coherent pump light, so that the reservoir density did not have time to build up.

These considerations hold quite generally for a stationary situation, with the only requirement that the flow is dynamically stable. Crucially, as it was pointed out in (Amelio and Carusotto [2020a]), the presence of a slow reservoir can in fact give rise to dynamical instabilities that prevent from reaching the stationary state by lowering the critical disorder threshold discussed in Fig. 1.11

of the previous Chapter. This point is remarked in Fig. 2.17, where in the (upper) lower panels the flow of a fluid without (with) reservoir is shown, as characterized (from left to right) by its density, phase and $g^{(1)}(\mathbf{r})$ coherence function of Eq. (1.53): while the phase and density patterns are quite similar in the two cases, the presence of the reservoir prevents from reaching the steady-state, with the vortex positions that perform small oscillations.

2.5 Conclusions

To summarize, in Section 2.1 we started with some preliminary remarks on the spin-dependence of the polariton-polariton interaction constant; we explained why a reliable measurement of g is challenging, one of the reasons being the presence of dark excitonic states. The measurement of the dispersion relation is the subject of Section 2.2, where we described in details the experiment (Stepanov et al. [2019]) which stimulated us to consider a model containing a reservoir of incoherent dark excitons.

In Section 2.3 we have formulated the model and reported a detailed theoretical study of the collective excitations of a resonantly driven polariton fluid in the presence of the reservoir. The excitons contribute to the average blueshift and lead to a renormalization of the interaction constant in the steady state. However, if the reservoir is characterized by a slow relaxation scale, they barely participate in the faster coherent dynamics of the fluid. As a consequence only the polariton-polariton Hartree energy determines the speed of sound of the Bogoliubov quasi-particles. Our study allows to fit reliably experimental data and obtain precise estimates on the fraction of dark excitons in the fluid, which can be crucial in investigations of the polariton-polariton interaction constant.

In the previous Chapter we demonstrated the Galilean invariance of the generalized GPE in the absence of a reservoir. On the contrary, we show in Section 2.4 that the presence of the reservoir of dark localized excitons fixes a privileged laboratory reference frame linked to the semiconductor cavity structure. This breaking of Galilean invariance is visible in the Bogoliubov dispersion of the collective excitations in the fluid and in the density modulation pattern generated by a defect: while the effective speed of sound probed by a defect at rest is univocally determined by the total blue shift of the polariton modes as in the experiments of Ref. Amo et al. [2009], the one probed by a moving defect is significantly smaller and mostly determined by the polariton contribution to the blue shift. This results is of crucial importance to reconcile the historical demonstrations of polariton superfluidity in Amo et al. [2009], Nardin et al. [2011] with the recent experiment in Stepanov et al. [2019].

Beyond the microcavity polariton systems on which we have focused here, our results can be straightforwardly applied to other physical realizations of fluids of light such as photons propagating in cavityless nonlinear optical media Carusotto [2014]. While a sort of Galilean invariance along the transverse plane holds for instantaneous Kerr-like nonlinearities Fontaine et al. [2018], a strong breaking of Galilean invariance is in fact expected to occur when the optical nonlinearity has a thermal nature Vocke et al. [2015]. This is a crucial feature that needs being duly taken into account when using quantum fluids of light as quantum simulators.

Part II: Coherence of extended lasing systems

Chapter 3

Theory of the coherence of extended 1D laser systems

In the first part of the Thesis we were concerned with the study of resonantly injected polariton fluids, where the phase of the field is inherited by the external drive. In this second part we will instead consider fluids of light and matter which spontaneously break the microscopic $U(1)$ symmetry, giving rise to a rather different phenomenology with respect to the first part; on the other hand, we will still be dealing with regimes amenable to the semi-classical field description. We will be continuously switching between lasing and polariton condensation, since these two paradigms share many analogies, in particular when the focus is on the universal behavior. While here we start with a topologically trivial laser system, in the next Chapter we will turn to the case of a 2D Harper-Hofstadter laser.

This Chapter is devoted to the study of the spatial and temporal coherence properties of generic spatially extended models of laser operation, having typically in mind arrays of laser resonators or polariton microcavities. First, in Section 3.1 we review the basic principles of lasing and the semiclassical derivation of the Schawlow-Townes linewidth for devices which, as traditionally considered in laser theory, are effectively point-like. In Section 3.2 we deal instead with Kardar-Parisi-Zhang KPZ) universality in infinitely extended 1D polariton quasi-condensates. The gap in the understanding of temporal coherence between point-like and infinite systems is finally bridged in Section 3.3, where the Schawlow-Townes linewidth is viewed as a finite-size effect with an additional broadening due to KPZ-like phase nonlinearities.

3.1 Coherent laser emission

The laser is one of the most fundamental tools in modern science Siegman [1987], Svelto [2010]. Its defining feature is the emission of radiation of unprecedented intensity and long coherence length and time. This makes laser sources essential ingredients in a wide range of applications and justifies the continuous theoretical and technological research of new devices. Also from a fundamental science perspectives, the physical mechanisms underlying laser oscillation represent an archetypical model at the crossroad of nonlinear physics, non-equilibrium statistical mechanics, and quantum optics (Haken [1983], Gardiner and Zoller [2004], Chiocchetta et al. [2017], Keeling et al. [2017]). A very brief review of these concepts is the goal of the next few pages.

3.1.1 The LASER principle

As it is well known (Cohen-Tannoudji et al. [1998]), the interaction of an excited atom with the electromagnetic vacuum induces the relaxation of the atom to a lower energy level with consequent spontaneous emission of a photon, with a rate given by

$$A = \frac{4|\mathbf{d}_{12}|^2\omega_{12}^3}{3\hbar c^3}, \tag{3.1}$$

where d_{12} and ω_{12} are the dipole moment and frequency associated with the atomic transition; one factor of ω_{12} is due to the square of the electric field of a single mode of the electromagnetic field, while a further ω_{12}^2 comes from the 3D density of the modes at that frequency.

On the other hand, let a train of photons in the same state interact with an excited atom and have a frequency quasi-resonant with an atomic downward transition: the relaxation and emission processes into the same state of the incident wave are then stimulated, with a rate proportional to the number of photons of the train. This enhancement builds on the bosonic nature of the photon that is implicit in the Maxwell equations. The experimental observations that radiation thermalizes and that it interacts with matter through quantized packets of energy related to its frequency via the Planck constant was enough for Einstein to make his famous prediction of stimulated emission in 1917.

Einstein's beautiful argument goes as follows. Let' s consider a bunch of two-level atoms in a large cavity and let N_e be the number of atoms in a state excited by ω_{12}. The energy stored in the elctromagnetic field, which is at thermal equilibrium with the atoms, is distributed according to the spectral density $u(\omega)$ and the rate of the process in which a photon gets absorbed and an atom excited is proportional, via a coefficient B_{abs}, to $u(\omega_{12})N_g$, with $N_g = N - N_e$ the number of atoms in the ground state. Considering only spontaneous emission and absorption, the rate equation for N_e reads

$$\frac{dN_e}{dt} = -AN_e + B_{abs}u(\omega_{12})N_g, \tag{3.2}$$

leading to the steady-state relation $N_g/N_e = A/(Bu(\omega_{12}))$. This result also implies that at high temperatures $N_g/N_e \simeq 0$, which is clearly inconsistent with the requirement that the atoms be in thermal equilibrium

$$\frac{N_g}{N_e} = \exp\left(\frac{\hbar\omega_{12}}{k_B T}\right), \tag{3.3}$$

which already requires the notion of the Planck constant to inter-convert frequency and energy of the photon. To enforce this constraint Einstein proposed the modified rate equation

$$\frac{dN_e}{dt} = -[A + B_{ste}u(\omega_{12})]N_e + B_{abs}u(\omega_{12})N_g, \tag{3.4}$$

for which at the steady-state

$$\frac{N_g}{N_e} = \frac{A + B_{ste}u(\omega_{12})}{B_{abs}u(\omega_{12})}. \tag{3.5}$$

The high temperature limit requires[1] $B_{ste} = B_{abs} \equiv B$; the Bolzmann condition Eq. (3.3) is consistent with the Planck law

$$u(\omega) = \frac{2\hbar\omega^3}{\pi c^3}\frac{1}{e^{\hbar\omega/k_B T} - 1}, \tag{3.6}$$

which relates A, B through $A/B = \frac{2\hbar\omega^3}{\pi c^3}$.

The idea that stimulated emission would provide a mechanism to amplify an incoming electromagnetic wave began to circulate and led to the proposal of the MASER (Microwave Amplification by Stimulated Emission of Radiation) by Basov and Prokhorov and to its first implementation by Townes and co-workers in 1954. One difficulty is that steady-state operation can' t rely on two-level atoms, because, even in the presence of optical pumping of the medium, one will always have $N_e \leq N_g$ at stationarity, so that absorption will dominate on stimulated emission. To stabilize an inversion of population 3-level atoms can be used, as studied by Basov and Prokhorov and illustrated on the left panel of Fig. 3.1.

A self-sustained LASER (Light Amplifier by Stimulated Emission of Radiation) can then be built by putting the gain medium in a cavity so to feed back the generated radiation to the excited atoms for other successive amplifications. Following the theoretical proposal by Schawlow and Townes [1958], the first[2] laser was realized by Maiman in 1960 and consisted in a ruby rod doped with chromium atoms that constituted the actual gain medium, used optical pumping from a xenon flashtube and delivered short pulses at random times. Devices capable of a continuous-wave

---

[1] If the excited level has a $g-$fold degeneracy then $B_{ste} = B_{abs}/g$.

[2] According to the "Laser" page of Wikipedia there has been some controversy on the first laser actually realized; the first one to be registered by the U.S. Patent Office was the one by Maiman.

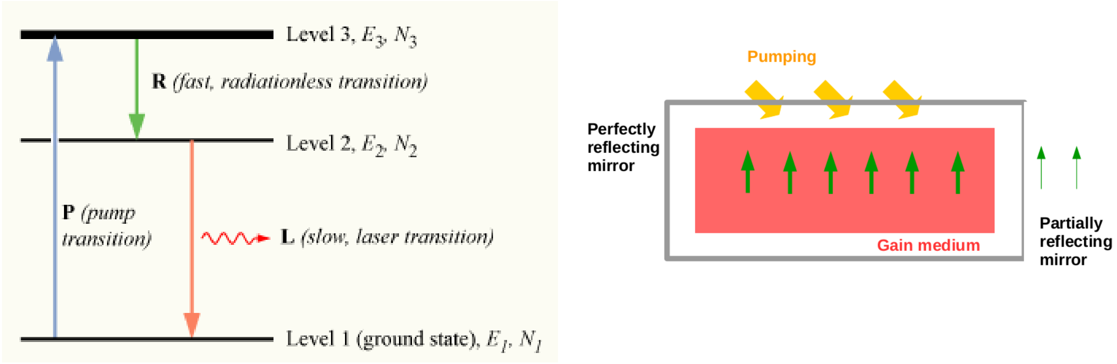
Level 3, E_3, N_3
R *(fast, radiationless transition)*
Level 2, E_2, N_2
P *(pump transition)*
L *(slow, laser transition)*
Level 1 (ground state), E_1, N_1
Pumping
Perfectly reflecting mirror
Gain medium
Partially reflecting mirror

Figure 3.1: *Principle of the LASER.* (left) Scheme of a 3-level atom used to achieve population inversion between the level 2 and 1. The level 3 is optically pumped and will experience a fast (possibly non-radiative) decay to state 2; notice that the poluation of 1 is always larger than the one of 3. (right) Basic ingredients of a typical laser device, like the original ruby laser; the green lines denote the oscillating electric field. Left plot taken from https://commons.wikimedia.org/w/index.php?curid=3631918.

emission or of Q-switching came soon afterwards, and Basov, Prokhorov and Townes were awarded the 1964 Nobel prize for their contributions to the development of the maser and of the laser.

The fundamental ingredients to understand the LASER self-sustained oscillation are an optical resonator or cavity, the gain medium, a pumping mechanism to induce population inversion in the gain medium and losses. To elucidate the mutual interplay of these elements we blend the treatments by Scully and Zubairy [1997] and Mandel and Wolf [1995], inspired to a model of the lasing operation due to Lamb [1964]. In this model lasing is described in terms of a classical electric field: on the one hand, this enters the equation of motion of the atoms and contributes to the evolution of the polarization vector; on the other hand, the polarization acts as a source term in the Maxwell equations, so that the electric field is determined self-consistently.

Starting with the atomic degrees of freedom, let' s first point out that the 3-level scheme pictured in Fig. 3.1 effectively allows to focus on a 2-level atom endowed with a unidirectional pumping from the ground-state to the excited state (while any optical pumping on a really 2-level atom would also come with stimulated emission processes into the pump wave). An adequate Master equation to describe the interaction of such an effective 2-level atom with a classical wave is provided by

$$\partial_t \hat{\rho}_{at} = -\frac{i}{\hbar}\left[\hat{H}_{at},\hat{\rho}_{at}\right] + \frac{P_{at}}{2}\mathcal{L}\left[\hat{\rho}_{at},\hat{\sigma}_+\right] + \frac{\gamma_{at}}{2}\mathcal{L}\left[\hat{\rho}_{at},\hat{\sigma}_-\right] + \frac{\gamma_{ph}}{2}\mathcal{L}\left[\hat{\rho}_{at},\hat{\sigma}_z\right]. \tag{3.7}$$

Here $\mathcal{L}\left[\hat{\rho},\hat{O}\right] = 2\hat{O}\hat{\rho}\hat{O}^\dagger - \{\hat{O}^\dagger\hat{O},\hat{\rho}\}$ denotes the Linblad super-operator, and the three Linblad terms, occurring with rates $P_{at}, \gamma_{at}, \gamma_{ph}$, correspond respectively to the pumping used to build the population inversion, to incoherent decay into the ground-state and to dephasing. This last phenomena is per example due to scattering with other atoms (or with phonons in a solid state medium), which leads to random Stark shifts which are local in space and time and result in a fluctuating transition frequency. The Hamiltonian term instead contains the coherent part of the interaction with light, so that stimulated emission is built in it:

$$\hat{H}_{at} = \frac{\omega_{21}}{2}\hat{\sigma}_z + \mathbf{E}(\mathbf{r}_0,t)\cdot\left(\mathbf{d}_{21}\,\hat{\sigma}_+ + \mathbf{d}_{21}^*\,\hat{\sigma}_-\right), \tag{3.8}$$

where we neglected an irrelevant total energy shift and $\mathbf{r}_0$ is the location of the atom.

The electric field needs to be found by solving self-consistently the Maxwell equations, and in particular the wave equation

$$\nabla^2\mathbf{E} - \frac{1}{c^2}\partial^2_{tt}\mathbf{E} = \frac{4\pi}{c^2}\partial^2_{tt}\mathbf{P}, \tag{3.9}$$

where $\mathbf{P}(\mathbf{r},t) = n_{at}(\mathbf{r})\mathbf{d}_{21}\langle e|\hat{\rho}(t)|g\rangle$ is the polarization vector of the gain medium, characterized by the atomic density $n_{at}(\mathbf{r})$. In writing this equation we have also assumed that the cavity is empty apart from the gain medium and that there are implicit boundary conditions. For a very good cavity and with the assumption that the lasing mode has very similar shape to one mode of the bare cavity $\mathbf{f}(\mathbf{r})$, we can use the ansatz

$$\mathbf{E}(\mathbf{r},t) = \mathbf{f}(\mathbf{r})\tilde{E}(t)e^{-i\omega^{las}t} + h.c. \tag{3.10}$$

Here $\tilde{E}(t)$ is a slowly varying envelope and $\mathbf{f}(\mathbf{r})$ satisfies the Helmoltz equation

$$\nabla^2\mathbf{f} = \frac{\omega_c^2}{c^2}\mathbf{f} \tag{3.11}$$

with proper boundary conditions. For example, in the case of a ring cavity $\mathbf{f}$ will be approximated by a plane wave times a polarization unit vector, or a sine in the case of a planar cavity. In the following we will assume that $\mathbf{f}(\mathbf{r})$ is approximatively constant and equal to $\mathbf{f}(\mathbf{r}_0)$ in the region occupied by the gain medium, so that any atom is subject to the same electric field.

Below we will keep the following time derivatives: $\partial^2_{tt}\mathbf{E} \simeq (\omega^{las})^2\mathbf{E} - 2i\omega^{las}\partial_t\tilde{E}(t)\mathbf{f}e^{-i\omega^{las}t} + h.c.$, the second term being necessary because of a partial cancellation of the first one by ω_c^2, and $\partial^2_{tt}\mathbf{P} \simeq (\omega^{las})^2\mathbf{P}$, since also $\mathbf{P}$ approximatively oscillates at the frequency ω_{las} (as discussed below). With these simplifications, Eq. (3.9) becomes

$$2i\omega^{las}\partial_t\tilde{E} = [\omega_c^2 - (\omega^{las})^2]\tilde{E} + 2\omega^{las}\mathcal{P}\rho_{eg} \tag{3.12}$$

where $\mathcal{P} = \frac{2\pi\omega_{las}}{\hbar\omega_c V_c}\mathbf{d}_{21}\cdot\int d\mathbf{r}\ \mathbf{f}(\mathbf{r})^* n_{at}(\mathbf{r})$ contains information about the overlap of the gain medium density with the cavity mode, which has been normalized according to $\int d\mathbf{r}\ |\mathbf{f}(\mathbf{r})|^2 = \hbar\omega_c V_c$: with this normalization $|\tilde{E}|^2$ represents the number of photons in the cavity volume V_c. Since as it will be apparent below $\omega^{las} \simeq \omega_c$, the further simplification $\omega_c^2 - (\omega^{las})^2 \simeq 2\omega^{las}(\omega^{las} - \omega_c)$ can be used. Finally, we introduce by hand some losses in the cavity mode with rate γ_c which can per example be attributed to the functional leakage of the laser emission or to absorption by the dielectric forming the cavity, so to arrive at

$$i\partial_t\tilde{E} = \left[\omega^{las} - \omega_c - \frac{i}{2}\gamma_c\right]\tilde{E} + \mathcal{P}\rho_{eg}. \tag{3.13}$$

Moreover, we just used the "slow" density matrix element

$$\rho_{eg}(t) = e^{i\omega^{las}t}\langle e|\hat{\rho}(t)|g\rangle, \tag{3.14}$$

while $\rho_{ee}(t) = \langle e|\hat{\rho}(t)|e\rangle$, and similarly for ρ_{gg}, ρ_{ge}. A more explicit form of Eq. (3.7) is then given in the so called Optical Bloch Equations (OBE)[3], in the frame defined by Eq. (3.14) and within the rotating wave approximation (RWA)

$$\dot{\rho}_{ee} = -\gamma_{at}\rho_{ee} + P_{at}\rho_{gg} + i\tilde{E}^*(t)\Omega_0^*\rho_{eg} - i\tilde{E}(t)\Omega_0\rho_{ge} \tag{3.15}$$

$$i\dot{\rho}_{eg} = \left[\omega_{21} - \omega^{las} - i\frac{P_{at} + \gamma_{at} + \gamma_{ph}}{2}\right]\rho_{eg} - \tilde{E}(t)\Omega_0(\rho_{ee} - \rho_{gg}) \tag{3.16}$$

where we defined the vacuum Rabi frequency of the filled cavity $\Omega_0 = \frac{\mathbf{f}(\mathbf{r}_0)\cdot\mathbf{d}_{21}}{\hbar}$.

The coupled Eqs. (3.13,3.15,3.16) can be solved numerically. However, to proceed further with the analysis, one now assumes that the dynamics of the atom as governed by $P_{at}, \gamma_{at}, \gamma_{ph}$ is faster than the dynamics of $\tilde{E}(t)$, so that at any time t the atom can be considered in its steady state: in this case we will speak of a class-A device, in contrast to a class B device where the dynamics of the gain medium has to be treated explicitely. The density matrix elements ρ_{ee}, ρ_{eg}, etc. are then expressed only as a function of $\tilde{E}(t)$:

$$\rho_{eg} = \frac{\tilde{E}(t)\Omega_0}{\omega_{21} - \omega^{las} - i\frac{P_{at}+\gamma_{at}+\gamma_{ph}}{2}}(\rho_{ee} - \rho_{gg}) \tag{3.17}$$

$$\rho_{ee} - \rho_{gg} = \frac{P_{at} - \gamma_{at}}{\left[P_{at} + \gamma_{at} + 2\frac{(P_{at}+\gamma_{at}+\gamma_{ph})|\tilde{E}(t)\Omega_0|^2}{(\omega_{21}-\omega^{las})^2 + (P_{at}+\gamma_{at}+\gamma_{ph})^2/4}\right]} \tag{3.18}$$

---

[3] In the derivation one writes $\rho = \frac{\hat{1}}{2} + (\rho_{ee} - \rho_{gg})\frac{\hat{\sigma}_z}{2} + \langle e|\hat{\rho}(t)|g\rangle\hat{\sigma}_+ + \langle g|\hat{\rho}(t)|e\rangle\hat{\sigma}_-$ and uses the commutators $\left[\frac{\hat{\sigma}_z}{2}, \hat{\sigma}_\pm\right] = \pm\hat{\sigma}_\pm$, $[\hat{\sigma}_+, \hat{\sigma}_-] = \hat{\sigma}_z$ and the anti-commutators $\{\hat{\sigma}_+, \hat{\sigma}_-\} = 1$, $\{\hat{\sigma}_+, \hat{\sigma}_+\} = 0$.

In particular, injecting ρ_{eg} in Eq. (3.13) and after some algebra, one arrives at the equation of the class-A laser

$$i\partial_t \tilde{E} = \left[\omega^{las} - \omega_c - \frac{i}{2}\gamma_c + \frac{i}{2}(1+i\zeta)^{-1}\frac{P}{1+|\tilde{E}|^2/n_s}\right]\tilde{E}, \tag{3.19}$$

where $P = 4\frac{\mathcal{P}\Omega_0}{P_{at}+\gamma_{at}+\gamma_{ph}}\frac{P_{at}-\gamma_{at}}{P_{at}+\gamma_{at}}, \zeta = 2\frac{\omega_{21}-\omega^{las}}{P_{at}+\gamma_{at}+\gamma_{ph}}$ and $n_s^{-1} = 1 + \frac{8}{1+\zeta^2}\frac{|\Omega_0|^2}{(P_{at}+\gamma_{at}+\gamma_{ph})(P_{at}+\gamma_{at})}$.

In order to determine the steady state operation, this (complex-valued) equation needs to be solved for $\omega^{las}, \tilde{E}_{ss}$. When $\omega_{21} = \omega_c \equiv \omega_0$, the lasing frequency coincides with $\omega^{las} = \omega_0$ and, since $\zeta = 0$ Eq. (3.19) simplifies to

$$i\partial_t \tilde{E} = \left[\omega^{las} - \omega_c - \frac{i}{2}\gamma_c + \frac{i}{2}\frac{P}{1+|\tilde{E}|^2/n_s}\right]\tilde{E}; \tag{3.20}$$

correspondingly, above the lasing threshold $P_{th} = \gamma_c$ the steady-state field intensity is given by $|\tilde{E}_{ss}|^2 = n_s(P-\gamma_c)/\gamma_c$. On the other hand, if $\omega_{21} \neq \omega_c$ the lasing frequency will be "pulled" from ω_c towards ω_{21}; since this mode-pulling depends on $|\tilde{E}(t)|^2$, a refractive index nonlinearity will be also present.

Another scenario, occurring for class B devices, is that the atomic degrees of freedom cannot be completely eliminated adiabatically, but still the gain medium is an incoherent one, or in other words γ_{ph} is very large, as it could be relevant to the density of carriers in a semiconductor laser. In this case the adiabatic strategy can be applied to Eq. (3.16) only, allowing for the elimination of ρ_{eg}. One remains with two coupled equations for the electric field $\tilde{E}$ and the population unbalance $\rho_{ee} - \rho_{gg}$ which have precisely the form (1.8,1.9) , introduced when discussing polariton lasing.

For completeness, notice that from Eqs. (3.9,3.15,3.16) one can read off the physics also for an amplifier, where a wave is passed through the gain medium and gets amplified but no feedback is present (no cavity). In practice, one reinjects the expression for ρ_{eg} in the Maxwell Eq. (3.9) to obtain a frequency dependent susceptibility, or equivalently a complex wavevector containing the information about the amplification factor per unit length. In particular, in the linear amplification regime where the incident wave is a weak one, one neglects the electric field in the correspective of Eq. (3.15) to get $\rho_{ee} - \rho_{gg} = \frac{P_{at}-\gamma_{at}}{P_{at}+\gamma_{at}}$. On the contrary, the amplification gets saturated for high incident fields, due to the denominator in Eq. (3.16).

3.1.2 Semiclassical theory and Schawlow-Townes linewidth

In the treatment above the electric field is purely classical. This approach is useful to get an estimate of the lasing frequency and threshold and of their dependence on the microscopic parameters; it is also possible to study the switch-on dynamics of the device, with the so called relaxation oscillations when the intensity is reaching its steady-state. This approach however tells us nothing about the linewidth and the photon distribution of the emission. While here we just mention that the instantaneous quantum state of the field can usually be approximated by a coherent state with Poissonian photon number statistics, we want discuss a bit more in details the issue of the linewidth.

The linewidth of a laser is the Full Width at Half Maximum of the spectral density of the emission, which under the assumptions discussed below has Lorenztian shape. Formally, a photodetection experiment will probe the correlation function

$$g^{(1)}(t) = \left\langle :\hat{E}^\dagger(t)\hat{E}(0): \right\rangle, \tag{3.21}$$

or its Fourier transform $S(\omega)$, where the double dots denote normal ordering of the quantum operators.

As recognized by Schawlow and Townes [1958] in their seminal paper, the intrinsic quantum mechanism, which sets the ultimate lower bound to the laser linewidth, is spontaneous emission into the same cavity mode in which lasing occurs. If the lasing field is viewed as a coherent state of a given phase, the spontaneous emission event acts like a kick of one quantum of intensity and random phase to the field.

We sketch here how a simple semiclassical treatment that grasps the basic aspects of the Schawlow-Townes line emerges from a fully quantum treatment (Mandel and Wolf [1995], Scully and Zubairy [1997]); this also enables to ask meaningful questions about the distributions of photons in the field. Since using here the optical Bloch equations (3.15, 3.16) would turn out to be a bit involved, it is possible to obtain the correct results by considering the small time perturbation expansion for the cavity-atom density matrix with initial conditions in a product state where the atom is in the excited level. Indeed, assuming that the dynamics of the cavity field is slow on the time-scale of the interaction with each atom, we can imagine that the field interacts with only one atom, shot through the cavity, at each time. This allows, having written down the time-dependent Schroedinger equation for the density matrix, to trace over the atomic degrees of freedom to yield a Master equation for the radiation density matrix $\hat{\rho}$. Introducing also cavity losses, the Master equation takes the form

$$\partial_t \hat{\rho} = \frac{A}{2}\mathcal{L}\left[\hat{\rho}, \hat{\psi}^\dagger\right] + \frac{C}{2}\mathcal{L}\left[\hat{\rho}, \hat{\psi}\right] + \frac{B}{8}\left(\hat{\psi}\hat{\psi}^\dagger\hat{\psi}\hat{\psi}^\dagger\hat{\rho} + 3\hat{\psi}\hat{\psi}^\dagger\hat{\rho}\hat{\psi}\hat{\psi}^\dagger - 4\hat{\psi}^\dagger\hat{\psi}\hat{\psi}^\dagger\hat{\rho}\hat{\psi} + h.c.\right) \tag{3.22}$$

where A, B, C are coefficients that can be determined from first principles.

The next step uses the fact that the density matrix has finite trace, so that in the coherent state basis $\rho(\phi, \psi) = \langle\phi|\hat{\rho}|\psi\rangle$ is an entire function of ϕ, ψ and it can be known on the plane $\phi = \psi$ without loss of information. This is referred to as the P or Glauber representation. It is then sufficient to write down an equation for the time-evolution of diagonal component $\rho(\psi, t)$ of the density matrix. Keeping only the first order term in the coefficient B, which is typically small, and assuming that the dynamics occurs close to the steady state of the laser and not too close to threshold, for which the distribution ρ is concentrated at large $|\psi|$, the evolution reads

$$\partial_t \rho(\psi, t) = A\frac{\partial^2}{\partial\psi\partial\psi^*}\rho + \frac{1}{2}\frac{\partial}{\partial\psi}\psi\left[B|\psi|^2 - A + C\right]\rho + \frac{1}{2}\frac{\partial}{\partial\psi^*}\psi^*\left[B|\psi|^2 - A + C\right]\rho. \tag{3.23}$$

This is a Fokker–Planck equation for $\rho(\psi, t)$, which, as expected from the theory of classical states of light, in a lasing state closely resembles a probability distribution. The crucial remark is that the Fokker-Planck equation associated with the semi-classical Langevin equation

$$i\partial_t \tilde{E} = \left[\omega^{las} - \omega_c - \frac{i}{2}\gamma_c + \frac{i}{2}(1 + i\zeta)^{-1}P(1 - |\tilde{E}|^2/n_s)\right]\tilde{E} + \sqrt{2D}\,\xi, \tag{3.24}$$

obtained by expanding Eq. (3.19) for small saturation term and adding the random drift of strength D (properly related to A, B, C), has precisely this same form. Also notice that in the Laplacian term of the Fokker-Planck equation it enters A but not C, meaning that the diffusion of ψ is due to the interaction with the gain medium but not to cavity losses, while in the Wigner representation also C enters in the diffusion term. This apparent contradiction is resolved by observing that in the P representation a coherent state is a delta function, and the diffusion term corresponds to a drift of the coherent state. In the Wigner representation instead a coherent state is a Gaussian with spread determined by the uncertainty principle, and the C contribution to the diffusion accounts for this finite variance.

Here we are not very interested in a microscopic derivation of the spontaneous emission rate or equivalently of D and refer to (Henry [1982], Scully and Zubairy [1997]) for a more quantitative discussion. Moreover, in what follows we will be mostly involved with any source of noise associated with a homogeneous broadening of the laser emission, for instance as due to collisions (Svelto [2010]); we will tend to use anyhow the expression Schawlow-Townes linewidth to denote the drift of the optical phase. A simple semiclassical approach based on (3.24) is illustrated below, without a formal derivation which would be cumbersome and not very instructive (Mandel and Wolf [1995]). Conversely, there exist also mechanisms of inhomogeneous broadening, such as due to Doppler shift in finite temperatures atomic clouds or to disorder; these do not fall in the Schawlow-Townes class characterized by a diffusion of the phase and in general do not feature a Lorenztian spectral distribution.

To grasp the nature of the Schawlow-Townes broadening, let' s then consider the semiclassical Langevin equation

$$i\partial_t \psi = \mathcal{W}(n)\psi + \sqrt{2D}\xi\ , \qquad \langle\xi^*(t)\xi(t')\rangle = \delta(t - t'), \tag{3.25}$$

where $n = |\psi|^2$ represents the intensity of the field and ξ is white noise with diffusion coefficient D, accounting for spontaneous emission and homogeneous broadening. Also, we enclose in $\mathcal{W}(n) = \mathcal{W}' + i\mathcal{W}''$ the dependence of the gain, absorption and refractive index properties of the medium on n, where for simplicity the atomic degrees of freedom have been eliminated. In the absence of the external noise, Eq. (3.25) has the $U(1)$ symmetry for the phase of the field; this is zero below the lasing threshold, while in the symmetry broken lasing phase its intensity satisfies $\mathcal{W}''(n_0) = 0$, the pedex denoting the solution without noise. The phase, instead, will rotate with frequency $\omega^{las} = \mathcal{W}'(n_0)$.

To deal analytically with Eq. (3.25) it is convenient to resort to the phase–density formalism: writing the field as $\psi = \sqrt{n}e^{i\phi}$ it holds

$$\partial_t \phi = -\mathcal{W}'(n) + \sqrt{\frac{D}{n}}\xi_1 \tag{3.26}$$

$$\partial_t n = 2\mathcal{W}''(n)\ n + 2\sqrt{nD}\ \xi_2 \tag{3.27}$$

where now one has two real uncorrelated noises $\langle \xi_l(t)\xi_l(t')\rangle = \delta(t-t')$, $l = 1, 2$. Assuming noise is small enough to cause minor perturbations δn to the density, one can use the linearized equations

$$\partial_t \phi = -\left.\frac{\partial \mathcal{W}'}{\partial n}\right|_{n_0} \delta n + \sqrt{\frac{D}{n_0}}\xi_1 \tag{3.28}$$

$$\partial_t \delta n = -\Gamma \delta n + 2\sqrt{Dn_0}\ \xi_2, \tag{3.29}$$

with $\Gamma = -2n_0 \left.\frac{\partial \mathcal{W}''}{\partial n}\right|_{n_0}$ the relaxation rate of the density fluctuations. Since in this limit both ϕ and n are Gaussian variables, the autocorrelation of the field reads

$$g^{(1)}(t) = \langle \psi^*(t)\psi(0)\rangle = n_0 e^{-\frac{1}{2}\langle[\phi(t)-\phi(0)]^2\rangle}. \tag{3.30}$$

On the other hand, the $U(1)$ symmetry of the model ensures that the dynamics of the phase is a diffusion with no restoring force, so the decay of coherence is described by the exponential

$$g^{(1)}(t) = n_0 e^{-\frac{\gamma_{ST}}{2}|t|}, \tag{3.31}$$

where the rate γ_{ST} is the celebrated Shawlow–Townes linewidth (Schawlow and Townes [1958]). In Fourier space, this corresponds to a Lorentzian power spectral density.

Integrating Eq. (3.29) one finds the fluctuations of the density[4]

$$\langle \delta n^2 \rangle = \frac{Dn_0}{\Gamma}, \tag{3.32}$$

which, after applying basic statistics to Eq. (3.28), entails

$$\gamma_{ST} = \frac{D}{2n_0}\left(1 + \alpha^2\right). \tag{3.33}$$

Here we call $\alpha = \frac{\partial \mathcal{W}'}{\partial n} / \frac{\partial \mathcal{W}''}{\partial n}$ the Henry factor, for its close analogy to the one introduced by Henry [1982]. The crucial feature of this formula is the density appearing at the denominator, connected with the following picture: the more photons in the resonator, the less the phase of the field is perturbed when a photon with a random phase is randomly emitted into the field. Plus, fluctuations of the field intensity or of the carrier density reflects in temporal variations of the refractive index, hence of the cavity resonance frequency, which ultimately leads to the supplemental broadening factor α.

In the following we will restrict the discussion of the linewidth to the simplest case $\mathcal{W}(n) = \frac{i}{2}\left[\frac{P}{1+n/n_s} - \gamma\right]$, corresponding to Eq. (3.20), from which it follows

$$i\partial_t \psi = \frac{i}{2}\left[\frac{P}{1+n/n_s} - \gamma\right]\psi + \sqrt{2D}\xi \tag{3.34}$$

and $\Gamma = \gamma(P-\gamma)/P$. In this case the linewidth reads

$$\gamma_{ST} = \frac{D}{2n_0}. \tag{3.35}$$

The Scawlow-Townes line in a strict sense, i.e. the ultimate quantum limit set by spontaneous emission, has been experimentally approached by Manes and Siegman [1971], making use of a He-Ne infrared gas laser in a lossy cavity, so to have very strong gain and associated noise but low intensity. We just mention other interesting experimental works regarding the linewidth in bad cavities (Kuppens et al. [1994]) and in Quantum Cascade Lasers (Bartalini et al. [2010]).

---

[4] curiously, using the fast density approximation $0 = \Gamma\delta n + 2\sqrt{Dn_0}\ \xi_2$ already in the first step leads to the correct linewidth, but to the wrong amplitude of the density fluctuations.

3.2 Kardar-Parisi-Zhang physics in 1D nonequilibrium fluids

In the previous Section, the temporal coherence of the light emitted by a laser device was studied in details. The Schawlow-Townes analysis indicates, in a broad sense, the treatment of homogeneous broadening when the laser field is described by the evolution of a single spatial mode. Some extensions have been developed in the context of open resonators, as we will briefly review in Section 4.2.4 when discussing the Petermann factor. In these works, the competition with other cavity modes leads to an enhancement of the Langevin diffusion constant for the lasing mode, but the quantity of interest remains the linewidth, while the spatial coherence of the lasing mode itself is not considered. This approach is expected to be adequate for devices consisting of a Fabry-Perot cavity with 3D confinement or for ring lasers.

In this Section we will consider arrays of coupled laser resonators or polariton condensation (which was already sketched in Section 1.2) in low dimensional structures, where the spatial coherence of the lasing field is a serious issue. Here we will focus on the spatio-temporal dynamics of a 1D nonequilibrium fluid, such as the lasing or polariton fields, described by the one–dimensional chain of N_x coupled nonlinear oscillators $x = 1, ..., N_x$

$$i\partial_t\psi_x = -J\psi_{x+1} - J\psi_{x-1} + gn_x\psi_x + \frac{i}{2}\left[\frac{P}{1+\frac{n_x}{n_S}} - \gamma\right]\psi_x + \sqrt{2D}\xi_x \ , \tag{3.36}$$

with periodic boundary conditions and independent noises $\langle \xi^*_x(t)\xi_{x'}(t')\rangle = \delta_{xx'}\delta(t-t')$. Equivalently, one can deal with the continuum version of Eq. (3.36)

$$i\partial_t\psi(x,t) = \left\{-\frac{1}{2m}\partial_x^2 + gn(x,t) + \frac{i}{2}\left[\frac{P}{1+n(x,t)/n_S} - \gamma\right]\right\}\psi(x,t) + \sqrt{2D}\ \xi(x,t)\ , \tag{3.37}$$

where $\langle \xi(x,t)^*\xi(x',t')\rangle = \delta(x-x')\delta(t-t')$ and $-J\psi_{x+1} - J\psi_{x-1}$ is replaced by $-\frac{1}{2m}\partial_x^2$, where the mass is related to the hopping via $m = 1/2J$ (the distance between the oscillators being 1). For the sake of completeness, we have also added a refractive index nonlinearity in the form of a polariton-polariton interaction $g|\psi|^2\psi$. This equation is the adiabatic approximation of Eqs. (1.8,1.9), introduced when we touched on incoherently excited polariton fluids and polariton condensation.

Extensions of this equation to include absorption nonlinearities or momentum dependent losses and to deal explicitely with the reservoir of carriers in the spirit of Eqs. (1.8,1.9) have been presented by He et al. [2015], Squizzato et al. [2018] with no major modifications in the final results. Another important remark is that, while for polariton fluids in a nanowire Eq. (3.37) is a proper approximation, for arrays of coupled semiconductor laser the situation is much more complicated: the tight-binding approximation expressed by Eq. (3.36), in which only a single mode per resonator can be excited, is in general not valid and an *ab initio* treatment from the Maxwell equations is needed, as discussed more in details at the end of the next Chapter.

3.2.1 Spatio-temporal phase dynamics

Let' s now study the stationary dynamics of an infinitely extended polariton wire, as described by Eq. (3.37).

To familiarize with the problem we start by reviewing the Bogoliubov approach. In the absence of noise, any plane wave $\psi_0(x,t) = \psi_0 e^{ik_x^{las}x - i\omega^{las}t}$ is a steady-state solution, provided that $\omega^{las} = (k_x^{las})^2/2m + \mu$, $\mu = gn_0$ and $n_0 \equiv |\psi_0|^2 = n_S(P/\gamma - 1)$. Because of the $U(1)$ invariance of the noiseless semicalssical laser equation under phase shifts $\psi(x,t) \to e^{i\varphi}\psi(x,t)$, the phase of ψ_0 is completely arbitrary. The linearized equations on top of the uniform state with $k_x^{las} = 0$ read

$$i\partial_t\delta\psi(x,t) = -\frac{1}{2m}\partial_x^2\delta\psi + \mu\left(2\delta\psi + \delta\psi^*\right) - \frac{i}{2}\Gamma\left(\delta\psi + \delta\psi^*\right) + \sqrt{2D}\ \xi\ , \tag{3.38}$$

with $\Gamma = \gamma(P-\gamma)/P$. It is also instructive to write this down in the density-phase formalism and in Fourier space:

$$\partial_t\begin{pmatrix}\delta\phi_k\\ \delta n_k\end{pmatrix} = \begin{pmatrix}0 & \frac{k^2}{4mn_0} + g\\ n_0\frac{k^2}{m} & -\Gamma\end{pmatrix}\begin{pmatrix}\delta\phi_k\\ \delta n_k\end{pmatrix} + \begin{pmatrix}\sqrt{\frac{D}{n_0}}\ \xi_{1,k}\\ 2\sqrt{Dn_0}\ \xi_{2,k}\end{pmatrix} \tag{3.39}$$

with $\langle \xi_{l,k}(t)\ \xi_{l',k'}(t')\rangle = \delta_{ll'}\delta_{kk'}\delta(t-t')$. The eigenvalues of the Bogoliubov matrix represent the elementary excitations of the system and have dispersion

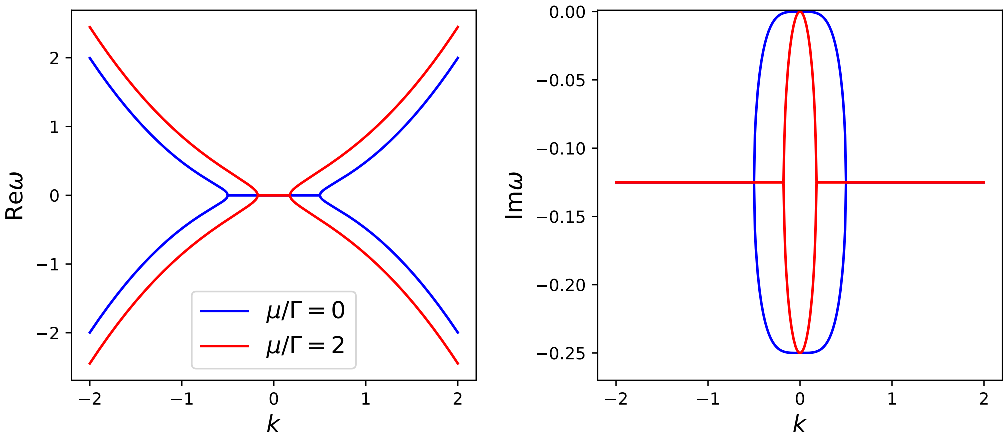

Figure 3.2: *Bogoliubov dispersion of polariton laser wire.* We depict the real (left) and imaginary (right) part of the Bogoliubov dispersion Eq. (3.40), in the presence and in the absense of polariton-polariton interactions. The Goldstone mode has a diffusive nature in this system. Parameters used: $m = 1, \Gamma = 0.25$.

$$\omega_\pm(k) = -i\frac{\Gamma}{2} \pm i\sqrt{\left(\frac{\Gamma}{2}\right)^2 - \frac{k^2}{m}\left(\frac{k^2}{m} + 2\mu\right) + i0^-}. \tag{3.40}$$

The real and imaginary parts are depicted respectively in in Fig. 3.2.a and b, showing the typical sticking of the branches in the real part and the corresponding opening of the imaginary branches, as prescribed by the particle-hole symmetry of the Bogoliubov problem. The $U(1)$ invariance ensures the existence of a purely phase-like mode at $k = 0$ with zero eigenvalue, which we call the Goldstone mode in analogy with equilibrium statistical mechanics and quantum field theory. The low frequency physics is dominated by the mostly phase-like modes belonging to the Goldstone dome: these are characterized by pole in

$$\omega_+(k) = -i\frac{k^2}{m\Gamma}\left(\frac{k^2}{m} + 2\mu\right); \tag{3.41}$$

notice the different asymptotic behaviors at small k, k^2 versus k^4, when the polariton-polariton interaction is present or not.

In the presence of an incoherent reservoir of carriers, as described by Eqs. (1.8,1.9) and originally studied by (Wouters and Carusotto [2007]), a third branch is present at zero real energy and with finite lifetime; also in this case, the slow frequency physics is expected to be dominated by the Goldstone dome.

The Bogoliubov approach in 1D is not self-consistent: as highlighted by Chiocchetta and Carusotto [2013], the spatial correlations can be computed evaluating $\langle \delta\phi_k^* \delta\phi_k \rangle$ at equal times from Eq. (3.39) and are predicted to decay exponentially with the distance. This is the prediction of the expected lack of long-range order in low dimensionality; since the Bogoliubov theory requires linearization on top of a uniform state, the Bogoliubov approximation is not internally consistent in 1D. Nontheless, the final result that the spatial correlations decay exponentially is correct, as we move to consider now in a more proper theoretical framework.

Here we will deal with Eq. (3.37) with the assumption of small noise amplitude. In this case we can safely treat density fluctuations as first order perturbations. However, since we are in 1D, the polariton field will describe a quasi-condensate dynamics, where the coarse-grained phase performs a random walk along the wire. As a result, it is not possible to treat the phase variations as a small deviation from the uniform state.

The strategy pursued by Gladilin et al. [2014] has then been to adiabatically get rid of density fluctuations and obtain a nonlinear equation for the phase. Let' s start by writing down Eq. (3.37) in the phase-density formalism with $\psi(x,t) = \sqrt{n_0 + \delta n(x,t)}e^{i\phi(x,t) - i\mu t} \simeq \sqrt{n_0}\left(1 + \frac{\delta n}{2n_0}\right)e^{i\phi(x,t) - i\mu t}$:

$$\partial_t \frac{\delta n}{2n_0} = -\frac{1}{2m}\left[2\partial_x \frac{\delta n}{2n_0}\partial_x \phi + \left(1 + \frac{\delta n}{2n_0}\right)\partial_x^2 \phi\right] - \Gamma\frac{\delta n}{2n_0} + \sqrt{\frac{D}{n_0}}\xi_1, \tag{3.42}$$

$$\partial_t \phi = -\frac{1}{2m}\left[\partial_x^2 \frac{\delta n}{2n_0} - (\partial_x \phi)^2\right] - 2\mu\frac{\delta n}{2n_0} + \sqrt{\frac{D}{n_0}}\xi_2. \tag{3.43}$$

Assuming fast relaxation of the intensity fluctuations, one can neglect all the terms containing δn but the one proportional to Γ and set

$$\frac{\delta n}{2n_0} \simeq -\frac{\Gamma^{-1}}{2m}\partial_x^2\phi + \Gamma^{-1}\sqrt{\frac{D}{n_0}}\xi_2. \tag{3.44}$$

Reinjecting this expression in the equation for the phase, one has to deal only with the dynamics of the phase, which is described by the Kuramoto–Sivashinsky equation (KSE)

$$\partial_t \phi = \frac{1}{2m}\left[-\frac{\Gamma^{-1}}{2m}\partial_x^4\phi - (\partial_x\phi)^2 + 2\mu\Gamma^{-1}\partial_x^2\phi\right] + \sqrt{\frac{D}{n_0}}\xi_1. \tag{3.45}$$

Importantly, here ϕ is the unwound phase living on the real axis, and not the compact one restricted to $[0, 2\pi]$. The characteristic scales of the system can be expressed as a function of the microscopic parameters:

$$\begin{aligned} l^* &= \left[\frac{J^4}{\Gamma^3 D n_0^{-1}}\right]^{1/7} \quad , \quad t^* = \left[\frac{J^2}{\Gamma^5 (D n_0^{-1})^4}\right]^{1/7} , \\ \phi^* &= \left[\frac{(D n_0^{-1})^2}{J\Gamma}\right]^{1/7} \quad , \quad \mu^* = \frac{1}{2}\left[\frac{\Gamma^6 (D n_0^{-1})^2}{J}\right]^{1/7} . \end{aligned} \tag{3.46}$$

Measuring space, time, (unwound) phase and Hartree potential in terms of l^*, t^*, ϕ^*, μ^* (and after sending $\phi \to -\phi$) the adimensional KSE reads

$$\partial_{\tilde{t}}\tilde{\phi} = \tilde{\mu}\partial_{\tilde{x}}^2 - \partial_{\tilde{x}}^4\tilde{\phi} + (\partial_{\tilde{x}}\tilde{\phi})^2 + \tilde{\xi}. \tag{3.47}$$

The renormalization group analysis shows that at long distances and times the KSE flows to the KPZ universality class (Ueno et al. [2005]), whose main features we state here, while a more formal introduction is left to the next Section. The KPZ equation reads

$$\partial_{\tilde{t}}\tilde{\phi} = \nu\partial_{\tilde{x}}^2\tilde{\phi} + \frac{\lambda}{2}(\partial_{\tilde{x}}\tilde{\phi})^2 + \sqrt{\mathcal{D}}\xi_1 \tag{3.48}$$

and it was originally proposed by Kardar et al. [1986] to describe the growth of interfaces. Its scaling behavior at low energies (and assuming an infinite system and stationary regime) is characterized by the correlation function

$$\Delta\tilde{\phi}_{\tilde{x},\tilde{t}}^2 \equiv \langle[\tilde{\phi}(\tilde{x},\tilde{t}) - \tilde{\phi}(0,0)]^2\rangle \tag{3.49}$$

and by two exponents χ, z which determine the asymptotic behavior of the spatial and temporal correlations respectively, according to $\Delta\tilde{\phi}_{\tilde{x},0}^2 \sim \tilde{x}^{2\chi}$ and $\Delta\tilde{\phi}_{0,\tilde{t}}^2 \sim \tilde{t}^{2\chi/z}$.

In $1D$ we have $\chi = 1/2$ for the roughness exponent and $z = 3/2$ for the dynamical exponent; even more precisely it holds

$$\Delta\tilde{\phi}_{\tilde{x},\tilde{t}}^2 = \left(\frac{1}{2}\lambda A^2 t\right)^{2/3} g_{KPZ}\left(\frac{\tilde{x}}{(2\lambda^2 A\tilde{t}^2)^{1/3}}\right) \tag{3.50}$$

where $A = \frac{\mathcal{D}}{2\nu}$ is the variance of $\partial_{\tilde{x}}\tilde{\phi}$. The universal function g_{KPZ} is known exactly (Prähofer and Spohn [2004]) and we here recall its limiting values $g_{KPZ}(u) - 2|u| \to 0$ for $u \to \infty$ and $g_{KPZ}(u) \to 1.150...$ for $u \to 0$. As a consequence, the equal–time correlation function has the random walk form $\Delta\tilde{\phi}_{\tilde{x},0}^2 = A|\tilde{x}|$, which is insensitive to the KPZ nonlinearity λ and can be captured by a linearized Bogoliubov analysis. In other words, only looking at the spatial correlations the dynamics is not distinguishable from the one of the linear ($\lambda = 0$) Edwards–Wilkinson (EW) model. In both cases, one has $\chi = 1/2$ which corresponds to an exponential decay of the spatial

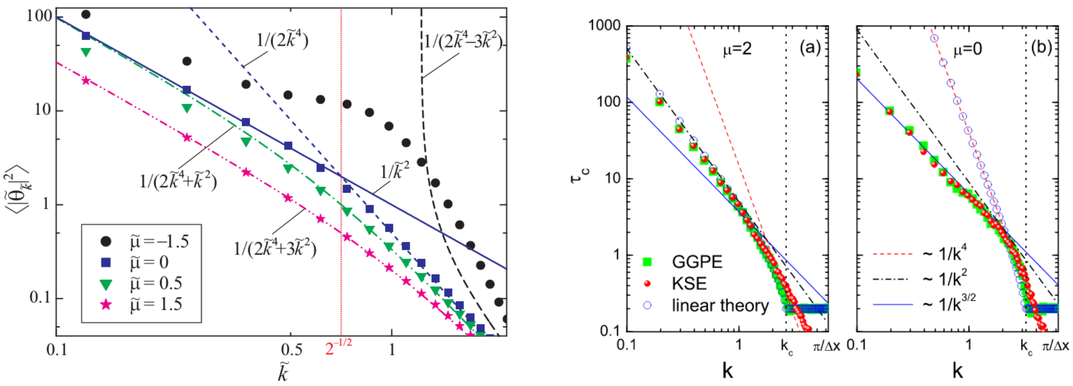

Figure 3.3: *Bogoliubov-KPZ crossover in polariton laser wires.* (left) The equal-time correlation function $\langle\tilde{\phi}^*_k\tilde{\phi}_k\rangle$ plotted a function of k for different values of $\tilde{\mu}$. (right) Decay time τ_k extracted from the correlator $\langle\psi_k(t)^*\psi_k(0)\rangle \simeq n_0 e^{-t/\tau_k}$. While in the presence of repulsive interactions the Bogoliubov prediction works very well for the system size explored here, when $\tilde{\mu}=0$ there is a clear emergence of the KPZ exponents at small k. Plots taken respectively from (Gladilin et al. [2014]) and (Ji et al. [2015]).

coherence (Gladilin et al. [2014], He et al. [2015]). A difference is instead visible in the spatio-temporal correlations, which have different exponents in the two models, namely $z=2$ in the linear EW model and $z=3/2$ in KPZ.

These concepts have been well illustrated in the works (Gladilin et al. [2014], Ji et al. [2015]), where the crossover between the linear and nonlinear theory at different observation length scales is higlighted. In particular in those works, the equal-time correlation function $\langle\tilde{\phi}^*_k\tilde{\phi}_k\rangle$ and the decay time τ_k, as extracted from the correlator $\langle\psi_k(t)^*\psi_k(0)\rangle \simeq n_0 e^{-t/\tau_k}$, are plotted a function of k and different values of $\tilde{\mu}$, see Fig. 3.3. In particular, when $\tilde{\mu}=0$ there is a clear crossover between the Bogoliubov prediction that works at small distances and the KPZ exponents that are visible at low momenta. Moreover, from both panels it emerges the role played by the polariton-polariton interaction: since this provides a stabilization mechanism (visible in the fact that the red modes in Fig. 3.2 are much more damped than the blue ones), flowing to the KPZ regime requires longer systems and longer times. For this reason in what follows we will focus on the numerically easier case $g=0$.

A numerical demonstration of the collapse of the coherence functions to the scaling form (3.75) will be instead given in Fig.4.10(b) of the next Section in comparison with the topological lasing case.

3.2.2 KPZ universality

Kardar, Parisi and Zhang in 1986 (Kardar et al. [1986]) proposed that the scaling properties of the dynamics of a growing interface can be captured by the KPZ equation

$$\partial_t h = \nu\nabla^2 h + \frac{\lambda}{2}(\nabla h)^2 + \sqrt{\mathcal{D}}\xi, \tag{3.51}$$

with[5] $\langle\xi(\mathbf{x},t)\xi(\mathbf{x}',t')\rangle = \delta(\mathbf{x}-\mathbf{x}')\delta(t-t')$. Here $h(\mathbf{x},t)$ is the height of the interface on a d-dimensional substrate, ν is called the surface tension and promotes a smooth surface, while the Langevin term describes stochastic noise.

The crucial term though is the nonlinear one. Realistic interfaces grow in the direction which is locally normal to the interface itself, so that in a small interval δt the interface front is pushed forward by an amount $\lambda\delta t$, denoted by the blue arrows in Fig. 3.4.a; this step has to be projected in the direction of the h axis, by multiplying by $1/\cos\theta$ where $\tan\theta = |\nabla h|$, as suggested by the magenta arrow in Fig. 3.4.a. Finally one assumes that the slope of the interface is always small, so that expanding for small angles yields $\delta h = \lambda\delta t(1+\frac{1}{2}\nabla h^2)$; the first term yields a constant growth velocity over all the substrate and is neglected.

---

[5] Some care needs to be paid since an equally used convention in the statistical mechanics literature is that the strength of the Langevin term is $2\mathcal{D}$ instead of $\mathcal{D}$... crucially, in the fundamental work Prähofer and Spohn [2004] there is a factor 2 missing in the first equation!

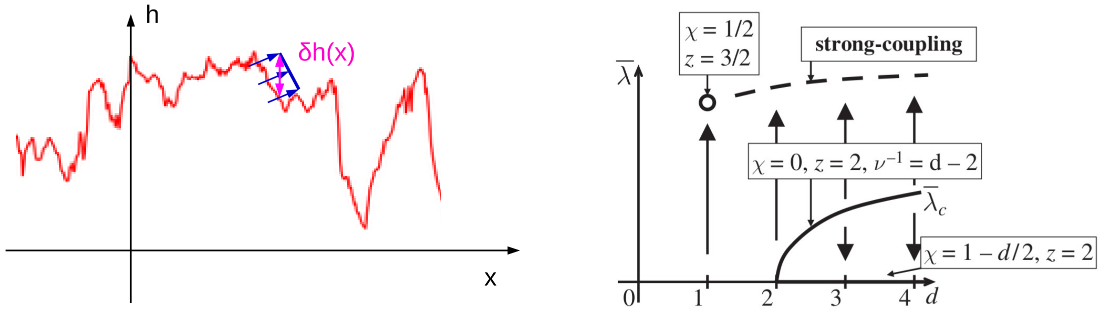

Figure 3.4: *Interface growth in the KPZ class.* (left) A typical $1d$ interface is plotted in red. The growth proceeds normally to the local front with a step $\lambda\delta t$ highlighted in blue, while it is the projection δh, in magenta in the figure, to enter the KPZ equation. (right) Diagram in different dimensionalities of the KPZ fixed points as characterized by the effective nonlinear parameter $\bar{\lambda}$; taken from Kamenev [2011].

There is also some connection between the KPZ equation and hydrodynamics. Defining $\mathbf{v} = -\nabla h$, the gradient of Eq. (3.51) yields the Burgers equation

$$\partial_t \mathbf{v} + \lambda \mathbf{v} \cdot \nabla \mathbf{v} = \nu \nabla^2 \mathbf{v} + \sqrt{\mathcal{D}}\boldsymbol{\xi}, \tag{3.52}$$

which is one form of the incompressible Navier-Stokes equations. The left-hand side is in the form of a convective derivative and suggests the invariance under the Galilean transformation to a frame moving at constant velocity $\mathbf{v}_0$

$$\mathbf{x}' = \mathbf{x} - \lambda \mathbf{v}_0 t \ , \qquad \mathbf{v}'(\mathbf{x}', t) = \mathbf{v}(\mathbf{x}, t) - \mathbf{v}_0; \tag{3.53}$$

in the KPZ framework this translates into the invariance under the tilt by the infinitesimal vector $\boldsymbol{\epsilon}$, that is

$$\mathbf{x}' = \mathbf{x} - \lambda \boldsymbol{\epsilon} t \ , \qquad h'(\mathbf{x}', t) = h(\mathbf{x}, t) + \boldsymbol{\epsilon} \cdot \boldsymbol{x}. \tag{3.54}$$

We now briefly sketch the path integral approach following Frey et al. [1996] and Kamenev [2011]. The Keldysh action can be obtained via the Martin-Siggia-Rose procedure starting with the integral over all field configurations and noise realizations

$$Z = \int D[\xi(\mathbf{x}, t)] e^{-\xi^2/2} \int D[h(\mathbf{x}, t)] \ \delta \left(\partial_t h - \nu \nabla^2 h - \frac{\lambda}{2} (\nabla h)^2 - \sqrt{\mathcal{D}} \xi \right) \tag{3.55}$$

At this point the Dirac delta is represented as $\delta(y(\mathbf{x}, t)) = \int D[p(\mathbf{x}, t)] \ e^{ipy}$, the noise ξ is Gaussianly integrated and the redefinition $p = 2ih^q$ is performed, so that we are left with

$$Z = \int D[h(\mathbf{x}, t)] D[h^q(\mathbf{x}, t)] \ e^{-S[h, h^q]} \tag{3.56}$$

where the Keldysh action for KPZ reads

$$S[h, h^q] = h^q \partial_t h - \nu h^q \nabla^2 h - \frac{\lambda}{2} h^q (\nabla h)^2 - \frac{\mathcal{D}}{2} (h^q)^2. \tag{3.57}$$

The correlation function in this formalism is obtained by adding a source term $\int d\mathbf{x}dt \ (jh + j^q h^q)$ to (minus) the action and taking the functional derivative

$$C(\mathbf{x}, t) = \langle h(\mathbf{x}, t) h(\mathbf{0}, 0) \rangle = \left. \frac{\delta^2 \log Z[j, j^q]}{\delta j(\mathbf{x}, t) \delta j(\mathbf{0}, 0)} \right|_{j, j^q = 0} . \tag{3.58}$$

Together with the correlator, it is in general necessary to consider the response function (or retarded Green's function)

$$G(\mathbf{x}, t) = \langle h(\mathbf{x}, t) h^q(\mathbf{0}, 0) \rangle = \left. \frac{\delta \langle h(\mathbf{x}, t) \rangle}{\delta j^q(\mathbf{0}, 0)} \right|_{j, j^q = 0} . \tag{3.59}$$

Since this is an out-of-equilibrium model, in principle the correlator and response function are not linked by a fluctuation-dissipation relation, as it occurs in equilibrium statistical mechanics. This is rooted in the fact that, in order to treat the dynamics, the Keldysh partition function is expressed in terms of two independent fields h, h^q, while in the Keldysh action for an system h and h^q are related by a symmetry transformation (Sieberer et al. [2015]).

At this point it is useful to rewrite the KPZ equation in Fourier space as

$$h(\mathbf{k},\omega) = G_0(\mathbf{k},\omega)\xi(\mathbf{k},\omega) + \frac{\lambda}{2}G_0(\mathbf{k},\omega)\int \frac{d\mathbf{q}}{(2\pi)^d}\frac{d\omega'}{2\pi}\,\mathbf{q}\cdot(\mathbf{k}-\mathbf{q})h(\mathbf{q},\omega')h(\mathbf{k}-\mathbf{q},\omega-\omega'), \tag{3.60}$$

where the bare response function is given by

$$G_0(\mathbf{k},\omega) = \frac{1}{-i\omega+\nu\mathbf{k}^2}, \tag{3.61}$$

corresponding to $G_0(\mathbf{k},t) = e^{-\nu\mathbf{k}^2 t}$ in real time, which can be also recognized as the kernel of the heat equation. When $\lambda = 0$ the KPZ equation reduces to the linear Edwards-Wilkinson (EW) equation, which is easily integrated and yields the bare correlator

$$C_0(\mathbf{k},\omega) = \frac{\mathcal{D}}{\omega^2+(\nu\mathbf{k}^2)^2}. \tag{3.62}$$

It is instructive to consider the perturbative renomalization group (RG) procedure applied to the KPZ equation. The idea is to progressively integrate out the high momentum[6] components of the fields and to write an effective action with renormalized parameters for the coarse-grained fields; assuming that λ is small, the renormalized parameters are computed perturbatively.

In practice one introduces an ultraviolet cutoff Λ and breaks the momentum space in two regions, $[0,\Lambda/b]$ and $[\Lambda/b,\Lambda]$ with $b>1$. The slow or coarse-grained component of the h field is $h_s(k,\omega) = h(k,\omega)$ for k in the first interval and zero otherwise; in a similar way one builds h^q_s and the fast fields h_f, h^q_f. The action is correspondingly split in the following manner:

$$S[h,h^q] = S_s[h_s,h^q_s] + S^0_f[h_f,h^q_f] + \delta S_{fs}\ , \quad \delta S_{fs} = -\frac{\lambda}{2}\int dx\,\left[h^q_s(\partial_x h_f)^2 + 2(h_f\partial_x h_f)(\partial_x h_s)\right] + \ldots \tag{3.63}$$

where in view of the next developments we have neglected a few terms and in the fast action we cut the nonlinear vertex. The fast degrees of freedom are then perturbatively integrated out

$$\int_{s,f} e^{-S} = \int_s e^{-S_s}\langle e^{-\delta S_{fs}}\rangle_{f,0} = \int_s e^{-S_s+\log\langle\exp[-\delta S_{fs}]\rangle_{f,0}}, \tag{3.64}$$

where the integrals imply integration over the fast and slow degrees of freedom and the average over the fast Gaussian system $\langle\cdot\rangle_{f,0} = \int_f \cdot\, e^{-S^0_f}$ has been introduced. At this point one expands the inner exponential in a series of λ, computes the Gaussian averages via the Wick theorem and takes the logarithm; the coefficients of the series in λ contain the slow fields and momenta, which are then included as a correction to the bare parameters. The one-loop corrections to $\nu, \mathcal{D}$ are expressed diagrammatically as[7]

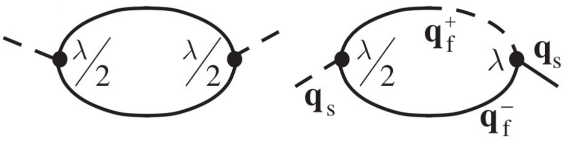

where the inner (outer) lines correspond to the fast (slow) fields and the dotted (solid) lines to h^q (h) respectively. The first diagram renormalizes the $\frac{\mathcal{D}}{2}(h^q)^2$ term, the second $\nu h^q\partial_x^2 h$. The one-loop renormalization of the vertex is instead determined by the two diagrams

---

[6] In principle one should do the same thing for the frequencies, but in practice performing this procedure on momenta is enough to cure the divergencies.

[7] plots taken from Kamenev [2011].

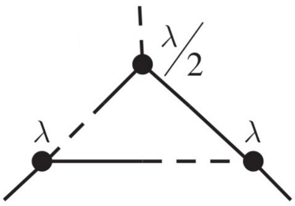

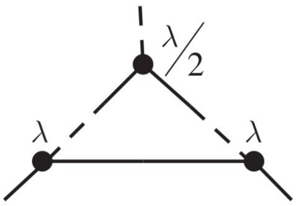

which however cancel out. The cancellation of the vertex corrections repeats itself at any order of perturbation theory, and there is a deep reason behind. Since h_s appears in the vertex δS_{fs} only through its spatial gradient, there is no correction to $h^q \partial_t h$. On the other hand, the Galilean or tilt invariance of the microscopic requires that the form of the convective derivative remains the same at each scale[8]: if $h^q \partial_t h$ is not renormalized, the nonlinear term λ is preserved in the RG flow too.

Before integrating out the fast degrees of freedom, one usually performs the rescaling $\mathbf{k} \to b\mathbf{k}$ so that the new momenta live in the original shell $[0, \Lambda]$ and the initial action with corrected parameters is recovered; also the field are correspondingly rescaled according to

$$\mathbf{r} \to \mathbf{r}/b, \quad t \to t/b^z, \quad h \to h/b^\chi, \quad h^q \to h^q/b^{\chi^q}, \tag{3.65}$$

which corresponds to zooming out the system and where the three exponents z, χ, χ^q appear. Because of the above discussion, it is convenient to implement explicitly the stationarity of $h^q \partial_t h$ under the RG flow, which is done by setting $\chi^q = -\chi - d$. In the absence of the nonlinearity the Edwards-Wilkinson equation is trivially scale-invariant provided that $\nu, \mathcal{D}$ are adimensional, with exponents that are then fixed to $z = 2, \chi = 1 - d/2$ by dimensional analysis. Since the scaling of the KPZ nonlinear term occurs with the exponent $2 - d - z - 2\chi - \chi^q$, the previous condition on χ^q implies that λ does not flow if

$$\chi + z = 2; \tag{3.66}$$

this is the fundamental relation between the exponents which stems from the tilt invariance of the KPZ equation.

The discrete RG steps are made into a continuous flow by setting $b = e^s$ and computing derivatives of the renormalized parameters with respect to s. It is convenient to introduce the effective KPZ nonlinearity $\bar{\lambda}(s) = \lambda \sqrt{\frac{2\nu(s)}{\mathcal{D}(s)^3}}$, which is the quantity that fully determines the dynamics of the adimensionalized KPZ equation

$$\partial_{\bar{t}} \bar{h} = \bar{\nabla}^2 \bar{h} + \frac{\bar{\lambda}}{2} (\bar{\nabla} \bar{h})^2 + \bar{\xi}. \tag{3.67}$$

The RG equation for $\bar{\lambda}$ reads

$$\partial_s \bar{\lambda}^2 = \left(\epsilon + \frac{1 - 2\epsilon}{1 - \epsilon/2} S_d \bar{\lambda}^2 \right) \bar{\lambda}^2 \tag{3.68}$$

with S_d the surface of the momentum sphere and $\epsilon = 2 - d$, while $\nu, \mathcal{D}$ flows as

$$\partial_s \nu = (z - d - 2\chi + S_d \bar{\lambda}^2)\nu, \qquad \partial_s \mathcal{D} = (z - 2 - \frac{\epsilon}{d} S_d \bar{\lambda}^2)\mathcal{D}. \tag{3.69}$$

From Eq. (3.68) it is clear that the Gaussian fixed point $\bar{\lambda} = 0$ is stable only if $d > 2$ [9]. In these dimensionalities there exist also another perturbative unstable fixed point for $\bar{\lambda}_c^2 = -\epsilon/S_d$; for small negative ϵ it is possible to inject $\bar{\lambda}_c$ in the RG equations and extract consistently χ, z from the requirement that $\partial_s \nu = \partial_s \mathcal{D} = 0$. One then finds $\chi = O(\epsilon^2), z = 2 - O(\epsilon^2)$ which express the tendency of the interface to become flat on large scales. As suggested by Fig. 3.4.b at even higher coupling constants the RG will flow towards a strong coupling regime which goes beyond this perturbative analysis.

---

[8] that a symmetry is preserved in the RG flow and no anomalies occur is formally proven by making use of the Ward identities (Frey and Täuber [1994]).

[9] that the critical dimension should be 2, it can be understood already at the level of the Gaussian theory, whose scaling entails that the dimension of the nonlinear coupling is $\epsilon/2 = 1 - d/2$, which is irrelevant in $d > 2$.

In low dimensions $d < 2$, instead, the Gaussian fixed points is always unstable and the surface roughens for any microscopic value of $\lambda \neq 0$. The perturbative analysis predicts in $d = 1$ the non-perturbative fixed point $\bar{\lambda}^2 = 1/(2S_1)$, leading to $\chi = 1/2, z = 3/2$; while the one-loop approach is in principle unreliable in this regime, this is by chance the correct result, as shown below.

This procedure can be applied also to the Kuramoto-Sivashinky equation introduced in the previous Section, as done by Ueno et al. [2005]. In particular, the same Galilean invariance argument holds so that λ is not renormalized in the RG flow; instead, the fourth derivative term turns out to be irrelevant and in general the surface tension term will be generated even if not present in the microscopic equation.

It is also important to mention that, while we have shown here the one-loop perturbative corrections, it is possible to set up a non-perturbative RG procedure (Canet et al. [2010]), which allows to study rigorously the flow in all dimensionalities.

In 1D the previous one-loop analysis leads to the correct result for the exponents in spite of the fact that it is not well justified. However, it is possible to deal with this case with simple and rigorous arguments. To start with, the Fokker-Planck equation associated with the KPZ equation reads

$$\partial_t P[h, \mathbf{x}, t] = \int d\mathbf{x} \frac{\delta}{\delta h(\mathbf{x})} \left[-\left(\nu \nabla^2 h + \frac{\lambda}{2} (\nabla h)^2 \right) P + \frac{\mathcal{D}}{2} \frac{\delta P}{\delta h(\mathbf{x})} \right], \tag{3.70}$$

the first term arising essentially from the conservation of probability (continuity equation) and the second from heat-like diffusion. The remarkable fact is that in $1d$ the field distribution

$$P[h] = e^{-\frac{\nu}{\mathcal{D}} \int dx (\partial_x h)^2} \tag{3.71}$$

is a stationary solution of the Fokker-Planck equation, as a consequence of $3\partial_x^2 h (\partial_x h)^2 = \partial_x (\partial_x h)^3$ being a full derivative. Importantly, it follows that, even though ν and $\mathcal{D}$ will both grow in the RG flow[10], the ratio $A = \frac{\nu}{2\mathcal{D}}$ is not renormalized and the equal time correlator

$$C(x, 0) = \langle h(x, 0) h(0, 0) \rangle = A|x| = C_0(x, 0) \tag{3.72}$$

is independent (of the very presence) of λ. In particular, one cannot determine from static and isolated snapshots of the system if the underlying microscopic equation is the linear EW or the nonlinear KPZ one. From Eq. (3.72) one can see that the roughening exponent is $\chi = 1/2$; then, from $\chi + z = 2$ as prescribed by the Galilean invariance, the dynamical exponent $z = 3/2$ is obtained. These results are strongly related to the invariance in $1d$ under the generalized time-reversal transformation

$$h(x, t) \to -h(x, -t) \ , \qquad h^q(x, t) \to h^q(x, -t) + 2A\partial_x^2 h(x, -t). \tag{3.73}$$

Exploiting this symmetry plus the causality constraint $G(x, t < 0) = 0$ for the response function, one can prove the fluctuation-dissipation relation

$$C(k, \omega) = \mathcal{D} |G(k, \omega)|^2 \tag{3.74}$$

or equivalently $G(k, t) = \frac{2\nu k^2}{\mathcal{D}} \theta(t) C(k, t)$ in real time.

In $1d$ the precise scaling of the steady-state solutions of the KPZ equation has been computed exactly by Prähofer and Spohn [2004] by expressing the 2-point correlator of the polynuclear growth model, which belongs to the KPZ universality class, in terms of a Painlevé II equation. The result, anticipated in the previous Section, is

$$C(\mathbf{x}, t) = \langle h(\mathbf{x}, t) h(\mathbf{0}, 0) \rangle = \left(\frac{1}{2} \lambda A^2 t \right)^{2/3} g_{KPZ} \left(\frac{x}{(2\lambda^2 A t^2)^{1/3}} \right) \tag{3.75}$$

with $g_{KPZ}(u) - 2|u| \to 0$ for $u \to \infty$ and $g_{KPZ}(u) \to 1.150...$ for $u \to 0$.

Last but not least, we mention that it is possible to study the growth process going beyond the correlation functions and looking directly at the stochastic properties of height variable. One indeed finds that

$$h(0, t) \simeq v_\infty t + (\kappa t)^{1/3} \chi(t), \tag{3.76}$$

---

[10] at the strong coupling fixed point ν and $\mathcal{D}$ do not converge.

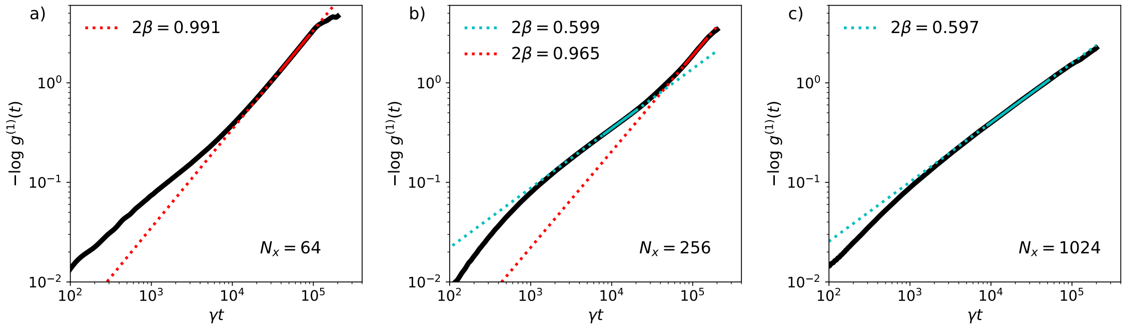

Figure 3.5: *Kardar-Parisi-Zhang to Schawlow-Townes crossover in the temporal coherence of finite, one-dimensional laser arrays* The numerical prediction of Eq. (3.36) for the logarithm of the equal–space time correlation function $-\log g^{(1)}(t)$ is plotted in loglog scale as a function of time for increasing system sizes $N_x = 64$ (left), $N_x = 256$ (middle), $N_x = 1024$ (right). In all cases, lasing occurs around $k_x^{las} = 0$. For a given temporal window, the decay of the coherence is dominated by a Schawlow–Townes–like diffusion $g^{(1)}(t) \sim e^{-B|t|}$ for small sizes [panel (a)] and by the KPZ behavior $g^{(1)}(t) \sim e^{-B|t|^{2/3}}$ for large sizes [panel (c)]. The crossover between the two regimes is visible for intermediate sizes [panel (b)]. The cyan and red lines are fits of $\log[-\log g^{(1)}(t)]$ with functions of the form $2\beta \log|t| + B'$. Other system parameters: $J = 0.5\gamma$, $P = 2\gamma$, $n_S = 1000, D = \gamma$.

where v_∞, κ are non-universal parameters and $\chi(t)$ is a random variable of zero mean and unit variance distributed according to three possible distributions well-known in random matrix theory: Tracy-Widow for the Gaussian Unitary Ensemble (TW-GUE) or for the Gaussian Orthogonal Ensemble (TW-GOE) or Baik-Rains (BR). These three possibilities define three sub-universality classes, which are selected by the KPZ dynamics depending on the boundary conditions; for an effectively infinite system at the steady-state the BR distribution is the relevant one. We point to the review by Takeuchi [2018] for more details and for the original references.

3.3 Linewidth of extended 1D laser systems*

(this Section closely follows Sec. II of Amelio and Carusotto [2019])

As explained before, in the Schawlow-Townes treatment very well known to laser theorists the spatial extension of the laser is irrelevant and the dynamics is effectively restricted to the phase of a single complex number, the main quantity of interest being the linewidth. On the contrary, in the statistical mechanics literature the focus has been so far on the KPZ scaling in 1D infinite systems. Even though the finite size corrections to the KPZ behaviour have been studied to some extent, the linewidth or coherence time at asymtotic timescales had never been considered before to our knowledge. In this Section we want to bridge the gap and study how spatial fluctuations affect the temporal coherence of the nonequilibrium field at very long times. To this purpose, the crucial quantity to study is the time dependence of the equal–space correlator

$$g^{(1)}(t) = \frac{1}{n_0} \left|\langle \psi^*(x,t)\psi(x,0)\rangle\right| , \tag{3.77}$$

which characterizes the temporal coherence of the emission. The dependence of $g^{(1)}$ on x has been dropped since we are considering a spatially uniform system.

Within the Bogoliubov approximation, modes of different momenta are decoupled. For a discrete lattice, one obtains with simple algebra that

$$\langle[\phi(x,t) - \phi(x,0)]^2\rangle = \frac{1}{N_x}\sum_x \langle[\phi(x,t) - \phi(x,0)]^2\rangle = \frac{1}{N_x}\sum_k \langle[\phi(k,t) - \phi(k,0)]^2\rangle \simeq$$

$$\simeq \frac{1}{N_x}\sum_k \left\langle \left[\int_0^t dt'\; e^{-i\omega_+(k)(t-t')}\sqrt{\frac{\bar{D}_k}{n_0}}\xi_1(t')\right]^2 \right\rangle = \frac{1}{n_0 N_x}\sum_k \bar{D}_k \int_0^t dt' e^{-2i\omega_+(k)(t-t')}. \tag{3.78}$$

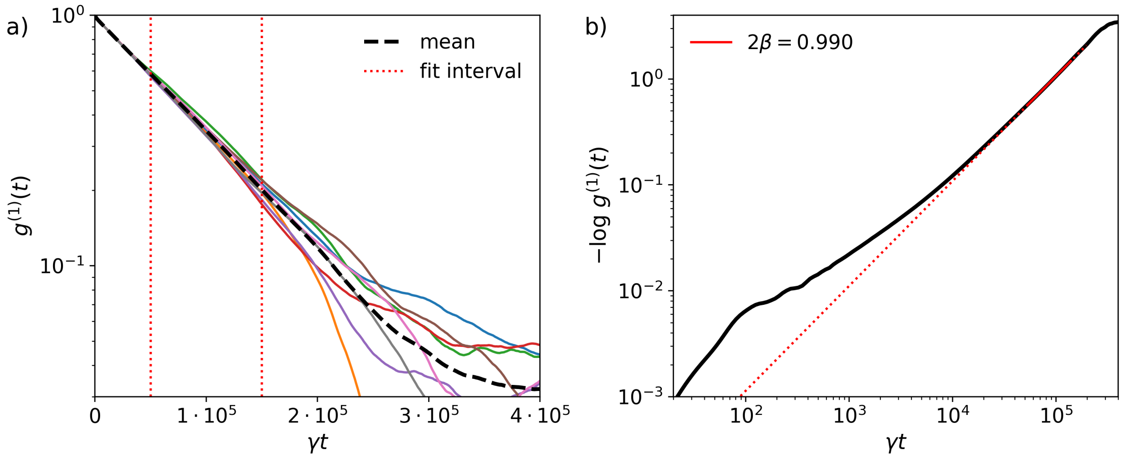

Figure 3.6: *Extraction of the coherence time.* (a) Correlation functions $g^{(1)}(t)$ extracted from 8 runs and their average, for $N_x = 128, J = 5\gamma$. Linear fitting between red dots yields τ_c. (b) Loglog plot of (minus) the logarithm of averaged $g^{(1)}(t)$. Red line is linear fit of $\log[-\log g^{(1)}(t)]$ with $2\beta \log|t| + B'$, highlighting the Schawlow–Townes regime.

where for illustrative purposes we have restricted the sum to the modes belonging to the Goldstone branch and close to $k = 0$. The effective drift coefficients $\bar{D}_k = \left(\frac{1}{2} + \frac{\Gamma}{2\sqrt{\Gamma^2 - 4(Jk^2)^2}}\right)^2 D$ are determined by the shape of the Bogoliubov modes and tend to D in the long-wavelength limit $k \to 0$. In this same limit, the lowest Bogoliubov mode has a diffusive character with $\omega_+(k) = -i\gamma_+(k) = -iJ^2\Gamma^{-1}k^4$, as reviewed in the previous Section. The factor $1/N_x$ in front of (3.78) can be interpreted by viewing the white spatial noise as randomly drawing noise realizations with a given k and unit strength at each site. The probability to pick a given mode is then $1/N_x$. Note that the "ultraslow decay of fluctuations" that was numerically observed in [Seclì et al., 2019] is a consequence of the softness of the diffusive Goldstone branch and thus a general feature of spatially extended lasers.

In a spatially finite system where k is quantized, only the $k = 0$ mode gives a finite contribution at long times, proportional to $|t|$; the contribution of all other modes decays instead exponentially with time. From this, one immediately obtains the expression of the Bogoliubov–Schawlow–Townes coherence time

$$\tau_c = \tau_{ST} = 2\gamma_{ST}^{-1} = \frac{2n_0N_x}{D} \tag{3.79}$$

that generalizes the Schawlow-Townes phase diffusion to the case of a finite laser array, n_0N_x being equal to the total number of photons. Notice that τ_{ST} does not depend on J. Moreover, the array can lase in any k_x^{las} depending on the initial conditions: the diffusive Goldstone dome will then feature an effective coupling J_{eff}, given by the curvature of the free array dispersion in k_x^{las}, but τ_{ST} will not depend on k_x^{las}. In any case, in the following of the Chapter we will stick to the case of zero winding number.

For the sake of discussion, the situation is a bit different for a strictly infinite array. In this case, the sum over discrete k modes has to be replaced by an integral in dk. This yield the Bogoliubov prediction $g^{(1)}(t) \sim e^{-B|t|^{3/4}}$, where B is a constant. The slower power-law decay stems from the fact that the specific $k = 0$ mode is now occurring with a probability zero. It is worth noting that a different scaling would be found in the presence of a nonlinear refractive index. In this case, the imaginary part of the Bogoliubov frequency would scale as $\gamma_+(k) \propto k^2$ in the long-wavelength $k \to 0$ limit (Wouters and Carusotto [2007]), leading to a slower decay $g^{(1)}(t) \sim e^{-B|t|^{1/2}}$ in an infinite one-dimensional system. Instead, the coherence time (3.79) of a finite Bogoliubov system is not changed by the refractive index nonlinearity.

Of course, the linearized Bogoliubov approximation, where different modes are decoupled, is not adequate for an infinite or large enough system, where nonlinear KPZ features set in.

For an infinite system a stretched exponential behavior

$$g^{(1)}(t) \sim e^{-B|t|^{2\beta}} \tag{3.80}$$

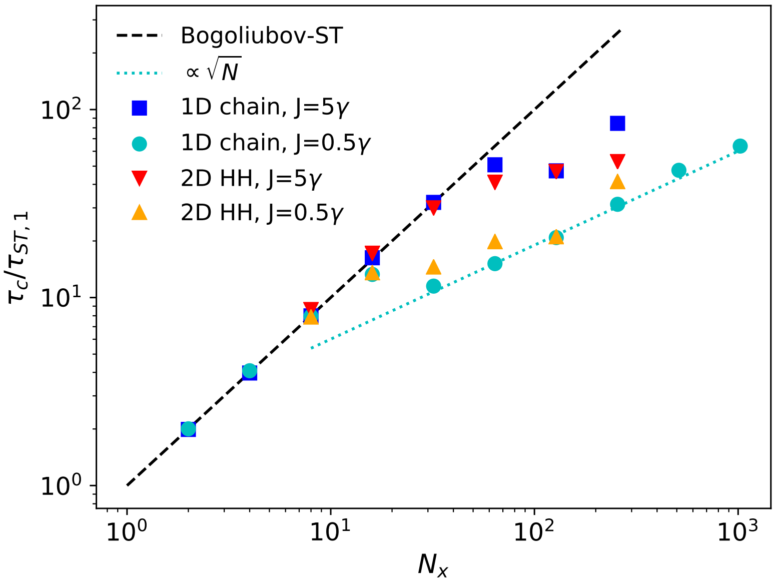

Figure 3.7: *Scaling of the coherence time with system size N_x.* The coherence time τ_c is extracted from the long-time exponential decay of coherence for different systems. Blue and cyan markers refer to the one-dimensional, topologically trivial arrays of laser resonators of Eq. (3.36) with different values of the inter-site coupling $J = 5\gamma$ and $J = 0.5\gamma$, and zero winding number. The red and orange markers refer to the topological laser case of Eq. (4.23) for the same two values of J. For each point, the value of the coherence time τ_c is normalized to an effective single-site coherence time $\tau_{ST,1}$. For the 1D array, this is defined by the Schawlow-Townes formula (3.79). For the topological 2D array, it is given by $\tau_{ST,1} \equiv \tau_{ST}/N_x$, with τ_{ST} being the Bogoliubov–Schawlow-Townes prediction (4.29) that includes the (small) Petermann correction.

was predicted in [He et al., 2015], with a universal $2\beta = 2\chi/z = 2/3$ and a non–universal value of the constant B.

If the system is sufficiently large but finite, the Bogoliubov approximation breaks down, but the spontaneously broken $U(1)$ symmetry still imposes that the coherence must decay at long times at least as fast as a pure exponential, $g^{(1)}(t) \sim e^{-|t|/\tau_c}$. In this case, we expect that the KPZ physics typical of the infinite chain should remain visible only for intermediate times, up to a saturation time scaling as $(N_x)^z$.

These arguments on the functional form of the temporal decay of coherence are quantitatively illustrated in Fig. 3.5, where we display the temporal correlation function computed by numerically solving Eq. (3.36) for three different system sizes $N_x = 64, 256, 1024$ initialized in the $k_x = 0$ state: the thick black line shows $-\log g^{(1)}(t)$, while the red and cyan lines are linear fits in the loglog scale of the plot. Keeping the same observation window, for small system sizes the temporal decay of the coherence $g^{(1)}(t)$ is mainly diffusive and follows an exponential law [panel (a)]. For very large sizes [panel (c)], the exponential Schawlow–Townes behavior is pushed at very long times so that only the KPZ stretched exponential $g^{(1)}(t) \sim e^{-B|t|^{2/3}}$ is clearly visible in the time window displayed in the plot. An attempt to see the exponents of both regimes on a single plot is shown in the plot for an intermediate size shown in panel (b): while a hint of them is visible, a complete separation of the two regimes would require a very large system sizes and very long observation times, which is numerically very demanding.

More specifically, the numerical effort required for the calculation of $\tau_c(N_x)$ grows up rapidly with N_x, since one has to access the dynamics at very long times, larger than the KPZ saturation time scaling as $\sim N_x^{3/2}$. For this reason, an intensive analysis of the accuracy of the data points reported in Fig. 2 of the main text has been restricted to the $N_x = 128, J = 5\gamma$ case.

For this dataset we performed 8 runs of duration $T = 10^8\gamma^{-1}$, the corresponding correlation functions $g^{(1)}(t)$ being reported in Fig. 3.6.a. Because of finite statistics, the resolution of $g^{(1)}(t)$ is limited and the curves reach a noisy plateaux at very large times. The average of the 8 runs is taken (more specifically the complex functions $\langle\psi^*(x,t)\psi(x,0)\rangle$ are averaged over all the runs and the absolute modulus is taken afterwards) and we extract τ_c by a linear fit of $\log g^{(1)}(t)$ in

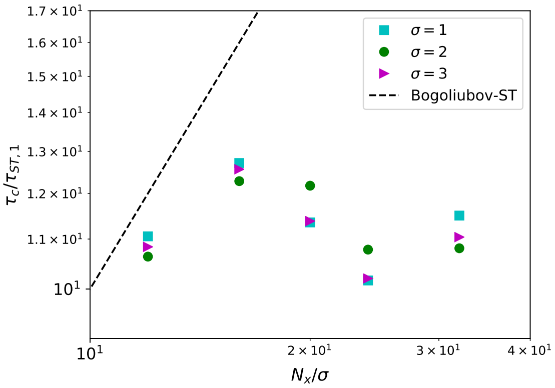

Figure 3.8: *Non-monotonic behavior of* $\tau_c(N_x)$*.* The coherence time $\tau_c(N_x)$, corresponding to the cyan points of Fig. 3.7, is studied for intermediate system sizes at different values of the rescaling parameter σ, which quantifies how fine the numerical grid is. The agreement between the different datasets suggests that the curious monotonic behavior observed is an instrinsic property of the continuous Kuramoto-Sivashinskii equation, and not an artifact of the grid discretization or an effect due to large density fluctuations.

the interval indicated by the red dots, which is of the order of τ_c itself. The same is done also for the single runs, resulting in a mean coherence time of $\gamma\tau_c \simeq 9.72 \cdot 10^4$ with a standard deviation of $0.73 \cdot 10^4$, which is approximatively the size of the marker in Fig. 2 of the main text. From the averaged correlation function instead we extracted $\gamma\tau_c \simeq 9.40 \cdot 10^4$. Recall that our goal here is mainly to establish deviations from the Bogoliubov–Schawlow–Townes prediction, which yields the much larger $\gamma\tau_{ST} \simeq 2.56 \cdot 10^5$.

The logarithm of the averaged $g^{(1)}(t)$ is plotted in loglog scale in Fig. 3.6.b. Here we fit the curve in the same interval of Fig. 3.6.a, to prove that τ_c has been computed by considering large enough times to be in the Schawlow-Townes regime.

Finally, we argue that this analysis allows to have a rough estimate of the uncertainty of τ_c also for the other sizes and couplings, for which we have performed a single run, instead of 8. In particular, for $N_x < 128$, the standard deviation computed here is an upper bound for the statistical error done by extracting $\tau_c(N_x)$ from a single simulation of duration T.

The KPZ scaling of $g^{(1)}(t)$ at intermediate times is a clear indication of the crucial role of nonlinear coupling between modes in determining the phase dynamics. While the linearized Bogoliubov theory predicts the (qualitatively correct) exponential form of the decay of coherence at long times, it is natural to wonder whether the KPZ nonlinear couplings are responsible for any quantitative deviation of the coherence time from the Bogoliubov–Schawlow–Townes prediction (3.79).

This issue is numerically investigated in Fig. 3.7 where we plot the numerical result for the coherence time τ_c in one-dimensional arrays of increasing sizes for two different values of the intersite coupling $J = 5\gamma$ (blue) and $J = 0.5\gamma$ (cyan) . To better highlight the KPZ features, we have normalized the coherence time to the single site Schawlow–Townes coherence time

$$\tau_{ST,1} \equiv \tau_{ST}/N_x = \frac{2n_0}{D}. \tag{3.81}$$

For all parameter choices, the coherence time follows the Bogoliubov scaling proportional to N_x until a certain critical size numerically compatible with the scaling of $l^* \sim J^{4/7}$ given in (3.46), after which its increase with N_x occurs at a much slower rate.

This marked deviation is indeed expected and can be understood looking at the KPZ equation (3.48): the total phase drift is the $\tilde{k} = 0$ part of the phase field, which can be decomposed in two statistically independent contributions

$$\tilde{\phi}(\tilde{x},\tilde{t}) = \tilde{\phi}_0(\tilde{t}) + \tilde{\phi}'(\tilde{x},\tilde{t}). \tag{3.82}$$

Here, $\tilde{\phi}_0$ accounts for the global phase evolution generated by the $\tilde{k} = 0$ component of noise,

$$\partial_{\tilde{t}}\tilde{\phi}_0 \equiv \sqrt{\mathcal{D}}\xi_1(\tilde{k} = 0,\tilde{t}), \tag{3.83}$$

and yields the Schawlow–Townes drift. Even though the equation for $\tilde{\phi}'(\tilde{x},\tilde{t})$ is independent of $\xi_1(\tilde{k}=0,\tilde{t})$, an additional evolution of $\tilde{\phi}'(\tilde{k}=0,\tilde{t})$ is induced by the finite $\tilde{k}$ components $\tilde{\phi}'(\tilde{k}\neq 0,\tilde{t})$ of the phase field via the KPZ nonlinearity λ. The additional phase noise induced by this nonlinear coupling is responsible for the deviation of the coherence time from the Bogoliubov-Schawlow-Townes prediction visible in Fig. 3.7.

We provide here some numerical evidence and theoretical argument that suggests that the exponent ρ characterizing the large N_x dependence $\tau_c \sim N_x^\rho$ should be $\rho = 1/2$ (Amelio et al. [2020a]). Indeed, let's assume a scaling behavior for the equal-space time phase correlator, in the form

$$\Delta\phi_{0,t} \sim t^{2/3} f\left(\frac{t}{N_x^{3/2}}\right), \tag{3.84}$$

so that for t smaller of the saturation time $O(N_x^{3/2})$ we can assume $f \sim 1$ and we recover the correct KPZ scaling. At longer times, instead, we make the ansatz $f(x) \sim x^{1/3}$ so that the correct diffusive time dependence is obtained: from $\Delta\phi_{0,t} \sim \frac{t}{N_x^{1/2}}$ we make the guess that $\tau_c \propto \sqrt{N_x}$ for very large N_x's. This is in good agreement with numerical data as taken for $J = 0.5\gamma$ up to $N_x = 1024$, see the cyan dotted line in Fig. 3.7, for which this scaling seems to be fulfilled at least over an order of magnitude.

The complex behaviour of $\tau_c(N_x)$ at intermediate N_x suggests that a quantitative explanation of the phenomenon requires a non–perturbative computation that we are starting to work out based on the so called Mode Coupling Approximation (Frey et al. [1996]). Here we limit to prove that the non-monotic behavior of $\tau_c(N_x)$ is an long-distance effect, and it is not due the weak value of the coupling J, which in principle could give rise to some nontrivial short-distance dynamics. This is studied by rescaling the microscopic parameters according to

$$J \to \sigma^2 J, \quad D \to \sigma D. \tag{3.85}$$

Plugging these transformations into Eqs. (3.46), we have that the only characteristic scale to be modified is $l^* \to \sigma l^*$, while the time and phase scales are unchanged. Rescaling also the physical size of the system according to $N_x \to \sigma N_x$, the effective size of the system N_x/l^* is unaffected. In Fig. 3.8 we show that $\tau_c(N_x)$ in the non-monotonic region is independent, within statistical fluctuations, of $\sigma = 1, 2$ or 3. This rules out that this strange behavior comes from discretization issues of the laser array equation. In parallel, this procedure also provides an *a posteriori* indirect check that the level of local noise is small enough to adiabatically remove the density degrees of freedom and the scales associated to the density dynamics, so to restrict to the “phase" scales of Eqs. (3.46). The non-monotonic behavior has then to be attributed to some long-distance property of the Kuramoto–Sivashinsky equation.

The results from Eq. (3.84) and other analyses will be presented in a future publication (Amelio et al. [2020a]).

3.4 Conclusions

In this Chapter we have studied the linewidth of 1D non-equilibrium quasi-condensates, as can be implemented by incoherently driven polariton wires or laser arrays.

In Section 3.1 we briefly gave the basics of laser theory and of the classical theory of the linewidth by Schawlow and Townes. In Section 3.2 we reviewed the theory of 1D non-equilibrium quasi-condensates, which have been recently studied in connection to polariton fluids, demonstrating that the low energy physics falls in the KPZ universality class.

The original results are contained Section 3.3: here we highlighted the crossover, as a function of the observation time, between KPZ scaling and phase diffusion in large but finite systems. We showed that the linewidth, that is the rate of the phase diffusion, for large systems deviates from the Bogoliubov prediction, with the further broadening being due to nonlinear phase fluctuations.

A similar linewidth enhancement is expected also for lasing in other lattice dimensionalities (with a smaller value of ρ in lower dimensions) as well as in equilibrium atomic condensates at zero temperature. For the sake of completeness, nonlinear mode couplings were predicted in (Sinatra et al. [2009]) to play a crucial role in the phase diffusion of equilibrium condensates, but have a different physical origin in Beliaev processes. The linewidth broadening effect we have reported here arises instead from spatial fluctuations; to what extent this phenomenon is qualitatively different in low dimensions, where long-range order cannot be established, remains the subject of future investigations.

Chapter 4

Theory of the coherence of the Harper-Hofstadter topological laser

The goal of the present Chapter is to apply the techniques developed in the previous Section to the study of a simple model of a 2D topological laser. This new concept of laser device holds a promise for practical applications, based on a few interesting properties arising from topology, including non-reciprocity of the emission and robustness to fabrication imperfections. Our work is the first study of the spatio-temporal coherence of topological lasers.

A due introduction to topological photonics and lasing is provided in Section 4.1, where the Harper-Hofstadter model is also presented in details. In Section 4.2 the Bogoliubov theory is applied to study the excitation modes and the coherence of the Harper-Hofstadter laser: in particular, it is shown how to map the edge dynamics to a 1D system and the Schawlow-Townes linewidth is computed. While this analysis holds for small arrays, in Section 4.3 large lattices are considered for which the phase dynamics on the edge is a nonlinear one and one can find the signatures of the KPZ universality. The robustness of the coherence properties in the presence of disorder is demonstrated in Section 4.4. Relevance for real devices is carefully considered in the final Section 4.5.

4.1 Topological lasers

In this Section we will review lasing in the edge modes of a topological structure. We will first introduce general topological features of linear photonic systems and then discuss the recent experimental realizations of lasing. The simple Harper-Hofstadter model is finally defined, which will be the basis for the investigations of the next Sections.

4.1.1 Topological photonics

Even though some sparse elements had been highlighted before, a systematic study of the topological properties of condensed matter systems started with the discovery of the Quantum Hall effect and the subsequent efforts to understand the quantization of the Hall conductance (Thouless et al. [1982]); the geometric aspects underlying the Integer Quantum Hall physics were uncovered by Simon [1983] and Kohmoto [1985]. A heterostructure containing a 2D quantum well can be doped and gated in such a way to form a 2D electron gas (2DEG). If an external magnetic field normal to the wafer is applied, the transport properties display very interesting features. In particular, the Hall conductance σ_H, defined as the current in the direction of the applied potential over the voltage generated along the transverse direction, turns out to be quantized in units of e^2/h at the integer values of the filling factor.

The Integer Quantum Hall phenomenology can be understood in terms of non-interacting electrons. In the presence of the magnetic field, the electronic states splits in highly degenerate bands, named Landau levels and separated by the cyclotron energy $\omega_B = eB/m$. Interactions and sample imperfections cause a broadening of the Landau levels with extended states living at the center of the band and localized states forming the tails. Moreover, to each Landau level it corresponds an

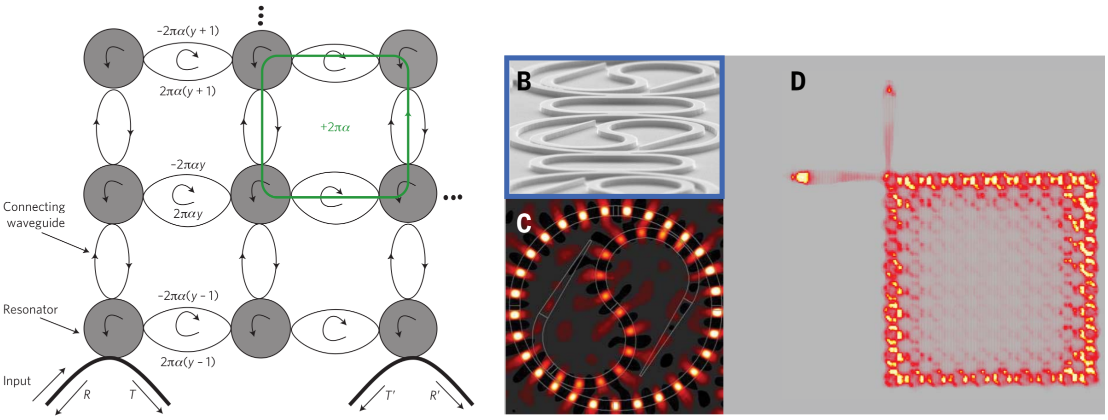

Figure 4.1: *Nonmagnetic topological laser.* (left) All-dielectric design of a $\pm 2\pi\alpha$ Berry phase per plaquette for (anti-)clockwise ring modes. This implements two symmetry-protected copies of the Harper-Hofstadter model with opposite magnetic field. (right) The addition of an S-shaped coupler in each resonator together with optical pumping of the edge of the lattice determine that the clockwise modes suppress, via gain competition and energy recirculation, the anti-clockwise modes, so to obtain chiral laser operation. Plots taken from (Hafezi et al. [2011]) and (Bandres et al. [2018]), respectively.

edge state which extends all over the boundary of the system and determines the quantization of the Hall conductivity.

Thouless et al. [1982] used the Kubo formula to write the Hall conductivity as

$$\sigma_H = -\frac{e^2}{h}\sum_n \nu_n, \tag{4.1}$$

where ν_n is the topological invariant of the n-th Landau level and can take only integer values; in the modern formulation it is called the Chern number of the band

$$\nu_n = \frac{1}{2\pi}\int_{1BZ} d^2\mathbf{k}\ \Omega_n(\mathbf{k}), \tag{4.2}$$

where we introduced the local Berry curvature

$$\Omega_n(\mathbf{k}) = i\langle\frac{\partial n(\mathbf{k})}{\partial k_x}|\frac{\partial n(\mathbf{k})}{\partial k_y}\rangle - i\langle\frac{\partial n(\mathbf{k})}{\partial k_y}|\frac{\partial n(\mathbf{k})}{\partial k_x}\rangle \tag{4.3}$$

and $|n(\mathbf{k})\rangle$ is the eigenstate of the n-th band of quasi-momentum $\mathbf{k}$. In introducing integration over the first Brillouin zone we assumed a lattice discretization of the 2DEG and periodic boundary conditions. This integer is a bulk topological invariant which determines the number and the chirality of the edge states at the boundary of the system; in a time-reversal invariant system $\nu_n = 0,\ \forall n$.

Because the remarkable transport properties arising from the Pauli principle play a major role in Quantum Hall systems, the application of the theory of topological band invariants remained limited to electronic systems for more than two decades. In the meanwhile, important advances were made for both non-interacting and interacting electron systems. For the former class of models, it is worth mentioning the proposals by Haldane [1988], where time-reversal symmetry is broken and one has nonzero Chern numbers without applying a magnetic field, and the Quantum Spin Hall Effect by Kane and Mele [2005], where a so-called Z_2 topological invariant is introduced for a time reversal invariant system. Concerning interacting systems instead, a tremendous effort has been profounded in the theoretical understanding of Fractional Quantum Hall states (Cage et al. [2012]); ongoing research is devoted to the experimental engineering and detection of anyons and Majorana fermions, which would provide a robust platform for quantum computation (Nayak et al. [2008]).

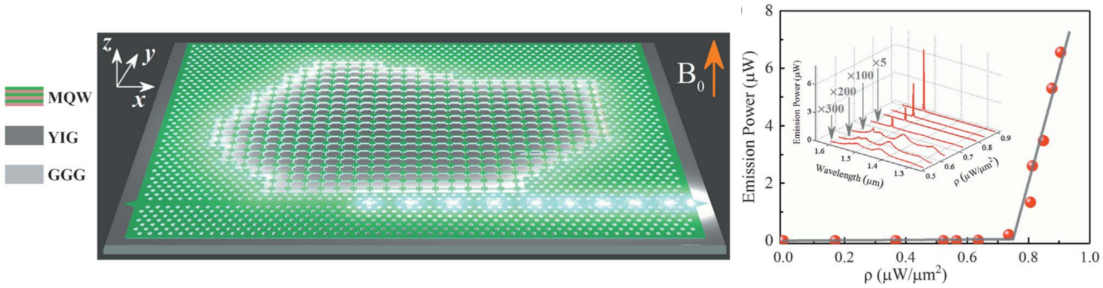

Figure 4.2: *Magnetic topological laser.* (left) Applying a magnetic field to a photonic crystal containing YIG elements allows to have nonreciprocal lasing in arbitrarily shaped geometries. (right) The power slope efficiency of the device display the typical behavior of a laser with a well defined threshold. In the inset, the spectral narrowing of the emission is demonstrated upon increasing the pump power. Plots taken from (Bahari et al. [2017]).

It was just with the work by Haldane and Raghu [2008] that the field of topological band engineering for photons took over: the authors remark that the Chern number is a feature of a single-particle problem with broken time-reversal symmetry; this condition can be achieved also without a real magnetic field and charged particles, in particular with optical waves[1]. Since photons are neutral, bosonic and non-conservative particles, the hallmark of topology is here probed by using the edge modes at the boundary of the lattice as directional waveguides. Moreover, because of the well-defined chirality of the edge modes in the gap between the bands, when disorder is present the edge states remain extended along the boundary of the system and can just hybridize with states of the same chirality: as a result, a wave travelling in such a mode won't be backscattered by disorder, which is commonly referred to as topological protection or topological robustness (Raghu and Haldane [2008]). The first experimental realization of these concepts by Wang et al. [2009] consisted of a two-dimensional magneto-optical photonic crystal in the microwave domain.

However, this and similar strategies do not allow to create strong magnetic fields for photons. A very interesting alternative path was pursued by Hafezi et al. [2011, 2013], where the two polarizations of the photon are exploited to build a Spin Hall system consisting of linear optical elements and a large bandgap can be obtained without breaking time-reversal symmetry (see Fig. 4.1.a below). A variety of other proposals based on artificial gauge fields, Floquet engineering (Rechtsman et al. [2013]), Thouless pumping, etc. has since thrived, as described in a few recent reviews (Lu et al. [2014], Ozawa et al. [2019]).

4.1.2 Topological lasers: Experimental implementations

In the last four years several groups have been able to obtain lasing in topological edge modes, with implementations spanning over a wide spectrum of topological insulator models, frequency ranges and material platforms. Some of these advances have been covered in the recent review paper by Ota et al. [2018].

The first platform is based on the all-dielectric design by Hafezi et al. [2011] to engineer a finite Berry phase around a plaquette by connecting the resonators of the lattice with waveguides of increasing lengths, depicted in Fig. 4.1.a. This creates a spin-Hall system where the role of the spin is played by the propagation verse around the ring. Bandres et al. [2018] modified this system by using the S-shaped resonators in Fig. 4.1.b-c to favour one of the two spins, which is effective because the lasing nonlinearity breaks the reciprocity of the Maxwell's equations in linear media. Moreover, they optically pumped only the external resonators, made of InGaAsP QWs, and obtained chiral laser emission, as depicted in Fig. 4.1.d. The topological bandgap obtained here was of 80 GHz, while with real magnetic fields one can reach few GHz.

In the meanwhile, Bahari et al. [2017] achieved topological lasing in a photonic crystal containing elements made of yttrium iron garnet (YIG), a gyrotropic material that upon application of a magnetic field breaks the time-reversal invariance of light propagation. By engineering the unit cell in different ways inside and outside of an arbitrarily shaped region (which in the paper resembled the United States, as pictured on the left of Fig. 4.2), one can define two topologically distinct regions, with a chiral edge mode living at the interface. In this experiment, all the inner region is optically pumped and lasing in the edge state is selected because of the sharp spectral profile of the gain medium, falling at the wavelength frequencies of around 1530 nm. Nice power efficiency characteristics and spectral narrowing above the lasing threshold were measured and are reported on the right panel of Fig. 4.2.

---

[1] Actually, that the theory of the geometric phase does not require quantum mechanics but applies also to classical waves had already been mentioned at the end of (Berry [1984]).

More recently, an electrically pumped device based on the Quantum Cascade Laser principle has been built on top of a valley-Hall photonic crystal by Zeng et al. [2020]. The emission is in the therahertz range and unfortunately several side-peaks appear in the spectrum, suggesting that many modes are lasing.

Single-mode emission at telecommunication wavelength was studied by Noh et al. [2020] by varying the degree of asymmetry of the unit cell of a photonic crystal, which is a way to control the bandgap of the associated valley-Hall topological insulator. For a properly chosen bandgap, one standing-wave mode of the system has quality factor much larger than the other ones, so that when optical pumping is switched on it wins the mode competition.

Other works, less relevant for our goals since no chiral transport is supported, have investigated lasing at the localized resonance of a 1D quasi-periodic Aubry-André-Harper model (Pilozzi and Conti [2016]) or in the 0-dimensional edge states of the so-called SSH chain (St-Jean et al. [2017], Parto et al. [2018], Han et al. [2019]), together with a high-performance topological bulk laser, exploiting band-inversion-induced reflection in an array of patterned nanodisks. We also mention a recent theoretical proposal by Yang et al. [2020] to obtained stable mode-locked laser operation, resulting in the emission of short intense pulses, in a Floquet system with one real and one synthetic dimension.

4.1.3 The Harper-Hofstadter laser

We now move to review an important model of laser device, which is obtained by amplifying the chiral edge modes of a Harper–Hofstadter topological insulator (Longhi et al. [2018], Seclì et al. [2019], Amelio and Carusotto [2019]). We will discuss both class-A and class-B devices and the differences between these two cases. In the former case, the dynamics of the carriers which provide the gain mechanism is assumed fast enough to be adiabatically eliminated. In the latter instead, the carrier dynamics is retained by relying on simple kinetic equations.

The idea is to start with a photonic lattice implementing the so-called Harper Hofstadter (HH) model (Ozawa et al. [2019]). In the Landau gauge, the HH Hamiltonian reads:

$$H = -J \sum_{x,y} \left\{ \hat{\psi}^\dagger_{x,y} \hat{\psi}_{x,y+1} + e^{-2\pi i \theta y} \hat{\psi}^\dagger_{x,y} \hat{\psi}_{x+1,y} + h.c. \right\} \tag{4.4}$$

where the sum runs over all the sites of the lattice, $x = 1, ..., N_x, y = 1, ..., N_y$, $\hat{\psi}_{x,y}$ is the photon annihilation operator at the site (x, y) and J a real hopping amplitude. The strength of the synthetic magnetic field is quantified by the flux θ per plaquette in units of the magnetic flux quantum. For rational $\theta = p/q$, the bulk eigenstates distribute in q bands.

As in the previous studies, we will focus in the following on a system with $\theta = 1/4$. Also, periodic (open) boundary conditions will be taken along the x-axis (y-axis), such that chiral edge states unidirectionally propagating along the $y = 1$ and $y = N_y$ edges appear in the energy gaps between the bands, as sketched in Fig. 4.3 (a). In particular, there are two edge modes living in the negative frequency gap: the one with positive group velocity is localized on the $y = 1$ side, while the one with negative group velocity on the $y = N_y$ side. Viceversa for the modes in the gap at positive frequencies.

Since we want to have lasing on top of this topological insulator, we briefly repeat the basic elements and notations introduced in the previous Chapter. We consider the lattice resonators to have losses with rate γ and a nonlinear refractive index captured by a photon-photon interaction constant g. To enable lasing, we fill the resonators with a gain medium. The effective number of inverted electronic transitions is given by the reservoir density $N_{x,y}$. In what follows we have in mind the experimental situation where we pump these transitions on the $y = 1$ edge of the system, with injection rate P. These electronic excitations can then feature stimulated emission into the electromagnetic mode of the resonators, with an efficiency R, or decay via other channels with rate γ_R. The state of the active medium will also affect the refractive index and hence the resonant frequency of the cavity mode via a contribution $g_R N_{x,y}$, which is at the origin of Henry's

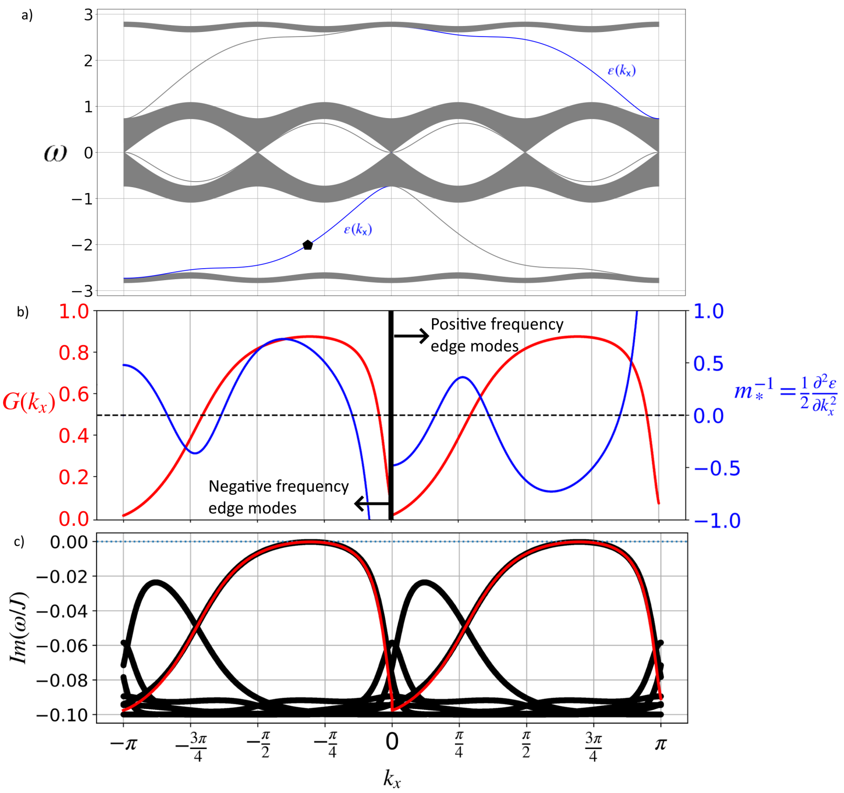

Figure 4.3: *Free theory.* Panel (a): energy bands of the conservative Harper-Hofstadter Hamiltonian Eq. (4.4) with flux $\theta = 1/4$ in a lattice of $N_y = 399$ sites along y and periodic boundary conditions along x. Blue color scale indicates edge modes localized on the $m = 0$ edge, with dispersion $\epsilon(k_x)$. The dark dot indicates the most localized edge mode of the bottom gap. Panel (b): $G(k_x)$ (red line) function versus curvature of the dispersion (blue line). Panel (c): imaginary part of the Bogoliubov spectrum over the vacuum solution at lasing threshold. Black (red) lines indicated result from the full 2D (1D effective) model. Parameters: $J = 1$, $\gamma = 0.2J$, $\beta P = 1.142\gamma$, $g_R = 0$.

linewidth enhancement factor (Henry [1982]). In the following, we will refer to it as reservoir-photon interaction.

Within this setting and adopting a semi-classical approximation for the electromagnetic field, the equations of motion are the Harper-Hofstadter version of Eqs. (1.8,1.9) and read

$$\begin{aligned} i\frac{\partial \psi_{x,y}(t)}{\partial t} =& -J\Big[\psi_{x,y+1} + \psi_{x,y-1} + e^{-2\pi i\theta y}\psi_{x+1,y} + e^{+2\pi i\theta y}\psi_{x-1,y}\Big] \\ &+ \Big[g|\psi_{x,y}|^2 + g_R N_{x,y} + \frac{i}{2}(RN_{x,y} - \gamma)\Big]\psi_{x,y} \end{aligned} \tag{4.5}$$

where the reservoir density $N_{x,y}$ is determined by the rate equation,

$$\frac{\partial N_{x,y}}{\partial t} = P\delta_{y,1} - (\gamma_R + R|\psi_{x,y}|^2)N_{x,y} \tag{4.6}$$

As far as losses overcome the gain, the steady-state of the device is the electromagnetic vacuum $\psi_{x,y} = 0$ and $N_{x,y=1} = P/\gamma_R$. A non-trivial steady state can be reached when the gain of one mode becomes higher than its losses. This defines a threshold P_{th} for the injection rate, which is calculated by linearizing Eq. (4.5) around the vacuum solution: passing to Fourier space along the periodic direction, this amounts to solve for each k_x the eigenvalue problem:

$$\omega\delta\psi_{k_x,y} = -J\Big[\delta\psi_{k_x,y+1} + \delta\psi_{k_x,y-1} + 2\cos(2\pi\theta y + k_x)\delta\psi_{k_x,y}\Big] + \frac{i}{2}\Big[(R - 2ig_R)\frac{P}{\gamma_R}\delta_{y,1} - \gamma\Big]\delta\psi_{k_x,y} \tag{4.7}$$

The spectrum of the corresponding $N_x \times N_x$ matrix, as sketched in Fig. 4.3.c, allows to determine the lasing threshold P_{th} at which the imaginary part of one eigenvalue becomes positive, meaning that the trivial solution is not dynamically stable anymore.

For $P > P_{th}$ the vacuum solution is then unstable and in a regime of parameters to be explored below the device can reach a dynamically stable stationary state. Due to the translational invariance along the x-axis, the steady-state can be written as:

$$\begin{cases} \psi^{ss}_{x,y}(t) = \psi^0_y e^{-i\mu t + ik^{las}_x x} \\ N_{x,y}(t) = N^0 \delta_{y,1}. \end{cases} \tag{4.8}$$

where the lasing frequency μ in general needs to be evaluated numerically and will be discussed below. Notice that, unless P is very close to P_{th}, both the lasing wavevector k^{las}_x and the global phase of ψ^0_y are randomly selected, depending on external noise or on the initial conditions (Seclì et al. [2019]); in particular, the spontaneous breaking of the global $U(1)$ symmetry of Eq. (4.5) is at the origin of the Goldstone mode discussed below, and determines the long time coherence properties of the device (Amelio and Carusotto [2019]).

In Fig. 4.3 (c) we illustrate that, under this pumping scheme, the lasing instability is stronger for the chiral edge states localized on the $y = 1$ side than for modes extending over the bulk. Moreover, among the chiral edge modes, the ones at the middle of the gap are more localized and feel a larger gain. Note also that in (c) the threshold value is $\beta P_{th} = 1.142\gamma > \gamma$ namely slightly above the single resonator threshold, since a chiral edge mode does not overlap totally with pumping due to slight penetration into the lossy bulk.

Furthermore, when the nonlinearity factors g, g_R can be neglected, the effective gain is equal for the negative and positive frequency edge modes, as in Fig. 4.3 (c), so lasing occurs with probability 1/2 in each gap, consistently with previous observations (Seclì et al. [2019]). This behaviour is due to an extended chiral symmetry inherited from the one of the HH model (Repellin and Goldman [2019]), that holds for the HH laser as long as $g, g_R = 0$. Indeed, in this case, for every steady-state solution $\psi^{ss}_{x,y}(t) = \psi^0_y e^{-i\mu t + ik^{las}_x x}$ of Eq. (4.5) it exists the related steady-state solution

$$\psi^{ss}_{x,y}(t) = (-1)^{x+y} (\psi^0_y)^* e^{+i\mu t + ik^{las}_x x}, \tag{4.9}$$

characterized by opposite frequency and wavevector $k_x + \pi$. This transformation, that can be defined only on a lattice, explains the structure of the HH spectrum, somehow symmetric with respect to zero energy. In the continuum problem, instead, the Landau levels can only have positive energy. We mention *en passant* that the relation between HH edge modes at the same energy living on different edges is provided by $\psi^0_{x,y} \to (\psi^0_{x,N_y-y+1})^*$, corresponding to the parity plus time reversal symmetry of the cyclotron orbits. When $g, g_R \neq 0$ instead, the symmetry (4.9) breaks down and the lasing state will have different properties in the two topological gaps; in particular, if $g_R > 0$ the lasing threshold is lower for the positive frequency modes than for the negative frequency modes (Longhi et al. [2018]). However, for realistic parameters and sufficient pumping intensity this effect remains small and the probability to lase in one or the other gap remains close to 1/2.

Finally, an important regime is identified when the dynamics of the reservoir is very fast compared to the other timescales of the device, i.e. $\frac{\gamma_R}{\gamma} \gg 1$. In this case we can make use of the adiabatic approximation and set to zero the left-hand side of Eq. (4.6), so that $N_{x,y} = \frac{P\delta_{y,1}}{\gamma_R + R|\psi_{x,y}|^2}$ instantaneously. For simplicity reasons we will switch off in most of the following also the refractive index nonlinearities $g = g_R = 0$ and refer to such a device as a class-A laser. The corresponding equations of motion read:

$$i\frac{\partial \psi_{x,y}(t)}{\partial t} = (\mathbf{H}\psi)_{x,y} + \frac{i}{2}\left(\frac{\beta P \delta_{y,1}}{1 + \beta|\psi_{x,y}|^2} - \gamma\right)\psi_{x,y}, \tag{4.10}$$

where $\beta = \frac{R}{\gamma_R}$ and $(\mathbf{H}\psi)_{x,y} = -J\left[\psi_{x,y+1} + \psi_{x,y-1} + e^{-2\pi i\theta y}\psi_{x+1,y} + e^{+2\pi i\theta y}\psi_{x-1,y}\right]$. This is precisely the model considered in (Seclì et al. [2019], Amelio and Carusotto [2019]).

4.2 Bogoliubov theory: elementary excitations and coherence*

(this Section builds on (Amelio and Carusotto [2019], Loirette-Pelous [2020]))

In the first part of this Section, we discuss the collective excitations on top of the stationary chiral lasing mode. A deeper understanding is also developed by means of a projection of the 2-dimensional model to a 1D effective equation. Here a major focus will be on the Goldstone branch: we will investigate in details its dependence on both the dispersion curvature and the edge localization of the original HH chiral modes.

In the second part we discuss the coherence of the topological laser within linearized theory. The chiral nature of the edge mode finds a clear hallmark in the spatio-temporal correlation functions; the linewidth is computed within the Bogoliubov scheme.

While in our treatment we focus on the case of a class-A device, we also provide a few remarks about generalization to class-B lasers.

4.2.1 Semi-analytical considerations on the steady-state

The aim of this Section is to get more insight about the physics of edge state lasing and the corresponding Bogoliubov modes. The Bogoliubov tratment, that we will sketch below, requires to compute numerically the steady state of the system by solving explicitly the equations of motion (4.10). Here we will first discuss more in details the steady-state, in particular close to the edge; this will eventually allow us to adopt an analytical scheme to grasp the edge dynamics by solution of a 1D effective laser model, which includes a momentum dependent effective gain. The Bogoliubov modes most localized on the edge, i.e. the ones which determine the slowest relaxation dynamics, are then quantitatively recovered within this dimensional reduction strategy.

This method relies on the fact that for $\gamma, P \ll J$ the eigenmodes of the driven-dissipative system resembles the ones of the bare HH model. The steady-state is an eigenstate of longitudinal momentum $\psi^{ss}_{x,y}(t) = \psi^{ss}_y e^{-i\mu t + i k_x^{las} x}$. The transverse part $\vec{\psi}^{ss} = \{\psi^{ss}_y\}$ will be a superposition of the HH eigenstates labeled by the lasing k_x^{las} momentum and another transverse index. Still, for computing the steady-state it is sufficient to consider the most localized mode, as also confirmed by numerics:

$$\lim_{\gamma/J \to 0} \psi^{ss}_y = A \phi_y(k_x^{las}) \tag{4.11}$$

where $\vec{\phi}(k_x^{las}) = \{\phi_y(k_x^{las})\}$ denotes the (transverse part of the) HH eigenstate at k_x^{las} most localized on the $y = 1$ edge. We assume the normalization $\sum_y |\phi_y|^2 = 1$ so that we need to find A. We can proceed by taking the equation of motion applied to $\psi^{ss}_{x,y}(t)$ (we call $\mathcal{B}$ the nonlinear HH Hamiltonian plus gain and loss operator) and then take the overlap of this vector with $\psi^{ss}_{x,y}(t)^*$ itself: in Dirac notation

$$0 = \langle \psi^{ss} | i\partial_t - \mathcal{B} | \psi^{ss} \rangle = \mu - \epsilon(k_x^{las}) - \frac{i}{2}\left[\frac{\beta P G(k_x^{las})}{1 + \beta|\psi_1^{ss}|^2} - \gamma\right] \tag{4.12}$$

where we introduced the edge mode dispersion $\epsilon(k_x)$ and the edge localization function $G(k_x) = |\phi_1(k_x)|^2$ that quantifies the overlap of the HH edge states with the $y = 1$ edge. Setting the real and imaginary parts to zero we arrive at

$$\lim_{\gamma/J \to 0} \mu = \epsilon(k_x^{las}) \tag{4.13}$$

$$\lim_{\gamma/J \to 0} |\psi_1^{ss}|^2 = P/P^{th} - 1 \tag{4.14}$$

with the lasing threshold $P^{th} = \frac{\beta^{-1}\gamma}{G(k_x^{las})}$.

These results are sufficient for the rest of the discussion. Still, for a deep understanding of the physics at play, it is necessary to inspect the first order γ/J corrections to ψ_y^{ss} close to the edge, for $y = 1, 2$. Our claim (checked via numerics) is that

$$\psi_1^{ss} = A\phi_1 \tag{4.15}$$

$$\psi_2^{ss} = A\phi_2 + iA\frac{\gamma}{2J}\frac{1 - |\phi_1|^2}{\phi_1} + O((\gamma/J)^2) \tag{4.16}$$

Importantly, notice that $\vec{\phi}$ has real entries. The overall radiative losses of the lasing mode are given by $\gamma N_x \sum_y |\psi_y^{ss}|^2 \simeq \gamma N_x A^2$, the second equality being true neglecting second order terms.

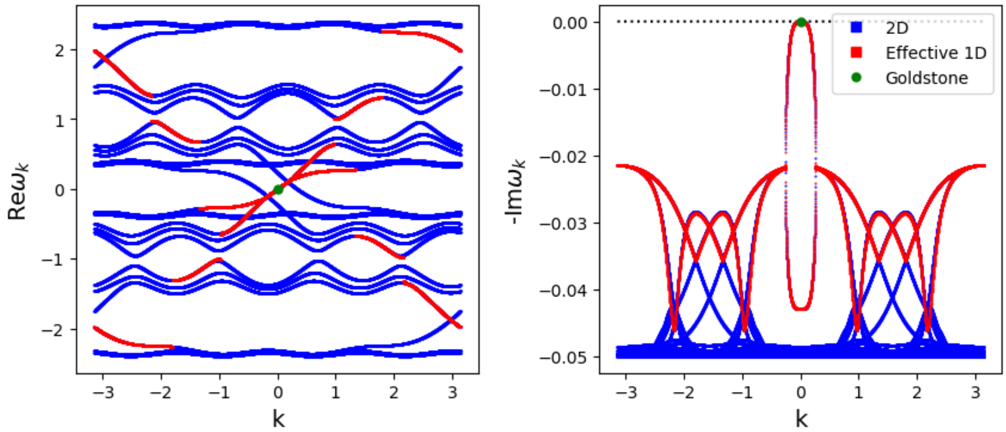

Figure 4.4: Typical real (left) and imaginary (right) part of the elementary excitations spectrum of a class-A laser . Blue (red) lines indicates results from the full 2D (1D effective) model. Parameters: $\gamma = 0.2J$, adiabatic approximation ($\gamma_R \gg \gamma$), $\beta P = 2\gamma$, $g = g_R = 0$, $k_x^{las} = -0.982$.

On the other hand all the power is injected in the $y = 1$ sites, which account for the losses $\gamma N_x |\psi_1^{ss}| = \gamma N_x A^2 |\phi_1|^2$. Density conservation at stationarity then implies that there is a current flowing out of the edge (from $y = 1$ to $y = 2$), provided exactly by the first order term in Eq. (4.16). Even if this term is order γ/J the associate current contains the tunneling rate J and is of order γ. In this way the total loss rate of the $y = 1$ sites is equal to that of the whole lattice $\gamma N_x A^2 |\phi_1|^2$.

This analysis suggests that the two fundamental quantities to understand the features of topological lasing and its collective excitations are the dispersion and localization of the HH edge states. The dependence on momentum of these quantities is fundamental in computing the Bogoliubov modes. The edge localization $G(k_x)$ represents the fraction of the lasing state that is amplified. Greater localization corresponds to a lower threshold. We plot $G(k_x)$ in Fig. 4.3.b (red line) together with the curvature m_*^{-1} of the HH edge dispersion (blue line). In Fig. 4.3.c the red line refers to the linear perturbations of the vacuum computed from a 1D laser model with a gain rescaled by $G(k)$, which recovers exactly the calculation with the full 2D model. This simple approach allows to calculate the lasing threshold and the amplitude of a steady chiral edge mode directly from the eigenmodes of the conservative problem.

4.2.2 Bogoliubov modes

Let' s now move to the collective excitations; leaving for a moment aside the previous semi-analytical considerations, the stationary lasing states of the system can be found numerically by evolving with Eq. (4.10). Then, the Bogoliubov method (Wouters and Carusotto [2007]) consists in linearizing the equation of motion via the ansatz

$$\psi_{x,y}(t) = [\psi_y^{ss} + \delta\psi_{x,y}(t)]e^{-i\mu t + ik_x^{las}x}. \tag{4.17}$$

The outcome, passing to Fourier space along the x-axis and in time, is a system of equations for $\delta\psi, \delta\psi^*$:

$$\omega\delta\psi_{k_x,y}(\omega) = (\mathbf{H}\delta\psi)_{k_x,y} + \mathbf{D}_y\delta\psi_{k_x,y} + \tilde{\mathbf{D}}_y\delta\psi^*_{-k_x,y} \tag{4.18}$$

and its complex conjugate evaluated at $(-k, -\omega)$, where $k = k_x - k_x^{las}$ and

$$\mathbf{D}_y = -\mu + \frac{i}{2}\left(\frac{\beta P \delta_{y,1}}{1 + \beta|\psi_1^{ss}|^2} - \gamma\right) - \frac{i}{2}\frac{\beta^2 P \delta_{y,1}|\psi_1^{ss}|^2}{(1 + \beta|\psi_1^{ss}|^2)^2}\,, \qquad \tilde{\mathbf{D}}_y = -\frac{i}{2}\frac{\beta^2 P \delta_{y,1}(\psi_1^{ss})^2}{(1 + \beta|\psi_1^{ss}|^2)^2}. \tag{4.19}$$

In particular, notice that $\mathbf{H}$ couples all the sites along y, so that in a given (k, ω) block $\delta\psi_{k,:}(\omega)$ is coupled to $\delta\psi_{-k,:}(-\omega)^*$ (the : implies a vector with indices $y = 1, ..., N_y$). The problem then reduces to diagonalizing numerically a $2N_y \times 2N_y$ Bogoliubov matrix for each k_x.

A typical example of an elementary excitations spectrum is reported in Fig. 4.4.b. In the real part of the spectrum, the excitations around the lasing mode (small ω and k) exhibit the typical sticking of non-equilibrium condensates. The branch in this region follows exactly the HH edge mode (properly shifted according to μ and k_x^{las}). In the imaginary part of the spectrum, we recognize the typical splitting between the Goldstone and the amplitude branches around the lasing mode, corresponding respectively to phase-like and density-like excitations. At $k = 0$ the Goldstone mode always has $\omega = 0$ as a consequence of the spontaneous breaking of the global $U(1)$ symmetry.

The peculiarity of the HH laser are the edge modes with the opposite chirality living around $k \sim \pm\pi$, which have longer lifetime because, being localized on the edge, benefit of the gain and decay as $\mathrm{Im}(\omega) \sim -i\frac{\Gamma}{2}$ (a more precise analysis is provided in the next Section) with $\Gamma = \gamma(1 - P_{th}/P)$ being the characteristic relaxation rate of the density fluctuations (see the previous Chapter). The excitations living in the bulk, instead, are basically lossy HH modes and decay as $\mathrm{Im}(\omega) \sim -i\frac{\gamma}{2}$.

Now we move to discuss the Bogoliubov edge modes. Let' s denote $\vec{\phi}(k) = \{\phi_y(k)\}$ the transverse part of the HH edge mode of wavevector $k_x = k_x^{las} + k$. If $\vec{\phi}(k)$ were equal to $\vec{\phi}(-k)$, the ansatz

$$\delta\psi_{x,y} = ue^{ikx}\phi_y(k) + ve^{-ikx}\phi_y(-k). \tag{4.20}$$

would be exact in the limit $\gamma/J \to 0$. However this is not the case and the Bogoliubov system is not close when inserting this ansatz, so that it is not possible to expand only on the HH edge modes, but a mixing with the bulk is expected. However, we close eyes and assume $\vec{\phi}(k) = \vec{\phi}(-k)$. Plugging in Eq.(4.18), multiplying by $\vec{\phi}(k)$ and summing over y, we get the Bogoliubov 2×2 problem

$$\omega \begin{pmatrix} u \\ v \end{pmatrix} = \begin{bmatrix} \epsilon(k) - \mu + \frac{i\gamma}{2}\left(\frac{G(k)}{G(0)} - 1\right) - \frac{i}{2}\Gamma\frac{G(k)}{G(0)} & -\frac{i}{2}\Gamma\frac{G(k)}{G(0)} \\ -\frac{i}{2}\Gamma\frac{G(-k)}{G(0)} & -\epsilon(-k) + \mu + \frac{i\gamma}{2}\left(\frac{G(-k)}{G(0)} - 1\right) - \frac{i}{2}\Gamma\frac{G(-k)}{G(0)} \end{bmatrix} \begin{pmatrix} u \\ v \end{pmatrix} \tag{4.21}$$

Expanding the dispersion of the edge statesup to second order $\epsilon(k) - \mu \approx v_g k + \frac{k^2}{2m_*}$, it is clear that the group velocity term acts like a diagonal term and does not play any role in determining the stability of the device (and similarly for all the odd terms in the small k expansion of the dispersion that here we have neglected). The term $\frac{G(k)}{G(0)} - 1$ is of geometric nature and describes the localization of the HH modes. The spectrum of this matrix is plotted in Fig. 4.4 (red lines), which shows that both the Goldstone and amplitude branches are quantitatively recovered, as well as the edge mode with opposite chirality.

We now discuss the slowest excitations to relax, that play a very important role in determining the spatio-temporal coherence properties of the laser operation (Amelio and Carusotto [2019]). If it were $G(k) = G(0)$, Eq. (4.21) would predict a quartic contribution to the lifetime of the Goldstone branch $\mathrm{Im}(\omega(k)) \sim -\frac{(k^2/2m_*)^2}{\Gamma}$; instead, the k-dependent localization function is responsible for a contribution $\sim a_2k^2$ independent of m_*. This is illustrated in Fig. 4.5, where the important observation is that at very small k the imaginary part of $\omega_+(k)$ does not depend on J/γ, which confirms that the k^2 behaviour is due to the momentum dependent localization of the HH edge modes. Still, the aforementioned $\vec{\phi}(k) \neq \vec{\phi}(-k)$ issue matters and quantitative agreement is not good: the numerical coefficient is $a_2^{fit} \simeq 0.045\gamma$ versus the theoretical prediction $a_2 \simeq 0.081\gamma$. In spite of this small shortcoming, our simple dimensional reduction argument allows to understand all the qualitative features of the edge Bogoliubov modes and motivates the presence of the k^2 behaviour, which is fundamental in determining the coherence properties of large lattices, in particular if $J \sim \gamma$ (Amelio and Carusotto [2019]). At greater k the curvature of the HH edge mode gives most of the k^4 contribution, and in practice one can just set $G(k) = G(0)$ (at least at $J \gg \gamma$). In this regime, the agreement is perfect and one can notice the scaling of the coefficient a_4 of $-\mathrm{Im}(\omega_+(k)) = a_2k^2 + a_4k^4 + \ldots$ with J^2, the theory prediction being in this regime $a_4k^4 = \frac{(k^2/2m_*)^2}{\Gamma}$.

Finally, we can summarize and reinterpret the results of this Section by saying that, when considering the low energy and small density fluctuation physics of edge, one can effectively deal with the 1D laser wire equation

$$i\partial_t\psi(x) = \left[\epsilon(\hat{k}_x) + \frac{i}{2}\left(G(\hat{k}_x)\frac{\beta P}{1 + \beta|\psi(x)|^2} - \gamma\right)\right]\psi(x), \tag{4.22}$$

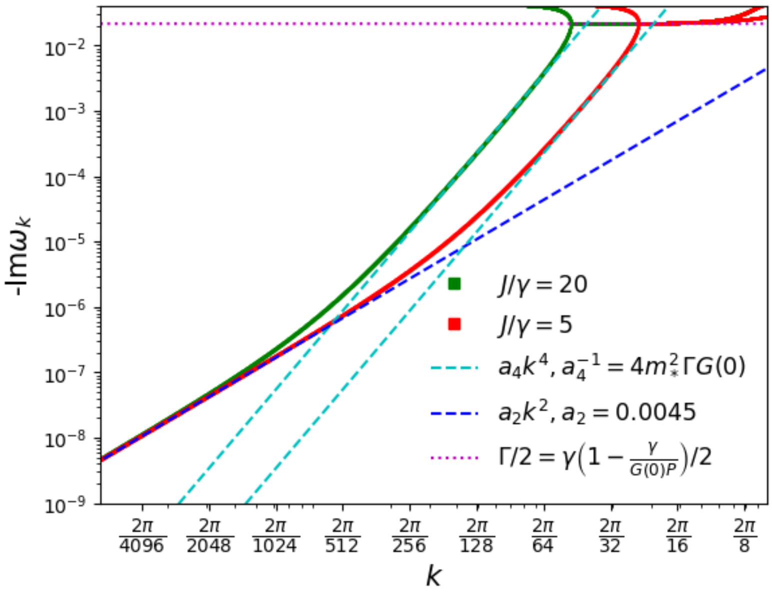

Figure 4.5: Scaling of Goldstone branch at small k. The red and green lines Goldstone branches have been calculated with the full 2D model for different hoping strengths. Blue dashed line is a linear fits of $-\text{Im}\omega_k$ with $a_2^{fit}k^2$: as predicted by theory a_2 is independent of J. Cyan dashed lines correspond to the a_4k^4 scaling of the 1D effective laser with $a_4 = (4m_*^2\Gamma G(0))^{-1}$. The ticks on the k-axis suggest what are the typical sizes for which the $\sim k^2$ regime is relevant. The density relaxation rate is given by $\Gamma/2$ (magenta dotted line), which is independent of J but depends on the degree of localization $G(0)$ of the edge mode and determines the frequency at which the amplitude and Goldstone branches split. Parameters: adiabatic approximation, $\gamma = 0.2$, $\beta P = 2\gamma$, $g = g_R = 0$, $k_x^{las} = -0.982$.

where the field lives on the real axis and $\hat{k}_x = -i\partial_x$. Notice that the edge localization and saturation terms do not commute. In particular, above we have explicitly demonstrated that this effective 1D equation recovers with excellent quantitative agreement the lasing instabilities (i.e. the Bogoliubov edge modes on top of the vacuum), the lasing threshold and the Bogoliubov dispersion of the lasing edge in the $\gamma/J \ll 1$ limit. These results are expected to be quite general and relevant to lasers built on top of different topological insulators, as recently confirmed for the Haldane model by Zapletal et al. [2020][2].

4.2.3 Chiral edge dynamics

In the following, we add the Peierls phases to the semi-classical equation (3.20) for the class A laser and study the temporal evolution of the field according to the stochastic equations

$$i\partial_t\psi_{x,y} = -J\left[\psi_{x,y+1} + \psi_{x,y-1} + e^{-2\pi i\alpha y}\psi_{x-1,y} + e^{2\pi i\alpha y}\psi_{x+1,y}\right] + \\ + \frac{i}{2}\left[\frac{P\delta_{y,1}}{1 + n_{x,y}/n_S} - \gamma\right]\psi_{x,y} + \sqrt{2D_{x,y}}\xi_{x,y}\ ; \quad (4.23)$$

we will adopt cylindrical boundary conditions where not otherwise stated. As mentioned in Section 3.1, the rate of spontaneous emission noise is typically of the order of the losses (at least not too far from the lasing threashold), so it is reasonable to take the diffusion coefficient to have form $D_{x,y} = (1+\delta_{y,1})\gamma/2$ (once again notice that in the semicalssical treatment the effective strength of the noise can be rescaled by changing n_S, so that the precise choice of D is not so important). In introducing a noise also in the unpumped bulk of the system we have assumed some homogeneous contribution also from thermal phonons or electronic scattering, while the stronger noise on the edge sites reflects the presence of gain and the consequent spontaneous emission processes. We have however checked that our results remain qualitatively identical if different spatial distributions of

---

[2] However they miss the momentum dependence of the edge localization and in fact use $G(k_x) \simeq G(0)$.

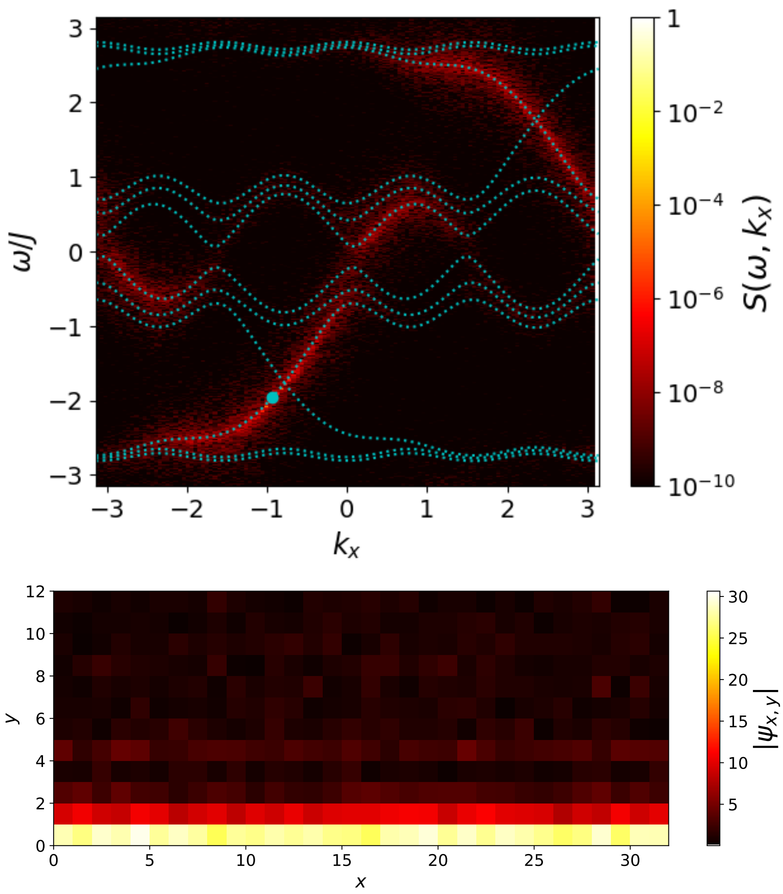

Figure 4.6: *Topological lasing.* Lower panel: typical snapshot of the field modulus distribution $|\psi(x,y)|$ at steady-state. Upper panel: Wavevector- and energy-resolved spectrum of the field on the $y=1$ edge. The dotted lines are the Harper–Hofstadter bands and the spectral intensities are normalized to the laser emission at $\omega^{las} \simeq -9.774\gamma$, $k_x^{las} = -2\pi\frac{19}{128}$. Numerical calculations were performed according to Eq. (4.23) for a lattice of size $N_x = 128$, $N_y = 12$ with periodic boundary conditions along x and a flux density $\alpha = 1/4$. System parameters: $J = 5\gamma$, $P = 2\gamma$, $n_s = 1000$, $D_{x,y} = (1+\delta_{y,1})\gamma/2$.

$D_{x,y}$ are used. We have also checked that the statistical results that are going to be discussed in the following of the paper are unchanged if different system geometries are considered, e.g. with open boundary conditions (see e.g. Fig. 4.9 below) We also mention the study (Peano et al. [2016]) of the chiral fluctuations in a similar configuration but in the linear amplifier regime.

The main features of the steady-state topological laser operation including noise are illustrated in Fig. 4.6. In the lower panel we plot a typical example of the field modulus $|\psi_{x,y}|$ for a finite $N_x = 32, N_y = 12$ cylindrical lattice, showing localization of the mode on the edge. The upper panel reports instead the power spectral density $S(k_x, \omega)$ of the field $\psi_{x,1}(t)$ on the $y = 1$ edge: the narrow lasing mode is strongly saturated on this scale and is indicated by the cyan circle. Noise-induced fluctuations distribute themselves over all modes but are concentrated on the ones with largest overlap with the $y = 1$ side, in particular on the two edge states with opposite chiralities. The spectral distribution roughly follows the dispersion of the optical modes in the underlying passive Harper–Hofstadter model indicated as a cyan dotted line, since, as shown above in Fig. 4.4.a, the real part of the Bogoliubov edge modes closely resembles the HH ones.

It is also interesting to discuss the emission spectrum from each site. In Fig. 4.7(a) we show the emission spectrum defined as

$$S(\omega) = \frac{1}{N_x}\sum_x |\psi(x,\omega)|^2 \tag{4.24}$$

for the parameters and lasing point shown in Fig. 4.6(b). In addition to the main lasing peak,

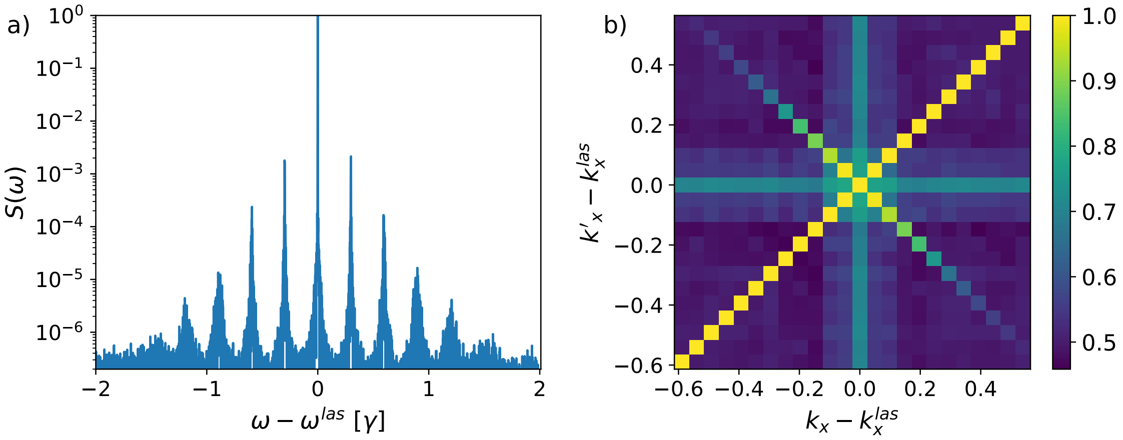

Figure 4.7: *Correlated side-peaks in the emission spectrum.* (a) Spectrum of the field on a single resonator located on the amplified edge. The spacing of the side–peaks is determined by the quantization of the wavevector k_x around the periodic direction. The side–peaks are generated by parametric scattering processes from the lasing mode into pairs of symmetrically located modes. (b) Color plot of the momentum-space correlation function (4.25) in the k_x, k'_x plane showing - among other- strong correlations along the anti-diagonal, that is within pairs of symmetrically located modes.

the emission spectrum displays a comb-like structure with a series of symmetric side-peaks: the frequency spacing is determined by the quantization of the momentum along the periodic direction and is approximatively $v_g \frac{2\pi}{N_x}$.

The visibility of the comb is not merely due to the existence of eigenstates at those specific values of the frequency, but their population by noise is enhanced by correlations. This is illustrated in Fig. 4.7(b) where we show the normalized momentum–space intensity–intensity correlation function

$$R^{(2)}(k_x, k'_x) = \frac{\langle n_{k_x} n_{k'_x} \rangle}{\sqrt{\langle n^2_{k_x} \rangle \langle n^2_{k'_x} \rangle}}. \tag{4.25}$$

Here, the momentum–space densities n_{k_x} are evaluated at the same time over the whole edge, $n_{k_x}(t) = |\psi(k_x, t)|^2$.

Several features are visible in this plot. The diagonal line for $k_x = k'_x$ is due to a trivial self-correlation and $R^{(2)}$ is here equal to 1. For generic pairs of modes, the thermal $g^{(2)}(k_x) = 2$ character of all $k_x \neq k_x^{las}$ modes implies that the background value is $R^{(2)} = 0.5$. When one (two) modes coincide with the lasing one, $R^{(2)}$ is equal to $1/\sqrt{2}$ (1), which explains the vertical and horizontal stripes and the central peak. The most interesting feature is the stripe on the anti-diagonal, corresponding to correlations between symmetrically located modes such that $k_x + k'_x = 2k_x^{las}$. For the first two pairs of side–peaks, this correlation is nearly perfect, indicating that these modes are populated in pairs by parametric scattering processes.

Of course, such correlations are not specific of topological systems but can be observed also in the 1D systems studied in the previous Chapter, albeit with a suppressed intensity due to the curvature of the dispersion. In analogy to exciton-polariton systems pumped around the magic angle (Carusotto and Ciuti [2013]), the magnitude of these parametric correlations is strongest if lasing is made to operate around the inflection point of the dispersion.

To characterize the spatio-temporal coherence of the emission, we now consider the fluctuations of the phase of the one-dimensional field living on the amplifying boundary of the Harper–Hofstadter lattice, $\psi(x, t) \equiv \psi_{x,1}(t)$.

In the steady-state of laser operation, the phase displays slow fluctuations around a carrier wavevector k_x^{las} and frequency ω^{las}: the former can be extracted from the (spatial) winding number of the phase around the system, the latter can be determined by fitting the evolution of the field phase on single sites. In the spectrum of Fig.4.6, they are indicated by the position of the cyan circle. While a precise determination of these quantities can be important from the applicative point of view, they are somehow uninteresting from the statistical mechanics point of view, since

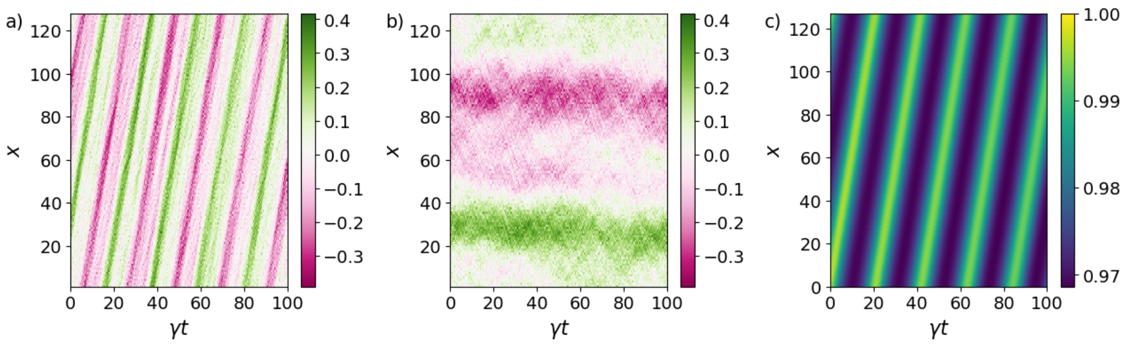

Figure 4.8: *Chiral motion of the phase fluctuations.* (a) Spatio-temporal plot of the slowly varying phase of a random realization of $\psi_{sl}(x,t)$, showing that the fluctuations chirally move around the system. (b) Spatio-temporal plot of the phase of $\psi_{CM}(x,t)$ in the co-moving frame: now the fluctuations are observed in their natural frame of reference and evolve slowly. (c) Correlation function $g^{(1)}(x,t)$: since the fluctuations move at v_g, after a time t the field in x is correlated with the one in $x+v_g t$. System parameters: $N_x=128, N_y=12, J=5\gamma, P=2\gamma, n_s=1000, D=2\gamma$.

they are mostly determined by the deterministic dynamics of the device and are weakly affected by the fluctuations.

In order to remove the carrier frequency and wavevector and concentrate on the stochastic fluctuations, we define the slowly varying field

$$\psi_{sl}(x,t) \equiv e^{-i(k_x^{las}x-\omega^{las}t)}\,\psi(x,t). \tag{4.26}$$

Looking at the phase of a typical realization of $\psi_{sl}(x,t)$ shown in Fig. 4.8(a), we easily recognize a phase fluctuation pattern that moves at a constant velocity and gets slowly distorted. The drift velocity can be inferred from the dispersion $\omega_{em}(k_x)$ of the lasing chiral edge mode, which has group velocity $v_g = \frac{d\omega_{em}}{dk_x}(k_x^{las})$ and curvature $J_{eff}(k_x^{las}) = \frac{1}{2}\frac{d^2\omega_{em}}{dk_x^2}(k_x^{las}) < J$.

In order to focus on the intrinsic dynamics of the phase fluctuations, we plot in Fig. 4.8(b) a typical realization of the phase evolution seen from the moving frame at v_g,

$$\psi_{CM}(x,t) \equiv \psi_{sl}(x+v_g t,t). \tag{4.27}$$

For the relatively strong inter-site coupling $J=5\gamma$ and relatively small system size $N_x=128$, the phase fluctuations develop very slowly and remain quite small. Their magnitude gets larger if the mean intensity n_0 is reduced, the inter-site coupling J is reduced, or larger systems are considered. This will be discussed in Sec. 4.3.

While the transformation to $\psi_{CM}(x,t)$ allows for a direct visualization of the phase dynamics, it is also possible to study the fluctuations circulating along the edge by computing the space–time correlation function of the original field,

$$g^{(1)}(x,t) = \frac{|\langle\psi^*(x,t)\psi(0,0)\rangle|}{\sqrt{\langle|\psi(x,0)|^2\rangle\langle|\psi(0,0)|^2\rangle|}}, \tag{4.28}$$

where the average is taken over the noise and invariance under temporal t and spatial x translations is assumed. This analysis requires no preliminary estimate of k_x^{las} and ω^{las} and will be our workhorse in the next sections. As it is apparent looking at the smooth stripes in Fig. 4.8(c), the analysis of $g^{(1)}(x,t)$ is the cleanest way to extract the velocity at which fluctuations travel. The result $v_g \simeq 6.07\,\gamma a$ is perfectly compatible with the group velocity $v_g \simeq 6.08\,\gamma a$ obtained from the linear dispersion of the chiral edge mode.

In numerical simulations the cylindrical configuration with periodic boundary conditions along x is convenient to collect more statistics by using translational invariance and recording all sites. In an experiment, instead, one can run very long measurements and it may be cumbersome to record correlations between any pair of sites. So it is useful to demonstrate that the above picture is unchanged also in the presence of open boundary conditions. For a rectangular lattice with the gain on the edge, we have lasing as already reported in the literature (Seclì et al. [2019]), see Fig. 4.9.a. Notice that the density is slightly higher at the corners, so that the denominator

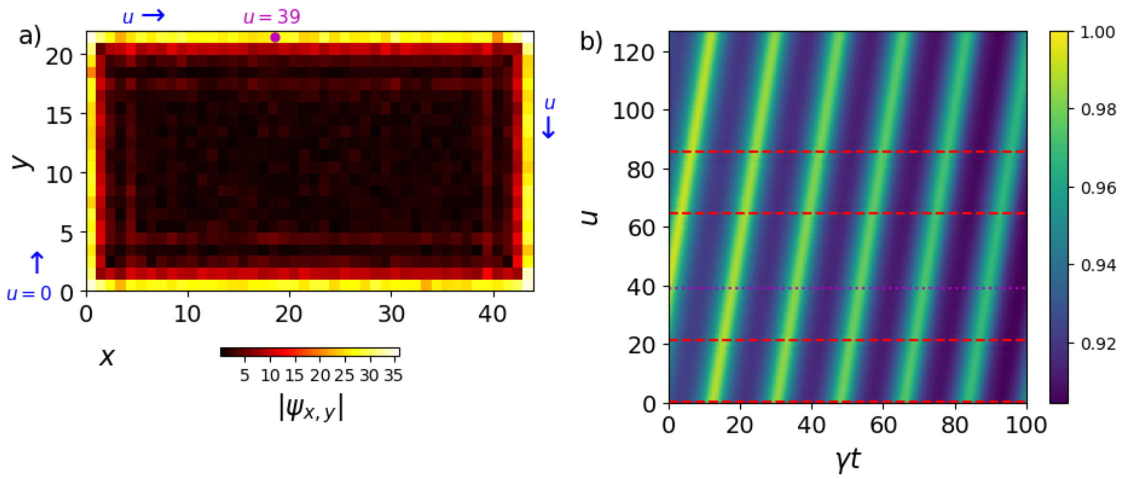

Figure 4.9: *Correlations around a rectangular lattice.* (a) Snapshot of the absolute value of the field in a rectangular $N_x = 44 \times N_y = 22$ lattice with open boundary conditions and amplifying medium along all the edge. (b) Correlation function $g^{(1)}(u, u_0, t) = \langle \psi^*(u,t)\psi(u_0,t)\rangle$ where u is a coordinate along the edge, with u_0 indicated in magenta. Red dashes correspond to the position of the corners. Except for the boundary conditions and the lasing point, which was not fixed via the initial conditions but was randomly selected by the dynamics, the parameters are the same as Figs. (4.6–4.8).

of Eq. (4.28) is not a constant. By defining an edge coordinate u (which starts from the lower left corner and runs clockwise) and measuring correlation functions with respect to a given point (indicated in magenta), we get the pattern of panel (b), analogous to Fig. 4.8.c. The phase picture of panels 4.8.a-b would be in general more complicated, because the lasing wavevector, which is a gauge dependent quantity, would be in general different on the four edges.

4.2.4 Linewidth and Petermann factor

In analogy to the topologically trivial laser discussed in the previous Chapter, within the linearized theory the very long time behaviour of the coherence is determined by the phase drift associated with the Goldstone mode and the $U(1)$ symmetry of the laser dynamics, with all other excitations modes being exponentially damped.

To start with, we illustrate the Bogoliubov approach in full generality for a lasing system. For a lattice of N sites (labelled as $\vec{x}$) of arbitrary dimensionality, let us call $\mathcal{L}_{las}$ the $2N \times 2N$ Bogoliubov matrix of the linearized dynamics on top of the lasing steady-state. Let $V = \{V_{\vec{x}\sigma,p}\}$ be the invertible matrix which diagonalizes $\mathcal{L}_{las}$, where the pseudo-spin $\sigma = \uparrow, \downarrow$ indicates the particle and hole components of the Bogoliubov problem and p labels the $2N$ eigenmodes. The Goldstone mode $V_{\vec{x}\sigma,G}$, that we assume to be unique with all other excitations having a finite life-time, is the eigenstate with zero eigenvalue. As usual, its spatial shape follows the one of the lasing mode. The effective noise acting on the lasing mode will be determined by the projection of the bare noise on it. For generality we consider a position dependent bare noise $D_{\vec{x}}$. Then, in the Bogoliubov approximation, the phase drift associated with the Goldstone mode is given by

$$\langle \Delta_t \phi^2 \rangle = \Phi_G^2 \sum_{\vec{x}} D_{\vec{x}} \; (V^{-1})_{G,\vec{x}\uparrow} (V^{-1})_{G,\vec{x}\downarrow} \; |t| \tag{4.29}$$

where the summation represents the projection of the noise on the Goldstone mode and

$$\Phi_G = \Phi_G(\vec{x}) = \frac{-i}{n_0(\vec{x})} \left[\psi_0^*(\vec{x}) V_{\vec{x}\uparrow,G} - \psi_0(\vec{x}) V_{\vec{x}\downarrow,G}\right] \tag{4.30}$$

is actually independent of $\vec{x}$ and provides the normalization of the Goldstone mode phase component.

For a system which is translationally invariant along x the Bogoliubov matrix can be made block-diagonal $\mathcal{L}_{las} = \bigoplus_{k_x} \mathcal{L}_{las}(k_x)$ with the transverse dependence of the Goldstone $V_{y\sigma,G}$ diagonalizing the $k_x = 0$ block. Then in Eq. (4.29) one should replace $\sum_{\vec{x}} \to N_x \sum_y$, $\psi_0(\vec{x}) =$

$\psi_0(y)e^{ik_x^{las}x} \to \psi_0(y)$ and, choosing the standard normalization of the modes, $V_{\vec{x}\sigma,G} \to V_{y\sigma,G}/\sqrt{N_x}$, $V^{-1}_{G,\vec{x}\sigma} \to V^{-1}_{G,y\sigma}/\sqrt{N_x}$. This approach leads to write $\tau_{ST} = N_x \tau_{ST,1}$, where $\tau_{ST,1}$ does not depend on N_x but in a subtle way via the discretization of k_x^{las}.

If $VV^\dagger = 1$ a very clear expression holds for the Schawlow–Townes line:

$$\gamma_{ST} = \frac{\sum_{\vec{x}} D_{\vec{x}} n_{\vec{x}}}{n_{tot}^2} = \frac{D_n}{n_{tot}} \tag{4.31}$$

with $n_{tot} = \sum_{\vec{x}} n_{\vec{x}}$ and $D_n = \sum_{\vec{x}} D_{\vec{x}} n_{\vec{x}} / \sum_{\vec{x}} n_{\vec{x}}$. This is for instance the case of a spatially uniform, topologically trivial system, for which the different wavevectors decouple and the sector of $\mathcal{L}_{las}(k_x = 0)$, corresponding to the lasing wavevector $\vec{k}_{las}$, is diagonalized by a 2×2 unitary matrix $VV^\dagger = 1$, since modulus and phase are decoupled for the lasing mode.

Equation (4.31) is no longer valid when $VV^\dagger \neq 1$. Let's consider the topological laser: the $k_x = 0$ sector has dimension $2N_y \times 2N_y$ and V is not unitary, so in general $VV^\dagger \neq 1$. However, for the considered parameters, it turns out that $VV^\dagger \simeq 1$, so the approximate expression

$$\gamma_{ST} = \frac{2}{\tau_{ST}} \simeq \frac{\sum_{x,y} n_{x,y} D_{x,y}}{\left[\sum_{x,y} n_{x,y}\right]^2} = \frac{D_n}{N_x \sum_y n_{1,y}} = \frac{D_n}{n_{tot}}. \tag{4.32}$$

is expected to provide an accurate approximation. We stress the scaling $\tau_{ST} \propto N_x$.

The non–orthogonality of V is also related to the so-called Petermann factor and excess noise, very well known in standard laser theory (Petermann [1979], Henry [1986], Siegman [1989b]).We try to sketch this analogy here following the ideas of (Hamel and Woerdman [1989], Siegman [1989a]). For a typical laser resonator the spatial distributions of loss and gain do not coincide: the typical case are a Fabry-Perot cavity or a ring cavity where the losses are mostly due to the outcoupling and are concentrated at the mirrors. As a consequence, the spatial form of the possible lasing modes is not the one of the empty cavity but it is deformed by the presence of gain; for example, in a ring cavity the field would be an exponentially amplified plane wave along each arm which at any mirror is damped by the reflection coefficient. One can also think of the electric field as experiencing several round trips through the cavity, where at each round trip it gets amplified in the bulk and weakened at the outcouplers.

Very close to threshold and restricting for now to the deterministic semiclassical dynamics, we can neglect the nonlinearities due p.e. to the saturation term and assume a linear dynamics as given by the operator $\mathcal{A}$. In the absence of gain and losses $\mathcal{A}$ is hermitian and its eigenmodes are the normal, mutually orthogonal modes of a perfect cavity; when gain and losses are present $\mathcal{A}$ is in general non-hermitian[3] but let' s assume that it is diagonalizable. The lasing mode $\mathbf{f}_0(\mathbf{x})$ will be a particular eigenvector of $\mathcal{A}$, presumably the one with eigenvalue ω^{las} with all other modes $\mathbf{f}_m(\mathbf{x})$ having damping eigenvalues. If we add by hand spontaneous emission noise, the evolution will be of the kind

$$i\partial_t \boldsymbol{\psi}(\mathbf{x},t) = \mathcal{A}\boldsymbol{\psi}(\mathbf{x},t) + \boldsymbol{\Xi}(\mathbf{x},t), \tag{4.33}$$

with the spontaneous emission noise $\boldsymbol{\Xi}(\mathbf{x},t)$ which can be taken of uniform strength for our goal. If we now want to project on the lasing mode, we would be temped to multiply by $\boldsymbol{f}_0(\mathbf{x})^*$ and integrate. However, since $\mathcal{A}$ is not hermitian, the modes are not orthogonal $\int d\mathbf{x}\, \boldsymbol{f}_m(\mathbf{x})^* \cdot \boldsymbol{f}_l(\mathbf{x}) \neq \delta_{lm}$. The correct way to do the projection is to consider the set of adjoint modes $\boldsymbol{\phi}_m(\mathbf{x})$, which are the eigenvectors of $\mathcal{A}^\dagger$, and require the normalization

$$\int d\mathbf{x}\, \boldsymbol{\phi}_m(\mathbf{x})^* \cdot \boldsymbol{f}_l(\mathbf{x}) = \delta_{lm}. \tag{4.34}$$

By bracketing Eq. (4.33) with $\int d\mathbf{x}\, \boldsymbol{\phi}_0(\mathbf{x})^*$, one then obtains a point-like equation *á la* Schawlow–Townes for the amplitude of the lasing mode $\psi(t)$

$$i\partial_t \psi(t) = \omega^{las}\psi(t) + \sqrt{2D\mathcal{K}}\,\xi(t) \tag{4.35}$$

where $\sqrt{2D}\,\xi(t) = \int d\mathbf{x}\, \boldsymbol{f}_0(\mathbf{x})^* \cdot \boldsymbol{\Xi}(\mathbf{x},t)$ only depends on the shape of the lasing mode, while the diffusion strength of the noise has been enhanced by the Petermann factor

$$\mathcal{K} = \int d\mathbf{x}\, \boldsymbol{\phi}_0(\mathbf{x})^* \cdot \boldsymbol{\phi}_0(\mathbf{x}), \tag{4.36}$$

---

[3] See (Grangier, Ph. and Poizat, J.-Ph. [1998]) for some nice consideration on the non-unitary origin of this dynamics.

which is related to the shape of all the modes of $\mathcal{A}$ and it is in general larger than one, since the $\{\boldsymbol{f}_m\}$ and $\{\boldsymbol{\phi}_m\}$ modes are not simultaneously normalizable. A very similar argument holds if one wants to start from the Maxwell wave equation with the second-order time derivative, as it is mostly done in the original literature.

This nice linear algebra insight strictly speaking is only valid very close to threshold (or in the linear amplifier regime) where the dynamics can be described by a linear operator; we stress, instead, that our generalization of this argument in the framework of the Bogoliubov formalism, where the orthogonality of the modes is related to the unitarity of V, holds even far above threshold. Notice also that close to threshold $\mathcal{A}$ corresponds to the particle-particle sector of the Bogoliubov matrix $\mathcal{L}$. The application of this strategy to another simple example, consisting of two coupled and asymmetrically pumped resonators, is illustrated in Appendix A.

Physically, the extra spontaneous emission noise is due to the coupling of different modes, as it has been clearly illustrated by Grangier, Ph. and Poizat, J.-Ph. [1998]. One can also distinguish between longitudinal and transverse Petermann factors, depending on the direction the mixing occurs in. Semiconductor lasers are often made of open resonators, where the Petermann factor can be of the order of tens or hundreds.

In analogy with these known results, we define here the transverse Petermann factor as the ratio

$$\mathcal{K} = \frac{\gamma_{ST}}{D_n/n_{tot}}. \tag{4.37}$$

Importantly, for the topological laser device this number is around $\mathcal{K} \simeq 1.002$ for $J = 5\gamma$ and $\mathcal{K} \simeq 1.1$ for $J = 0.5\gamma$; we attribute the small discrepancy with respect to 1 to the fact that the lasing mode is very slightly distorted in the nonlinear steady-state with respect to the HH mode of the Hamiltonian model, the amount of distortion depending on J/γ, see discussion around Eqs. (4.15,4.16).

In conclusion, within the linearized Bogoliubov approximation, the laser emission is for all practical purposes determined only by the total number of photons in the device, which is the textbook, optimal case. This confirms that topological guiding in the edge mode is immune from the linewidth broadening effects typical of lasing in open resonators with gain guiding.

4.3 Nonlinear phase physics*

(this Section builds on (Amelio and Carusotto [2019]))

The discussion of the emission spectrum presented in the previous subsection gives first hints of the complexity of the fluctuation dynamics in an extended device. Here we will build a complete theoretical picture of the spatio-temporal coherence of the topological laser.

To get a first hint on the behaviour, we can make the assumption, as already argued in Section 4.2, that the field on the edge can be described in the comoving frame by the 1D equation

$$i\partial_t\psi_{_{CM}}(x,t) = (-J_{eff}+i\eta)\partial_x^2\psi_{_{CM}} + \frac{i}{2}\left[\frac{P_{eff}}{1+n_S|\psi_{_{CM}}|^2}-\gamma\right]\psi_{_{CM}} + \sqrt{2D}\,\xi. \tag{4.38}$$

Here J_{eff} is given by the curvature of the bare Harper–Hofstadter topological mode, P_{eff} is chosen as to retrieve the numerical mean intensity n_0 on the edge, and η accounts phenomenologically for the k-dependent localization of the lasing mode on the edge of the lattice and the consequent k-dependence of gain. We mention that a finite η would arise also in the 1D chain if a dissipative coupling described by a non-vanishing imaginary part of J (Longhi and Feng [2018], Aleiner et al. [2012], Harrison et al. [2020]) were considered.

Assuming a fast relaxation of the intensity fluctuations, we can then restrict our attention to the dynamics of the phase. By neglecting terms containing four derivatives (both the linear, Galilean-preserving ones and the nonlinear, Galilean-breaking ones[4]), one gets to a motion equation for the

---

[4] The phase equation associated with Eq. (4.38) reads

$$-\partial_t\phi = -\eta\nabla^2\phi + J_{eff}(\nabla\phi)^2 - \frac{J_{eff}}{2n_0}\Gamma_{eff}^{-1}\nabla^2\left[-2\eta n_0(\nabla\phi)^2 - 2J_{eff}n_0\nabla^2\phi\right] +$$

$$+\frac{\eta}{n_0}\Gamma_{eff}^{-1}\nabla\phi\cdot\nabla\left[2\eta n_0(\nabla\phi)^2 + 2J_{eff}n_0\nabla^2\phi\right] + \sqrt{\frac{D}{n_0}}\xi_1$$

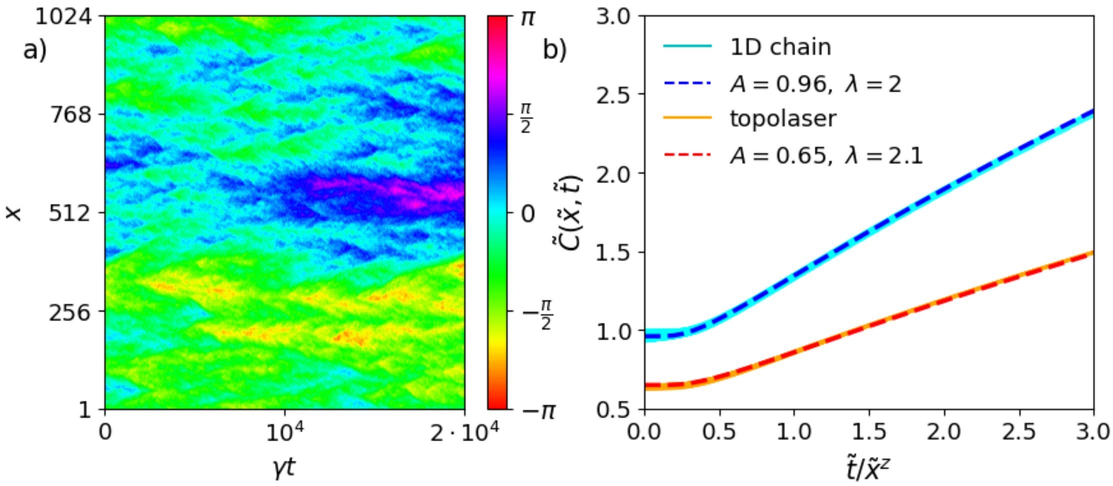

Figure 4.10: *KPZ dynamics on the topological edge mode.* (a) Typical example of the steady–state space-time dynamics of the phase of the field $\psi_{CM}(x,t)$ on the system edge seen from the comoving frame. (b) Correlators $\tilde{C}(\tilde{t},\tilde{x}^z)$ for $x=\pm30,...,\pm160$ (small lines) for the topological device lasing into the $k_x=-2\pi\frac{155}{1024}$ mode (orange) and for the non-topological one-dimensional array lasing in the $k_x=0$ mode (cyan). Red and blue dashed lines indicate the KPZ universal function (4.43) on which all curves collapse. System parameters: $N_x=1024$, $J=0.5\gamma$, $P=2\gamma$, $n_S=1000$, $D_{x,y}=\gamma/2(1+\delta_{y,1})$.

phase of the KPZ form:

$$\partial_t\phi=\eta\partial_x^2\phi-\frac{J_{eff}^2}{\Gamma}\partial_x^4\phi-J_{eff}(\partial_x\phi)^2+\sqrt{\frac{D}{n_0}}\xi. \tag{4.39}$$

Since η is the less controlled parameter of the model, we do not perform the usual KPZ rescaling (He et al. [2015]) to yield an equation containing the effective nonlinearity as the only one parameter. Rather, we rely on the rescaling Eqs. (3.46) with the effective parameters $J\to J_{eff}, P\to P_{eff}$; this transformation does not depend on η [5] and yields

$$\partial_{\tilde{t}}\tilde{\phi}=\frac{\eta t_*}{l_*^2}\partial_{\tilde{x}}^2\tilde{\phi}-\partial_{\tilde{x}}^4\tilde{\phi}+(\partial_{\tilde{x}}\tilde{\phi})^2+\tilde{\xi}. \tag{4.40}$$

In these units we then expect the KPZ nonlinearity to be close to $\lambda=2$; this value is also protected from renormalization induced by the quartic derivative term in the KSE (Ueno et al. [2005]). It is thus natural to expect that the coherence of the topological laser will closely resemble the one of the generic extended laser discussed in Chapter 3. In what follow, we proceed to numerically verify this statement on simulations of the stochastic laser equations in the topological two-dimensional lattice.

Based on our previous discussion, we expect that the KPZ universal dynamics occurs, in a lattice of N_x sites, on timescales shorter than the saturation time $\sim N_x^z$ (after which the Schawlow–Townes like behavior described above sets in) but larger than the timescales where the linear Bogoliubov dynamics and non–universal effects dominate. Having a sizable window where to observe KPZ physics then requires the system to be large enough, precisely it should be at least $N_x a\gg\sqrt{2}\pi l^*$ (Gladilin et al. [2014]). We thus consider a large system of length $N_x=1024$ with periodic boundary conditions along x and with $N_y=12$ points along the open direction y. In order to clearly observe KPZ physics while keeping intensity fluctuations within 15% and having a tractable system size, it is beneficial to use a small inter-site coupling $J=0.5\gamma$.

One may argue that such a value of the coupling J (and thus of the topological gap) is comparable with the bare linewidth γ. Such narrow topological gaps are very relevant for experimental implementations (Bahari et al. [2017]), but it is not a priori obvious whether in this regime the chiral edge modes survive losses. While this is indeed a serious issue to observe chiral edge propagation in passive systems, it is a crucial result of laser theory that the laser linewidth above

---

[5] Actually, also the dependence on Γ_{eff} is such that, given the measured n_0, any uncertainty on the value of P_{eff} will only affect the KPZ coefficient of the Laplacian.

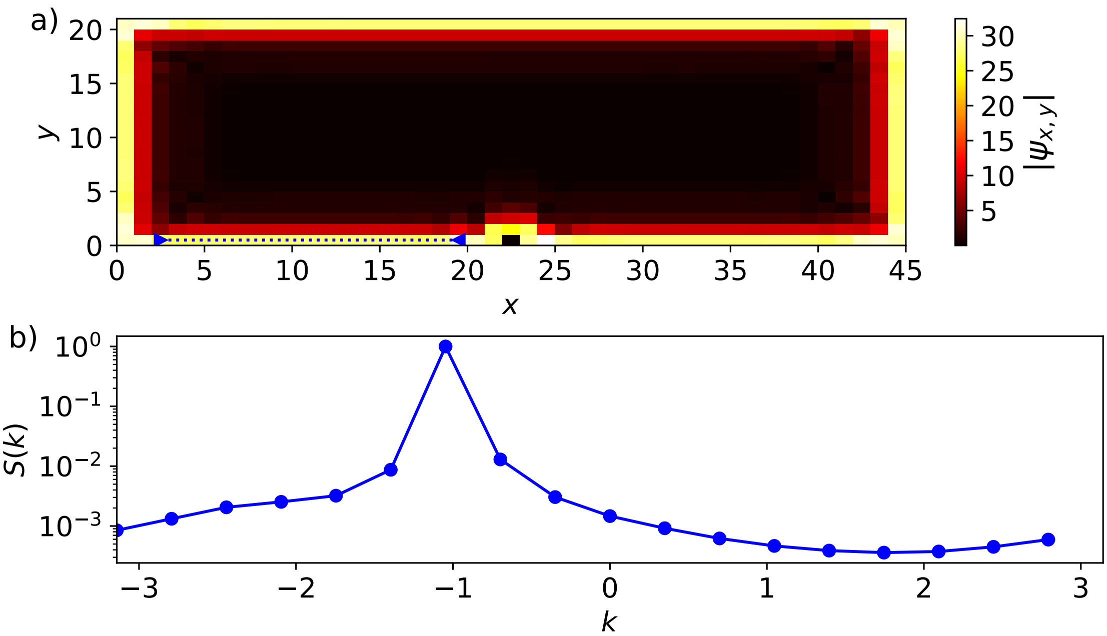

Figure 4.11: *Small-bandgap topological lasing.* A 45×21 Harper–Hofstadter lattice with $J = 0.5\gamma$ and open boundary conditions is built with a strong defect on an edge. Amplifying the edges result in topological lasing: the modulus of the field is visible in panel (a) and the momentum-space intensity along the blue dots is plotted in panel (b)Both panels show no trace of backscattering. In this case the chiral mode on the lower edge goes from left to right, since for this negative k the group velocity is positive.

threshold can be orders of magnitude smaller than γ. Our numerical simulations confirm stable lasing into the chiral edge mode even for small J/γ: in particular, we consider a strong defect on the boundary of a rectangular lattice (so that also the corners act like defects) and put gain all over the edge of the system. Starting the simulation with a small random seed, the fields reach a steady-state which displays the usual features of a topological laser and is able to go around the strong defect, as it is shown in Fig. 4.11. In panel (a) we depict the modulus of the field, while the absence of backscattering is demonstrated by plotting, in panel (b), the Fourier intensity $S(k)$ of the field along the blue dots of panel (a). This indicates that the emission is narrow and single-peaked in momentum space, and corresponds to positive group velocity (as it is visible in Fig. 4.6 of the main text).

To numerically highlight the KPZ physics we have performed 20 simulations of the full two-dimensional lattice of duration $\gamma T = 5 \cdot 10^5$, starting from a plane wave with the wavevector value for which the Harper–Hofstadter eigenstate is most localized on $y = 1$, that is $k_x = -2\pi\frac{155}{1024}$. For each run, after a suitable equilibration time, the correlation function $\langle\psi^*(x, t + \bar{t})\psi(0, \bar{t})\rangle$ on the edge site is computed and then averaged over the 20 trials to yield $g^{(1)}(x, t)$. The typical dynamics occurring in a time $\gamma T = 2 \cdot 10^4$ is depicted in Fig. 4.10(a), where the phase of the field $\psi_{CM}(x, t)$ along the edge is shown in the comoving frame: a structure similar to the fractal structure of interface growth can be recognized.

Defining the correlation function in the comoving frame as

$$g^{(1)}_{CM}(x, t) = |\langle\psi^*_{CM}(x, t)\psi_{CM}(0, 0)\rangle| \tag{4.41}$$

and the rescaled correlator as

$$\tilde{C}(\tilde{t}, \tilde{x}^z) \equiv -2(\phi^*)^{-2}\tilde{x}^{-2\chi} \log g^{(1)}_{CM}(\tilde{x}, \tilde{t}), \tag{4.42}$$

KPZ universality requires that

$$\tilde{C}(\tilde{x}, \tilde{t}) = \tilde{C}(\tilde{t}/\tilde{x}^z) = \left(\frac{1}{2}\lambda A^2 s\right)^{2/3} g_{KPZ}\left(\frac{1}{(2\lambda^2 A s^2)^{1/3}}\right) \tag{4.43}$$

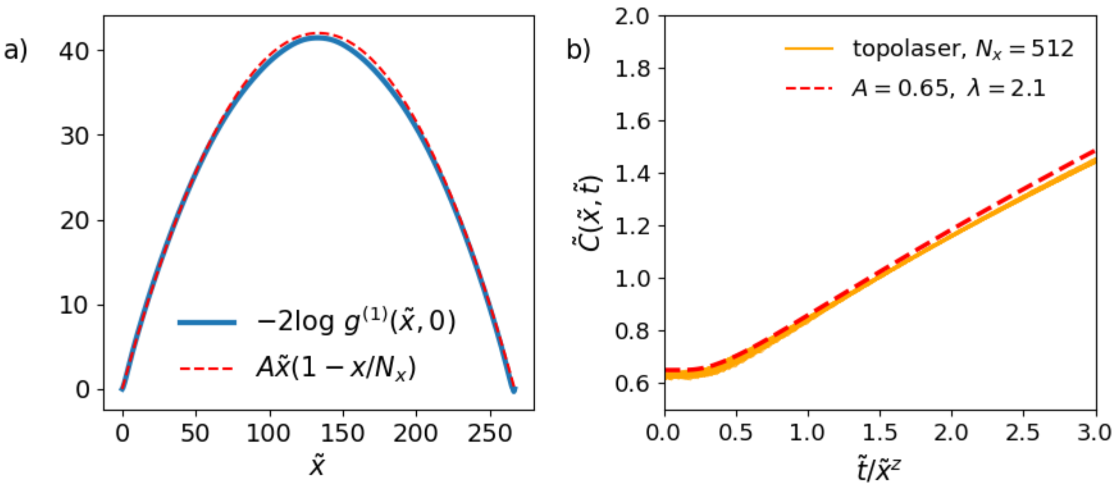

Figure 4.12: *Finite–size effects in KPZ dynamics.* We assess finite-size effects by considering the correlation functions of a topological laser of length $N_x = 512$ in the KPZ regime (parameters like Fig. 6 of the main text). (a) Equal-time spatial correlation function. For an infinite system one would have $-2\log\, g^{(1)}(\tilde{x},0) = A|\tilde{x}|$; finite-size effects are kept into account by adding the Brownian bridge factor. (b) The correlation functions (orange) collapse, in very good approximation, onto the same universal scaling function of the twice longer system $N = 1024$ (red dashes).

with $s = \tilde{t}/\tilde{x}^z$ and $z = 3/2$ on the right-hand side and g_{KPZ} a universal function discussed in Sec.3.2. In particular, one has $\tilde{C}(0) = A = \frac{\mathcal{D}}{2\nu}$.

A series of curves of $\tilde{C}(\tilde{x},\tilde{t})$ for $x = \pm 30, ..., \pm 160$ is plotted as orange lines in Fig.4.10(b) as a function of $\tilde{t}/\tilde{x}^z$: to correct for the finite size effects, we actually plot $\tilde{C}(\tilde{x},\tilde{t})/(1-|x|/N_x)$. The rational behind this trick is that the probability of having an equal-time jump of $\phi(x)-\phi(0)$ in an infinite system is proportional to the Gaussian $e^{-\frac{\Delta\phi^2}{Ax}}$. In a finite system with periodic boundary conditions one has to multiply the probabilities of making the jump by crossing or not the boundary of the system $e^{-\frac{\Delta\phi^2}{Ax}} \times e^{-\frac{\Delta\phi^2}{A(L-x)}} = e^{-\frac{\Delta\phi^2}{Ax(1-x/L)}}$, which is called a Brownian bridge. With this strategy the theoretical prediction perfectly matches the numerical spatial correlation function, as shown in Fig. 4.12.a. Coming back to Fig.4.10(b), the collapse of the different lines onto a single curve demonstrates that within an excellent approximation (the corrected against finite size effects version of) $\tilde{C}$ only depends on $\tilde{t}/\tilde{x}^z$, as expected from the KPZ scaling. This result for the topological laser is to be compared to an analogous analysis for a trivial one-dimensional array with the same physical parameters lasing in the $k = 0$ mode as discussed in Sec.3.2. Also in this case, the different lines (cyan) collapse on a single curve, confirming the expected KPZ scaling.

The crucial point about Fig.4.10(b) is that the phase, the space and the time have been rescaled by the ϕ^*, l^*, t^* values obtained from Eqs. (3.46) using the effective masses and gain parameters: for the topological laser, J_{eff} is the curvature of the Harper–Hofstadter band at the lasing point and P_{eff} is chosen in order to reproduce the observed intensity on the edge. For instance, $J_{eff} \simeq 0.319\gamma$ hence $l^* \simeq 1.92$ here.

As explained in Section 3.2, the Renormalization Group analysis (Ueno et al. [2005]) predicts for the non-topological $1D$ array lasing in the $k^{las} = 0$ mode that the rescaled KSE Eq. (3.48) flows to the low energy effective KPZ theory Eq. (3.47) with $\lambda = 2$, since, thanks to the Galilean invariance holding for KSE and KPZ equations, the nonlinear coupling is not renormalized. This is confirmed by our simulations, which show that the rescaled correlation functions indeed collapse to a unique curve as shown in Fig.4.10(b) and this curve is excellently fitted (blue dashed line) using (4.43) with $\lambda = 2$ and $A = 0.96$, as expected from the Galilean invariance argument.

For the topological laser, the curves again collapse onto a single curve, which is well fitted using $\lambda = 2.1$ and $A = 0.65$ (red dashed line). Note that an upper bound for the fitted value of the nonlinearity is provided by the value $\lambda = 2.3$ with $A = 0.63$. We checked that these effective KPZ parameters λ, A do not depend significantly on the size of the system, in other words the renormalization flow has reached its fixed point. This is shown in Fig. 4.12.b, where the correlation functions of a shorter $N_x = 512$ long system (orange lines) fall close to the scaling function fitted

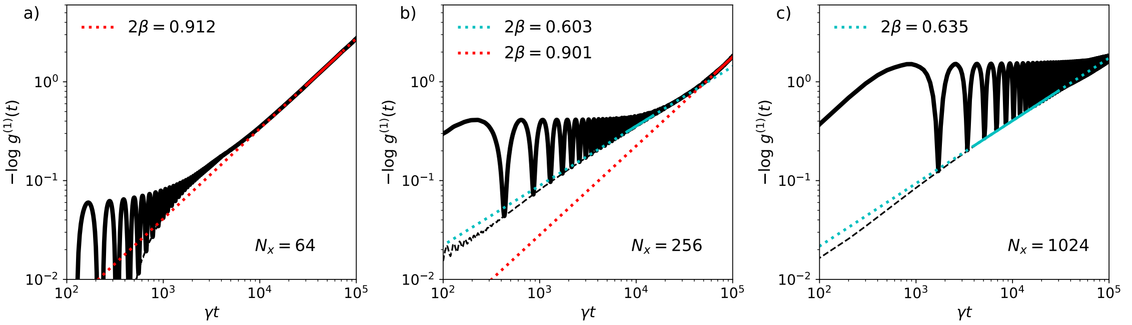

Figure 4.13: *Kardar-Parisi-Zhang to Schawlow-Townes crossover in a finite–size topological laser.* This plot is the analogue of Fig. 3.5 for the topological laser. The thick black lines correspond to the logarithm of the temporal correlation for a given site on the edge of the lattice. The thin dashed lines show the temporal evolution of the coherence $-\log g^{(1)}_{CM}(t)$ seen from the reference frame comoving with the edge state. For increasing system sizes and a given temporal window, a crossover between an exponential (red fits) and a KPZ (cyan fits) decay of the coherence is observed. The amplitude of the oscillations is inversely proportional to the spatial coherence of the device. In the long-time limit, only the global phase matters and the oscillations fade away.

from the $N_x = 1024$ data (red dashes, the same as Fig. 4.10.b).

In contrast to the non-topological case, for the topological laser there is no a priori guarantee that a Galilean invariant KSE holds microscopically; all the contrary, an analysis along the lines of (Gladilin et al. [2014], Altman et al. [2015]) suggests that a rescaling with J_{eff} still yields a microscopic $\lambda = 2$, but other terms should also be added in Eq. (3.47), e.g. of the kind $\partial_x^2\phi(\partial_x\phi)^2$, $(\partial_x^2\phi)^2$, $\partial_x^3\phi\partial_x\phi$, etc. These additional terms come from effective imaginary derivatives due to the k_x dependent localization of the Harper–Hofstadter eigenstates on the edge; in particular, they break Galilean invariance and one may expect that they significantly renormalize the effective KPZ parameters, since they contain the same number (four) of derivatives as the KSE term. However, it turns out from our numerics that the renormalization of λ remains small.

Still, it is interesting to note that the curves for the topological laser (in the properly rescaled units) sit below the ones of the trivial one-dimensional laser array and are correspondingly fitted by a KPZ form with a lower A. This feature can be traced back to the imaginary term proportional to η in (4.38) that accounts for the k-dependence of the edge mode penetration in the bulk. This term stabilizes the emission and makes the topological device more coherent than the 1D laser with the corresponding J_{eff}, P_{eff}. The crucial role of η in topological devices is apparent already at the level of Bogoliubov analysis (Loirette-Pelous [2020]), at least for class-A lasers.

We conclude this section with a brief remark on the experimental protocol to assess KPZ physics. The analysis of the correlation functions $g^{(1)}_{CM}(x,t)$ shown in Fig.4.10.b was carried out in the reference frame comoving with the chiral mode. Typical experiments measure correlation functions between different times $g^{(1)}(x,t)$ and different points in the laboratory frame. However, since the correlation functions in the comoving and laboratory frames are simply related by $g^{(1)}_{CM}(x,t) = g^{(1)}(x - v_g t, t)$, the interesting $g^{(1)}_{CM}$ can be extracted by a straightforward post-processing of $g^{(1)}(x,t)$ measured in the laboratory frame. Graphically, this amounts to tilt the correlation function of Fig. 4.8(c) with the suitable v_g so to have the maximum of $g^{(1)}(x,t)$ at $x = 0$ for all times t.

Finally, it is interesting to compare the linewidth as extracted from the numerical simulations of the stochastic equations with the Bogoliubov calculation. The numerical predictions for the coherence time of the topological laser are shown by the red and orange triangles in Fig. 3.7 (from the previous Chapter) as a function of the system size. The dashed line shows the theoretical prediction Eq. (4.29). From these results, one concludes that the topological laser behaves again similarly to the topologically trivial one-dimensional laser array: on one hand, the agreement with the Bogoliubov-Schawlow-Townes model of phase diffusion is excellent for small N_x and the coherence grows proportionally to N_x. On the other hand, a much slower growth of the coherence time with N_x is found for larger systems.

As a final point, it is interesting to note that the Bogoliubov-Schawlow–Townes prediction

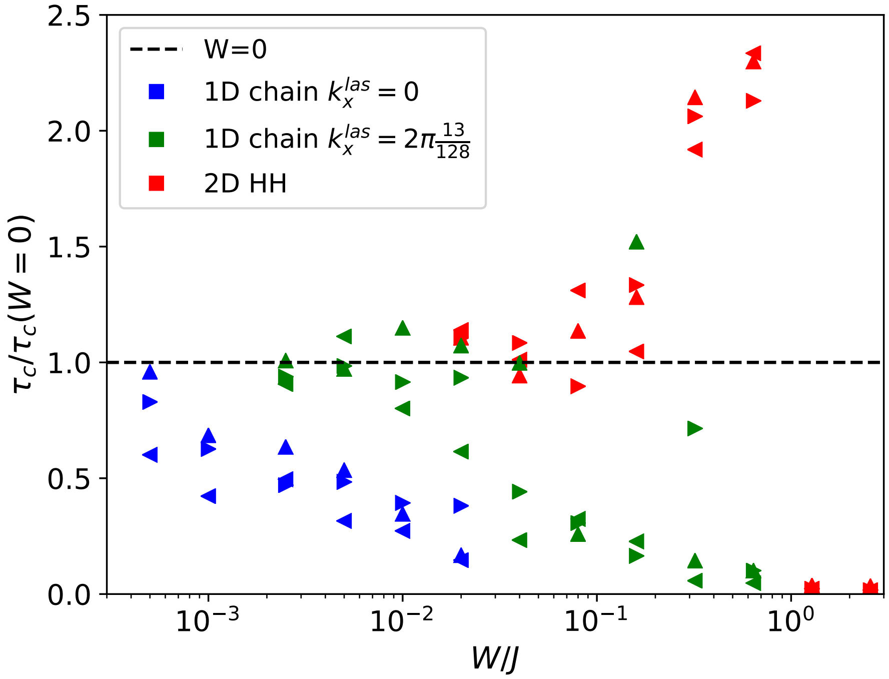

Figure 4.14: *Topological robustness of the temporal coherence.* Plot of the coherence time normalized to the clean system value, as a function of the strength W of the disorder. Different markers refer to different realizations of disorder. Blue and green markers are for a non-topological one-dimensional laser array lasing at $k^{las}=0$ (blue) or $k^{las}=2\pi\frac{13}{128}$ (green). Red markers are for the topological laser with periodic boundary conditions (squares and triangles) and with open boundary conditions (crosses). Same marker shapes correspond to the same spatial distribution of the disorder potential except for the overall strength W.

that well captures the emission linewidth for small systems does not depend on J_{eff} nor on the dispersion of the Bogoliubov modes at $k_x \neq 0$. On the other hand, the deviation observed for larger systems does strongly depend on J_{eff}, which pinpoints the crucial role of the KPZ nonlinearities illustrated above [6].

4.4 Lasing and coherence in disordered arrays*

(this Section builds on (Amelio and Carusotto [2019]))

The general message of the previous Section was that the coherence properties of a topological laser follow the same KPZ dynamics as the ones of a topologically trivial, one-dimensional laser array. This conclusion is not restricted to the well-known KPZ features in the infinite system limit, but also applies to the dependence of the coherence time on the system size and to its marked deviations from the Bogoliubov Schawlow-Townes prediction.

In this Section we investigate the effect of static disorder on the coherence of the laser emission. A certain degree of fabrication imperfections and inhomogeneities is in fact expected to be always present in any real device. As we are now going to see, our numerical study points out a dramatically different behaviour of topologically trivial vs. topological systems: disorder has a strong impact on the coherence of a topologically trivial system, a small amount of disorder being able to give a wide range of realization-dependent, chaotic and multi-mode phenomena. On the other hand, the temporal coherence of a topological laser is robust against a sizable disorder and emission remains well monochromatic as long as the disorder magnitude is not so large to close the topological gap.

---

[6] For this plot we chose the k_x^{las} corresponding to the maximally localized Harper–Hofstadter eigenvector, but the results are qualitatively independent of this choice. Fixing k_x^{las} is however needed if one is to compute the KPZ correlation functions by running parallel simulations.

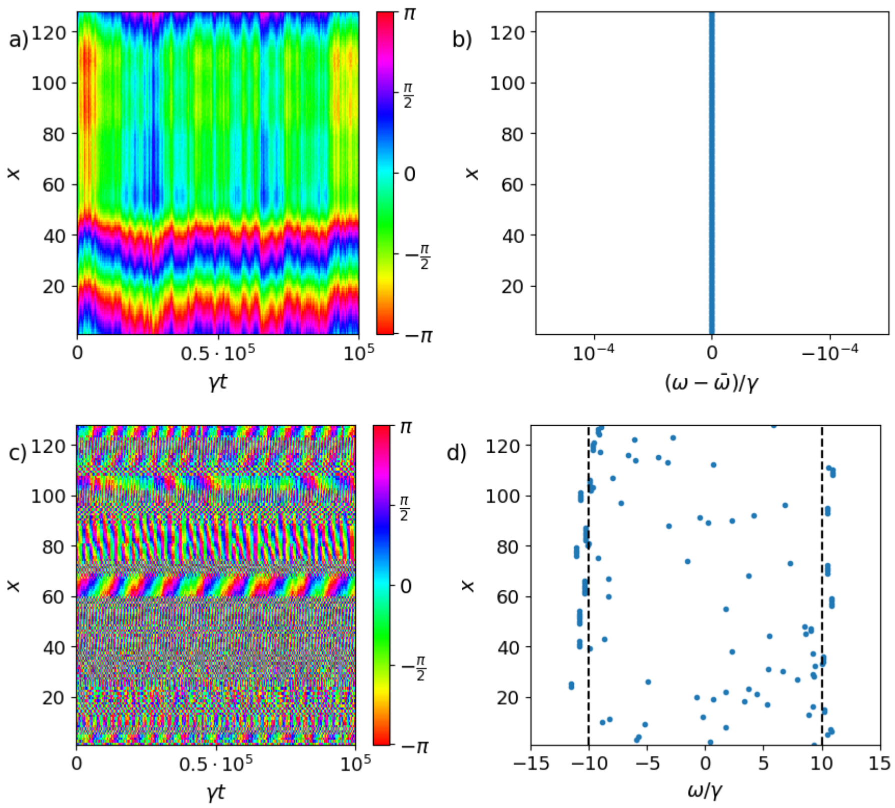

Figure 4.15: *Lasing in a disordered non-topological 1D array.* For a relatively weak disorder $W = 0.02J$ we report (a) the evolution of the phase of the field starting from an initial condition in a plane-wave form with $k_x^{las} = 0$ for a given realization of disorder and (b) the lasing frequency of each site on the edge, measured with respect to the spatial average of the lasing frequencies. The spatial behavior of the phase is changed by disorder without affecting the spatial coherence, and, very curiously, all sites lase at the same frequency even though the coherence time is reduced to $\tau_c/\tau_c(W=0) \sim 0.1$ (while the intensity of the field is on average unaffected). Panels (c-d) are the same as panels (a-b) except for the much stronger disorder $W = 0.32J$: the lattice breaks up in small domains lasing at distinct frequencies spread in the frequency interval between the the band edges of the system (vertical black dashes).

4.4.1 Lasing in non-topological 1D arrays with disorder

We start by considering the effect of on–site disorder on the lasing properties of a non-topological array of resonators. We do not aim here to a general discussion of the theory of lasing in disordered systems or to make a connection with random lasers (Wiersma [2008]), but our purpose is just to provide a benchmark to assess the features of a topological laser.

Along all this section, a disordered potential is added to Eqs. (3.36) and (4.23) in the form,

$$i\partial_t \psi_{\vec{x}} = \ldots + W\mathcal{G}(0,1)\psi_{\vec{x}}, \tag{4.44}$$

where $\mathcal{G}(0,1)$ is a Gaussian random variable with mean 0 and variance 1. For the sake of definiteness, we restrict here to the $N_x = 128$ and $J = 5\gamma$ case. The lasing dynamics in the presence of disorder is in general very complex, but, since our ultimate goal is a qualitative comparison with the topological laser, we focus here on the coherence time of the system for various values of disorder W, and in particular on whether there is a clear threshold value of disorder above which coherence collapses.

For linear waves, the sensitivity of the eigenstates at a given energy to a static perturbation is proportional to the spectral density of states. Then, in order to have a fair comparison of the trivial and topological cases, we consider lasing both at $k^{las} = 0$ and at $k^{las} = 2\pi\frac{13}{128}$. This latter case has a finite group velocity (and hence a density of states) comparable to the one of the chiral edge mode of the Harper–Hofstadter model in its central part and for these reasons we propose it as the proper benchmark for the topological laser.

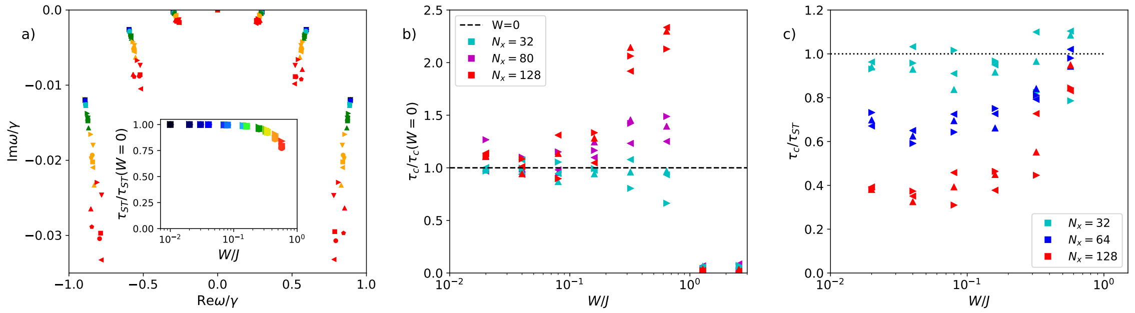

Figure 4.16: Panel a): Bogoliubov modes ω_λ in the Goldstone dome for a $N_x = 128, J = 5\gamma$ topological array in the presence of disorder, plotted as $\mathrm{Im}\,\omega_\lambda$ versus $\mathrm{Re}\,\omega_\lambda$. Different marker shapes correspond to different realizations of disorder and colder to warmer colors point at increasing values of W/J. Remarkably, the lifetime of the Bogoliubov modes is significantly reduced for $W \sim 0.5J$, so that longer times and larger arrays are required to observe appreciable nonlinear effects in the phase dynamics. Inset: Bogoliubov-Schawlow-Townes prediction for the coherence time τ_{ST} for increasing disorder strength W/J, plotted in units of the coherence time in the clean sample. b) Plot of the ratio $\tau_c(W)/\tau_c(0)$ as a function of the disorder strength W/J for different system sizes $N_x = 32, 80, 128$; in particular note how the enhanced coherence time at intermediate W/J is only observed for large enough systems. c) Plot of the ratio $\tau_c(W)/\tau_{ST}(W)$ as a function of disorder strength W/J for different system sizes $N_x = 32, 64, 128$, showing how the linewidth recovers the Bogoliubov prediction for smaller arrays and for stronger disorder close to the threshold.

In Fig. 4.14, we plot the coherence time normalized to the value in the absence of disorder. In particular, we use an exponential fit to extract the coherence time τ_c for each site (an exponential fit is used even if the shape of $g^{(1)}(t)$ is in general very complex) and we plot the average over the lattice. Markers with the same shape indicate that the same realization of disorder and the same initial conditions have been used, while only the overall strength factor W is varied.

Looking at the blue and green points in the plot, we see that already a very small disorder has a marked impact on the coherence time of the device. As expected, the threshold value depends on k_x^{las}, as visible comparing the blue dataset for lasing at $k^{las} = 0$ and the green dataset for a finite k^{las} where the density of states is smaller. While a detailed description of the variety of possible behaviours for different disorder realizations goes beyond the scope of this work, some illustrative examples are shown in Fig. 4.15. In the left panels the phase of $\psi_{sl}(x,t)$ is plotted in the slowly varying frame, while in the right panels the frequency of each site $\omega(x)$, defined as the peak of the spectrum of the field on that site, is plotted with respect to the spatial average $\bar{\omega} = \frac{1}{N_x}\sum_x \omega(x)$, with the exception of panel Fig. 4.15.d where the absolute frequency is plotted instead. In particular, for intermediate disorder $W \sim 0.08J$ laser operation may get fragmented with different portions of the sample lasing at different frequencies (panels (c,d)). Calculations for different realizations of disorder suggest that coherence can be greatly reduced even in the absence of fragmentation (as shown in panel b) of the same figure) and without affecting the intensity of the field, thus showing that there is no general one-by-one correspondence between the power slope efficiency and the robustness of coherence robustness to static disorder. Finally, curious non-monotonic behaviors can also be observed in some other realizations.

4.4.2 Topological robustness to disorder

The same protocol was repeated for the topological laser on a $N_x = 128$ times $N_y = 12$ stripe with $J = 5\gamma$, periodic boundary conditions along y and gain localized on the $y = 1$ row of sites. The results are reported as red datasets in Fig. 4.14. Simulations were also performed with fully open boundary conditions and gain distributed along the whole edge, yielding the same conclusions. In contrast to the non-topological case discussed in the previous subsection, the behavior of the topological laser remains quite regular in the presence of disorder and different realizations show very similar features.

For weak disorder strengths W, disorder has a negligible impact: as naively expected, scattering on defects is topologically suppressed as the laser field in the chiral edge mode is able to continuously travel around the system almost undisturbed. The temporal and spatial coherence properties of

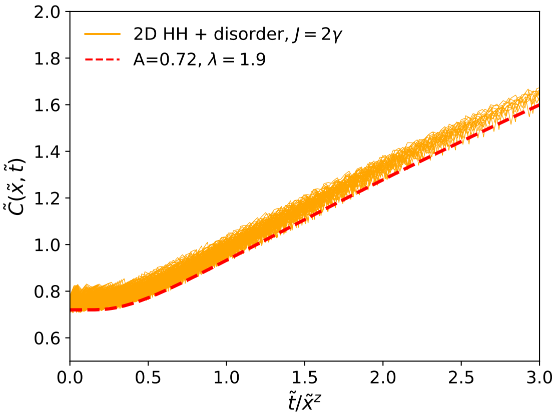

Figure 4.17: *KPZ dynamics in disordered topological laser.* Correlators $\tilde{C}(\tilde{t}, \tilde{x}^z)$ for $x = \pm 70, ..., \pm 300$ (small orange lines) for the topological device lasing in the presence of disorder of strength $W = 0.032J$. The wrinkles are not due to statistical noise, but arise because of the disorder (the data are relative to a specific realization). The red dashed line indicates the KPZ universal function (4.43) fitted on the clean sample. System parameters: $N_x = 1024$, $J = 2\gamma$, $P = 2\gamma$, $n_S = 1000$, $D_{x,y} = \gamma/2(1 + \delta_{y,1})$.

the clean system are thus very well preserved. For strong disorders, topological protection breaks down and the coherence displays a marked threshold at a value of disorder $W_c \sim J$, that is on the order of the topological gap of the underlying Harper–Hofstadter model. Beyond this value, spatial and temporal coherence are rapidly lost.

The most intriguing regime is for intermediate values of the disorder strength, where we observe a surprising and systematic enhancement of the temporal coherence. A tentative explanation for this expected behavior can be put forward in terms of the KPZ dynamics. Even though they are too small to destroy the topology, these values of W/J are strong enough to hamper the nonlinear phase dynamics that is responsible for the deviation from the Bogoliubov-Schawlow-Townes prediction seen in Fig. 3.7. As a result, for intermediate W the coherence time recovers the Bogoliubov–Schawlow–Townes prediction (4.29).

This interpretation is substantiated by the analysis reported in Fig. 4.16. As a first step, in panel a) we plot the real and imaginary parts of the lowest Bogoliubov eigenfrequencies (Loirette-Pelous [2020], Zapletal et al. [2020]) for a few realizations of disorder and different disorder strengths indicated by the shape and color of the markers. As usual in such calculations, the computation consisted in reaching the noiseless steady-state via the deterministic evolution in the presence of disorder and then finding the eigenmodes of the linearized evolution around the steady-state by diagonalizing Bogoliubov matrix. From the plot, it is apparent how disorder has a strong effect in reducing the lifetime of the excitation modes. Physically, this behaviour can be understood in terms of the fluctuation modes being pushed by the disorder deeper into the non-amplifying bulk of the lattice. Since the Bogoliubov-Schawlow-Townes coherence time is not sensitive to the decay rate of fluctuation modes, this effect is however not enough to explain the numerical observation shown in Fig. 4.14: As reported in the inset, a computation using the linearized Bogoliubov-Schawlow-Townes recipe of Eq. (4.32) rather predicts a slightly decreased coherence time for increasing disorder.

On the other hand, as the precursor of KPZ physics in a linearized analysis is typically given by the softening of the Bogoliubov modes, the faster decaying modes reported in Fig. 4.16.a hint to a suppression of the effective nonlinear coupling responsible for the KPZ-broadened linewidth. This intuition is quantitatively tested by repeating our calculation of the coherence time for different system sizes. As we have seen in Fig.3.7, the KPZ nonlinearity has in fact no effect on small systems, but it dramatically reduces the coherence of large systems.

Panels b) and c) of Fig. 4.16 fully confirms this mechanism. For the small $N_x = 32$ system size for which Fig.3.7 showed an accurate agreement with Schawlow-Townes, we find in panel b) that no enhancement is present and the coherence time remains nearly constant up to the threshold value W_c for which topological protection is broken. Panel c) show the same data on a different scale, with the coherence time normalized to the Bogoliubov-Schawlow-Townes prediction plotted in the inset of panel a). For small lattices $N_x = 32$, the relative coherence time $\tau_c/\tau_{ST} \approx 1$ up to W_c, showing that the Bogoliubov-Schawlow-Townes prediction is accurate and the KPZ nonlinearity plays no role. For the large system with $N_x = 128$, the relative coherence time τ_c/τ_{ST} is suppressed at small disorders by the KPZ nonlinearity and only recovers the unit value as the threshold W_c is approached and the KPZ nonlinearity is no longer effective. We have checked that these considerations remain valid for different noise distribution $D_{x,y}$, as it is displayed in Fig. S9.

Work in progress (Amelio and Carusotto [2020b]) is focusing on the direct measurement of KPZ correlations in the disordered case. We report in Fig. 4.17 the analogue of Fig. 4.10.b but in the presence of disorder. In particular we used a value $W = 0.032J$ close to the threshold for observing KPZ physics: for W below this value the clean red dashed line is recovered, while for stronger values the scaling behavior breaks and the orange region broadens considerably. This threshold is consistent with the crossover point one can see in Fig. 4.14 and we just discussed, above which τ_c gets enhanced.

As a last point, it is worth commenting on the dependence of these results on the specific value of k^{las}, that is the winding number $k^{las} N_x/(2\pi)$ of the lasing mode. For a non-topological one-dimensional system, we have seen in the blue and green datasets of Fig.4.14 that lasing at different k^{las} give very different robustness to disorder. On the other hand, we have found that topological lasing is quite insensitive to the specific value of k^{las} that can be chosen for laser operation (Seclì et al. [2019]). The simulations of the topological laser can thus be started with arbitrary initial conditions on the field, finding almost identical behaviours at the steady–state. This further demonstrates that the topological device is able to automatically reach a stable and coherent steady–state emission.

4.5 Discussion*

(this Section builds on (Amelio and Carusotto [2019]))

Our calculations are based on a simple model that brings together two main ingredients: lasing, meant as an archetype of nonlinear physics, and topologically protected chiral edge states. We give a rather complete treatment of this model. However, many additional elements that would be essential to quantitatively describe real-life devices have been neglected in our study. In this subsection we discuss to what extent our results are expected to apply to realistic devices, in particular the recent semiconductor-based realizations (Wittek et al. [2017], Bandres et al. [2018], Bahari et al. [2017], Zeng et al. [2020], St-Jean et al. [2017], Parto et al. [2018]), and in which properties the main deviations are expected to occur.

First of all, we have focused our attention on an idealized gain medium with a temporally instantaneous response. This is a good approximation for a gain medium with a fast relaxation rate, in which the electronic dynamics in the medium can be adiabatically eliminated in favour of the electromagnetic field dynamics. Furthermore, we have assumed that the optical nonlinearity reduces to gain saturation, and does not affect the real part of the refractive index. This would be a good approximation only if laser operation occurs near the center of the amplification band, otherwise mode pulling effects typically set in.

While these elements are essential in order to make quantitative predictions for a specific device, we do not expect they will introduce qualitative changes: as it was shown in (Gladilin et al. [2014], He et al. [2015], Squizzato et al. [2018]), the characteristic length and time scales over which the KPZ regime is observed are of course modified in the presence of reactive optical nonlinearities, but not the universal scaling behaviour. Of course, this is valid as long as the additional features –in particular the slow carrier dynamics– do not introduce dynamical instabilities akin to those predicted in (Longhi et al. [2018], Baboux et al. [2018], Loirette-Pelous [2020]) or multi-mode lasing behaviours. Inspection of the experimental spectra reported in (Bahari et al. [2017], Harari et al. [2018]) agree with our numerical calculation in giving a stable single-mode emission, so this does not appear to be a concern for existing experiments.

Concerning the coherence time, it is well known that the details of the gain medium (Whittaker and Eastham [2009], Pick et al. [2015]) can have a sizable impact on the linewidth, but they typically do not change the exponential functional form of the long time coherence decay. In particular, the intensity-dependence of the refractive index is typically responsible of an additional linewidth broadening effect as intensity fluctuations translate (often in temporally non-local way determined by the carrier dynamics) into fluctuations of the cavity mode frequency and thus in a diffusion of the phase. The ensuing linewidth broadening effect is quantified by the so-called Henry factor, which in semiconductor lasers can be as large as a few tens. In realistic topological lasers, we expect that this broadening source will sum up with the Petermann factor and the broadening factor arising from the nonlinear phase dynamics illustrated in Fig. 3.7.

The effect of a non-instantaneous response of the gain medium requires some distinctions. On one hand, a slow carrier dynamics breaking our adiabaticity assumption should not introduce any additional linewidth broadening effect (Pick et al. [2015]). On the other hand, the restricted frequency-band of gain that is often associated to a non-instantaneous response of the gain medium may enhance both spatial and temporal coherence since lasing typically occurs at the point of maximum gain and the weaker amplification of fluctuating side-modes results in a faster effective damping ν in (3.48) and η in (4.39). A theoretical study of the role of a frequency-dependent amplification in favoring laser operation in the topological edge modes over bulk modes as observed in (Bahari et al. [2017]) will be the topic of a forthcoming publication (Secli and Carusotto [2019]).

Another important issue to be carefully considered is the actual validity of the tight-binding approximation in a specific topological system and the possibility of a complex nonlinear dependence of the tight-binding parameters on the circulating light intensity. The tight-binding approximation performed in our calculations consists in solving the nonlinear dynamics of the field on a discrete lattice of coupled single-mode resonators instead of dealing *ab initio* with the full nonlinear Maxwell equations in the microscopic geometry of the underlying topological structure. Powerful methods to this purpose have been developed, e.g. the so-called SALT – Steady-state Ab initio Laser Theory (Türeci et al. [2006]) but they remain computationally very expensive compared to the tight-binding model: they allow to compute the deterministic steady-state and then compute the Schawlow-Townes linewidth within the linearized approach, but have never been pushed to more subtle KPZ features. Also the recent works on KPZ physics in lasers (Altman et al. [2015], Gladilin et al. [2014], Ji et al. [2015], He et al. [2015], Lauter et al. [2017], Squizzato et al. [2018]) did not start from a microscopic description of the system, but were rather based on model equations of the Complex Ginzburg Landau family.

Since our conclusions on the spatio-temporal coherence are based on universal properties, we can anyway expect they are independent of the underlying microscopic model, so they should extend to generic realizations of the topological laser concept, irrespectively of the material platform under investigation. The only crucial assumption is that the dynamics can be described by a unique classical stochastic field, or in the laser terminology that the emission is a single mode one. This assumption needs to be verified *ab initio* for each model, and it remains to be investigated to what extent topology can help to phase-lock the field at the different sites of the array into a single, spatially extended mode. Certainly, the fact that the edge and bulk HH modes have very different spatial profiles can be helpful to achieve this goal, as studied in more detail by Noh et al. [2020], who managed to get single-mode operation by exploiting the fact that for large enough topological bandgaps one cavity mode has a quality factor considerably larger than the other modes, and as pointed out also in connection to supersymmetric laser arrays (Khajavikhan et al. [2020]).

4.6 Conclusions

In this Chapter we have investigated the spatio-temporal coherence properties of topological arrays of coupled laser resonators, discussing analogies and differences between lasing in a non-topological one-dimensional chain and chiral edge-state lasing in a 2D topological Harper–Hofstadter lattice, introduced in Section 4.1. A main focus of our work has been to clarify how the spatial fluctuations of a non-equilibrium classical field impact on its temporal coherence.

To attack this question, the Bogoliubov spectrum and temporal coherence have been computed in Section 4.2. In particular, for relatively small systems in the Schawlow-Townes regime the topological laser emission is by a transverse Petermann factor very close to one: this further clarifies the nature of the topological localization on the edge, proving that the coherence is not affected by the geometry of the cavity, as it instead occurs for lasing in open resonators. For all practical purposes the coherence time is then determined by the total number of photons in the device.

Moreover, provided one reasons in the reference frame moving at the group velocity of the chiral mode, the results of Chapter 4.3 are found to directly apply to the chiral laser emission in the edge states of extended topological devices. More precisely, the Kardar-Parisi-Zhang universality is numerically demonstrated and also concerning the very long time coherence the KPZ physics starts playing a central role in larger lattices, where the Schawlow-Townes linewidth gets strongly broadened by the nonlinear dynamics of spatial fluctuations.

The key novelty of topological lasing is visible in disordered systems, discussed in Section 4.4. While for clean samples the spatio-temporal correlations behave very similarly for the topological and trivial devices, topological protection entails a much larger resilience to fabrication imperfections. For the non-topological arrays, static disorder is in fact able to spatially localize the lasing mode and/or break it into several disconnected and incoherent pieces. On the other hand, the topological protected chiral motion of the edge state of a topological laser device is able to phase-lock the different sites and thus maintain the spatial and temporal coherence across the whole sample up to much larger values of the disorder strength on the order of the topological gap. In this regime, the many individual sites participating to the topological lasing operation emit in a coherent way as a single, very large and powerful laser in spite of fabrication disorder. These results open exciting perspectives both for technological applications and for studies of fundamental physics using topological lasers.

From the theoretical point of view, ongoing research includes the classification of the different Kardar-Parisi-Zhang universality subclasses for our model (Squizzato et al. [2018]) and the extension of our study to arrays of realistic semiconductor lasers and other kinds of non-equilibrium condensates, e.g. exciton-polaritons. As we argued in Section 4.5, since our results on the coherence properties are based on universal properties of the stochastic spatio-temporal field dynamics, we expect that our conclusions apply, with a proper rescaling of the coherence length and time, also to class B devices provided the laser emission is a single mode one. In this respect, the important open question is to assess whether the topology is able to overcome the different destabilization mechanisms that hinder single mode laser operation in spatially extended semiconductor laser arrays. On a longer run, a natural step involves the generalization of the topological laser concept to photonic lattices in higher dimensionalities and with different band topologies (Ozawa et al. [2019]), possibly exploiting the synthetic dimension concept for mode-locked emission (Yang et al. [2020]).

From the experimental side, the effectively periodic boundary conditions naturally enjoyed by a chiral edge mode are extremely promising to suppress undesired spatial inhomogeneities and boundary effects in experimental studies (Baboux [2020]) of the critical properties of different non-equilibrium statistical models.

On the application side, we have shown that the coherence properties of a topological laser are robust against the static fabrication disorder that is unavoidably present in any realistic system. While a marked robustness to disorder was established for the single-mode character of the emission and the power slope efficiency of the laser device in (Harari et al. [2018]), here we have demonstrated that robustness also holds with respect to the coherence properties of the emission. This confirms the strong promise that topological lasers hold for practical opto-electronic applications.

Conclusions and Outlooks

In this Thesis we have studied the physics of polariton fluids and laser arrays in different regimes. Here we want to summarize the most important results and future research directions, leaving to the Conclusions of each Chapter for more details and for the reference to the specific Sections.

Part I deals with resonantly driven polariton fluids: in Chapter 1 we presented a numerical study of steady-state flows off a finite laser spot. In particular, we highlight the extremely nonlinear response of the flow to the pump parameters, correcting some wide-spread misconceptions in the literature: our work thus candidates as the fundamental theoretical reference for studies of polaritons ejected by a finite laser spot. The experimental investigation of the quantum pressure term is being currently pursued by Alberto Bramati's group.

In Chapter 2 we treat polariton dynamics in the presence of dark excitonic states. The Chapter revolves around the experimental measurement of the polariton dispersion relation and the observation of a reduced speed of sound with respect to a fully coherent polariton model. We show that this feature can be accounted for by the presence of an incoherent excitonic reservoir and we can provide estimates of the reservoir contribution to the total polariton blueshift. Moreover, we point out the crucial difference of the impact of the reservoir on static versus dynamical properties, also in the light of a formal Galilean boost argument. We expect these conclusions to inform quite generally on driven nonlinear waves coupled to a density variable with a slow dynamics.

In Part 2 we turn to lasing systems and incoherently driven polariton condensates, where the macroscopic state spontaneously break the microscopic $U(1)$ symmetry. The general goal of this Part is understanding how spatial fluctuations affect temporal coherence in low dimensional and topological systems.

In Chapter 3 we have elucidated the behavior of large 1D laser arrays or polariton quasi-condensates at very long times, when the KPZ universal physics turns into a Scahwlow–Townes-like phase diffusion. This is characterized by a linewidth which experiences an extra broadening sensible to the lack of long range order. Our results propose the linewidth as a very interesting observable for future studies of non-equilibrium fluids. Current research is also focusing on the quantitative understanding of the non-trivial linewidth behavior with the system size, on the application of these concepts to other models and on the relevance of our analysis for experimentally available laser arrays. In particular, an intriguing question concerns the limits of applicability of the Bogoliubov method to real devices, since in traditional laser theory this approach is completely absent; the treatment of multimode lasing within this formalism represents a closely related challenge.

Finally, in Chapter 4 we report the first study of the coherence properties of a topological laser and illustrate the structure of the spatio-temporal correlators of the edge mode laser emission. In particular, a dimensional reduction is carefully discussed; moreover, while for small system sizes the Bogoliubov analysis is valid, for large enough systems the results of Chapter 3 apply after a proper change of frame. In the Bogoliubov regime, the computation of Petermann factors very close to 1 confirms the nature of edge mode lasing, in contrast to the case of gain guiding in open resonators. Our method provides an elegant generalization of the usual approach to the

Petermann factor, and it will be interesting to apply it to other situations (Appendix A is a first small anticipation of this program). Another remarkable result is the robustness of the coherence properties to disorder, which (up to a certain threshold) surprisingly helps in stabilizing the device. In the close future, it will be very interesting to study existing devices and try to probe the generic behavior of the correlation functions found here. Our work represents also an important step towards understanding the potential of topological semiconductor lasers for practical applications.

Acknowledgements

Here I want to thank especially those with whom I have shared most of my PhD days up on the hill.

At the top of the list, of course, there appear Elia Laughlin Macaluso (office mate and master of the Quantum Hall), Luca Bogoliubov Giacomelli (office mate, adventure companion since the first day, many discussions on Bogoliubov) and Donato Leggett Romito (office disturber and smoker fellow).

The experimental folks closely follow: Arturo, Carmelo and Wies, whom luckily I see more in my free time than at work. Also I have pretty much enjoyed the company of all the BEC members (past and present), the super efficient Physics secretaries Micaela e Lucia, the other PhD fellows (here I just mention Martina, Chiara, Matteo, Santo, Alberto) and other random people from the department (Raika in primis).

Then I have to thank and acknowledge all my scientific collaborations, in particular Davide Galli for teaching me about Helium II, Anna Minguzzi and Maxime Richard for a couple of excellent papers together, the other topolaser guys Matteo Seclì and Aurelian Loirette-Pelous, Leonie-Canet and Davide Squizzato who introduced me to the KPZ equation, Daniele De Bernardis for a few ultra-interesting discussions, Antoine Georges for his hospitality at College de France, Alessio Chiocchetta for our recent efforts and many others. A special mention goes to Giacomo Mazza: we have been thinking really a lot on very fascinating questions, let’ s hope we will have many opportunities to fight again about physics!

Last but not least, thanks a lot boss Iacopo for your supervision, for the freedom you left me to pursue my own research directions and also for many laughs together!

Appendix A: Petermann factor of two coupled resonators

Here we want to compute the Petermann factor of a simple system by applying the Bogoliubov method described in Eqs. (4.29,4.37). The system we consider consists of two resonators with the same bare frequency which we set to zero, coupling J and losses γ_1, γ_2. The crucial ingredient, though, is that we amplify only the first resonator with pumping rate P. The equations of the two oscillators then read

$$i\partial_t \psi_1 = -J\psi_2 + \frac{i}{2}\left[\frac{P}{1+|\psi_1|^2/n_S} - \gamma_1\right]\psi_1,$$

$$i\partial_t \psi_2 = -J\psi_1 - \frac{i}{2}\gamma_2\psi_2.$$

It is easy to check that, for $J > \gamma/2$, the steady-state $\psi_i(t) = \psi_i^0 e^{-i\omega_0 t}$ satisfies

$$\psi_2^0 = -\frac{J}{\omega_0 + i\gamma_2/2}\psi_1^0$$

$$\omega_0 = \pm\sqrt{J^2 - (\gamma_2/2)^2}$$

$$|\psi_1^0|^2 = n_S(P/\gamma_{12} - 1)\ , \qquad \gamma_{12} = \gamma_1 + \gamma_2.$$

Also notice that the two resonators have the same steady-state intensity $\psi_2^0 = |\psi_1^0|e^{i\phi}$; moreover, when $\gamma_2 \ll J$, $\phi \sim \gamma_2/J$. This solution is stable above the exceptional point $J > \gamma_2$ of the bare system, see (Zhang et al. [2018]) and references within for exceptional points and linewidth broadening.

The Bogoliubov equations read

$$i\partial_t \delta\psi_1 = (-\omega_0 + \frac{i}{2}\gamma_2)\delta\psi_1 - J\delta\psi_2 - \frac{i}{2}\Gamma(\delta\psi_1 + \delta\psi_1^*)$$

$$i\partial_t \delta\psi_2 = (-\omega_0 - \frac{i}{2}\gamma_2)\delta\psi_2 - J\delta\psi_1$$

corresponding to the Bogoliubov matrix

$$\mathcal{L} = \begin{pmatrix} -\omega_0 - \frac{i}{2}(\Gamma - \gamma_2) & -\frac{i}{2}\Gamma & -J & 0 \\ -\frac{i}{2}\Gamma & \omega_0 - \frac{i}{2}(\Gamma - \gamma_2) & 0 & J \\ -J & 0 & -\omega_0 - \frac{i}{2}\gamma_2 & 0 \\ 0 & J & 0 & \omega_0 - \frac{i}{2}\gamma_2 \end{pmatrix}$$

where $\Gamma = \gamma_{12}(P - \gamma_{12})/P$.

Applying the strategy discussed in Eqs. (4.29,4.37), the resulting Petermann factor is presented in the plot below, obtained for $\gamma_1 = \gamma_2 = \gamma$. In this model the distortion of the bare mode that produces the Petermann factor is not a modification of the intensities of the two resonators but a relative phase twist.

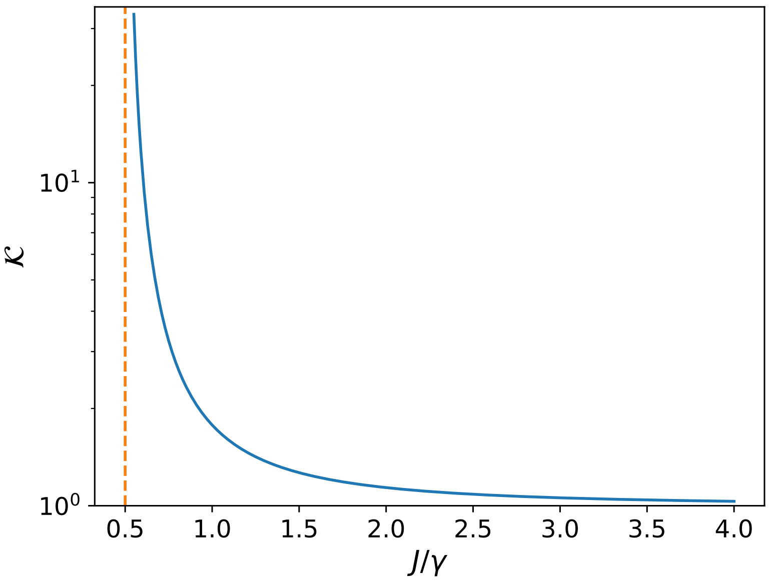

Bibliography

I. L. Aleiner, B. L. Altshuler, and Y. G. Rubo. Radiative coupling and weak lasing of exciton-polariton condensates. *Phys. Rev. B*, 85:121301, Mar 2012. doi: 10.1103/PhysRevB.85.121301. URL `https://link.aps.org/doi/10.1103/PhysRevB.85.121301`. (cited on p. 100)

Ehud Altman, Lukas M. Sieberer, Leiming Chen, Sebastian Diehl, and John Toner. Two-dimensional superfluidity of exciton polaritons requires strong anisotropy. *Phys. Rev. X*, 5: 011017, Feb 2015. doi: 10.1103/PhysRevX.5.011017. URL `https://link.aps.org/doi/10.1103/PhysRevX.5.011017`. (cited on pp. 104 and 110)

T. Amand, D. Robart, X. Marie, M. Brousseau, P. Le Jeune, and J. Barrau. Spin relaxation in polarized interacting exciton gas in quantum wells. *Phys. Rev. B*, 55:9880–9896, Apr 1997. doi: 10.1103/PhysRevB.55.9880. URL `https://link.aps.org/doi/10.1103/PhysRevB.55.9880`. (cited on p. 36)

Ivan Amelio and Iacopo Carusotto. Theory of the coherence of topological lasers, *arxiv:1911.10437*, 2019. (cited on pp. 5, 78, 88, 90, 93, 100, 105, and 109)

Ivan Amelio and Iacopo Carusotto. Perspectives in superfluidity in resonantly driven polariton fluids. *Phys. Rev. B*, 101:064505, Feb 2020a. doi: 10.1103/PhysRevB.101.064505. URL `https://link.aps.org/doi/10.1103/PhysRevB.101.064505`. (cited on pp. 4, 23, 31, 46, 58, and 59)

Ivan Amelio and Iacopo Carusotto. Robust simulation of statistical mechanics with laser arrays. 2020b. (cited on p. 109)

Ivan Amelio, Davide Emilio Galli, and Luciano Reatto. Probing quantum turbulence in 4he by quantum evaporation measurements. *Phys. Rev. Lett.*, 121:015302, Jul 2018. doi: 10.1103/PhysRevLett.121.015302. URL `https://link.aps.org/doi/10.1103/PhysRevLett.121.015302`. (cited on p. 6)

Ivan Amelio, Alessio Chiocchetta, and Iacopo Carusotto. On the linewidth of 1d non-equilibrium quasi-condensates. 2020a. (cited on p. 82)

Ivan Amelio, Anna Minguzzi, Maxime Richard, and Iacopo Carusotto. Galilean boosts and superfluidity of resonantly driven polariton fluids in the presence of an incoherent reservoir. *Phys. Rev. Research*, 2:023158, May 2020b. doi: 10.1103/PhysRevResearch.2.023158. URL `https://link.aps.org/doi/10.1103/PhysRevResearch.2.023158`. (cited on pp. 4, 5, 15, 19, 21, 45, and 54)

A. Amo, S. Pigeon, D. Sanvitto, V. G. Sala, R. Hivet, I. Carusotto, F. Pisanello, G. Leménager, R. Houdré, E Giacobino, C. Ciuti, and A. Bramati. Polariton superfluids reveal quantum hydrodynamic solitons. *Science*, 332(6034):1167–1170, 2011. ISSN 0036-8075. doi: 10.1126/science.1202307. URL `http://science.sciencemag.org/content/332/6034/1167`. (cited on pp. 4, 23, 24, 31, and 34)

Alberto Amo, Jérôme Lefrère, Simon Pigeon, Claire Adrados, Cristiano Ciuti, Iacopo Carusotto, Romuald Houdré, Elisabeth Giacobino, and Alberto Bramati. Superfluidity of polaritons in semiconductor microcavities. *Nature Physics*, 5:805 EP –, Sep 2009. URL `https://doi.org/10.1038/nphys1364`. (cited on pp. 18, 24, 34, 35, 59, and 60)

Philip W Anderson. More is different. *Science*, 177(4047):393–396, 1972. (cited on p. 3)

Vincenzo Ardizzone, Luisa De Marco, Milena De Giorgi, Lorenzo Dominici, Dario Ballarini, and Daniele Sanvitto. Emerging 2d materials for room-temperature polaritonics. *Nanophotonics*, 8(9):1547 – 1558, 2019. doi: https://doi.org/10.1515/nanoph-2019-0114. URL `https://www.degruyter.com/view/journals/nanoph/8/9/article-p1547.xml`. (cited on p. 14)

M. Artoni, I. Carusotto, G. C. La Rocca, and F. Bassani. Fresnel light drag in a coherently driven moving medium. *Phys. Rev. Lett.*, 86:2549–2552, Mar 2001. doi: 10.1103/PhysRevLett.86.2549. URL `https://link.aps.org/doi/10.1103/PhysRevLett.86.2549`. (cited on p. 21)

GE Astrakharchik and LP Pitaevskii. Motion of a heavy impurity through a bose-einstein condensate. *Physical Review A*, 70(1):013608, 2004. (cited on pp. 23 and 58)

A. Baas, J. Ph. Karr, H. Eleuch, and E. Giacobino. Optical bistability in semiconductor microcavities. *Phys. Rev. A*, 69:023809, Feb 2004. doi: 10.1103/PhysRevA.69.023809. URL `https://link.aps.org/doi/10.1103/PhysRevA.69.023809`. (cited on p. 16)

F Baboux. Kpz... *in preparation*, 2020. (cited on p. 111)

F. Baboux, D. De Bernardis, V. Goblot, V. N. Gladilin, C. Gomez, E. Galopin, L. Le Gratiet, A. Lemaître, I. Sagnes, I. Carusotto, M. Wouters, A. Amo, and J. Bloch. Unstable and stable regimes of polariton condensation. *Optica*, 5(10):1163–1170, Oct 2018. (cited on pp. 50, 57, and 109)

Babak Bahari, Abdoulaye Ndao, Felipe Vallini, Abdelkrim El Amili, Yeshaiahu Fainman, and Boubacar Kanté. Nonreciprocal lasing in topological cavities of arbitrary geometries. *Science*, 358 (6363):636–640, 2017. ISSN 0036-8075. doi: 10.1126/science.aao4551. URL `https://science.sciencemag.org/content/358/6363/636`. (cited on pp. 5, 87, 101, 109, and 110)

Daniele Bajoni, Pascale Senellart, Aristide Lemaître, and Jacqueline Bloch. Photon lasing ingaas-microcavity: Similarities with a polariton condensate. *Physical Review B*, 76(20), Nov 2007. ISSN 1550-235X. doi: 10.1103/physrevb.76.201305. URL `http://dx.doi.org/10.1103/PhysRevB.76.201305`. (cited on pp. 12 and 38)

Dario Ballarini, Davide Caputo, Galbadrakh Dagvadorj, Richard Juggins, Milena De Giorgi, Lorenzo Dominici, Kenneth West, Loren N. Pfeiffer, Giuseppe Gigli, Marzena H. Szymańska, and Daniele Sanvitto. Directional goldstone waves in polariton condensates close to equilibrium. *Nature Communications*, 11(1), January 2020. doi: 10.1038/s41467-019-13733-x. URL `https://doi.org/10.1038/s41467-019-13733-x`. (cited on p. 37)

Miguel A Bandres, Steffen Wittek, Gal Harari, Midya Parto, Jinhan Ren, Mordechai Segev, Demetrios N Christodoulides, and Mercedeh Khajavikhan. Topological insulator laser: Experiments. *Science*, 359(6381):eaar4005, 2018. (cited on pp. 86, 87, and 109)

S Bartalini, S Borri, P Cancio, Antonio Castrillo, I Galli, G Giusfredi, D Mazzotti, Livio Gianfrani, and P De Natale. Observing the intrinsic linewidth of a quantum-cascade laser: beyond the schawlow-townes limit. *Physical review letters*, 104(8):083904, 2010. (cited on p. 69)

J. J. Baumberg, P. G. Savvidis, R. M. Stevenson, A. I. Tartakovskii, M. S. Skolnick, D. M. Whittaker, and J. S. Roberts. Parametric oscillation in a vertical microcavity: A polariton condensate or micro-optical parametric oscillation. *Phys. Rev. B*, 62:R16247–R16250, Dec 2000. doi: 10.1103/PhysRevB.62.R16247. URL `https://link.aps.org/doi/10.1103/PhysRevB.62.R16247`. (cited on p. 15)

AC Berceanu, E Cancellieri, and FM Marchetti. Drag in a resonantly driven polariton fluid. *Journal of Physics: Condensed Matter*, 24(23):235802, 2012. (cited on pp. 18, 23, and 58)

Oleg L. Berman, Roman Ya. Kezerashvili, and Yurii E. Lozovik. Drag effects in a system of electrons and microcavity polaritons. *Phys. Rev. B*, 82:125307, Sep 2010. doi: 10.1103/PhysRevB.82.125307. URL `https://link.aps.org/doi/10.1103/PhysRevB.82.125307`. (cited on p. 45)

Michael Berry. Quantal phase factors accompanying adiabatic changes. *Proceedings of the Royal Society of London. A. Mathematical and Physical Sciences*, 392(1802):45–57, March 1984. doi: 10.1098/rspa.1984.0023. URL `https://doi.org/10.1098/rspa.1984.0023`. (cited on p. 87)

J. S. Blakemore. Semiconducting and other major properties of gallium arsenide. *Journal of Applied Physics*, 53(10):R123–R181, 1982. doi: 10.1063/1.331665. URL `https://doi.org/10.1063/1.331665`. (cited on p. 10)

Nataliya Bobrovska, Elena A. Ostrovskaya, and Michał Matuszewski. Stability and spatial coherence of nonresonantly pumped exciton-polariton condensates. *Phys. Rev. B*, 90:205304, Nov 2014. doi: 10.1103/PhysRevB.90.205304. URL `https://link.aps.org/doi/10.1103/PhysRevB.90.205304`. (cited on pp. 50 and 57)

Nataliya Bobrovska, Michał Matuszewski, Konstantinos S Daskalakis, Stefan A Maier, and Stéphane Kéna-Cohen. Dynamical instability of a nonequilibrium exciton-polariton condensate. *ACS Photonics*, 5(1):111–118, 2017. (cited on pp. 50 and 57)

Robert W Boyd. *Nonlinear optics*. Academic press, 2019. (cited on pp. 15 and 16)

Marvin E Cage, Kv Klitzing, AM Chang, F Duncan, M Haldane, RB Laughlin, AMM Pruisken, and DJ Thouless. *The quantum Hall effect*. Springer Science & Business Media, 2012. (cited on p. 86)

Léonie Canet, Hugues Chaté, Bertrand Delamotte, and Nicolás Wschebor. Nonperturbative renormalization group for the kardar-parisi-zhang equation. *Phys. Rev. Lett.*, 104:150601, Apr 2010. doi: 10.1103/PhysRevLett.104.150601. URL `https://link.aps.org/doi/10.1103/PhysRevLett.104.150601`. (cited on p. 77)

Davide Caputo, Dario Ballarini, Galbadrakh Dagvadorj, Carlos Sánchez Muñoz, Milena De Giorgi, Lorenzo Dominici, Kenneth West, Loren N. Pfeiffer, Giuseppe Gigli, Fabrice P. Laussy, Marzena Szymanska, and Daniele Sanvitto. Topological order and thermal equilibrium in polariton condensates. *Nature Materials*, 17:145 EP –, Dec 2017. URL `https://doi.org/10.1038/nmat5039`. Article. (cited on p. 34)

I. Carusotto, M. Artoni, G. C. La Rocca, and F. Bassani. Transverse fresnel-fizeau drag effects in strongly dispersive media. *Phys. Rev. A*, 68:063819, Dec 2003. doi: 10.1103/PhysRevA.68.063819. URL `https://link.aps.org/doi/10.1103/PhysRevA.68.063819`. (cited on p. 21)

Iacopo Carusotto. Superfluid light in bulk nonlinear media. *Proceedings of the Royal Society A: Mathematical, Physical and Engineering Sciences*, 470(2169):20140320, 2014. (cited on p. 60)

Iacopo Carusotto and Cristiano Ciuti. Probing microcavity polariton superfluidity through resonant rayleigh scattering. *Phys. Rev. Lett.*, 93:166401, Oct 2004. doi: 10.1103/PhysRevLett.93.166401. URL `https://link.aps.org/doi/10.1103/PhysRevLett.93.166401`. (cited on pp. 4, 15, 17, 18, 19, 21, 25, 26, 28, 29, and 34)

Iacopo Carusotto and Cristiano Ciuti. Spontaneous microcavity-polariton coherence across the parametric threshold: Quantum monte carlo studies. *Phys. Rev. B*, 72:125335, Sep 2005. doi: 10.1103/PhysRevB.72.125335. URL `https://link.aps.org/doi/10.1103/PhysRevB.72.125335`. (cited on p. 15)

Iacopo Carusotto and Cristiano Ciuti. Quantum fluids of light. *Rev. Mod. Phys.*, 85:299–366, Feb 2013. doi: 10.1103/RevModPhys.85.299. URL `https://link.aps.org/doi/10.1103/RevModPhys.85.299`. (cited on pp. 4, 13, 16, 20, 24, 26, 28, 29, and 96)

Igor Y. Chestnov, Yuri G. Rubo, and Alexey V. Kavokin. Pseudodrag of a polariton superfluid. *Phys. Rev. B*, 100:085302, Aug 2019. doi: 10.1103/PhysRevB.100.085302. URL `https://link.aps.org/doi/10.1103/PhysRevB.100.085302`. (cited on p. 45)

A. Chiocchetta, A. Gambassi, and I. Carusotto. *Laser Operation and Bose–Einstein Condensation: Analogies and Differences*, pages 409–423. Cambridge University Press, 2017. doi: 10.1017/9781316084366.022. (cited on p. 63)

Alessio Chiocchetta and Iacopo Carusotto. Non-equilibrium quasi-condensates in reduced dimensions. *EPL (Europhysics Letters)*, 102(6):67007, 2013. (cited on p. 71)

C. Ciuti, V. Savona, C. Piermarocchi, A. Quattropani, and P. Schwendimann. Role of the exchange of carriers in elastic exciton-exciton scattering in quantum wells. *Phys. Rev. B*, 58:7926–7933, Sep 1998. doi: 10.1103/PhysRevB.58.7926. URL `https://link.aps.org/doi/10.1103/PhysRevB.58.7926`. (cited on pp. 4 and 36)

C. Cohen-Tannoudji, B. Diu, and F. Laloe. *Quantum Mechanics*. Number v. 1 in Quantum Mechanics. Wiley, 1991. ISBN 9780471164333. URL `https://books.google.it/books?id=iHcpAQAAMAAJ`. (cited on p. 20)

Claude Cohen-Tannoudji, Jacques Dupont-Roc, and Gilbert Grynberg. *Atom—Photon Interactions*. Wiley, April 1998. doi: 10.1002/9783527617197. URL `https://doi.org/10.1002/9783527617197`. (cited on p. 63)

Aymeric Delteil, Thomas Fink, Anne Schade, Sven Höfling, Christian Schneider, and Ataç İmamoğlu. Towards polariton blockade of confined exciton–polaritons. *Nature Materials*, 18(3): 219–222, February 2019. doi: 10.1038/s41563-019-0282-y. URL `https://doi.org/10.1038/s41563-019-0282-y`. (cited on p. 37)

Yaojun Du, Sung Sakong, and Peter Kratzer. As vacancies, ga antisites, and au impurities in zinc blende and wurtzite gaas nanowire segments from first principles. *Physical Review B*, 87:75308–, 02 2013. doi: 10.1103/PhysRevB.87.075308. (cited on p. 11)

E. Estrecho, T. Gao, N. Bobrovska, D. Comber-Todd, M. D. Fraser, M. Steger, K. West, L. N. Pfeiffer, J. Levinsen, M. M. Parish, T. C. H. Liew, M. Matuszewski, D. W. Snoke, A. G. Truscott, and E. A. Ostrovskaya. Direct measurement of polariton-polariton interaction strength in the thomas-fermi regime of exciton-polariton condensation. *Phys. Rev. B*, 100:035306, Jul 2019. doi: 10.1103/PhysRevB.100.035306. URL `https://link.aps.org/doi/10.1103/PhysRevB.100.035306`. (cited on pp. 4, 36, 37, and 54)

Q Fontaine, T Bienaimé, S Pigeon, E Giacobino, A Bramati, and Q Glorieux. Observation of the bogoliubov dispersion in a fluid of light. *Physical review letters*, 121(18):183604, 2018. (cited on p. 60)

Erwin Frey and Uwe Claus Täuber. Two-loop renormalization-group analysis of the burgers–kardar-parisi-zhang equation. *Phys. Rev. E*, 50:1024–1045, Aug 1994. doi: 10.1103/PhysRevE.50.1024. URL `https://link.aps.org/doi/10.1103/PhysRevE.50.1024`. (cited on p. 76)

Erwin Frey, Uwe Claus Täuber, and Terence Hwa. Mode-coupling and renormalization group results for the noisy burgers equation. *Physical Review E*, 53(5):4424, 1996. (cited on pp. 74 and 82)

Crispin Gardiner and Peter Zoller. *Quantum noise: a handbook of Markovian and non-Markovian quantum stochastic methods with applications to quantum optics*, volume 56. Springer Science & Business Media, 2004. (cited on pp. 13 and 63)

Dario Gerace and Iacopo Carusotto. Analog hawking radiation from an acoustic black hole in a flowing polariton superfluid. *Physical Review B*, 86(14):144505, 2012. (cited on pp. 23 and 34)

Vladimir N. Gladilin, Kai Ji, and Michiel Wouters. Spatial coherence of weakly interacting one-dimensional nonequilibrium bosonic quantum fluids. *Phys. Rev. A*, 90:023615, Aug 2014. doi: 10.1103/PhysRevA.90.023615. URL `https://link.aps.org/doi/10.1103/PhysRevA.90.023615`. (cited on pp. 5, 71, 73, 101, 104, 109, and 110)

Grangier, Ph. and Poizat, J.-Ph. A simple quantum picture for the petermann excess noise factor. *Eur. Phys. J. D*, 1(1):97–104, 1998. doi: 10.1007/s100530050069. URL `https://doi.org/10.1007/s100530050069`. (cited on pp. 99 and 100)

G. Grosso, G. Nardin, F. Morier-Genoud, Y. Léger, and B. Deveaud-Plédran. Soliton instabilities and vortex street formation in a polariton quantum fluid. *Phys. Rev. Lett.*, 107:245301, Dec 2011. doi: 10.1103/PhysRevLett.107.245301. URL `https://link.aps.org/doi/10.1103/PhysRevLett.107.245301`. (cited on p. 32)

M. Hafezi, S. Mittal, J. Fan, A. Migdall, and J. M. Taylor. Imaging topological edge states in silicon photonics. *Nature Photonics*, 7(12):1001–1005, October 2013. doi: 10.1038/nphoton.2013.274. URL `https://doi.org/10.1038/nphoton.2013.274`. (cited on p. 87)

Mohammad Hafezi, Eugene A. Demler, Mikhail D. Lukin, and Jacob M. Taylor. Robust optical delay lines with topological protection. *Nature Physics*, 7(11):907–912, August 2011. doi: 10.1038/nphys2063. URL `https://doi.org/10.1038/nphys2063`. (cited on pp. 86 and 87)

Hermann Haken. *Synergetics*. Springer Berlin Heidelberg, 1983. doi: 10.1007/978-3-642-88338-5. URL `https://doi.org/10.1007/978-3-642-88338-5`. (cited on p. 63)

F. D. M. Haldane and S. Raghu. Possible realization of directional optical waveguides in photonic crystals with broken time-reversal symmetry. *Phys. Rev. Lett.*, 100:013904, Jan 2008. doi: 10.1103/PhysRevLett.100.013904. URL `https://link.aps.org/doi/10.1103/PhysRevLett.100.013904`. (cited on p. 87)

F Duncan M Haldane. Model for a quantum hall effect without landau levels: Condensed-matter realization of the" parity anomaly". *Physical review letters*, 61(18):2015, 1988. (cited on p. 86)

W. A. Hamel and J. P. Woerdman. Nonorthogonality of the longitudinal eigenmodes of a laser. *Phys. Rev. A*, 40:2785–2787, Sep 1989. doi: 10.1103/PhysRevA.40.2785. URL `https://link.aps.org/doi/10.1103/PhysRevA.40.2785`. (cited on p. 99)

Changhyun Han, Myungjae Lee, Ségolène Callard, Christian Seassal, and Heonsu Jeon. Lasing at topological edge states in a photonic crystal l3 nanocavity dimer array. *Light: Science & Applications*, 8(1):1–10, 2019. (cited on p. 88)

Gal Harari, Miguel A Bandres, Yaakov Lumer, Mikael C Rechtsman, Yi Dong Chong, Mercedeh Khajavikhan, Demetrios N Christodoulides, and Mordechai Segev. Topological insulator laser: theory. *Science*, 359(6381):eaar4003, 2018. (cited on pp. 5, 109, and 111)

Stella L Harrison, Helgi Sigurdsson, and Pavlos G Lagoudakis. Synchronization in optically trapped polariton stuart-landau networks. *Physical Review B*, 101(15):155402, 2020. (cited on p. 100)

Liang He, Lukas M. Sieberer, Ehud Altman, and Sebastian Diehl. Scaling properties of one-dimensional driven-dissipative condensates. *Phys. Rev. B*, 92:155307, Oct 2015. doi: 10.1103/PhysRevB.92.155307. URL `https://link.aps.org/doi/10.1103/PhysRevB.92.155307`. (cited on pp. 5, 70, 73, 80, 101, 109, and 110)

Peisong He and Zhaoxin Liang. Drag force of a exciton-polariton condensate under non-resonant pumping. 2020. (cited on p. 59)

C. Henry. Theory of the linewidth of semiconductor lasers. *IEEE Journal of Quantum Electronics*, 18(2):259–264, February 1982. doi: 10.1109/JQE.1982.1071522. (cited on pp. 5, 6, 68, 69, and 89)

C. Henry. Theory of spontaneous emission noise in open resonators and its application to lasers and optical amplifiers. *Journal of Lightwave Technology*, 4(3):288–297, March 1986. doi: 10.1109/JLT.1986.1074715. (cited on p. 99)

J. J. Hopfield. Theory of the contribution of excitons to the complex dielectric constant of crystals. *Phys. Rev.*, 112:1555–1567, Dec 1958. doi: 10.1103/PhysRev.112.1555. URL `https://link.aps.org/doi/10.1103/PhysRev.112.1555`. (cited on p. 12)

A. Imamoḡlu, H. Schmidt, G. Woods, and M. Deutsch. Strongly interacting photons in a nonlinear cavity. *Phys. Rev. Lett.*, 79:1467–1470, Aug 1997. doi: 10.1103/PhysRevLett.79.1467. URL `https://link.aps.org/doi/10.1103/PhysRevLett.79.1467`. (cited on p. 13)

J.D. Jackson. *Classical electrodynamics*. Wiley, 1975. ISBN 9780471431329. URL `https://books.google.it/books?id=_7rvAAAAMAAJ`. (cited on p. 21)

J.V. Jelley. *Čerenkov Radiation, and Its Applications*. United Kingdom Atomic Energy Authority, 1958. (cited on p. 31)

Kai Ji, Vladimir N. Gladilin, and Michiel Wouters. Temporal coherence of one-dimensional nonequilibrium quantum fluids. *Phys. Rev. B*, 91:045301, Jan 2015. doi: 10.1103/PhysRevB.91.045301. URL `https://link.aps.org/doi/10.1103/PhysRevB.91.045301`. (cited on pp. 5, 73, and 110)

Reginald Victor Jones. 'fresnel aether drag' in a transversely moving medium. *Proceedings of the Royal Society of London. A. Mathematical and Physical Sciences*, 328(1574):337–352, 1972. (cited on p. 21)

R. T. Juggins, J. Keeling, and M. H. Szymańska. Coherently driven microcavity-polaritons and the question of superfluidity. *Nature Communications*, 9(1), October 2018. doi: 10.1038/s41467-018-06436-2. URL `https://doi.org/10.1038/s41467-018-06436-2`. (cited on p. 18)

A. M. Kamchatnov and L. P. Pitaevskii. Stabilization of solitons generated by a supersonic flow of bose-einstein condensate past an obstacle. *Phys. Rev. Lett.*, 100:160402, Apr 2008. doi: 10.1103/PhysRevLett.100.160402. URL `https://link.aps.org/doi/10.1103/PhysRevLett.100.160402`. (cited on p. 24)

Alex Kamenev. *Field Theory of Non-Equilibrium Systems*. Cambridge University Press, 2011. doi: 10.1017/CBO9781139003667. (cited on pp. 74 and 75)

C. L. Kane and E. J. Mele. Quantum spin hall effect in graphene. *Phys. Rev. Lett.*, 95:226801, Nov 2005. doi: 10.1103/PhysRevLett.95.226801. URL `https://link.aps.org/doi/10.1103/PhysRevLett.95.226801`. (cited on p. 86)

Mehran Kardar, Giorgio Parisi, and Yi-Cheng Zhang. Dynamic scaling of growing interfaces. *Physical Review Letters*, 56(9):889–892, March 1986. doi: 10.1103/physrevlett.56.889. URL `https://doi.org/10.1103/physrevlett.56.889`. (cited on pp. 5, 72, and 73)

J. Kasprzak, M. Richard, S. Kundermann, A. Baas, P. Jeambrun, J. M. J. Keeling, F. M. Marchetti, M. H. Szymanska, R. André, J. L. Staehli, V. Savona, P. B. Littlewood, B. Deveaud, and Le Si Dang. Bose-einstein condensation of exciton polaritons. *Nature*, 443:409 EP –, Sep 2006. URL `https://doi.org/10.1038/nature05131`. Article. (cited on pp. 4, 10, 14, and 24)

Alexey Kavokin, Jeremy J. Baumberg, Guillaume Malpuech, and Fabrice P. Laussy. *Microcavities*. Oxford University Press, December 2007. doi: 10.1093/acprof:oso/9780199228942.001.0001. URL `https://doi.org/10.1093/acprof:oso/9780199228942.001.0001`. (cited on p. 9)

J. Keeling, L. M. Sieberer, E. Altman, L. Chen, S. Diehl, and J. Toner. *Superfluidity and Phase Correlations of Driven Dissipative Condensates*, pages 205–230. Cambridge University Press, 2017. doi: 10.1017/9781316084366.013. (cited on p. 63)

LV Keldysh and AN Kozlov. Collective properties of excitons in semiconductors. *Sov. Phys. JETP*, 27(3):521, 1968. (cited on p. 12)

Mercedeh Khajavikhan, Mohammad Hokmabadi, Jae Hyuck Choi, and Demetrios Christodoulides. Topological and supersymmetric laser arrays (Conference Presentation). In Alexey A. Belyanin and Peter M. Smowton, editors, *Novel In-Plane Semiconductor Lasers XIX*, volume 11301. International Society for Optics and Photonics, SPIE, 2020. doi: 10.1117/12.2548507. URL `https://doi.org/10.1117/12.2548507`. (cited on p. 110)

Mahito Kohmoto. Topological invariant and the quantization of the hall conductance. *Annals of Physics*, 160(2):343–354, April 1985. doi: 10.1016/0003-4916(85)90148-4. URL `https://doi.org/10.1016/0003-4916(85)90148-4`. (cited on p. 85)

V. Kohnle, Y. Léger, M. Wouters, M. Richard, M. T. Portella-Oberli, and B. Deveaud-Plédran. From single particle to superfluid excitations in a dissipative polariton gas. *Phys. Rev. Lett.*, 106:255302, Jun 2011. doi: 10.1103/PhysRevLett.106.255302. URL `https://link.aps.org/doi/10.1103/PhysRevLett.106.255302`. (cited on p. 38)

D.N. Krizhanovskii, G. Dasbach, A.A. Dremin, V.D. Kulakovskii, N.A. Gippius, M. Bayer, and A. Forchel. Impact of exciton localization on the optical non-linearities of cavity polaritons. *Solid State Communications*, 119(7):435–439, August 2001. doi: 10.1016/s0038-1098(01)00266-6. URL `https://doi.org/10.1016/s0038-1098(01)00266-6`. (cited on p. 37)

SJM Kuppens, MP Van Exter, and JP Woerdman. Quantum-limited linewidth of a bad-cavity laser. *Physical review letters*, 72(24):3815, 1994. (cited on p. 69)

K. G. Lagoudakis, F. Manni, B. Pietka, M. Wouters, T. C. H. Liew, V. Savona, A. V. Kavokin, R. André, and B. Deveaud-Plédran. Probing the dynamics of spontaneous quantum vortices in polariton superfluids. *Phys. Rev. Lett.*, 106:115301, Mar 2011. doi: 10.1103/PhysRevLett.106.115301. URL `https://link.aps.org/doi/10.1103/PhysRevLett.106.115301`. (cited on p. 24)

Willis E Lamb. Theory of an optical maser. *Physical Review*, 134(6A):A1429, 1964. (cited on p. 65)

LD Landau, EM Lifshitz, and LP Pitaevskii. Statistical physics, part 2. *Course of theoretical physics*, 9:67, 1981. (cited on p. 18)

L.D. Landau, E.M. Lifshits, and L.P. Pitaevskiĭ. *Electrodynamics of continuous media:*. Pergamon international library of science, technology, engineering, and social studies. Pergamon, 1984. ISBN 9780080302751. URL `https://books.google.it/books?id=j7nvAAAAMAAJ`. (cited on p. 21)

Roland Lauter, Aditi Mitra, and Florian Marquardt. From kardar-parisi-zhang scaling to explosive desynchronization in arrays of limit-cycle oscillators. *Phys. Rev. E*, 96:012220, Jul 2017. doi: 10.1103/PhysRevE.96.012220. URL `https://link.aps.org/doi/10.1103/PhysRevE.96.012220`. (cited on p. 110)

Marco Liscidini and Lucio Claudio Andreani. Photonic crystals: An introductory survey. In *Organic and Hybrid Photonic Crystals*, pages 3–29. Springer International Publishing, 2015. doi: 10.1007/978-3-319-16580-6_1. URL `https://doi.org/10.1007/978-3-319-16580-6_1`. (cited on pp. 9 and 10)

Aurelian Loirette-Pelous. Theory of chiral edge state lasing in a two-dimensional topological system. *in preparation. A. Pelous' Master thesis is available at arXiv:1912.03911*, 2020. (cited on pp. 5, 90, 104, 108, and 109)

S. Longhi and L. Feng. Invited article: Mitigation of dynamical instabilities in laser arrays via non-hermitian coupling. *APL Photonics*, 3(6):060802, 2018. doi: 10.1063/1.5028453. URL `https://doi.org/10.1063/1.5028453`. (cited on p. 100)

S. Longhi, Y. Kominis, and V. Kovanis. Presence of temporal dynamical instabilities in topological insulator lasers. *EPL (Europhysics Letters)*, 122(1):14004, June 2018. doi: 10.1209/0295-5075/122/14004. URL `https://doi.org/10.1209/0295-5075/122/14004`. (cited on pp. 5, 88, 90, and 109)

Ling Lu, John D. Joannopoulos, and Marin Soljačić. Topological photonics. *Nature Photonics*, 8(11):821–829, October 2014. doi: 10.1038/nphoton.2014.248. URL `https://doi.org/10.1038/nphoton.2014.248`. (cited on p. 87)

Leonard Mandel and Emil Wolf. *Optical Coherence and Quantum Optics*. Cambridge University Press, September 1995. doi: 10.1017/cbo9781139644105. URL `https://doi.org/10.1017/cbo9781139644105`. (cited on pp. 65, 67, and 68)

K. R. Manes and A. E. Siegman. Observation of quantum phase fluctuations in infrared gas lasers. *Phys. Rev. A*, 4:373–386, Jul 1971. doi: 10.1103/PhysRevA.4.373. URL `https://link.aps.org/doi/10.1103/PhysRevA.4.373`. (cited on p. 69)

Gaël Nardin, Gabriele Grosso, Yoan Léger, Barbara Pietka, François Morier-Genoud, and Benoît Deveaud-Plédran. Hydrodynamic nucleation of quantized vortex pairs in a polariton quantum fluid. *Nature Physics*, 7:635 EP –, Apr 2011. URL `https://doi.org/10.1038/nphys1959`. Article. (cited on pp. 24, 28, 30, 34, 59, and 60)

Chetan Nayak, Steven H. Simon, Ady Stern, Michael Freedman, and Sankar Das Sarma. Non-abelian anyons and topological quantum computation. *Rev. Mod. Phys.*, 80:1083–1159, Sep 2008. doi: 10.1103/RevModPhys.80.1083. URL `https://link.aps.org/doi/10.1103/RevModPhys.80.1083`. (cited on p. 86)

T. W. Neely, E. C. Samson, A. S. Bradley, M. J. Davis, and B. P. Anderson. Observation of vortex dipoles in an oblate bose-einstein condensate. *Phys. Rev. Lett.*, 104:160401, Apr 2010. doi: 10.1103/PhysRevLett.104.160401. URL `http://link.aps.org/doi/10.1103/PhysRevLett.104.160401`. (cited on pp. 24 and 29)

H. S. Nguyen, D. Gerace, I. Carusotto, D. Sanvitto, E. Galopin, A. Lemaître, I. Sagnes, J. Bloch, and A. Amo. Acoustic black hole in a stationary hydrodynamic flow of microcavity polaritons. *Phys. Rev. Lett.*, 114:036402, Jan 2015. doi: 10.1103/PhysRevLett.114.036402. URL `https://link.aps.org/doi/10.1103/PhysRevLett.114.036402`. (cited on pp. 23, 28, and 34)

Wanwoo Noh, Hadiseh Nasari, Hwi-Min Kim, Quynh Le-Van, Zhetao Jia, Chi-Hsin Huang, and Boubacar Kanté. Experimental demonstration of single-mode topological valley-hall lasing at telecommunication wavelength controlled by the degree of asymmetry. *Optics Letters*, 45(15):4108, July 2020. doi: 10.1364/ol.399053. URL `https://doi.org/10.1364/ol.399053`. (cited on pp. 88 and 110)

Yasutomo Ota, Ryota Katsumi, Katsuyuki Watanabe, Satoshi Iwamoto, and Yasuhiko Arakawa. Topological photonic crystal nanocavity laser. *Communications Physics*, 1(1):1–8, 2018. (cited on p. 87)

Tomoki Ozawa, Hannah M. Price, Alberto Amo, Nathan Goldman, Mohammad Hafezi, Ling Lu, Mikael C. Rechtsman, David Schuster, Jonathan Simon, Oded Zilberberg, and Iacopo Carusotto. Topological photonics. *Rev. Mod. Phys.*, 91:015006, Mar 2019. doi: 10.1103/RevModPhys.91.015006. URL `https://link.aps.org/doi/10.1103/RevModPhys.91.015006`. (cited on pp. 87, 88, and 111)

T. K. Paraïso, M. Wouters, Y. Léger, F. Morier-Genoud, and B. Deveaud-Plédran. Multistability of a coherent spin ensemble in a semiconductor microcavity. *Nature Materials*, 9(8):655–660, July 2010. doi: 10.1038/nmat2787. URL `https://doi.org/10.1038/nmat2787`. (cited on p. 16)

Midya Parto, Steffen Wittek, Hossein Hodaei, Gal Harari, Miguel A. Bandres, Jinhan Ren, Mikael C. Rechtsman, Mordechai Segev, Demetrios N. Christodoulides, and Mercedeh Khajavikhan. Edge-mode lasing in 1d topological active arrays. *Phys. Rev. Lett.*, 120:113901, Mar 2018. doi: 10.1103/PhysRevLett.120.113901. URL `https://link.aps.org/doi/10.1103/PhysRevLett.120.113901`. (cited on pp. 88 and 109)

Vittorio Peano, Martin Houde, Florian Marquardt, and Aashish A. Clerk. Topological quantum fluctuations and traveling wave amplifiers. *Phys. Rev. X*, 6:041026, Nov 2016. doi: 10.1103/PhysRevX.6.041026. URL `https://link.aps.org/doi/10.1103/PhysRevX.6.041026`. (cited on p. 95)

K. Petermann. Calculated spontaneous emission factor for double-heterostructure injection lasers with gain-induced waveguiding. *IEEE Journal of Quantum Electronics*, 15(7):566–570, July 1979. doi: 10.1109/jqe.1979.1070064. URL `https://doi.org/10.1109/jqe.1979.1070064`. (cited on p. 99)

A. Pick, A. Cerjan, D. Liu, A. W. Rodriguez, A. D. Stone, Y. D. Chong, and S. G. Johnson. Ab initio multimode linewidth theory for arbitrary inhomogeneous laser cavities. *Phys. Rev. A*, 91:063806, Jun 2015. doi: 10.1103/PhysRevA.91.063806. URL `https://link.aps.org/doi/10.1103/PhysRevA.91.063806`. (cited on pp. 109 and 110)

Maciej Pieczarka, Marcin Syperek, Łukasz Dusanowski, Jan Misiewicz, Fabian Langer, Alfred Forchel, Martin Kamp, Christian Schneider, Sven Höfling, Alexey Kavokin, and Grzegorz Sęk. Ghost branch photoluminescence from a polariton fluid under nonresonant excitation. *Phys. Rev. Lett.*, 115:186401, Oct 2015. doi: 10.1103/PhysRevLett.115.186401. URL `https://link.aps.org/doi/10.1103/PhysRevLett.115.186401`. (cited on p. 37)

Maciej Pieczarka, Eliezer Estrecho, Maryam Boozarjmehr, Olivier Bleu, Mark Steger, Kenneth West, Loren N. Pfeiffer, David W. Snoke, Jesper Levinsen, Meera M. Parish, Andrew G. Truscott, and Elena A. Ostrovskaya. Observation of quantum depletion in a non-equilibrium exciton–polariton condensate. *Nature Communications*, 11(1), January 2020. doi: 10.1038/s41467-019-14243-6. URL `https://doi.org/10.1038/s41467-019-14243-6`. (cited on p. 37)

C. Piermarocchi, F. Tassone, V. Savona, A. Quattropani, and P. Schwendimann. Nonequilibrium dynamics of free quantum-well excitons in time-resolved photoluminescence. *Phys. Rev. B*, 53: 15834–15841, Jun 1996. doi: 10.1103/PhysRevB.53.15834. URL `https://link.aps.org/doi/10.1103/PhysRevB.53.15834`. (cited on p. 52)

S. Pigeon, I. Carusotto, and C. Ciuti. Hydrodynamic nucleation of vortices and solitons in a resonantly excited polariton superfluid. *Phys. Rev. B*, 83:144513, Apr 2011. doi: 10.1103/PhysRevB.83.144513. URL `https://link.aps.org/doi/10.1103/PhysRevB.83.144513`. (cited on pp. 4, 24, and 30)

Simon Pigeon and Alberto Bramati. Sustained propagation and control of topological excitations in polariton superfluid. *New Journal of Physics*, 19(9):095004, sep 2017. doi: 10.1088/1367-2630/aa849c. (cited on p. 33)

Laura Pilozzi and Claudio Conti. Topological lasing in resonant photonic structures. *Phys. Rev. B*, 93:195317, May 2016. doi: 10.1103/PhysRevB.93.195317. URL `https://link.aps.org/doi/10.1103/PhysRevB.93.195317`. (cited on p. 88)

Lev Pitaevskii and Sandro Stringari. *Bose-Einstein condensation and superfluidity*, volume 164. Oxford University Press, 2016. (cited on pp. 13, 17, 18, 24, 26, and 45)

D. Porras, C. Ciuti, J. J. Baumberg, and C. Tejedor. Polariton dynamics and bose-einstein condensation in semiconductor microcavities. *Phys. Rev. B*, 66:085304, Aug 2002. doi: 10.1103/PhysRevB.66.085304. URL `https://link.aps.org/doi/10.1103/PhysRevB.66.085304`. (cited on p. 13)

Michael Prähofer and Herbert Spohn. Exact scaling functions for one-dimensional stationary KPZ growth. *Journal of Statistical Physics*, 115(1/2):255–279, April 2004. doi: 10.1023/b:joss.0000019810.21828.fc. URL `https://doi.org/10.1023/b:joss.0000019810.21828.fc`. (cited on pp. 72, 73, and 77)

S. Raghu and F. D. M. Haldane. Analogs of quantum-hall-effect edge states in photonic crystals. *Phys. Rev. A*, 78:033834, Sep 2008. doi: 10.1103/PhysRevA.78.033834. URL `https://link.aps.org/doi/10.1103/PhysRevA.78.033834`. (cited on p. 87)

Mikael C. Rechtsman, Julia M. Zeuner, Yonatan Plotnik, Yaakov Lumer, Daniel Podolsky, Felix Dreisow, Stefan Nolte, Mordechai Segev, and Alexander Szameit. Photonic floquet topological insulators. *Nature*, 496(7444):196–200, April 2013. doi: 10.1038/nature12066. URL `https://doi.org/10.1038/nature12066`. (cited on p. 87)

C. Repellin and N. Goldman. Detecting fractional chern insulators through circular dichroism. *Phys. Rev. Lett.*, 122:166801, Apr 2019. doi: 10.1103/PhysRevLett.122.166801. URL `https://link.aps.org/doi/10.1103/PhysRevLett.122.166801`. (cited on p. 90)

S. R. K. Rodriguez, W. Casteels, F. Storme, N. Carlon Zambon, I. Sagnes, L. Le Gratiet, E. Galopin, A. Lemaître, A. Amo, C. Ciuti, and J. Bloch. Probing a dissipative phase transition via dynamical optical hysteresis. *Phys. Rev. Lett.*, 118:247402, Jun 2017. doi: 10.1103/PhysRevLett.118.247402. URL `https://link.aps.org/doi/10.1103/PhysRevLett.118.247402`. (cited on p. 16)

D. Sanvitto, F. M. Marchetti, M. H. Szymańska, G. Tosi, M. Baudisch, F. P. Laussy, D. N. Krizhanovskii, M. S. Skolnick, L. Marrucci, A. Lemaître, J. Bloch, C. Tejedor, and L. Viña. Persistent currents and quantized vortices in a polariton superfluid. *Nature Physics*, 6(7): 527–533, May 2010. doi: 10.1038/nphys1668. URL `https://doi.org/10.1038/nphys1668`. (cited on p. 24)

D. Sanvitto, S. Pigeon, A. Amo, D. Ballarini, M. De Giorgi, I. Carusotto, R. Hivet, F. Pisanello, V. G. Sala, P. S. S. Guimaraes, R. Houdré, E. Giacobino, C. Ciuti, A. Bramati, and G. Gigli. All-optical control of the quantum flow of a polariton condensate. *Nat. Phot.*, 5:610–614, 2011. (cited on pp. 24 and 34)

D. Sarkar, S. S. Gavrilov, M. Sich, J. H. Quilter, R. A. Bradley, N. A. Gippius, K. Guda, V. D. Kulakovskii, M. S. Skolnick, and D. N. Krizhanovskii. Polarization bistability and resultant spin rings in semiconductor microcavities. *Phys. Rev. Lett.*, 105:216402, Nov 2010. doi: 10.1103/PhysRevLett.105.216402. URL `https://link.aps.org/doi/10.1103/PhysRevLett.105.216402`. (cited on pp. 4, 16, 35, 37, 45, and 48)

I. G. Savenko, T. C. H. Liew, and I. A. Shelykh. Stochastic gross-pitaevskii equation for the dynamical thermalization of bose-einstein condensates. *Physical Review Letters*, 110(12), March 2013. doi: 10.1103/physrevlett.110.127402. URL `https://doi.org/10.1103/physrevlett.110.127402`. (cited on p. 34)

Vincenzo Savona, Carlo Piermarocchi, Antonio Quattropani, Paolo Schwendimann, and Francesco Tassone. Optical properties of microcavity polaritons. *Phase Transitions*, 68(1):169–279, February 1999. doi: 10.1080/01411599908224518. URL `https://doi.org/10.1080/01411599908224518`. (cited on p. 9)

A. L. Schawlow and C. H. Townes. Infrared and optical masers. *Phys. Rev.*, 112:1940–1949, Dec 1958. doi: 10.1103/PhysRev.112.1940. URL `https://link.aps.org/doi/10.1103/PhysRev.112.1940`. (cited on pp. 5, 64, 67, and 69)

T.E. Schlesinger. Gallium arsenide. In *Encyclopedia of Materials: Science and Technology*, pages 3431–3435. Elsevier, 2001. doi: 10.1016/b0-08-043152-6/00612-4. URL `https://doi.org/10.1016/b0-08-043152-6/00612-4`. (cited on pp. 10 and 11)

M.O. Scully and M.S. Zubairy. *Quantum Optics*. Cambridge University Press, 1997. ISBN 9781139643061. URL `https://books.google.it/books?id=9lkgAwAAQBAJ`. (cited on pp. 65, 67, and 68)

M. Secli and I. Carusotto. Harper-hofstadter topological laser with frequency-dependent gain. In *2019 Conference on Lasers and Electro-Optics Europe European Quantum Electronics Conference (CLEO/Europe-EQEC)*, pages 1–1, 2019. (cited on p. 110)

Matteo Seclì, Massimo Capone, and Iacopo Carusotto. Theory of chiral edge state lasing in a two-dimensional topological system. *Phys. Rev. Research*, 1:033148, Dec 2019. doi: 10.1103/PhysRevResearch.1.033148. URL `https://link.aps.org/doi/10.1103/PhysRevResearch.1.033148`. (cited on pp. 79, 88, 90, 97, and 109)

I A Shelykh, A V Kavokin, Yuri G Rubo, T C H Liew, and G Malpuech. Polariton polarization-sensitive phenomena in planar semiconductor microcavities. *Semiconductor Science and Technology*, 25(1):013001, dec 2009. doi: 10.1088/0268-1242/25/1/013001. (cited on pp. 12 and 36)

L. M. Sieberer, A. Chiocchetta, A. Gambassi, U. C. Täuber, and S. Diehl. Thermodynamic equilibrium as a symmetry of the schwinger-keldysh action. *Phys. Rev. B*, 92:134307, Oct 2015. doi: 10.1103/PhysRevB.92.134307. URL `https://link.aps.org/doi/10.1103/PhysRevB.92.134307`. (cited on p. 75)

A. E. Siegman. Excess spontaneous emission in non-hermitian optical systems. i. laser amplifiers. *Phys. Rev. A*, 39:1253–1263, Feb 1989a. doi: 10.1103/PhysRevA.39.1253. URL `https://link.aps.org/doi/10.1103/PhysRevA.39.1253`. (cited on p. 99)

A. E. Siegman. Excess spontaneous emission in non-hermitian optical systems. ii. laser oscillators. *Phys. Rev. A*, 39:1264–1268, Feb 1989b. doi: 10.1103/PhysRevA.39.1264. URL `https://link.aps.org/doi/10.1103/PhysRevA.39.1264`. (cited on p. 99)

Anthony E. Siegman. *Lasers*. Oxford University Press, 1987. (cited on p. 63)

Barry Simon. Holonomy, the quantum adiabatic theorem, and berry's phase. *Phys. Rev. Lett.*, 51:2167–2170, Dec 1983. doi: 10.1103/PhysRevLett.51.2167. URL `https://link.aps.org/doi/10.1103/PhysRevLett.51.2167`. (cited on p. 85)

A. Sinatra, Y. Castin, and E. Witkowska. Coherence time of a bose-einstein condensate. *Physical Review A*, 80(3):033614, Sep 2009. ISSN 1094-1622. (cited on p. 82)

David Snoke and Peter Littlewood. Polariton condensates. *Physics Today*, 63(8):42–47, August 2010. doi: 10.1063/1.3480075. URL `https://doi.org/10.1063/1.3480075`. (cited on p. 12)

Davide Squizzato, Léonie Canet, and Anna Minguzzi. Kardar-parisi-zhang universality in the phase distributions of one-dimensional exciton-polaritons. *Phys. Rev. B*, 97:195453, May 2018. doi: 10.1103/PhysRevB.97.195453. URL `https://link.aps.org/doi/10.1103/PhysRevB.97.195453`. (cited on pp. 5, 70, 109, 110, and 111)

P. St-Jean, V. Goblot, E. Galopin, A. Lemaître, T. Ozawa, L. Le Gratiet, I. Sagnes, J. Bloch, and A. Amo. Lasing in topological edge states of a one-dimensional lattice. *Nature Photonics*, 11 (10):651–656, September 2017. doi: 10.1038/s41566-017-0006-2. URL `https://doi.org/10.1038/s41566-017-0006-2`. (cited on pp. 88 and 109)

Petr Stepanov, Ivan Amelio, Jean-Guy Rousset, Jacqueline Bloch, Aristide Lemaître, Alberto Amo, Anna Minguzzi, Iacopo Carusotto, and Maxime Richard. Dispersion relation of the collective excitations in a resonantly driven polariton fluid. *Nature Communications*, 10(1), August 2019. doi: 10.1038/s41467-019-11886-3. URL `https://doi.org/10.1038/s41467-019-11886-3`. (cited on pp. 4, 12, 16, 33, 35, 37, 38, 45, 46, 48, 52, 54, 56, and 60)

Rui Su, Sanjib Ghosh, Jun Wang, Sheng Liu, Carole Diederichs, Timothy C. H. Liew, and Qihua Xiong. Observation of exciton polariton condensation in a perovskite lattice at room temperature. *Nature Physics*, 16(3):301–306, January 2020. doi: 10.1038/s41567-019-0764-5. URL `https://doi.org/10.1038/s41567-019-0764-5`. (cited on p. 14)

Yongbao Sun, Yoseob Yoon, Mark Steger, Gangqiang Liu, Loren N. Pfeiffer, Ken West, David Snoke, and Keith A. Nelson. Direct measurement of polariton-polariton interaction strength. *Nature Physics*, 13:870 EP –, Jun 2017. URL `https://doi.org/10.1038/nphys4148`. Article. (cited on pp. 4, 35, 36, and 37)

Orazio Svelto. *Principles of Lasers*. Springer US, 2010. doi: 10.1007/978-1-4419-1302-9. URL `https://doi.org/10.1007/978-1-4419-1302-9`. (cited on pp. 63 and 68)

MH Szymańska, J Keeling, and PB Littlewood. Nonequilibrium quantum condensation in an incoherently pumped dissipative system. *Physical review letters*, 96(23):230602, 2006. (cited on p. 14)

W. C. Tait. Quantum theory of a basic light-matter interaction. *Phys. Rev. B*, 5:648–661, Jan 1972. doi: 10.1103/PhysRevB.5.648. URL `https://link.aps.org/doi/10.1103/PhysRevB.5.648`. (cited on p. 22)

N. Takemura, S. Trebaol, M. Wouters, M. T. Portella-Oberli, and B. Deveaud. Polaritonic feshbach resonance. *Nature Physics*, 10(7):500–504, June 2014. doi: 10.1038/nphys2999. URL `https://doi.org/10.1038/nphys2999`. (cited on p. 36)

Kazumasa A Takeuchi. An appetizer to modern developments on the kardar–parisi–zhang universality class. *Physica A: Statistical Mechanics and its Applications*, 504:77–105, 2018. (cited on p. 78)

F. Tassone and Y. Yamamoto. Exciton-exciton scattering dynamics in a semiconductor microcavity and stimulated scattering into polaritons. *Phys. Rev. B*, 59:10830–10842, Apr 1999. doi: 10.1103/PhysRevB.59.10830. URL `https://link.aps.org/doi/10.1103/PhysRevB.59.10830`. (cited on p. 36)

D. J. Thouless, M. Kohmoto, M. P. Nightingale, and M. den Nijs. Quantized hall conductance in a two-dimensional periodic potential. *Phys. Rev. Lett.*, 49:405–408, Aug 1982. doi: 10.1103/PhysRevLett.49.405. URL `https://link.aps.org/doi/10.1103/PhysRevLett.49.405`. (cited on pp. 85 and 86)

Hakan E. Türeci, A. Douglas Stone, and B. Collier. Self-consistent multimode lasing theory for complex or random lasing media. *Phys. Rev. A*, 74:043822, Oct 2006. doi: 10.1103/PhysRevA.74.043822. URL `https://link.aps.org/doi/10.1103/PhysRevA.74.043822`. (cited on p. 110)

K. Ueno, H. Sakaguchi, and M. Okamura. Renormalization-group and numerical analysis of a noisy kuramoto-sivashinsky equation in $1+1$ dimensions. *Phys. Rev. E*, 71:046138, Apr 2005. doi: 10.1103/PhysRevE.71.046138. URL `https://link.aps.org/doi/10.1103/PhysRevE.71.046138`. (cited on pp. 72, 77, 101, and 103)

S. Utsunomiya, L. Tian, G. Roumpos, C. W. Lai, N. Kumada, T. Fujisawa, M. Kuwata-Gonokami, A. Löffler, S. Höfling, A. Forchel, and Y. Yamamoto. Observation of bogoliubov excitations in exciton-polariton condensates. *Nature Physics*, 4(9):700–705, August 2008. doi: 10.1038/nphys1034. URL `https://doi.org/10.1038/nphys1034`. (cited on pp. 37 and 38)

Filippo Vicentini, Fabrizio Minganti, Riccardo Rota, Giuliano Orso, and Cristiano Ciuti. Critical slowing down in driven-dissipative bose-hubbard lattices. *Phys. Rev. A*, 97:013853, Jan 2018. doi: 10.1103/PhysRevA.97.013853. URL `https://link.aps.org/doi/10.1103/PhysRevA.97.013853`. (cited on p. 16)

David Vocke, Thomas Roger, Francesco Marino, Ewan M Wright, Iacopo Carusotto, Matteo Clerici, and Daniele Faccio. Experimental characterization of nonlocal photon fluids. *Optica*, 2(5):484–490, 2015. (cited on p. 60)

K. Vogel and H. Risken. Quantum-tunneling rates and stationary solutions in dispersive optical bistability. *Phys. Rev. A*, 38:2409–2422, Sep 1988. doi: 10.1103/PhysRevA.38.2409. URL `https://link.aps.org/doi/10.1103/PhysRevA.38.2409`. (cited on p. 16)

P. M. Walker, L. Tinkler, B. Royall, D. V. Skryabin, I. Farrer, D. A. Ritchie, M. S. Skolnick, and D. N. Krizhanovskii. Dark solitons in high velocity waveguide polariton fluids. *Phys. Rev. Lett.*, 119:097403, Aug 2017. doi: 10.1103/PhysRevLett.119.097403. URL `https://link.aps.org/doi/10.1103/PhysRevLett.119.097403`. (cited on pp. 4, 35, 37, 45, 46, and 48)

Daniel F Walls and Gerard J Milburn. *Quantum optics*. Springer Science & Business Media, 2007. (cited on p. 13)

Zheng Wang, Yidong Chong, J. D. Joannopoulos, and Marin Soljačić. Observation of unidirectional backscattering-immune topological electromagnetic states. *Nature*, 461(7265):772–775, October 2009. doi: 10.1038/nature08293. URL `https://doi.org/10.1038/nature08293`. (cited on p. 87)

Esther Wertz, Lydie Ferrier, DD Solnyshkov, Robert Johne, Daniele Sanvitto, Aristide Lemaître, Isabelle Sagnes, Roger Grousson, Alexey V Kavokin, Pascale Senellart, et al. Spontaneous formation and optical manipulation of extended polariton condensates. *Nature physics*, 6(11):860, 2010. (cited on p. 25)

D. M. Whittaker and P. R. Eastham. Coherence properties of the microcavity polariton condensate. *EPL (Europhysics Letters)*, 87(2):27002, jul 2009. doi: 10.1209/0295-5075/87/27002. (cited on p. 109)

Diederik S. Wiersma. The physics and applications of random lasers. *Nature Physics*, 4(5):359–367, May 2008. doi: 10.1038/nphys971. URL `https://doi.org/10.1038/nphys971`. (cited on p. 106)

T Winiecki, B Jackson, J F McCann, and C S Adams. Vortex shedding and drag in dilute bose-einstein condensates. *Journal of Physics B: Atomic, Molecular and Optical Physics*, 33(19):4069, 2000. URL `http://stacks.iop.org/0953-4075/33/i=19/a=317`. (cited on pp. 24 and 29)

S. Wittek, G. Harari, M. A. Bandres, H. Hodaei, M. Parto, P. Aleahmad, M.C. Rechtsman, Y. D. Chong, Demetri N. Christodoulides, Mercedeh Khajavikhan, and Mordechai Segev. Towards the experimental realization of the topological insulator laser. In *Conference on Lasers and Electro-Optics*, page FTh1D.3. Optical Society of America, 2017. doi: 10.1364/CLEO_QELS.2017.FTh1D.3. URL `http://www.osapublishing.org/abstract.cfm?URI=CLEO_QELS-2017-FTh1D.3`. (cited on p. 109)

M. Wouters, T. K. Paraïso, Y. Léger, R. Cerna, F. Morier-Genoud, M. T. Portella-Oberli, and B. Deveaud-Plédran. Influence of a nonradiative reservoir on polariton spin multistability. *Phys. Rev. B*, 87:045303, Jan 2013. doi: 10.1103/PhysRevB.87.045303. URL `https://link.aps.org/doi/10.1103/PhysRevB.87.045303`. (cited on p. 37)

Michiel Wouters. Resonant polariton-polariton scattering in semiconductor microcavities. *Phys. Rev. B*, 76:045319, Jul 2007. doi: 10.1103/PhysRevB.76.045319. URL `https://link.aps.org/doi/10.1103/PhysRevB.76.045319`. (cited on p. 36)

Michiel Wouters and Iacopo Carusotto. Excitations in a nonequilibrium bose-einstein condensate of exciton polaritons. *Phys. Rev. Lett.*, 99:140402, Oct 2007. doi: 10.1103/PhysRevLett.99.140402. URL `https://link.aps.org/doi/10.1103/PhysRevLett.99.140402`. (cited on pp. 14, 50, 57, 71, 79, and 92)

Michiel Wouters and Iacopo Carusotto. Probing the excitation spectrum of polariton condensates. *Phys. Rev. B*, 79:125311, Mar 2009. doi: 10.1103/PhysRevB.79.125311. URL `https://link.aps.org/doi/10.1103/PhysRevB.79.125311`. (cited on p. 38)

Michiel Wouters and Iacopo Carusotto. Superfluidity and critical velocities in nonequilibrium bose-einstein condensates. *Phys. Rev. Lett.*, 105(2), JUL 8 2010. ISSN 0031-9007. doi: 10.1103/PhysRevLett.105.020602. (cited on pp. 18, 22, and 23)

Zhaoju Yang, Eran Lustig, Gal Harari, Yonatan Plotnik, Yaakov Lumer, Miguel A. Bandres, and Mordechai Segev. Mode-locked topological insulator laser utilizing synthetic dimensions. *Phys. Rev. X*, 10:011059, Mar 2020. doi: 10.1103/PhysRevX.10.011059. URL `https://link.aps.org/doi/10.1103/PhysRevX.10.011059`. (cited on pp. 88 and 111)

Peter Yu and Manuel Cardona. *Fundamentals of semiconductors: physics and materials properties*. Springer Science & Business Media, 2010. (cited on pp. 4 and 11)

Joanna M. Zajac and Wolfgang Langbein. Parametric scattering of microcavity polaritons into ghost branches. *Phys. Rev. B*, 92:165305, Oct 2015. doi: 10.1103/PhysRevB.92.165305. URL `https://link.aps.org/doi/10.1103/PhysRevB.92.165305`. (cited on p. 38)

Petr Zapletal, Bogdan Galilo, and Andreas Nunnenkamp. Long-lived elementary excitations and light coherence in topological lasers. *Optica*, 7(9):1045, August 2020. doi: 10.1364/optica.391718. URL `https://doi.org/10.1364/optica.391718`. (cited on pp. 94 and 108)

Yongquan Zeng, Udvas Chattopadhyay, Bofeng Zhu, Bo Qiang, Jinghao Li, Yuhao Jin, Lianhe Li, Alexander Giles Davies, Edmund Harold Linfield, Baile Zhang, Yidong Chong, and Qi Jie Wang. Electrically pumped topological laser with valley edge modes. *Nature*, 578(7794): 246–250, February 2020. doi: 10.1038/s41586-020-1981-x. URL `https://doi.org/10.1038/s41586-020-1981-x`. (cited on pp. 5, 88, and 109)

Jing Zhang, Bo Peng, Şahin Kaya Özdemir, Kevin Pichler, Dmitry O. Krimer, Guangming Zhao, Franco Nori, Yu xi Liu, Stefan Rotter, and Lan Yang. A phonon laser operating at an exceptional point. *Nature Photonics*, 12(8):479–484, July 2018. doi: 10.1038/s41566-018-0213-5. URL `https://doi.org/10.1038/s41566-018-0213-5`. (cited on p. 117)